Università degli Studi di Cagliari

PHD DEGREE

Cycle XXXIII

TITLE OF THE PHD THESIS

Light vector meson production at forward rapidity in pp collisions at $\sqrt{s}$ = 5.02 TeV with ALICE

Scientific Disciplinary Sector(s)

Particle and nuclear Physics

PhD Student:	Mr. Alex Chauvin
Coordinator of the PhD Programme	Prof. Paolo Ruggerone
Supervisor	Prof. Alessandro De Falco

Final exam. Academic Year 2020 – 2021
Thesis defence: March 2021 Session

À celle qui m’a fait écrire ces mots mais qui ne pourra pas les lire

Abstract

Among the four fundamental forces, three of them occur at low scale. These three forces are all described in the so-called Standard Model of particles. Among them the force keeping the protons and neutrons bound together, the strong force, is of special interest in this presentation. This force is described by the Quantum Chromo-Dynamics (QCD) theory. Hadrons, such as protons and neutrons, are composed of gluons and quarks. Quarks are kept bound, at least by pairs by the strong force mediated via the gluons and cannot be dissociated. Only in the case of a high energy density (equivalent to high temperature) or at high baryon chemical potential, quarks and gluons can propagate freely, forming a Quark Gluon Plasma (QGP). This state is expected to have existed during the first micro- seconds of the Universe. These extreme conditions can actually be reproduced using heavy-ion collisions at the Large Hadron Collider (LHC). The QGP is expected to be created in the most central heavy ion collisions such as in Pb-Pb collisions at $\sqrt{s_{NN}}$ = 5.02 TeV. Used as a reference, pp collisions where the QGP is not expected to be created are also performed. The QGP can be studied, and its equation of state evaluated investigating the particle yields resulting from these collisions. Different probes of existence of the QGP are studied, in this thesis we investigate the low mass vector mesons with the dimuon decay channel at low mass ($m_{\mu\mu}$ <2 GeV/c^2) measured in A Large Ion Collider Experiment (ALICE). Only interacting electroweakly within the medium, the dimuon decay channel is considered as a clean probe and allows the reconstruction of various mesons among which the ω and the ϕ meson. Due to its $s\bar{s}$ content, the ϕ meson has the particularity of having strange content, but a null net strangeness content. For this reason, the ϕ meson is a particular probe to study the so-called strangeness enhancement, an effect proposed as a signature of the QGP. However, the ω meson is composed of light flavour quarks and can be used as a reference for a strange hadron production.

Recently observed in small collision systems (such as pp), the strangeness enhancement is benefiting of a regain of interest. In this thesis the results on the ω and ϕ mesons production in pp collision at $\sqrt{s}$ = 5.02 TeV at forward rapidity with ALICE is presented. This thesis present the production of these mesons as a function of their transverse momentum, rapidity and multiplicity and the comparison to various model predictions.

Acknowledgement

I would like first to thank the University of Cagliari, and more especially the Physics department of Cagliari for the financing of this work and for hosting me during these three years.

The ALICE group of Cagliari gave me the possibility to work on low-mass dilepton. I thank Alessandro De Falco, my supervisor during these three years for his patience and Ester for our discussions on the muon arm.

Je tiens notament à remercier le groupe ALICE de Lyon, et notamment Antonio Uras et Brigitte Cheynis qui m'ont acceulli pendant plusieurs mois à l'INPL, ou plutôt à l'IP2I. Evidemment un grand merci à Antonio avec qui la transition Sardaigne-France fit plus facile. Il n'est sans dire que j'ai beaucoup apprécié le temps qu'il a pris pour répondre à mes questions, surtout quand celles-ci venaient en fin de journée. En plus de la pertinences de ses remarques quant à mon analyse, il y avait aussi la forme. Quand la frustration de buter sur un problème peut monter, il est toujours mieux d'avoir quelqu'un qui arrive à toujours gérer la situation *con calma*. Il en va de même pour Brigitte pour qui *avec gaieté* irait mieux. Merci à elle pour avoir toujours été disponible, et pour amener de la complicité dans le groupe. Il est sans dire que j'ai apprécié nos moment à Lyon, surtout quand il s'agissait d'organiser une dégustation de foie gras. Je remercie aussi mes compagnones de bureau Lucrezia ainsi que Yanchun pour les échanges que l'ont a eus, que ce soit sur l'estimation de la multiplicité ou bien sur Baby K. Je ne peux que leur souhaiter le meilleurs pour leurs thèses.

It is also important to me to thanks the ALICE collaboration and especially the PWG-LF that gave me many useful feedback on my work.

Obviously I can not omit my origins, and especially Mr. T., the Haaland of Physics and all the team from Munich. Thanks to them and to all the good moments there, I am LMEE4ever.

I thank also my colleagues from Cagliari for their support and for introducing me to Sar-

dinia, I can only wish the best to all of them. A special thanks to Samuel parce découvrir un nouveau pays c'est toujours mieux à deux.

Pour finir je voudrais remercier ma famille pour leur support constant et surtout à ma soeur pour avoir pu être là où je n'étais pas.

Contents

Introduction

Low mass vector meson (ρ, ω, ϕ) production provides key information on the hot and dense state of strongly interacting matter produced in high-energy heavy ion collisions. Among the different probes, strangeness enhancement can be accessed through the measurement of ϕ meson production. Although expected to occur only in the most central heavy-ion collisions, strangeness enhancement was recently observed in smaller collision systems such as pp and p-Pb. Furthermore, the general measurement of particle production is of special interest as so far no general model can fully describe this effect (meaning the kinematic distributions, the yield and correlations of vector mesons all together). Indeed at low transverse momentum (p_{T}), non-perturbative processes dominate, described by various phenomenological models, while at high p_{T}, particle production can be obtained from perturbative calculations [1].

pp collisions are considered as a baseline for heavy-ion collisions, since they are not expected to create a hot and dense state of strongly interacting matter. In recent measurements performed at CERN by the ALICE and CMS experiments, features such as strangeness enhancement were observed in these collisions. Indeed, recent measurements have shown that the effects such as strangeness enhancement do not depend on the collision system nor its energy, but rather on the multiplicity of the event.

The aim of this work is to study the production of the ϕ and ω mesons in pp collisions at $\sqrt{s}$ = 5.02 TeV. Their production is studied at forward rapidity $2.5 < y < 4$ in their dimuon decay channel using the ALICE detector. A general appendix explaining the different variables used in high energy physics, and more generally in ALICE can be found in A.

This thesis will present in Chapter 1 a general overview of the Physics motivations for the measurements performed, and will also present the latest results related to this topic. In Chapter 2 the ALICE apparatus is described, with particular attention to the muon spectrometer,

the main detector used in the analysis presented in this work. Chapter 3 presents the general framework to perform the extraction of low-mass dimuons. On top of the different techniques used to analyse the signal, this chapter will also cover the parametrisation of the Monte Carlo generator used in the analysis. Chapter 4 presents the results obtained on the measurement of the ω and ϕ production at $\sqrt{s}$ =5.02 TeV as a function of kinematic variables such as their transverse momentum (p_{T}) and rapidity (y). In this Chapter, the results obtained at 5.02 TeV are compared to the other measurements performed at other centre-of-mass energy, and at central rapidity. Chapter 5 focuses on the ω and ϕ production as a function of multiplicity. A particular focus on the multiplicity estimation will also be presented in this chapter.

Chapter 1

Physics motivations

1.1 Quantum Chromodynamics in the Standard Model

1.1.1 The Standard Model

The Standard Model is a general framework theory developed during the last 60 years aiming to describe three out of the four fundamental forces observed in nature. The Standard Model describes the electromagnetic, weak and strong interactions under a single model considering quantum dynamics and special relativity[2]. Introducing the quark model in the mid-60^s [3], predicting an existing substructure of baryons and mesons, the Standard Model has been reinforced by the discoveries of all its predicted fundamental particles such as the tau neutrino[4], the top quark[5][6], and the latest, the Higgs boson[7].

Considering group theory, this framework relies on the symmetries observed between the different fundamental particles depending on their various characteristics: mass, spin, isospin, hypercharge, electric charge, colour charge, leptonic number and other quantum numbers. Mathematically, the Standard Model(SM) is represented by the symmetry

$$G_{SM} = SU(3)_c \times SU(2)_L \times U(1)_Y. \tag{1.1}$$

The $SU(3)_c$ component represents the symmetry acting on the colour charge responsible for the strong interaction, between quarks and gluons. The theory that describes this interaction is Quantum ChromoDynamics (QCD). The $SU(2)_L \times U(1)_Y$ part of the group represents the

symmetry acting on left-handed particles (L) and with an hypercharge (Y). These two last elements incorporate both the weak and electromagnetic part of the model, and are generally referred to as the electroweak part of the Standard Model.

In the Standard Model, the fundamental particles, either fermions or bosons, all summarised in figure 1.1, have distinct roles:

- fermions: they are classified into 3 different generations, of quarks (u,d), (s,c), (t,b) and leptons (e^-,ν_{e^-}), (μ^-,ν_{μ^-}), (τ^-,ν_{τ^-}). Quarks are the elemental parts of composite particles such as baryons (made up of 3 quarks) and mesons (made of a quark and an antiquark).

- bosons: they mediate the different interactions. The gauge bosons are the ones carrying the different forces: the γ is the mediator of the electromagnetic force, the $W^{+/-}$ and the Z^0 are respectively the charged and neutral current of the weak interaction and the gluons (g) carry the strong interaction. Then comes the Higgs boson (also called Brout-Englert-Higgs boson), a Goldstone boson created by the spontaneous symmetry breaking of the $SU(2)_L \times U(1)_Y$ symmetry. The coupling of particles to the field created by the Higgs bosons will assign them a mass.

1.1.2 Quantum ChromoDynamics

Quarks cannot be observed alone. Instead they associate among each others and create colourless bound states called hadrons. They can either be mesons or baryons.

Since baryons such as the Δ^{++} made of three up quarks (uuu) exist and in order not to violate the Pauli exclusion rule, an additional degree of freedom is associated to each up quark: the so-called colour charge which can take three values, named red(r), blue(b), green(g) (and corresponding anticolours). This is the basis of the construction of the $SU(N_c = 3)_c$ symmetry group, where gluons are the vectors in the adjoint representation. Hence, there are $N_c^2 - 1 = 8$ different gluons as listed below:

- $(r\bar{b} + b\bar{r})/\sqrt{2}$
- $-i(r\bar{b} - b\bar{r})/\sqrt{2}$
- $(r\bar{g} + g\bar{r})/\sqrt{2}$
- $-i(r\bar{g} - g\bar{r})/\sqrt{2}$
- $(b\bar{g} + g\bar{b})/\sqrt{2}$
- $-i(b\bar{g} - g\bar{b})/\sqrt{2}$

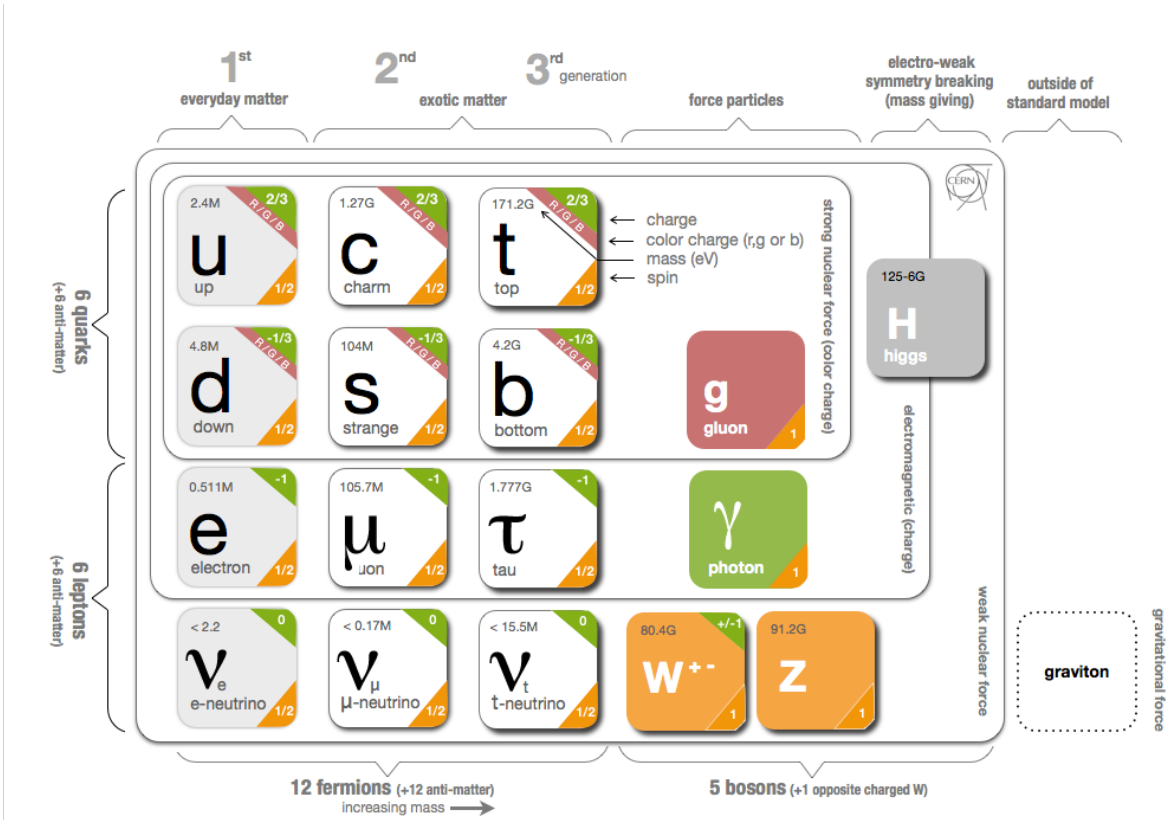

Figure 1.1: Table summarising the different fundamental particles from the Standard model

- $(r\bar{r} - b\bar{b})/\sqrt{2}$
- $(r\bar{r} + b\bar{b} - 2g\bar{g})/\sqrt{6}$

The strong force is represented by the exchange of gluons among coloured particles such as gluons themselves and quarks, giving the name of Quantum ChromoDynamics(QCD) to this model. The potential between the quarks can be expressed as

$$V(r) = -\frac{4}{3}\frac{\alpha_S \hbar c}{r} + kr, \tag{1.2}$$

where r is the distance between two quarks, $\hbar$ the Planck's constant, α_S the coupling constant, and k a constant with a measured value of 0.85 GeV/fm. This potential will then increase infinitely with the distance between two quarks .

1.1.2.1 The running coupling constant α_S

Concerning the coupling constant α_S, it has to be pointed out that this value is not a proper constant value, but varies with the transferred momentum Q in deep inelastic scatterings mediated by the strong force where $Q \gg m_q$, with m_q the mass of light quarks. At first order, the running coupling constant $\alpha_S(Q)$ can be expressed as

$$\alpha_S(Q) = \frac{6\pi}{(11N_c - 2N_f)ln(Q/\Lambda_{QCD})}, \tag{1.3}$$

where N_c and N_f represent respectively the number of colors (3) and light flavour quarks for which $m_q \ll \Lambda_{QCD} \sim 260$ MeV with Λ_{QCD} being a parameter referred to as the QCD-scale.

As shown in figure 1.2, the values obtained from various collision systems and in different observation channels coincide with the predictions obtained by perturbative QCD theory. From the trend of α_S, it can be observed that for low-Q values, α_S is becoming large, leading to color confinement. For large Q ($\gg \Lambda_{QCD}$) oppositely the coupling strength becomes negligible, leading to the so-called asymptotic freedom regime.

1.1.2.2 Chiral symmetry

Another property of the QCD lagrangian is the chiral symmetry, meaning a symmetry of the system by the transformation of the helicity [1] of quarks considered in the limit of $m_q = 0$. This symmetry is respected only in the case of $m_q = 0$ which can be considered approximately true for u and d quarks with a lagrangian mass of $m_q \sim 0$. However when considered in vacuum ($T = 0$), the quarks are dressed with gluons, resulting in a larger effective mass $m_q^{eff.} \sim 300$ MeV. This implies that the mass of quarks is generated spontaneously during the confinement, and reciprocally restored during deconfinement, leading to the chiral symmetry restoration.

A common way to look at this symmetry is to consider a condensate of quarks in the QCD vacuum as

$$< 0|\Psi\overline{\Psi}|0 > = < \Psi\overline{\Psi} > = < \overline{\Psi_L}\Psi_R + \overline{\Psi_R}\Psi_L > = 0, \tag{1.4}$$

[1] The helicity is the projection of the spin of a particle on its momentum: $h = \overrightarrow{s} \cdot \overrightarrow{p} \;/\; \| \overrightarrow{p} \|$. If the value of the helicity is positive, the particle is considered as right-handed, in the opposite case it is considered as left-handed

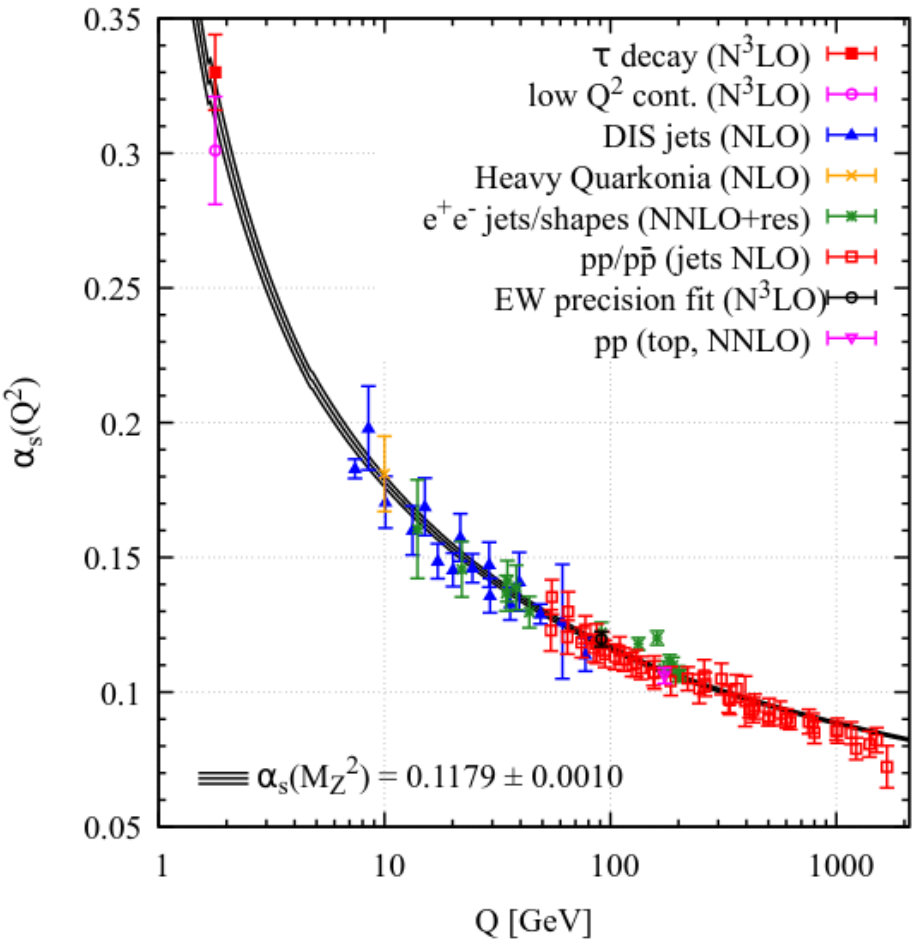

Figure 1.2: Summary of measurements of α_S as a function of momentum transfer Q. The respective degrees of pQCD calculation used for the extraction of α_S are indicated [8]

where Ψ represents a quark field, which can be decomposed into left and right handed components as

$$\Psi_{L,R} \rightarrow \frac{1}{2}(1 \pm \gamma_5)\Psi. \tag{1.5}$$

As the handness of the quark field is conserved under chiral symmetry in the limit of massless quarks, a null vaccum expectation value $< \Psi\overline{\Psi} > = 0$ is obtained for a high energy density such as in the Quark Gluon Plasma (QGP) [9].

Nevertheless a mass difference between chiral partners such as ρ (vector meson) and a_1(axial vector meson) is observed: $m_\rho = 776\ MeV/c^2$ while $m_{a_1} = 1230\ MeV/c^2$, implying a spontaneous breaking of the chiral symmetry at finite temperature $< \Psi\overline{\Psi} > (T) \neq 0$ [10].

1.2 The Quark Gluon Plasma

1.2.1 A new state of matter

As originally indicated in 1964[11] and later developed[12], above a certain critical temperature T_C the hadronic matter cannot exist anymore. Hadrons are dimensionful colour-neutral bound states of more basic pointlike coloured quarks and gluons. Above T_C this treatment of hadronic matter no longer stands, instead it is treated considering its pointlike coloured quarks and gluons constituents (becoming the degrees of freedom of the system) [13]. This deconfinement transition leads to a colour-conducting state called the Quark Gluon Plasma (QGP). The phase diagram of the strongly interacting matter can be shown as a function of the temperature and of the baryon chemical potential μ_B (corresponding to the energy needed to add one more baryon to the system) as shown in figure 1.3, where the QGP appears as the phase that can be obtained increasing T or μ_B.

In order to make predictions on the existence of such state of matter, the use of lattice QCD (lQCD) is required. Lattice QCD is an approach which allows to explore the non-perturbative domain of QCD matter by discretizing the QCD lagrangian in a 2-dimensional lattice [14]. The space between two lattice sites, defining the resolution of the calculation, can be minimized to $\sim 1/\Lambda_{QCD}$, leading to the recovery of the QCD continuum. To perform these calculation, several parameters, like the masses of the light quarks and mesons, are used as input. At finite temperature, lQCD allows to study the QCD equation of state, which can be used to characterise the transition of the hadronic matter to QGP. According to this technique, an existing cross-over as shown in figure 1.4 is found at low μ_B for a temperature close to the critical temperature T_C, where a mixed phase of QGP and hadron gas could exist. On top of this, the lQCD also predicts the existence of a critical point where for higher baryonic chemical potential the transition from QGP to the hadron gas becomes of the first order.

Out of the region of validity of the lQCD, at high μ_B and low temperature, the existence of color superconductors is expected. These high baryo-chemical potential values could be present in neutron stars [16], which would turn them into another source of observables to complete the picture of the Equation of State (EoS) of the QGP.

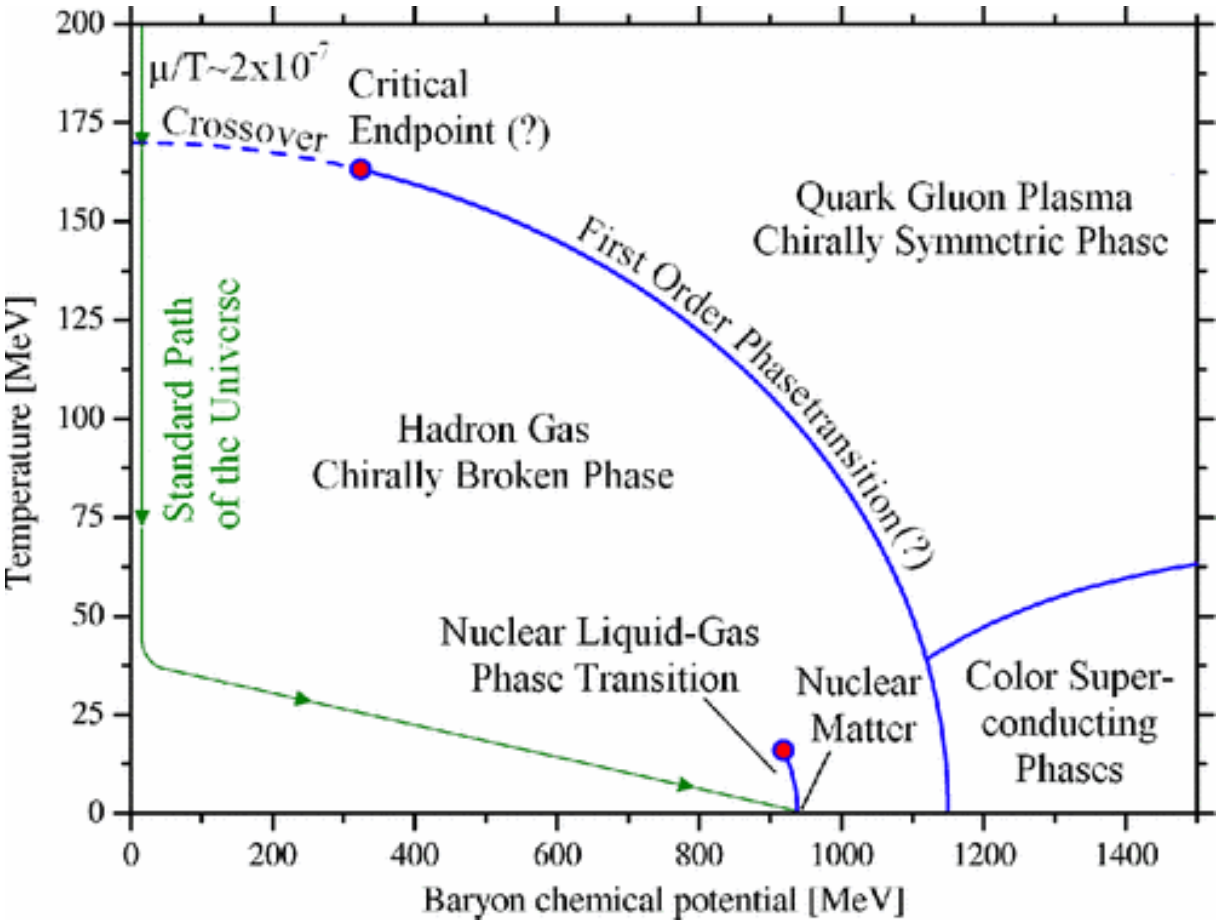

Figure 1.3: Phase diagram of the Quark Gluon plasma. The green line indicates the supposed history of hadronic matter in the very first moments after the Big Bang.

1.2.2 Creating the QGP

As discussed in the previous section, in order to create the QGP, a high temperature and/or energy density has to be reached. These conditions are expected to be satisfied in ultra-relativistic heavy-ion collisions. Then, depending on the beam used and its energy, the medium created in the collision will stand in a specific place in the T-μ_B plane, possibly reaching the critical energy density ϵ_C.

The model describing the full evolution of the medium created in these collisions is the Bjorken model[17]. This model gives a description of the system evolution along time and space using hydrodynamics and Boltzmann statistics, starting from the collision at $\tau_0 = 0$ and colliding particles with a radius R. The crossing time of the colliding particles will then be

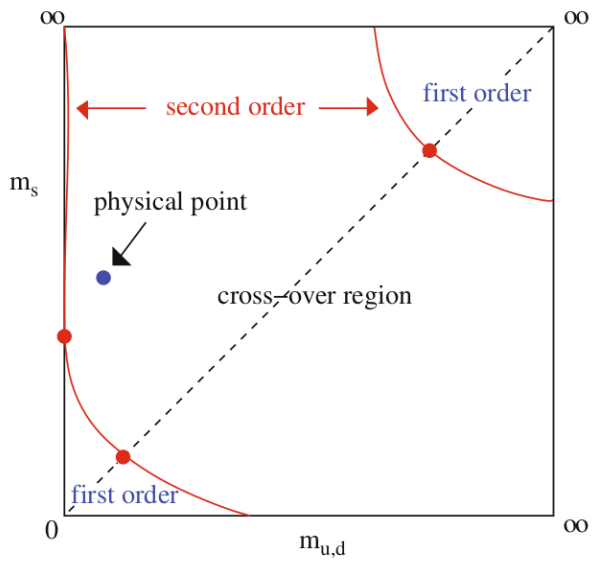

Figure 1.4: Lattice QCD results for the order of the phase transition from Quark Gluon Plasma to hadron gas at baryon density $\mu_B = 0$ [15]

$\tau_{cross} = 2R/\gamma \sim 0.2fm/c$, with γ the Lorentz factor.

The various stages of the collision are the following:

- $\tau_0 < \tau < \tau_{Eq}$ (1 fm/c): the pre-equilibrium state occurring right after the collision, when multiple interactions occur among the different partons involved in the reaction, until the thermalisation of the medium is reached;

- $\tau_{Eq} < \tau < \tau_{Hadr.}$ (10 fm/c): when thermalization is reached, if the energy density is larger than the critical one a quark-gluon plasma is created. The medium then expands following the laws of hydrodynamics. When expanding, the medium cools down until its temperature falls below the critical temperature T_C and partons hadronise;

- $\tau_{Hadr.} < \tau < \tau_{Ch.}$: then the system still remains in a chemical equilibrium until reaching a chemical freezeout temperature $T_{Ch.}$, starting from which the number of different particle species is fixed;

- $\tau_{Ch.} < \tau < \tau_{Kin.}$ (20-50 fm/c): then the produced particles can still interact between each other through elastic collisions while flying away; the kinematic freeze-out is then

reached at temperature T_{fo}, when particles cannot interact anymore and just propagate to the detector.

1.3 Hadron production via dilepton decay

Dilepton production is one of the main channels to investigate the QGP. Produced at various stages of the collisions, dileptons, which consist of a pair of correlated leptons (e^+e^-, $\mu^+\mu^-$), can be considered as the clock of the collision. Originating from the decay of a large variety of particles, their study invokes different physical processes of interest. Since dileptons only interact electromagnetically (and electroweakly), they can be propagated directly from their creation to detectors without interacting with the QGP. For this reason dileptons are considered as clean probes for the QGP investigation. At low (invariant) masses the dileptons ($m_{ll} < 2$ GeV/c) are coming from two main sources: light-flavour mesons and open heavy flavour decays.

The QGP is expected to be thermalised leading to a black-body radiation reflecting its temperature. The produced thermal photons could decay into lepton pairs which would enter the low-mass region[2].

1.3.1 Open-Heavy Flavours

Heavy flavour (charm, bottom, $Q\overline{Q}$) pairs are produced at the early stages of the collision via inelastic hard-scattering processes[18]. Once created, heavy quarks can hadronise separately, mostly forming hadrons with light flavour quarks such as the $D^{0,\pm}$ (charmed mesons) or a $B^{0,\pm}$ (bottom meson). It can be noted that baryons such as the Λ_c^+ ($= udc$) and Λ_b^0 ($= udb$) can also be created but at lower rates.

Due to the large mass of the heavy-flavour quarks composing them, these mesons carry the information from the initial $Q\overline{Q}$ pair. Bottom and charmed hadrons can then decay semi-leptonically with a branching ratio of about 10%, as represented on the schematic view in

[2]Since this thesis focuses on pp collisions at $\sqrt{s}$ =5.02 TeV, this contribution is not considered and further details are not given.

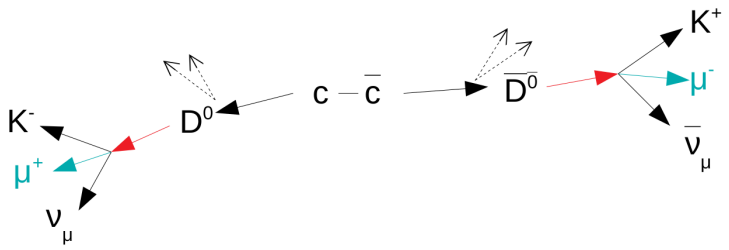

Figure 1.5: Schematic view of a pair of open-charm hadrons both undergoing a semi-muonic decay

figure 1.5. Thus if both open-heavy flavour hadrons decay semi-leptonically, a correlated opposite charged lepton pair is created carrying the information on the original $Q\overline{Q}$ state.

Since leptons are created in independent decays and part of the energy is carried by the other decay products, the invariant mass distribution of these correlated lepton pairs results in a continuum dominating the dilepton signal in the mass region from the ϕ peak to the J/Ψ peak resonances(1-3 GeV/c^2). The contribution from open-heavy flavours was measured in pp collisions at $\sqrt{s}$ = 13 TeV by ALICE via the dielectron decay channel [19] and results are shown in figure 1.6. From this results the contribution from open-heavy flavours is shown to dominate the invariant mass spectrum for 1.5< m <2.5 GeV/c^2.

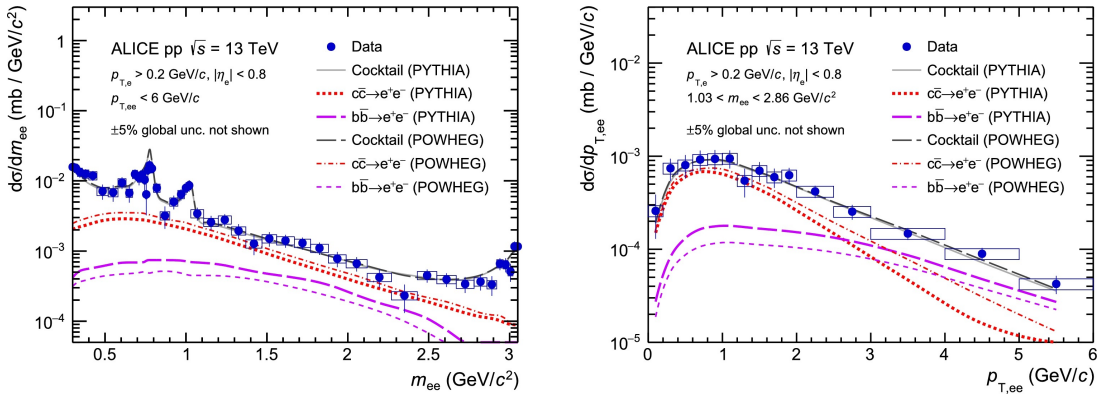

Figure 1.6: Invariant mass (**left**) and $p_{T,ee}$ (**right**) spectra of e^+e^- pairs measured by ALICE in inelastic pp collisions at $\sqrt{s}$ = 13 TeV [19]

1.3.2 Hadron Decays

Focusing on hadrons decaying into dileptons in the low-mass region ($m_{l^+l^-} < 1.5$ GeV/c^2, the main contributors are the η, η', ρ, ω and ϕ mesons. Following the SU(3) representation of flavours in the quark model considering the 3 light quarks (u, d and s), there are nine possible combinations to form a meson as shown in:

$$3 \times \overline{3} = 8 \oplus 1 \tag{1.6}$$

The physical states are actually a mixing of the SU(3) octet Φ_8 and singlet Φ_1 having the same J^{PC}[3] quantum numbers defined as follows:

$$\begin{aligned} \psi_1 &= \frac{1}{\sqrt{3}}(u\overline{u} + d\overline{d} - 2s\overline{s}), \\ \psi_8 &= \frac{1}{\sqrt{6}}(u\overline{u} + d\overline{d} + s\overline{s}) \end{aligned} \tag{1.7}$$

then applying the mixture such that

$$\begin{aligned} f\prime &= \psi_8 cos\theta - \psi_1 sin\theta, \\ f &= \psi_8 sin\theta + \psi_1 cos\theta \end{aligned} \tag{1.8}$$

with θ the mixing angle.

In the case of the η and η' mesons having $J^{PC} = 0^{-+}$ a mixing angle of $\theta_P = -11.3°$ and $\theta_P = -14.1(2.8)°$ is found (where P stands for pseudo-scalar)[20] based on lQCD calculation.

The η-meson has a mass of 547.862 $\pm$ 0.017 MeV and can either decay into a muon pair with a Branching Ratio (BR) of BR ($\eta \rightarrow \mu^+\mu^-$) = $(5.8 \pm 0.8) \times 10^{-6}$ or via a Dalitz-decay with BR ($\eta \rightarrow \gamma\mu^+\mu^-$)) = $(3.1 \pm 0.4) \times 10^{-4}$ [8]. In the case of a Dalitz-decay the η-meson decays into one real and one virtual photon decaying in a second step in a muon pair ($\eta \rightarrow \gamma\gamma* \rightarrow \gamma\mu^+\mu^-$). The η-meson can also decay into two virtual photons, but due to helicity conservation this decay is suppressed. The various possible decays of the η-meson in muon pairs are shown in figure 1.7.

The $\eta\prime$-meson has a mass of 957.78 $\pm$ 0.06 MeV and can create a muon pair via a Dalitz-decay with BR($\eta\prime \rightarrow \gamma\mu^+\mu^-$) = $1.09 \pm 0.27 \times 10^{-4}$[8].

[3] J stands for the total angular momentum of the meson, P is the parity defined as P = $(-1)^{l+1}$ with l the orbital angular momentum, C is the charge conjugation obtained as C = $(-1)^{l+s}$ with s=0 if the quark spins are

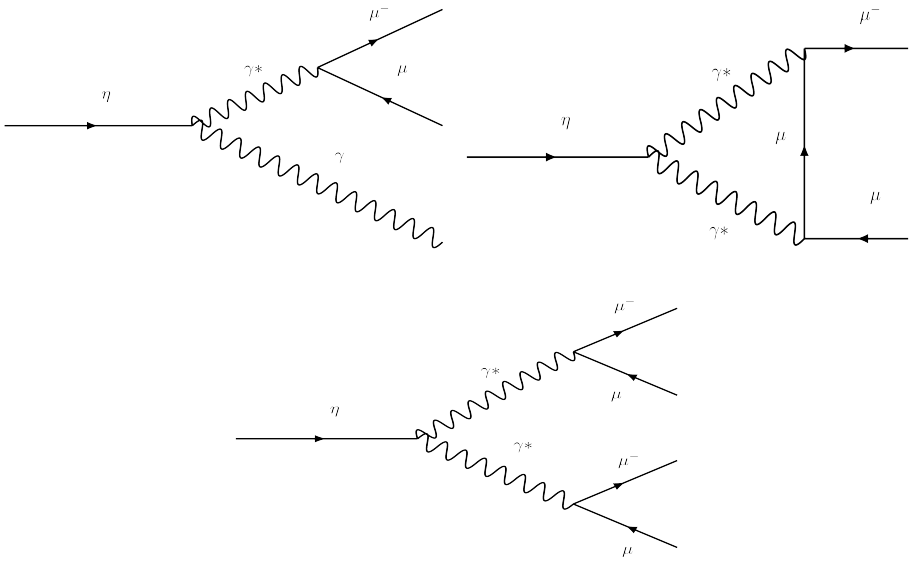

Figure 1.7: Feynman diagrams of the η-meson decays contributing to the dimuon channel. The top left diagram represent the Dalitz decay, the top right one the dimuon decay, and the bottom one the double virtual photon decay.

For what concerns the vector mesons with $J^{PC} = 1^{--}$, the mixing as described in equation 1.8 is also applied. In this case the mixing angle is $\theta_V = 39.2°$, a value close to the pure value (35.3°) for which the ϕ meson would be in a pure $s\overline{s}$ state. The ω, ϕ and ρ mesons can then be considered as

$$\phi \sim s\overline{s}, \tag{1.9}$$

$$\omega \sim \frac{1}{\sqrt{2}}(u\overline{u} + d\overline{d}), \tag{1.10}$$

$$\rho \sim \frac{1}{\sqrt{2}}(u\overline{u} - d\overline{d}). \tag{1.11}$$

The ρ meson has a non-null isospin I=1, which is the neutral state of the isospin-triplet (also called ρ^0). Due to its small lifetime $\tau_\rho \approx 1.3$ fm/c, the ρ meson actually presents a broad resonance, with a 147.8 $\pm$ 0.9 MeV $/c^2$ width.

The ϕ-meson has a mass of 1019.461$\pm$0.016 MeV $/c^2$ while the ω and the ρ have similar masses, respectively of 782.65$\pm$0.12 MeV $/c^2$ and 775.26$\pm$0.25 MeV $/c^2$. All these vector mesons can decay into a pair of leptons, with the exception for the ω the possibility to have

antiparallel and s=1 if they are parallel.

a Dalitz decay with a neutral pion and a virtual photon ($\omega \rightarrow \pi^0\gamma\star \rightarrow \pi^0\mu^+\mu^-$). Having a longer lifetime respectively of 23 and 46 fm/c, the ω and the ϕ mesons show a smaller resonance width.

In the presence of a QGP, the hadronisation processes occurs right after passing the (predicted) cross-over. Thus, the different production rates of these particles give an insight of the partial restoration of chiral symmetry[21]. Actually, from calculations, depending on the lifetime of hadrons, their spectral distribution is expected to be modified as one can see in figure 1.8.

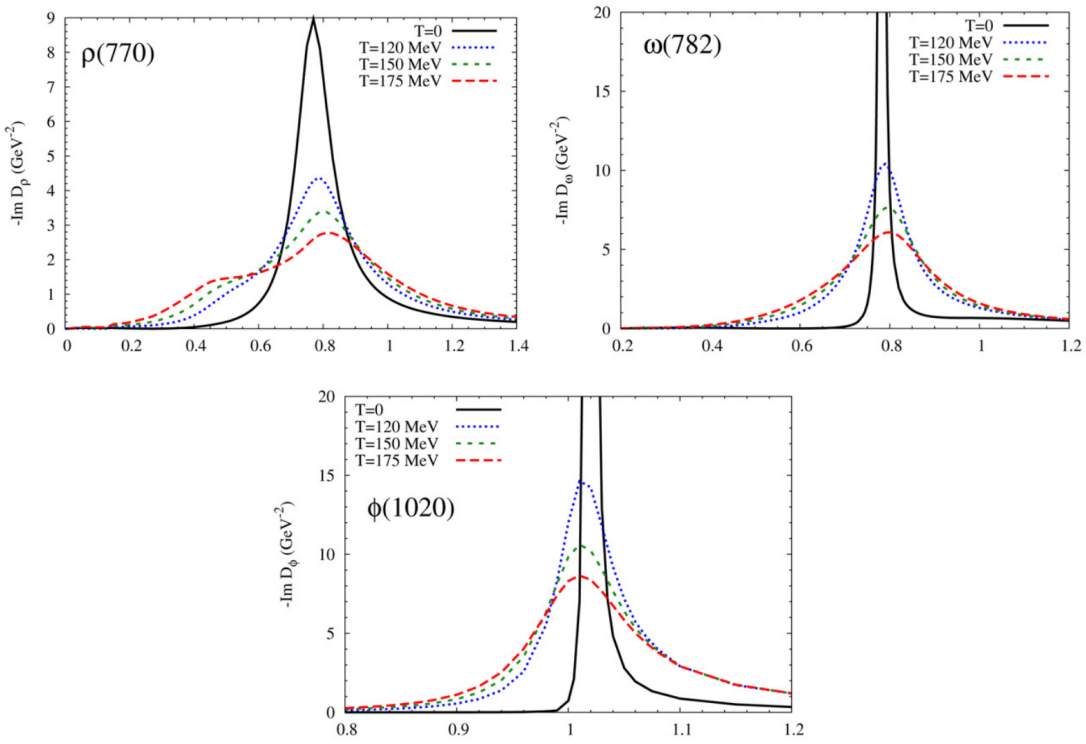

Figure 1.8: In-medium spectral functions for the ρ, ω and ϕ mesons at different stage of the evolution of the medium at SPS energy obtain from theoretical predictions [22]

1.4 Strangeness as a probe of the QGP

1.4.1 Hadronisation process

Up to now lattice QCD remains the only method to describe and predict particle production in nucleus-nucleus collisions evaluating the QCD lagrangian statistically. The hadronisation process can be described using a bulk model where the behaviour of the system created during a collision reaches a temperature $T \leq T_c$, where T_c is a transition (from confined to deconfined matter) temperature found to be 154 ± 9 MeV [23] or 156 ± 9 MeV[24] depending on the model for a small, non-vanishing μ_b such as in systems produced in collisions at the LHC. Thus the system can be described as an hadronic gas as:

$$\frac{P}{T^4} = \frac{1}{T^3} \frac{\partial ln(Z(V,T,\mu))}{\partial V} \tag{1.12}$$

where P is the pressure, T the temperature, V the volume and μ ($= \mu_B, \mu_Q, \mu_s$) the chemical potential encoding the baryonic, electric charge and strangeness state of the hadron gas.

Fitting this model to results obtained by the ALICE collaboration as in [25], the different variables of the models can be extracted via the measurement of the yield of light flavour hadrons at mid-rapidity [26][27]. A temperature $T_{cf} = 156.5 \pm 1.5$ MeV for the chemical freeze-out is found (coinciding within errors with T_c predicted by lQCD). A baryonic chemical potential consistent with zero, $\mu_B = 0.7 \pm 3.8\, MeV$ and a volume $V = 5280 \pm 410\, fm^3$ of the fireball is obtained for the most central Pb-Pb collisions (0-10%) at $\sqrt{s_{NN}} = 2.76\, TeV$[4]. The best fit of this model to the measurements performed in ALICE [26]-[28] is shown in figure 1.9. An overall agreement of this thermal model with the yield of light, anti and upper nuclei is found. The deviations observed for protons and the Ξ show that the first would prefer a lower T_{cf} while the second a higher T_{cf}. These deviations still require to be understood if they are coming from physical processes not taken into account of the thermal model, or could be neglected invoking the Occam's razor principle.

[4] In this model, no strangeness suppression factor γ_S is considered and the strangeness chemical potential ensures the conservation on average such that $V \sum_i n - iS_i = 0$.

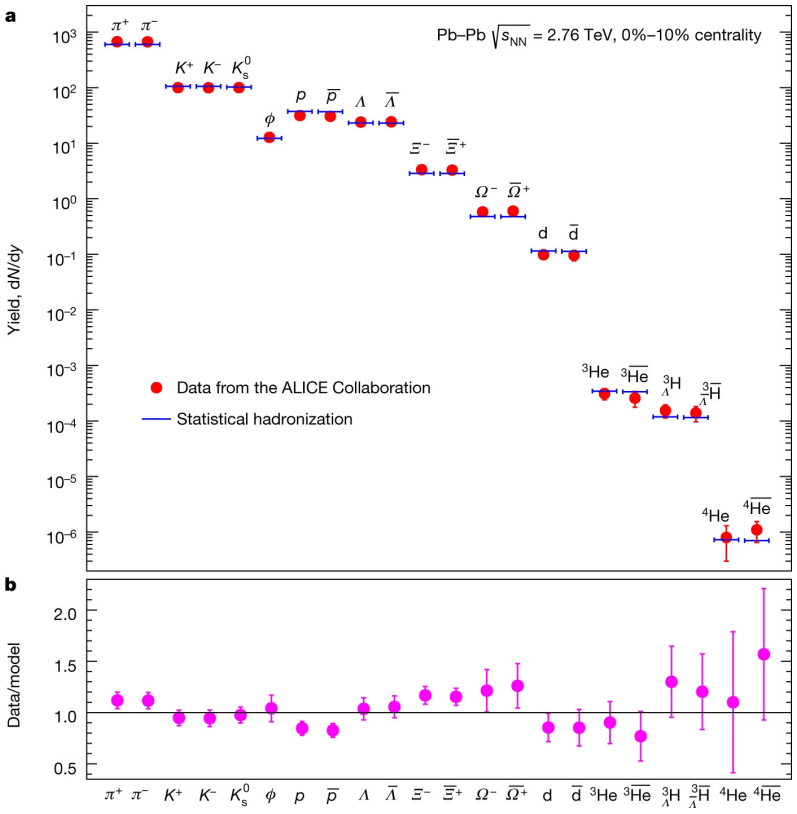

Figure 1.9: a: dN/dy measurements for different hadrons at mid-rapidity by the ALICE collaboration (red dots)in Pb-Pb collisions at $\sqrt{s_{NN}} = 2.76\ TeV$ in 0-10% collisions compared to the predictions of the statistical hadronisation model (blue bars). b: Ratio data to model considering the error from data as the quadratic sum of statistical and systematic uncertainties.

1.4.2 Strangeness production

Contrary to up and down quarks, there are no strange quarks among the valence quarks of the nucleon, but since the mass of the strange quark is light enough, strange hadrons are expected to be abundantly created in ultrarelativistic heavy-ion collisions. Strangeness production can occur at two different phases of the collision, involving different production mechanisms.

At the early stages of the collision, $s\bar{s}$ pairs can be created via hard partonic scattering processes, like gluon splitting ($g \rightarrow s\bar{s}$), flavour creation ($gg \rightarrow s\bar{s}$ and $q\bar{q} \rightarrow s\bar{s}$) or flavour excitation ($gs \rightarrow gs$ and $qs \rightarrow qs$) by acting on a strange quark from the sea quarks of the involved nucleons. These processes can be treated perturbatively (using pQCD) and produce strange hadrons with a high p_T.

Later in the process, during hadronisation, non-perturbative processes such as string fragmentation[29] dominate the creation of strangeness. The resulting strange hadrons arising from these mechanisms dominate the low-p_T region.

1.4.3 Strangeness enhancement

The attempt of the statistical hadronisation model is to give a canonical description of the medium that will lead to the calculation of particle abundancies [30]. In the model, in the case of the presence of the QGP, a grand-canonical ensemble would be used to describe the strangeness content of the medium just like for the light-flavour quarks. Because of the mass of the strange quark, this description would not be valid to describe the strangeness production in the absence of QGP, instead a canonical ensemble should be preferred for the strangeness production, but not for light-flavour particles which can still be described with a grand-canonical ensemble. This forces the strange quarks to be created locally, and not globally; this is the strangeness canonical suppression effect [31][30].

This effect, which is considered as a signature of the QGP, that were expected to be created in the most central heavy-ion collisions, had to be rethought after the measurements performed by the ALICE collaboration [32]. As shown in figure 1.10, an enhancement of the strange particle yield with respect to the light-flavour π meson is observed from low to high multiplicity events, regardless of the collision system. This enhancement is also observed to be more pronounced for hadrons having a larger strangeness content and reaches a saturation value for $\langle dN_{ch}/d\eta \rangle \geq 100$[5] .

It has also to be noted that the increase for a particle with a null-net strangeness content such as the ϕ meson is also observed, as shown in detail in figure 1.11. In this figure the $\phi/(\pi^+ + \pi^-)$ ratio exhibits an increase for $\langle dN_{ch}/d\eta \rangle_{|\eta|<0.5} < 100$. Furthermore, at high multiplicity, an agreement with the statistical hadronisation model [35] is found.

[5]Here $dN_{ch}/d\eta$ stands for the estimation of charged particles per pseudo-rapidity unit produced in $|\eta| < 0.5$

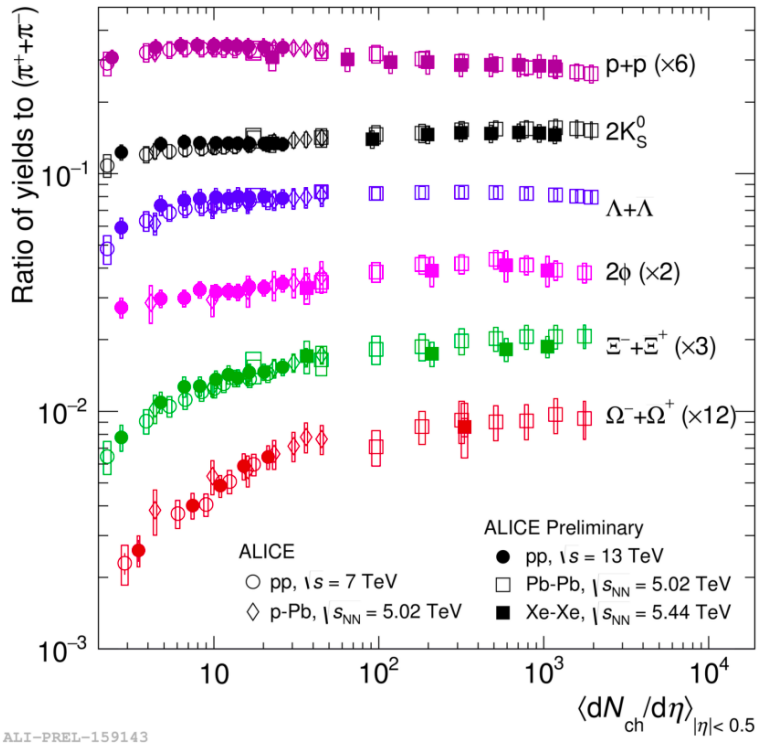

Figure 1.10: Ratio to pion of integrated yields for p, K^0_s, Λ, ϕ, Ξ and Ω. The evolution with multiplicity at mid-rapidity, $dN_{ch}/d\eta$ for $|\eta| < 0.5$, is reported for several systems and energies, including pp at $\sqrt{s}$ = 7 TeV [33], p-Pb at $\sqrt{s_{NN}}$ = 5.02 TeV[34], and also the ALICE preliminary results for pp at $\sqrt{s}$ = 13 TeV, Xe-Xe at $\sqrt{s_{NN}}$ = 5.44 TeV and Pb-Pb at $\sqrt{s_{NN}}$ = 5.02 TeV are included for comparison. Error bars show the statistical uncertainty, whereas the empty boxes show the total systematic uncertainty.

1.4.4 Strangeness in the thermal models

In order to explain this strangeness enhancement the statistical hadronisation model was recently developed. To describe the medium crated during nucleus-nucleus collisions, models are using a thermal approach, meaning that the fireball created by the collision has reached thermalisation. In this approach, the partition function for the hadron resonance gas Z as already considered in eq. 1.12 can be decomposed, as developed in [36] (for $T \lessapprox T_C$) such that

$$lnZ(T,V,\mu) \approx \sum_{i \in mesons} ln\mathcal{Z}_{m_i}(T,V,\mu_Q,\mu_S) + \sum_{i \in baryons} ln\mathcal{Z}_{m_i}(T,V,\mu_Q,\mu_S,\mu_B), \quad (1.13)$$

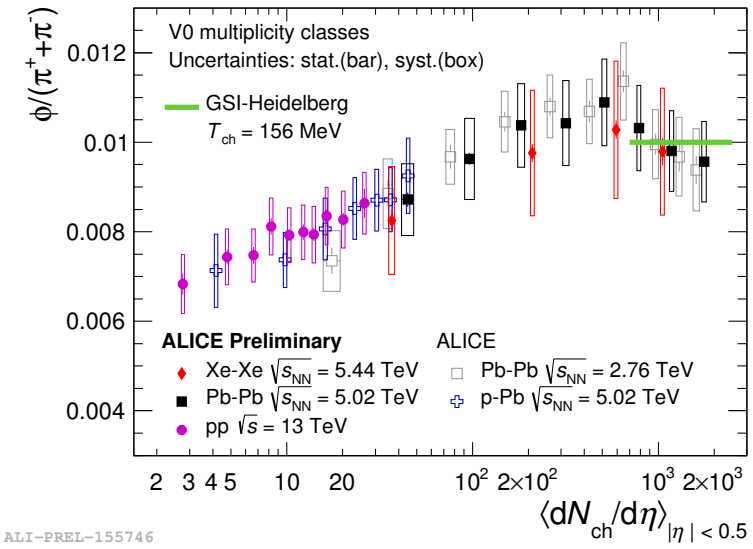

Figure 1.11: Multiplicity dependence of p_T-integrated ϕ / π yield ratio across different collision systems. The phi-meson (reconstructed via the K^+K^- decay channel) and pions are measured in the central rapidity interval, $|y| < 0.5$. Statistical (bars) and systematic (boxes) uncertainties are indicated.

with m_i the mass of a given hadron. Each partition function can be expressed as

$$Z_{m_i}^{M/B}(T, V, \mu)) = \mp \frac{V}{2\pi^2} \int_0^\infty dk\ k^2\ ln(1 \mp z_i exp(-\epsilon_i/T)) \tag{1.14}$$

with T the medium temperature, V its volume, $\epsilon_i = \sqrt{k^2 + m_i}$ and z_i the fugacity which can be expressed as follows

$$z_i = exp((\vec{\mu_i} \cdot \vec{q})/T) = exp((\mu_B B_i + \mu_Q Q_i + \mu_S S_i)/T). \tag{1.15}$$

The multiplicity of each species can then be estimated using the Boltzmann approximation such that

$$< n_i >= d_i \frac{VT}{(2\pi)^3} \int d^3k \frac{1}{\gamma_s^{-s_i}\ exp((\epsilon_i - \vec{\mu_i} \cdot \vec{q})/T) \pm 1}, \tag{1.16}$$

where $d_i = 2J_i+1$ is the spin degeneracy factor, s_i is the number of strange quarks/antiquarks of the hadron, V denotes the overall equivalent hadron gas volume, γ_s the parameter describing the strangeness suppression, the so-called *strangeness suppression factor*.

The strangeness suppression factor accounts for deviations from chemical equilibrium: a state in which, e.g. strangeness is suppressed compared to the equilibrium value. Values dif-

ferent than unity implies additional dynamics not contained in the statistical operator and not consistent with uniform phase space density [37]. As the Grand-Canonical model was found to overestimate the particle productions, the $\gamma_s^{-s_i}$ factor was actually introduced to reproduce the yield of strange hadrons in data[38]. This is particularly the case if data are taken in small collision systems (low multiplicity events) where the fireball volume is small, or at low collision energies, where the temperature is low. In such cases, a thermal description requires exact implementation of charge conservation which is usually described in the canonical ensemble.

If considering the canonical ensemble to describe the fireball, the quantum numbers representing the system are forced to be conserved locally. Thus, in a pp collision B = Q = 2, and S = 0 will always have to be conserved locally. In the case of strangeness, this translates into the creation of a s and $\bar{s}$ quarks locally, to conserve the net strangeness content. This model can actually reproduce the production of strange hadrons with a net strangeness content ($|S| > 0$) in small systems. Nevertheless, in the case of the ϕ meson with a null net strangeness, its production would not be suppressed canonically.

1.5 Experimental results on low-mass vector mesons

The ω meson was discovered in 1961[39][40] at the Lawrence Berkeley National Laboratory followed two years after by the discovery of the ϕ at the Alternating Gradient Synchrotron (AGS) at the Brookhaven National Laboratory[41]. Then with increasing $\sqrt{s}$ and the use of various collision systems, the production of vector mesons has been studied into details, first at the Brookhaven National Laboratory with the E802 and E917 experiments, then at CERN using the Super Proton Synchrotron (SPS) with the NA38, CERES, NA49, NA50 and NA60 experiments, with the Brookhaven's Relativistic Heavy Ion Collider (RHIC) by the PHENIX and STAR experiments and nowadays at CERN with the Large Hadron Collider using the ATLAS, CMS and ALICE experiments. In the following sections, details on vector meson measurements in pp and heavy-ion collisions will be given.

1.5.1 Results from RHIC

At RHIC Au-Au collisions at $\sqrt{s_{NN}}$ = 62.4, 130 and 200 GeV have been delivered. On top of these heavy-ion collisions, p-p, d-Au and Cu-Cu collisions were provided at $\sqrt{s_{NN}}$ = 200 GeV to the PHENIX and STAR experiments.

First from the PHENIX experiment, an extended view on the mesons-m_T scaling has been observed in all different collision systems[42][43][44]. Indeed, the production of both the ω (shown in figure 1.12(a) and ϕ (in figure 1.12(b)) were found to respect the m_T scaling and their differential production as a function of p_{T} was found to be accurately described by Lévy-Tsallis distributions. A Lévy-Tsallis distribution 1.17 [45, 46] is defined as

$$f_{LT}(p_{\mathrm{T}}) = \frac{A(n-1)(n-2)}{nT[nT+m(n-2)]} p_{\mathrm{T}} \left[1 + \frac{m_{\mathrm{T}} - m}{nT}\right]^{-n}, \tag{1.17}$$

where $m_T = \sqrt{p_{\mathrm{T}}^2 + m_{\omega/\phi}^2}$ is the transverse mass. This function can be regarded as a non-extensive generalisation of the usual exponential (Boltzmann-Gibbs) distribution with an effective temperature *T*. This becomes a purely exponential function for small-p_{T} and a purely power-law of the $-n$ order function for large-p_{T} values, thus allowing a different description of the processes leading to the hadron production either at low-p_{T} or at high-p_{T}.

For what concerns the strangeness enhancement study, the STAR experiment could complete the picture provided at the SPS [47]. As shown in figure 1.13, the results provided by STAR also show an enhancement of strangeness for baryons with a net strangeness content. In this case, the baryons $\Lambda(|S|=1)$, Ξ^- ($|S|=2$),Σ^- ($|S|=3$) all shown an increase with the centrality. The enhancement is also shown to be more pronounced with higher $|S|$. In the case of protons, no enhancement as a function of number of participant is observed. Furthermore, a lower enhancement is observed in STAR where the centre-of-mass energy is higher.

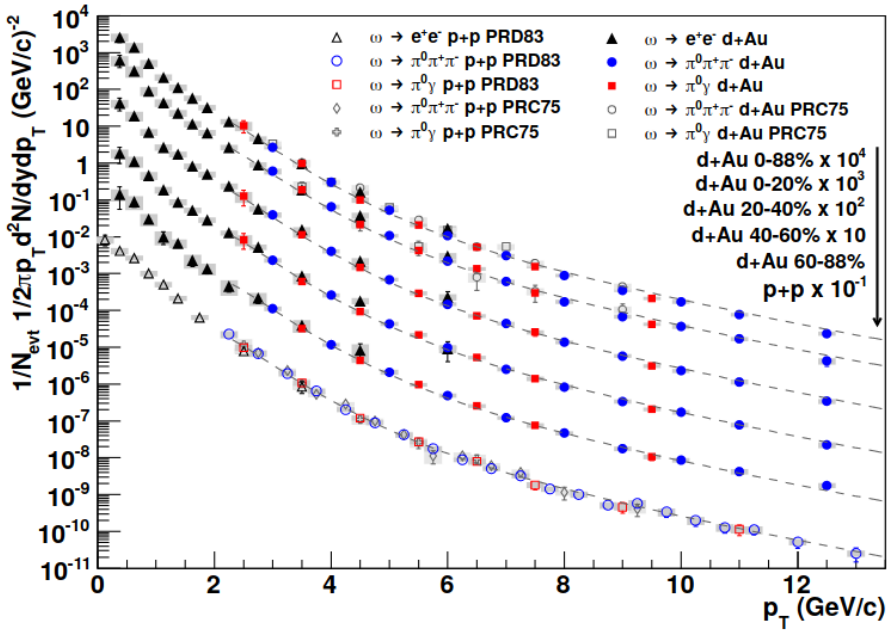

(a) Invariant p_T spectra of the ω meson for different centrality bins in p-p and d-Au collisions at $\sqrt{s_{NN}}$=200 GeV. The spectra are fitted with exponential and Tsallis functions shown by the dashed and solid lines, respectively

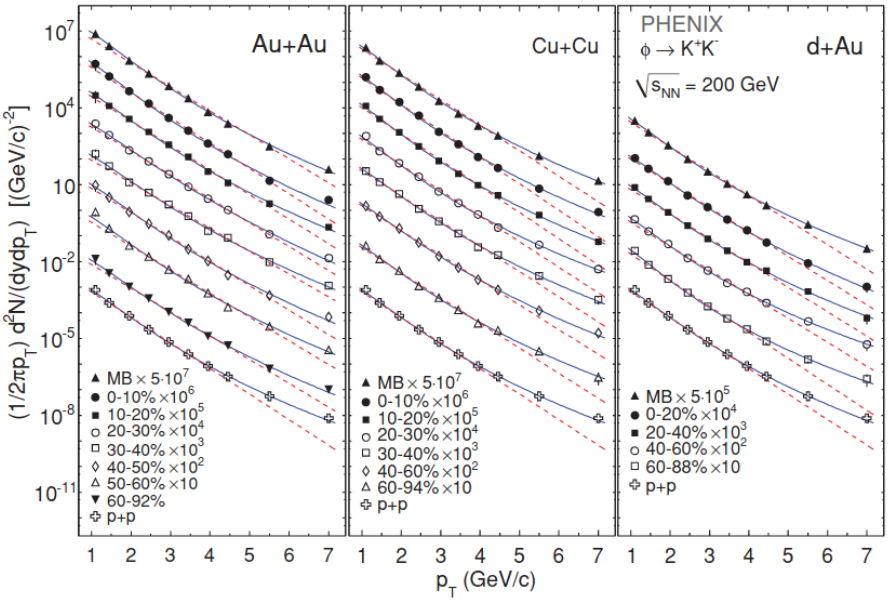

(b) Invariant p_T spectra of the ϕ meson for different centrality bins in Au-Au, Cu-Cu, d-Au, and p-p collisions at $\sqrt{s_{NN}}$=200 GeV. The statistical and systematic uncertainties are smaller than the size of the symbols. The spectra are fitted with exponential and Tsallis functions shown by the dashed and solid lines, respectively

Figure 1.12

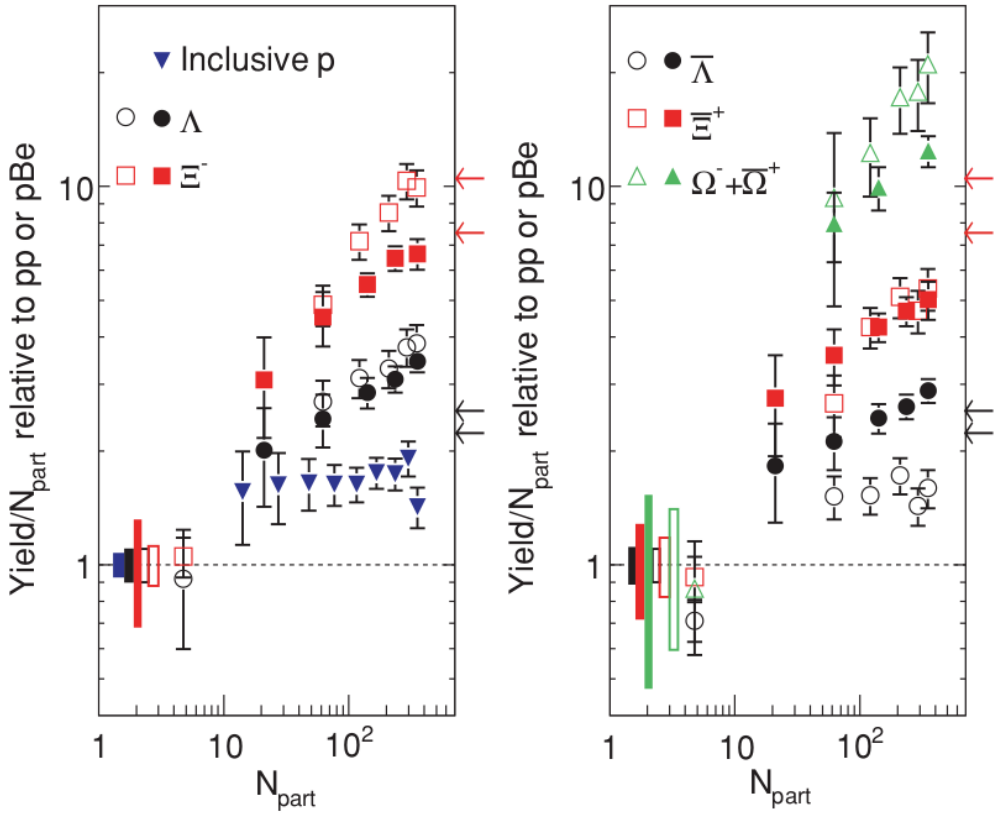

Figure 1.13: Hadron yields measured at midrapidity as a function of $< N_{Part} >$. Boxes at unity show statistical and systematic uncertainties combined in the p+p (p+Be) data. Error bars on the data points represent those from the heavy ions. The solid markers are for Au+Au at $\sqrt{s_{NN}}$=200 GeV and the open symbols for Pb+Pb ($|y|< 0.5$) at $\sqrt{s_{NN}}$=17.3 GeV. The arrows on the right axes mark the predictions from a GC formalism model when varying T from 165 to 170 MeV. The red arrows indicate the predictions for Ξ and the black arrows those for Λ

1.5.2 Results from ALICE

Benefiting from a large range of collisions systems and centre-of-mass energies provided by the LHC, ALICE could analyse strangeness enhancement in a broad multiplicity region. The LHC provided collisions at $\sqrt{s}$ = 2.76, 5.02, 7 and 8 TeV in pp, at $\sqrt{s_{NN}}$ = 5.02 and 8.16 TeV in p-Pb and at $\sqrt{s_{NN}}$ = 2.76, 5.02 TeV in Pb-Pb collisions. At these energies of pp collisions, strangeness relative to light-flavours particles becomes higher than at SPS, giving the possibility of the study of strangeness enhancement in small systems.

1.5.2.1 Strangeness enhancement in ALICE

Similarly to previous measurements, the study of strangeness enhancement focused on the extraction of hadrons with a net strangeness content [1]. In figure 1.14(b) a hardening of the strange particles p_{T} spectra with multiplicity could be observed, with the hardening being more pronounced for higher-mass particles. The same observation was reported for p-Pb collisions [48], where this hardening and several other features associated to collective behaviour, such as hydrodynamic, are observed in high multiplicity events [49]. In figure 1.14(a) the strange to non-strange particle yield ratio is represented. The relative yields show consistent results among the different collision systems. In this figure it can also be noted that in pp collisions, the multiplicity can reach the one observed in peripheral Pb-Pb collisions [48]. As no significant dependence on the centre-of-mass energy is observed at the LHC for inclusive inelastic collisions, the origin of strangeness production in hadronic collisions is driven by the characteristics of the final state independently of the collision system or energy. Such behaviour cannot be reproduced by any of the MC models commonly used (and presented here), suggesting that further developments are required to obtain a complete understanding of strangeness production.

To understand the source of this strangeness enhancement, different possibilities have been investigated. Results are presented in [1]. First the study found that the strangeness enhancement is not related to a different behavior depending on either if the hadron is a meson or a baryon. This is shown in figure 1.15(a), where the relative yield of Λ/K^0_S (both $|S|$=1 hadrons) is found to be multiplicity independent in pp and p-Pb collisions. Figure 1.15(b) presents the

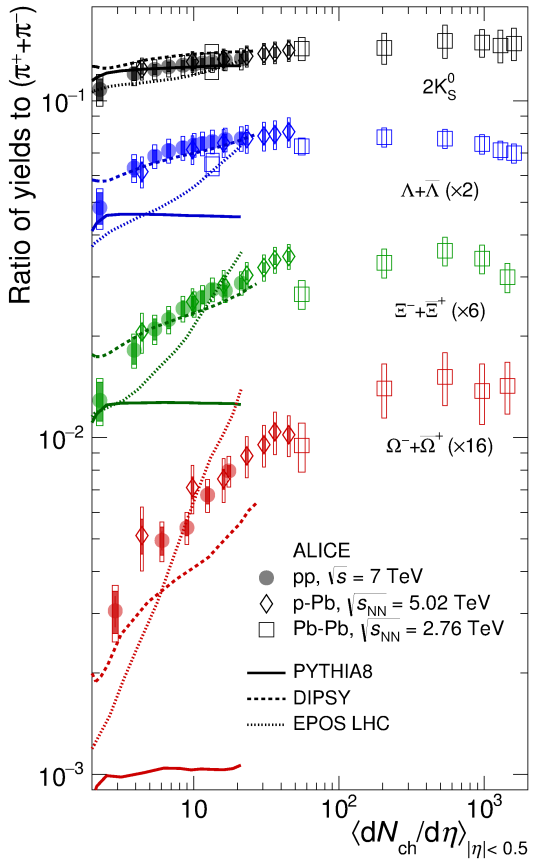

(a) Relative ratio of particle yields to the $\pi^+ + \pi^-$ yield. The error bars show the statistical uncertainty, the empty and dark-shaded boxes show the total systematic uncertainty and the contribution uncorrelated across multiplicity bins, respectively. The values are compared to calculations from MC models and to results obtained in p–Pb and Pb–Pb collisions at the LHC. For Pb–Pb results the ratio $2\Lambda/(\pi^+ + \pi^-)$ is shown. The indicated uncertainties all represent standard deviations. [1]

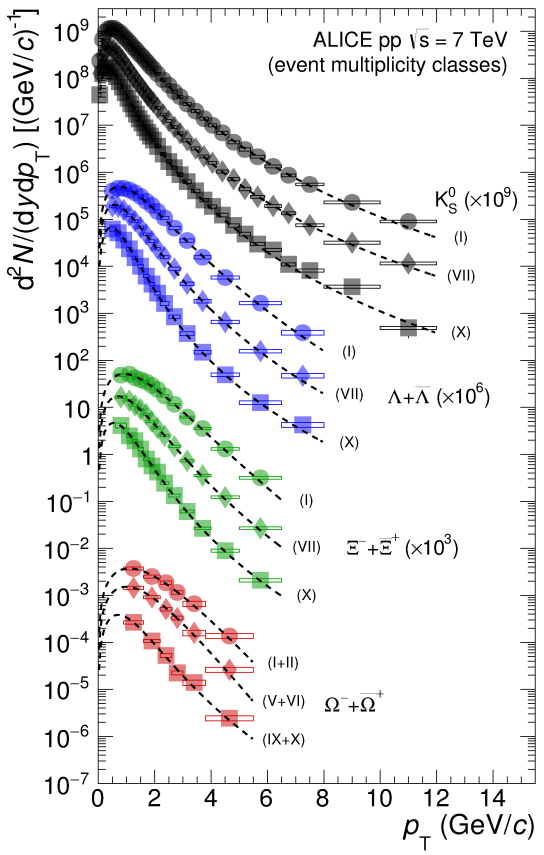

(b) Particle yields for a selection of event classes, indicated by roman numbers in brackets, with decreasing multiplicity. The error bars show the statistical uncertainty, the empty boxes show the total systematic uncertainty. The data are scaled by different factors to improve the visibility. The dashed curves represent Tsallis–Lévy fits to each individual distribution to extract integrated yields. The indicated uncertainties all represent standard deviations. [1]

Figure 1.14

relative enhancement of hadron production with respect to the π yield. This result shows that the strangeness enhancement is observed for all strange hadrons and is related to their net strangeness content. Later, a study focusing on the Ξ production (see [50]), could investigate the mass dependency of strangeness enhancement. As presented in figure 1.16, the ratio of

neutral Ξ^* ($m_{\Xi^{*0}}$ = 1.532 GeV/c^2) over charged Ξs (with m_{Ξ^-} = 1.314 GeV/c^2) shows no modification as a function of multiplicity. As they are both baryons with the same S=2 content, their only difference is their mass. Thus, from this result one can retain that the strangeness enhancement is not mass dependent.

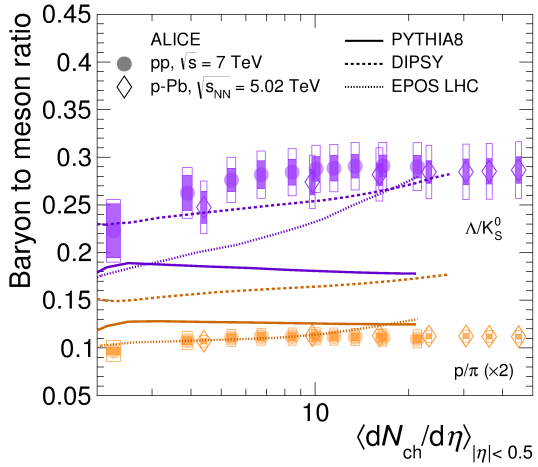

(a) Ratios of baryon to meson yields as a function of multiplicity. The yield ratios are measured in the rapidity interval $|y|<$ 0.5 . The error bars show the statistical uncertainty, the empty and dark-shaded boxes show the total systematic uncertainty and the contribution uncorrelated across multiplicity bins. The values are compared to calculations from MC models in pp collisions at and to results obtained in p–Pb collisions at the LHC.

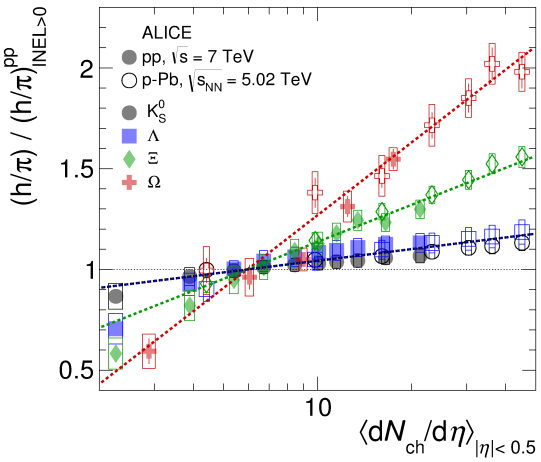

(b) Hadron to pion yield ratios normalised by the value in all inelastic pp collision a function of multiplicity. The error bars show the statistical uncertainty. The empty boxes represent the remaining uncorrelated uncertainties. The lines represent a simultaneous fit of the results with the empirical scaling formula. T

Figure 1.15

As shown in figure 1.11, the ϕ meson shows an enhancement as a function of multiplicity. This is a specific breakthrough as so far in models the strangeness enhancement was believed to scale with the net strangeness and not the quark content.

In figure 1.17 (taken from [51])the ϕ/π ratio increases from the lowest-multiplicity pp collisions to mid-central Pb–Pb collisions. The canonical statistical model (CSM) with a chemical freeze-out temperature of 156 MeV predicts that this ratio should have a small dependence on the multiplicity, since the ϕ would not be subjected to canonical suppression and thus ne-

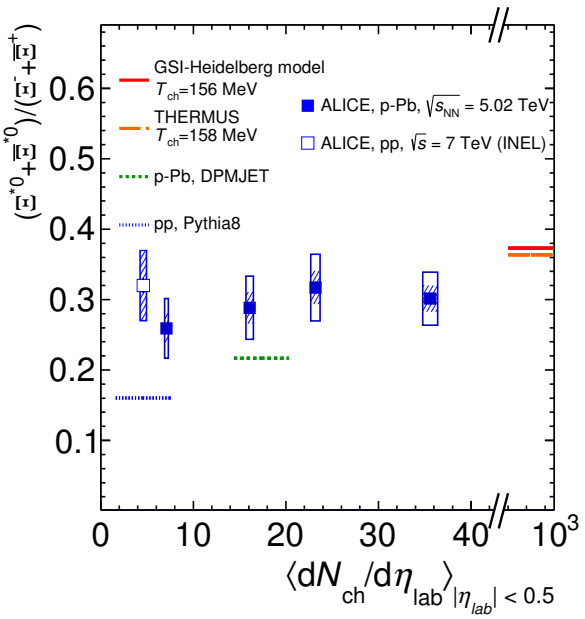

Figure 1.16: Ξ^{*0} to $\Xi^{+/-}$ yield ratio as a function of multiplicity. Statistical uncertainties (bars) are shown as well as total systematic uncertainties (hollow boxes) and systematic uncertainties uncorrelated across multiplicity (shaded boxes). Model predictions are also shown as lines at their appropriate abscissa.

glecting the γ_S factor. The results of the CSM calculation are found to be inconsistent with the observed trend of the ratio. For pp collisions at 13 TeV, the increasing trend of the ratio is reproduced fairly well by the EPOS-LHC[6] and DIPSY[7] models, while the PYTHIA[8] calculations (the features of these models are described in E) underestimate the magnitude of the ratio. The ϕ/K ratio also follows a similar trend in the three collision systems. It is fairly constant, although there is an apparent small increase with multiplicity from the lowest values up to $\simeq$ 400. EPOS-LHC somewhat overestimates the ratio, but is closer to the measured values than PYTHIA, which significantly underestimates ϕ/K. While PYTHIA6 and DIPSY underestimate the ratio, both results exhibit small increases with increasing multiplicity, which is qualitatively similar to the measured trend. The CSM calculation does not describe the behavior of the measured ratio for the range spanned by the ALICE pp measurements.

[6]EPOS: encoding collective radial expansion considering a core-corona model of the fireball

[7]DIPSY: PYTHIA extension considering color ropes

[8]PYTHIA: considering string fragmentation in the color reconnection scheme

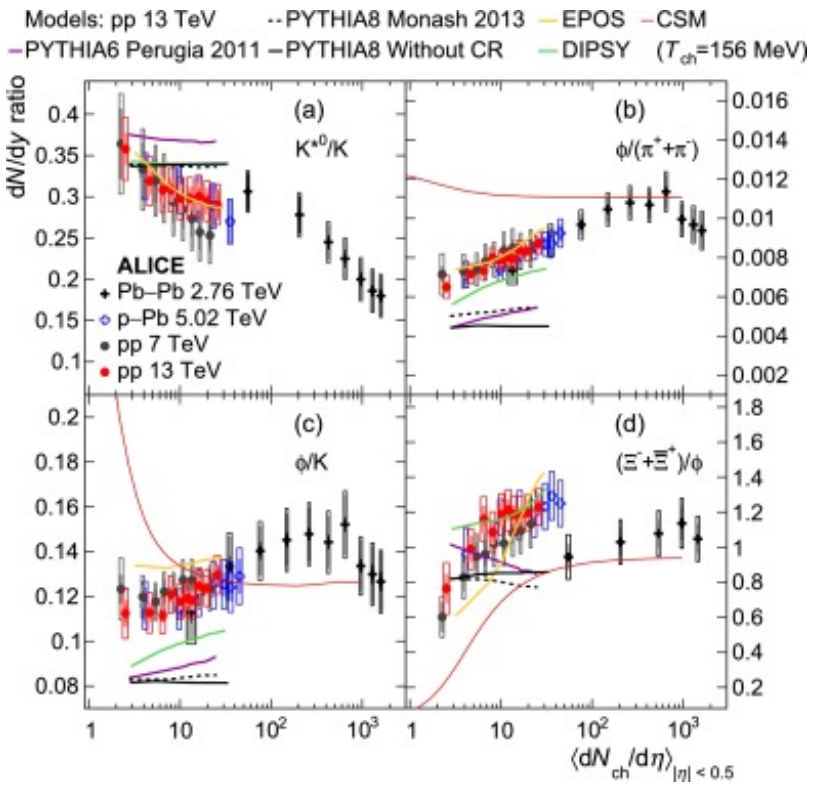

Figure 1.17: Ratios of p_{T}-integrated particle yields in pp collisions as a function of multiplicity. These measurements are compared with data from p-Pb collisions at $\sqrt{s}$ =5.02 TeV and Pb-Pb collisions at $\sqrt{s}$ =5.02 TeV. Results are also compared to common event generators and a Canonical Statistical Model (CSM) calculation. Taken from [51]

In addition to comparing the yields of ϕ to pions and kaons, it may be instructive to compare it to Ξ. These two particles contain the same number of strange valence (anti)quarks: ϕ is a $s\bar{s}$ bound state and Ξ contains two strange valence quarks. However, Ξ would be subject to canonical suppression, unlike the strangeness-neutral ϕ. The Ξ/ϕ ratio increases with increasing multiplicity for low-multiplicity collisions and is then fairly constant for a wide range of multiplicities: from pp and p–Pb collisions at to central Pb–Pb collisions. There is a possible small increase in the Ξ/ϕ ratio from $\langle\, dN_{ch}/d\eta \,\rangle_{|\eta|<0.5} \sim 7$ to the highest-multiplicity p–Pb collisions, as well as a difference on the 1.5σ level between the p–Pb and Pb–Pb measurements at $\langle\, dN_{ch}/d\eta \,\rangle_{|\eta|<0.5}$ ∼50. Nevertheless, there is no clear increase in the ratio for $\langle\, dN_{ch}/d\eta \,\rangle_{|\eta|<0.5} > 7$. The decrease in with decreasing $\langle\, dN_{ch}/d\eta \,\rangle_{|\eta|<0.5}$ for low multiplici-

ties could be interpreted as evidence of canonical suppression in small systems; the canonical statistical model predicts a decrease in the Ξ/ϕ ratio with decreasing $\langle\, dN_{ch}/d\eta \,\rangle_{|\eta|<0.5}$ that is qualitatively similar to the measured data. However, canonical suppression would also result in an increase in the ϕ/K ratio with decreasing multiplicity, which is not observed. Given that Ξ and K have different numbers of strange valence (anti)quarks, it is expected that Ξ would be more affected by canonical suppression.

Chapter 2

The ALICE detector and the muon arm

2.1 The Large Hadron Collider

The Large Hadron Collider (LHC) is a particle collider located at the main site of the *Centre Européen pour la Recherche Nucléaire* (CERN). The main purpose of the collider is the investigation of the limits of the Standard Model using hadron beams, either protons or lead and xenon ions. The beams can be brought to high energy ($\sqrt{s}$ = 13 TeV in pp collisions and $\sqrt{s_{NN}}$ = 5.02 TeV) as the collider benefits from its superconducting dipole magnets providing a field of 8.3 T and a circumference of 27 km that makes this accelerator the biggest in the world.

Figure 2.1 displays the full accelerator complex located at CERN including the accelerators located upstream of the LHC. The beams (such as protons) which will be collided in the LHC are first produced in the LINAC2 (a linear accelerator). Once created they are injected in a first accelerator ring, the BOOSTER. Once reaching an energy of 1.4 GeV the protons are injected in the Proton Synchrotron (PS). In this second booster, protons are ramped-up to an energy of 25 GeV. Then protons are sent to the Super Proton Synchrotron (SPS), a booster with a 7 km circonference. This ring accelerates the protons up to an energy of 450 GeV and injects the beam into the final accelarator, the LHC ring. It can be spotted in here that the beams leaving the SPS can also be directly used for collisions such as for the NA61/SHINE experiment.

In the case of heavy ions (like Pb ions), they are created in the LINAC3 accelerator and then accelerated in the Low Energy Ion Ring (LEIR) reaching an energy of 72 MeV/nucleon.

Then they are injected successively in the PS, then in the SPS for an extra boost, and finally in the LHC. A list of the different characteristics of the LHC are listed in the table 2.1.

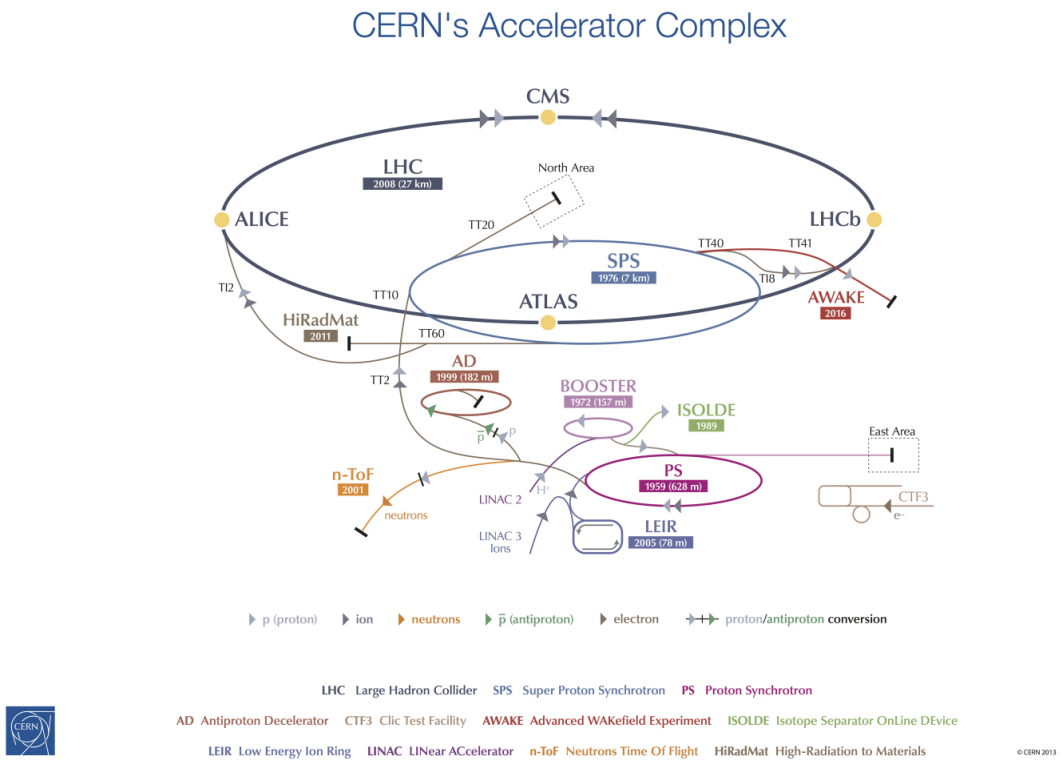

Figure 2.1: The LHC and the CERN accelerator complex

Quantity	Number
Circumference	26 659 m
Dipole operating temperature	1.9 K
Nominal energy protons	6.5 TeV
Nominal energy heavy-ions	2.56 TeV/nucleon
Number of bunches per proton beam	2808
Number of protons per bunch (at start)	1.2×10^{11}
Number of turns per second	11 245
Number of collisions per second	10^9

Table 2.1: Features of the LHC accelerator

The first collisions were performed in 2009 with pp collisions at $\sqrt{s} = 900$ GeV. Then other

pp collisions (at 2.76, 5.02, 7, 8, 13 TeV), p-Pb collision (at 5.02, 8.16 TeV), Pb-Pb collisions (at 2.76, 5.02 TeV), and Xe-Xe (at 5.44 TeV) have been performed at higher energies. The different collisions are studied by four main experiments, namely: ALICE, ATLAS, CMS and LHCb. The ATLAS and CMS were originally built for the detection of the Higgs boson, which was discovered in 2012. Now both collaborations focus their research on signals of physics beyond the Standard Model. Both ATLAS and CMS include also a heavy-ion program. LHCb is a forward detector designed to study the physics of heavy-quarks (beauty and charm) but has recently started a heavy-ion collisions program. Concerning ALICE, it is the only large experiment at the LHC specially designed to investigate the QGP in central heavy-ion collisions.

2.2 The ALICE apparatus

ALICE is the main experiment devoted to the study of QGP at CERN. The ALICE Collaboration counts more than 1800 scientists representing 176 institutes among 41 countries.

With 19 different detectors, ALICE is a general-purpose detector allowing the investigation of the various probes to characterise the QGP. As represented in figure 2.2, the detector covers the full azimuthal angle and most of the detectors are located at central rapidity.

The apparatus can be described into two main parts:

- the central barrel detectors: covering the pseudo-rapidity region $|\eta|<0.8$, located inside a large solenoid, which provides a homogeneous magnetic field of 0.5 T along the beam axis. The detector closest to the interaction point is the Inner tracking System (ITS) which is used as a vertexer, multiplicity estimator, and for Particle IDentification (PID) and tracking. Come upstream the Time Projection Chamber (TPC) used for precision PID and tracking, and the Transition Radiation Detector (TRD) for electron identification. The last detector used for PID is the Time Of Flight (TOF) detector. Then behind them, the ElectroMagnetic Calorimeter (EMCal) and the Di-jet Calorimeter (DCal) are located at opposite azimuthal angles allowing the study of hadronic and electromagnetic jets.

- The forward detectors: they are composed of a muon arm used for muon tracking, and

detectors used for triggering, multiplicity and centrality estimation such as the V0, the T0, and the Zero Degree Calorimeter (ZDC).

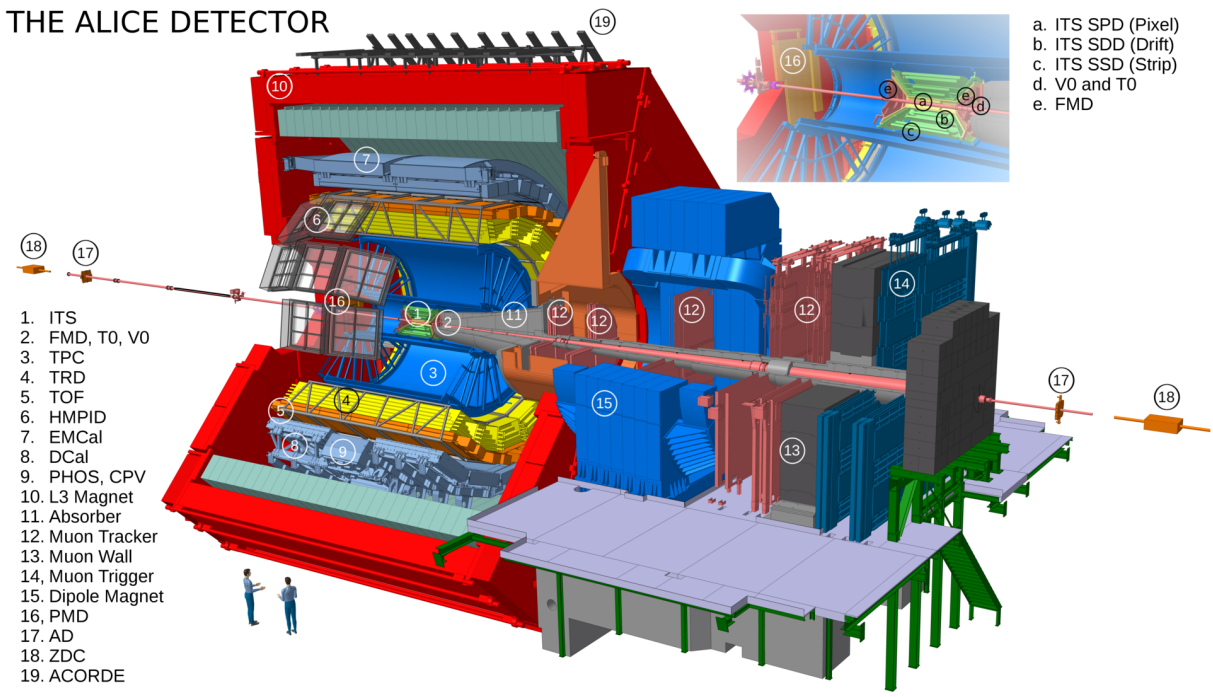

Figure 2.2: Schematic view of the ALICE detector during Run-2 data taking. A closer view of the Inner Tracking System can be seen in the top right corner of the caption

2.3 Detectors Used For Dimuons Studies

2.3.1 The Inner Tracking System

The Inner Tracking System (ITS) is the detector closest to the Interaction Point (IP) and is composed of six cylindrical layers located from 3.9 to 44 cm around the centre of the beam pipe covering the $|\eta|<$ 0.9 region. The ITS consists of three groups, each of two layers:

- the Silicon Pixel Detector (SPD): it is the innermost part of the detector, covering the $|\eta|<$ 1.4 region. It consists of two layers of silicon pixel detectors with a resolution of 50 x 425 μm^2 (the first at 3.9 and the second at 7.0 cm from the IP). The passage of a charged particles through these layers will trigger a hit (or a binary response) from the

chip it passed through. This allows the SPD to be used either for vertexing, tracking and multiplicity estimation.

- the Silicon Drift Detector (SDD): it is made of the two central layers of the ITS located at 12.7 and 24 cm from the IP. These layers are composed of 260 SDD of 0.3 mm thick silicon wafer. Besides determining the coordinates of the charged particles crossing it, the SDD also measures the deposited charge, thus allowing for both tracking and particle identification.

- the Silicon Strip Detector (SSD): it is composed of the two outermost layers of the ITS, located at 38 and 43 cm from the IP. Similarly to the SDD, the SSD accounts for the energy loss of charged particles through its strips, thus can be used for tracking and particle identification.

Altogether, these different layers make the ITS a complete detector. Furthermore, when linking two hits from the SPD layers, a so-called tracklet is formed. Combining the different tracklets observed in an event a first estimate of the vertex position can be done with 10 μm resolution. As it will be shown later in the analysis (see section 5.1), the multiplicity at central rapidity can be estimated based on the tracklets from the SPD. The SDD and the SSD complete the performances of the ITS giving the possibility to perform tracking and PID at very low-p_T (starting at 100 MeV/c), a kinematic region which is not accessible to the other tracking detectors as the TPC and the TOF, where the magnetic field bends out these low-p_T charged particles before reaching these detectors. In figure 2.3 two event displays are shown. The top figure displays a pp event where six tracks have been reconstructed out of the different hits (yellow dots). The bottom picture displays a central Pb-Pb event. One can notice the high multiplicity in these events, that justifies the necessity of a high resolution for the SPD, in order not to saturate the occupancy and thus have a good estimate of the number of charged particles coming from the collision.

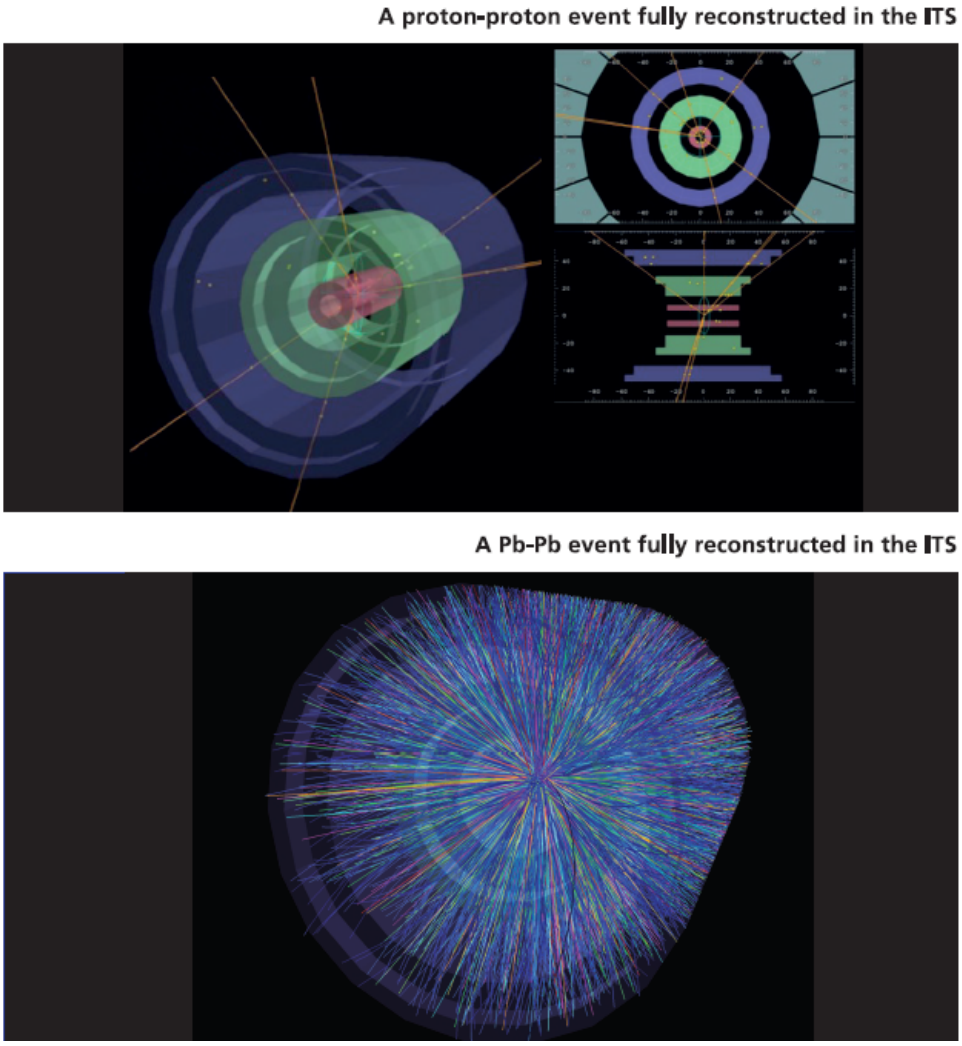

Figure 2.3: Event display in 3D of the ITS for pp and Pb-Pb collisions. In the top figure, the red layers are the SPD, the green ones the SDD, and the blue ones the SSD.

2.3.2 The V0

The V0 detector is composed of two sets of plastic scintillators arranged in two discs on both sides of the interaction point. The first set is the V0A[1] is situated at 3.40 m from the IP and covers the $2.8 < \eta < 5.1$ pseudo-rapidity region. The second, the VOC[2] is located at 90 cm from the IP - actually in front of the hadron absorber (which is part of the muon arm) - and covers the $-3.7 < \eta < -1.7$ pseudo-rapidity region [52].

[1] in V0A, the "A" stands for ATLAS as this disc in on the ATLAS side of ALICE

[2] in V0C, the "C" stands for CMS as this disc in on the CMS side of ALICE

The V0A is composed of 32 counters arranged in 4 rings of 8 sectors, and the V0C of 32 counters with eight counters on its two inner rings and 16 on the two outer rings. When a particle passes through one of this counters, scintillation light is produced driven 3 m away of the detector via fibres to photomultipliers to be collected. Then, as shown on the left plot in figure 2.4, benefiting from the asymmetry of the position of the disks, a slight delay of 8 ns is expected between both signals. This allows to reject the beam-gas and gas-gas event occurring in the beam pipe by requiring a signal in both V0A and V0C. This selection can be performed online and triggers Minimum Bias (MB) events to select a large part of inelastic events without introducing a selection bias.

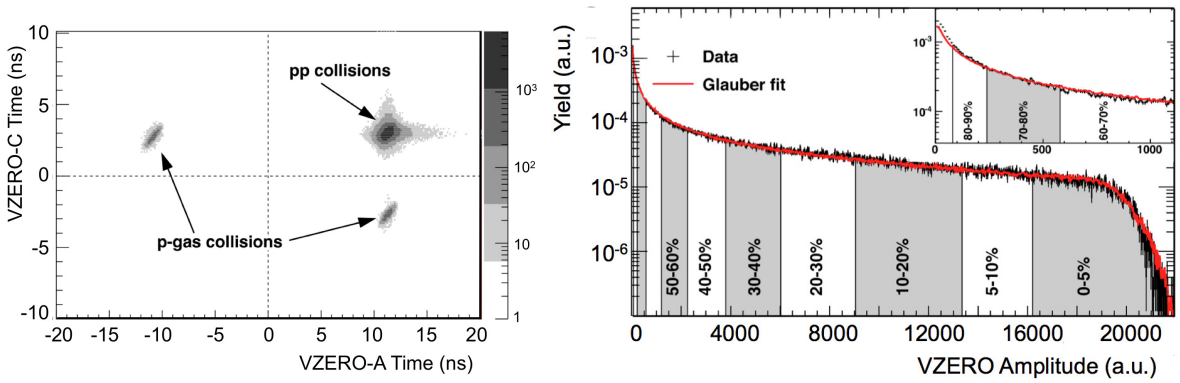

Figure 2.4: **Left**: Time of signal received by both V0 arrays taking as reference (the dashed line) the time of the collisions at the interaction point in pp collisions at 7 TeV. **Right**: Event distribution as a function of the integrated signal received in the V0 in Pb-Pb collisions at 2.76 TeV. The red line shows the fit to a Glauber model [53]

Part of the V0 signal is treated offline and used to account for the total amount of charge given by the counter. Since the number of particles detected by the V0 arrays scales with the number of initially produced particles, the V0 can be used as a multiplicity estimator. As shown in the right plot in figure 2.4, the distribution of events as a function of the signal in the V0 can be used to classify the events according to their multiplicity and can be reproduced by the Glauber model [53].

2.3.3 The Muon Arm

The ALICE muon arm is a magnetic spectrometer dedicated to the detection of muons used to study the production of low-mass mesons (ρ, ω, ϕ), open-heavy flavours ($c\bar{c}$, $b\bar{b}$), quarkonia (J/Ψ, $\Psi(2s)$, $\Upsilon(1s)$, $\Upsilon(2s)$, $\Upsilon(3s)$) and gauge bosons ($W^{\pm}$, Z^0). The arm covers the pseudo-rapidity region of -4 $<$ η $<$ -2.5 corresponding to a rapidity of 2.5 $<$ y $<$ 4[3] in symmetric collision systems such as pp and Pb-Pb systems. Similarly to most of the detectors in the central barrel, the arm also benefits from full azimuthal coverage. As shown in figure 2.2, the muon arm is composed of different subparts which are highlighted in figure 2.5. A picture of the muon arm is presented in figure 2.6.

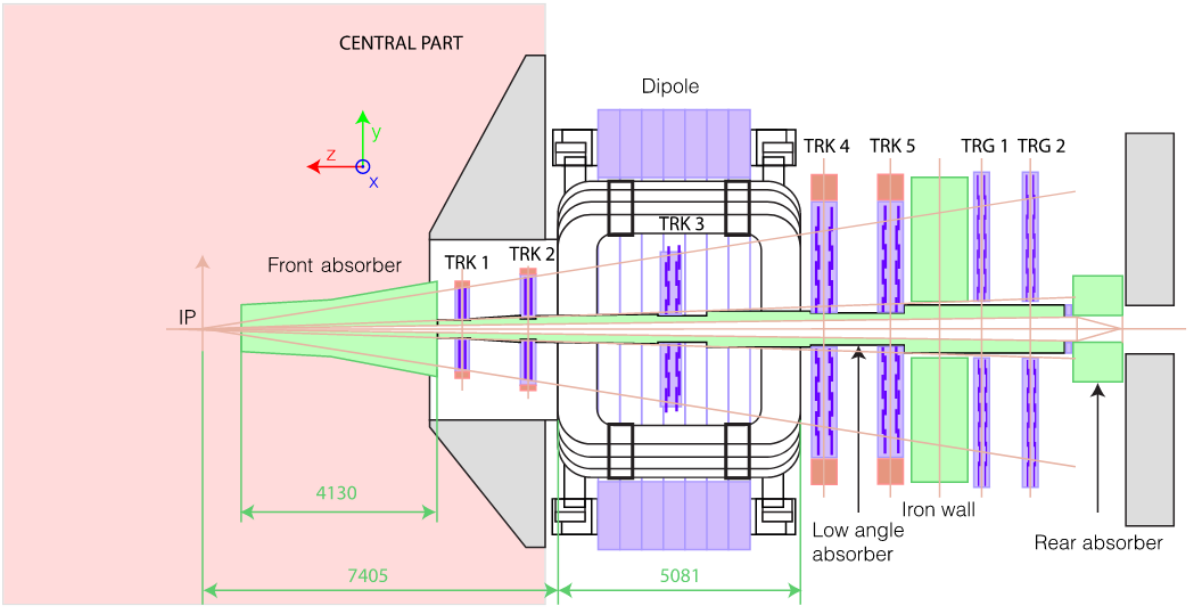

Figure 2.5: Schematic representation of the ALICE muon arm

2.3.3.1 The Absorbers

A system of absorbers is installed in the muon spectrometer. The system is composed of a front absorber, placed close to the interaction point, and a muon filter placed between the tracking and trigger systems. A back absorber and the beam shield complete the system. Muons, besides

[3]In ALICE the muon arm is located at forward rapidity at -2.5 $<$ η $<$ -4, however by convention we use positive values when referring to rapidity (y)

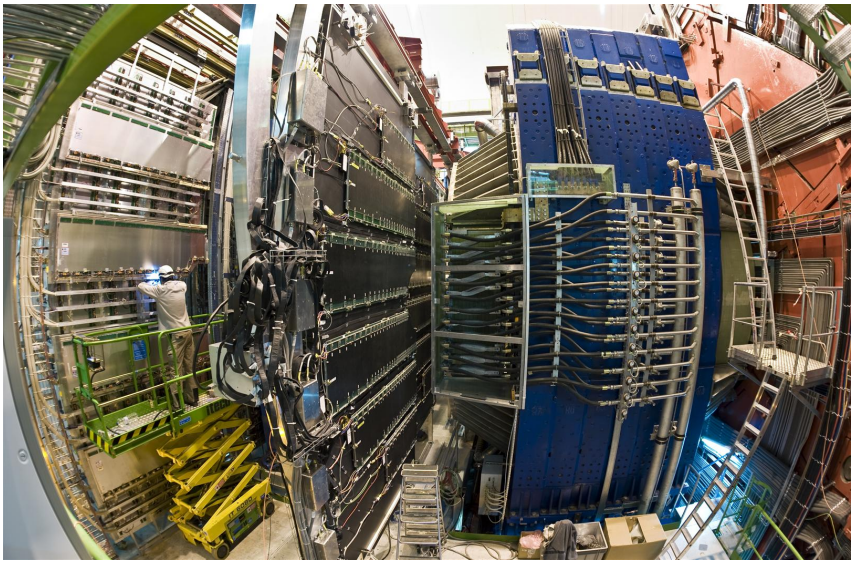

Figure 2.6: Picture of the ALICE Muon arm

neutrinos, are the only particles which cross the absorber without originating a shower, being subjected only to multiple scattering and excitation/ionization energy loss. Thus, the absorber complex reject all particles created in a collision, with the exception of muons.

The front absorber is placed right after the V0C disk at 90 cm from the IP. It absorbs all particles except muons and reduces the number of muons produced by the weak decay of pions and kaons. These hadrons are indeed absorbed within the detector before their decay, reducing the amount of hadrons by a factor ~ 100. The absorber is a 4.3 m long wall. In order not to deteriorate the muon signal, the upstream part of the absorber is mostly composed of carbon and concrete (elements with a small atomic number) to limit the energy loss and the multiple scattering for the muons. The back part of the absorber is made of interleaved layers of lead and boronated polyethene (with a high atomic number) absorbing low energy photons and neutrons (see figure 2.7). The absorber length expressed in terms of radiation lengths and hadronic interaction lengths is $\sim 60\ X_0$ and $\sim 10\ \lambda_l$ respectively.

The muon filter is a 1.2 m long iron wall situated between the last tracking station and the first trigger station. Its aim is to reject secondary hadrons escaping from the front absorber and muons, mainly coming from the decay of kaons and pions within the front absorber, with

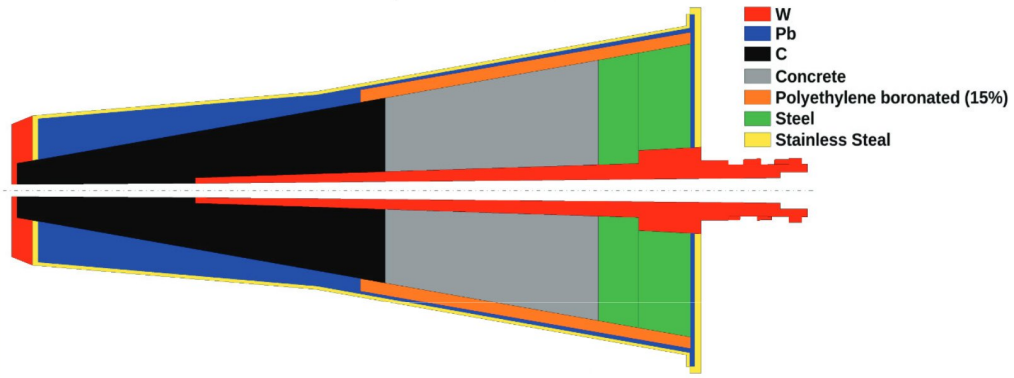

Figure 2.7: Front absorber structure in ALICE

a momentum of less than 4 GeV/c.

The beam shield is a protection made of tungsten, iron and stainless steel surrounding the beam pipe all along the spectrometer. Its role is to prevent the detector from high rapidity primary particles, but also beam-gas interactions occurring in the beam pipe.

The back absorber consists of a 1 m thick iron wall located behind the muon trigger to protect it from beam-gas interactions taking place in the beam pipe.

2.3.3.2 The Dipole Magnet

The dipole magnet is surrounding the third tracking station [54]. This warm magnet is composed of an iron yoke and of two excitation coils. The latest benefit from a water-cooling system ensuring operative temperatures from 15 to 25 °C. It provides a maximal field of 0.7 T at its center along the the x-axis (according to the sketch 2.5) and an integrated field $\int Bdz =$ 3 T.m. As the deflection angle (defined in the yz-plane) scales with the particle rigidity, the magnet is used to measure the charge and momentum of the muons.

2.3.3.3 The Tracking Stations

The Tracking Stations are used to reconstruct the muon tracks, thus allowing for the measurement of their momentum through the bending of their trajectories in the magnetic field. There are five different tracking stations, each of them made of two identical detection layers

called Muon Chambers (MCH). The first station is located behind the front absorber at 5.4 m from the IP; the second before the dipole magnet at 6.6 m; the third station is surrounded by the magnet at 9.7 m from the IP; the two last stations are placed between the magnet and the muon filter, respectively at 12.65 and 14.25 m from the IP.

The MCH are made of cathode pad chambers. A picture of the pad and strip chambers is shown in figures 2.9(a) and 2.9(b). To reduce the muon multiple scattering when crossing the chambers, they are made of a composed material that limits the material budget to less than $3\%\ X_0$. The different chambers, represented in figure 2.8 are Multi-Wire Proportional Chambers (MWPC), made of a plane of anode wires between two cathodes planes (cathode pad chambers, CPC). All the wires are immersed into a CO_2 (20%) and Ar (80%) mixture and brought to high tension ($> 1600V$) [55]. In order to limit the occupancy rate[4] of the pads under 5% their segmentation must be really fine. The CPCs were chosen as they can have a high granularity read-out and reach a spatial resolution lower than 100 μm in the bending plane (the yz-plane). This allows a resolution of 100 MeV/c^2 at the Υ peak giving the ability to distinguish the different bottomonium states. Additionally, this high granularity with a maximum hit density of $5.10^{-2}\ cm^{-2}$ satisfies the requirements to record central Pb-Pb collisions where hundreds of tracks can hit the muon chambers.

2.3.3.4 The Trigger Stations

The trigger system is composed of two stations, MT1[5] and MT2, located right after the iron wall, at 16 and 17 m from the interaction point. Each station is composed of two Resistive Plate Chambers (RPC). The RPCs are made of high resistivity bakelite and separated by a 2 mm gas layer ionised when a charged particle passes through it. These thin gas layers (and the high voltage applied to the electrodes) leads to a fast drift of the produced electron avalanche to the strips. On one side, the strips are oriented to measure the y-coordinate (to estimate the deviation in the non-bending plane), on the other side strips are aligned along the x-coordinate (for the deviation in the bending plane). The signal from the strips (obtained in a same active part of the trigger) is sent to a set of local trigger boards where a fast estimate of the track

[4]The occupancy rate is the proportion of fired strips (or pads) over their total amount in a given chamber

[5]MT: Muon Trigger

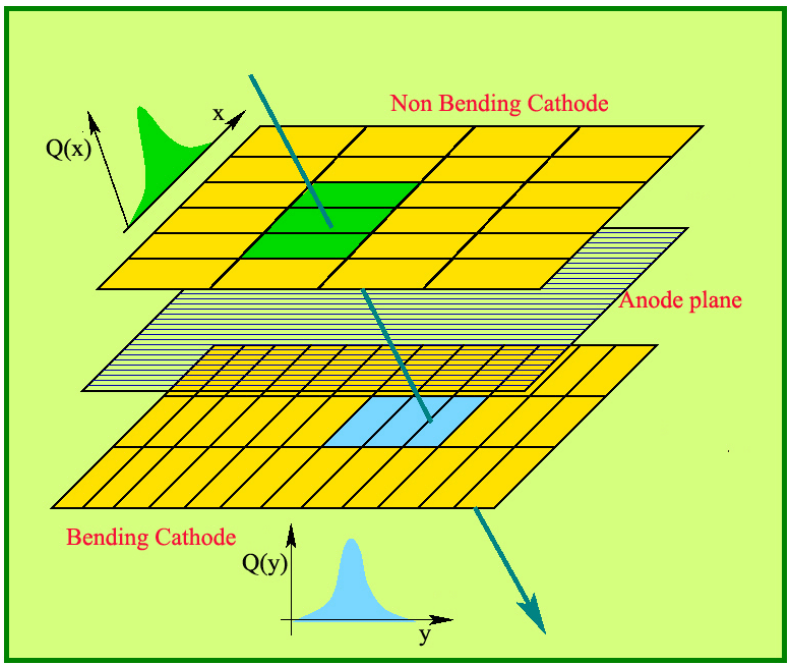

Figure 2.8: Representation of the mechanism of a cathode pad chamber used for muon tracking

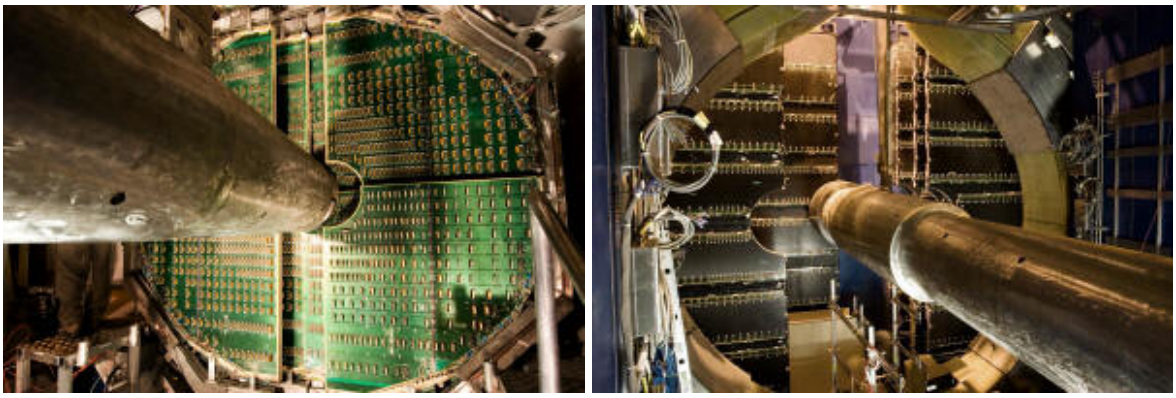

(a) Small muon chambers with their quadrant arrangement used for the first and second stations

(b) Large muon chambers with their slat arrangement used for the third, fourth, fifth stations

Figure 2.9

momentum is performed. This allows to reconstruct a tracklet between MT1 and MT2 and to have an estimate on the p_T of the muon. The trigger is fired if at least three of the four possible RPC planes return a signal compatible to a tracklet in the muon trigger system.

The muon arm trigger rejects residual hadrons and part of the muons coming from the decay of kaons and pions. As these muons are soft and present low-p_{T} values, they can be

rejected by applying a criterion on the p_T of the tracklet reconstructed by the trigger. The values on the p_{T} threshold range from $p_{\mathrm{T}} > 0.5$ GeV/c to 2 GeV/c The low-p_{T} threshold ($p_{\mathrm{T}} > 0.5$ GeV/c) allows the study of the ϕ and ω mesons to low resonance transverse momenta (~ 0.5 GeV/c). Higher muon p_{T} thresholds can be used to lower the combinatorial background and reduce the acquisition rate, but deteriorate the ϕ and ω extraction at low p_{T}.

2.4 Data Acquisition

Due to the high frequency of collisions, ALICE requires a high-performance Data AcQuisition (DAQ) system. It would indeed be impossible for the experiment to record all the events because of the different acquisition time of the various detectors, and because of data storage limitation. The idea is then to trigger the record of an event if several conditions are satisfied in order not to saturate the DAQ system. Then the acquisition rate can be reduced by deciding to record only a given fraction of the events: in this case, a downscaling factor is applied.

Another point is that part of the analyses do not need the information from all the different detectors so triggers can be clusterised. This is the case for dimuons analyses which do not require the information from most of central detectors. These clusters trigger the acquisition of part of the detectors even if other detectors do not respond, or are just not included. An example of these clusters is the MUFAST (SPD, MCH, MTR, V0, T0) including all the required information for dimuon analysis.

2.4.1 Triggering System

Once the various trigger signals are sent to the ALICE Central Trigger Processor (CTP)[56], this decides, depending on the selected criteria and available bandwidth, to record the event or not. The decision times of the CTP are separated into different trigger levels, depending on the time the trigger signal takes to reach the CPT:

- Level 0 (L0): the fastest triggering system with a ~ 1.2 μs latency time composed of the V0, T0, SPD, EMCAL and the MTR,
- Level 1 (L1): dealing with the TRD and ZDC information with a 6.5 μs latency,

- Level 2 (L2): the slowest triggering system, coming from the TPC where the drifting time of the electrons in the detector delay the triggering leading to an 88 μs latency.

A list or interesting triggers for this analysis is presented in table 2.2.

Detector	Signal Name	Requirement
V0	INT5	signal in V0A or in V0C
	INT7	signal in V0A and in V0C
	HighMultV0	signal in V0A and in V0C passing a threshold
MTR	0MSL	Single-Muon low-p_T
	0MSH	Single-Muon high-p_T
	0MUL	Dimuon unlike-sign low-p_T
	0MLL	Dimuon like-sign low-p_T

Table 2.2: Table of available triggers from the VZERO and the muon triggers

Most of the events analysed in central barrel require to have a signal from the TPC which is the main particle identifier device. As all the events can not be processed as it would occupy too much storage, a selection of the events based on their quality is used to trigger the event record. As the TPC has an intrinsic latency due to the drift of the electrons, a subset of the information (and also of the SPD) from the previous events is used to partially reconstruct the events. The reconstruction of the event is performed by the High-Level Trigger (HLT) which on top of partially reconstructing the events, performs quality selection, mostly based on the reconstructed tracks (number of clusters assigned, number of tracklets), and compresses the data without any physical loss.

2.4.2 Acquisition System

The Data Acquisition (DAQ) system of ALICE has been specially designed to support either the high event rate from pp but especially coming from Pb-Pb collisions. Once a specific trigger is fired, its signal is sent to the Front-End Read-Out (FERO) of the concerned detectors. When the detector spots the signal, it is transferred to a computing farm, the Local Data Concentrators (LDC) reconstructing sub-events using the Detector Data Link (DDL). If the LDCs

are occupied, data can be stored on a data buffer, a ReadOut Receiver Card (RORC). Then the data are analysed using the HLT, and depending on its decision, the full or just a part of the event is reconstructed by the Global Data Collector (GDC). Finally, the reconstructed events are recorded on a Permanent Data Storage (PDS) support.

2.4.3 Data Reconstruction

Once stored, data are saved under the Event Summary Data (ESD) format containing all the required information on the event, either for the different analyses or for offline calibration of the detectors. As these files can become too heavy for particular analyses purpose, they are filtered, without losing any physical content, giving the Analysis Object Data (AOD) format. The AODs are used in the present analysis.

To perform the analysis on the large amount of data recorded by ALICE (more than 1 PByte per year) specific computing resources are used. First, the LHC Computing Grid (LCG) allows the access to all the reconstructed events in all the different access points of the grid. On the grid one can also access the additional information on data such as the polarity of the magnetic field, the detector alignment or the scalers in the Offline Condition Data Base (OCDB). Additional information, mostly related to the beam condition, can be found in the ALICE logbook.

Chapter 3

Data selection, MC simulations and signal extraction

The results of two different analyses are presented in this thesis. Both studies are performed on the same data sample of pp collisions at $\sqrt{s}$ = 5.02 TeV recorded by ALICE. The first analysis, focusing on the kinematic distributions of the ω and ϕ mesons, will be presented in Chapter 4 and is mentioned as the *multiplicity integrated analysis*. The second analysis aims attention at the multiplicity dependence of ω and ϕ mesons production and is presented in Chapter 5. It is referred as the *multiplicity dependent analysis*. In the present chapter, the items common to both analyses are detailed. They include the event and track selection, the signal extraction and the Monte Carlo simulations.

3.1 Data, run and event selection

3.1.1 Data periods and run selection

The analyses presented in this thesis are performed on pp collisions at $\sqrt{s}$ = 5.02 TeV recorded by ALICE. These collisions were provided by the LHC and recorded during three different periods. One was produced in 2015, the LHC15n period, and two in 2017, the LHC17p and LHC17q periods. For the analyses presented in this work, only the periods from 2017 are kept as they show similar detectors responses and together enclose around ten times more events

(single pp collisions) than the one produced in 2015.

Runs are requested to pass the different quality assurance for the relevant detectors used in the analyses[1]. In the *multiplicity integrated analysis*, that will be presented in Chapter 4, the relevant detectors are the forward muon spectrometer and the V0. In the *multiplicity dependent analysis* discussed in Chapter 5, the relevant detectors are the same as in the *multiplicity integrated analysis* plus the SPD sub-detector of the ITS, which is used to estimate the multiplicity. The quality assurance (QA) is an offline control of each detector's response during a run. In the muon arm's case, the run QA consists of an ensemble of checks on the various information from the detectors. Values such as the mean number of tracks per triggered event and the charge asymmetry of the reconstructed tracks are controlled to ensure that the detector response returns physically coherent results. The selected runs are listed in Appendix B. There is a total of 51 runs, all with the same magnet polarity ($--$). The additional requirement that the SPD satisfies its QA criteria does not change the number of considered runs. However, it can be pointed out that among these runs, ten of them were running with neither TPC nor TOF.

3.1.2 Event selection

After passing the run selection, each event is controlled and selected depending on the fired triggers. Events are required to satisfy the MB trigger (kINT7) provided by the V0 detector as described in section 2.3.2 to include the largest possible number of inelastic events without introducing any selection bias in data.

In order to reject the beam-gas and gas-gas interaction occurring in the beam pipe, the *Physics Selection* (PS) flag is required. This selection consists of a set of cuts applied to reject background and poor quality events. Its main feature consists on checking the coincidence time of the signal obtained from the two scintillators V0A and V0C. If the signal occurred at the

[1]Quality assurance for the LHC17p period: `https://twiki.cern.ch/twiki/pub/ALICE/MuonppQA2017/muonQALHC17pmuoncalopass1.pdf`
QA for the LHC17q period: `https://twiki.cern.ch/twiki/pub/ALICE/MuonppQA2017/muonQALHC17qmuoncalopass1.pdf`

level of the interaction point of the ALICE detector, the V0A trigger (located 329 cm from the interaction point) should be fired $\sim$ 11 ns after the expected collision time (given by the LHC clock) and the V0C (87 cm from the interaction point) after $\sim$ 3 ns. Thus, the PS selection removes events showing a negative and too high arrival time in the V0A and V0C, rejecting background events such as beam-gas and gas-gas interactions. On top of the *Physics Selection*, the rejection of pile-up in the SPD is applied. This selection is performed to remove events in which more than one collision was considered during the same SPD integration time. Indeed, if more than one collision occurs during the SPD integration time, tracks can be associated to the wrong vertex, and the total number of tracks associated with the event would lead to an artificial increase of event multiplicity. Additionally, events are requested to occur within 20 cm from the ITS center, where a fair resolution on the vertex position is found.

The selections applied to events are thus the following:

- Minimum Bias triggered,
- Physics Selection with SPD pile-up rejection,
- $|V_Z|<$ 20 cm,
- Number of tracklets used for the vertex reconstruction: $N^{Vtx}_{Contrib.} \geq 1$

For the *multiplicity dependent analysis*, events are requested to pass the $INEL > 0$ requirement. This requirement is satisfied if at least one charged particle is reconstructed by the SPD within $|\eta|< 1$ and is assigned to the vertex. As in this analysis the multiplicity estimation is performed using the SPD information, additional requirements are made for the event quality. The vertex is requested to fall in the $-10 < V_Z^{SPD} < 10$ cm region, where the measure of the number of tracklets in the SPD (within $|\eta|<1$) can be determined. The algorithm for the estimation of the z-coordinate of the primary vertex consists in the correlation of reconstructed points belonging to the first layer of the SPD with reconstructed points belonging to the second one within a small azimuthal window (by default set to $\Delta\varphi_{12}$=0.01 rad). The uncertainty on the position of the vertex is estimated based on the contributions of SPD reconstructed point resolution and multiple scattering. In the case of low-multiplicity events, few SPD points will be considered for its estimate, leading to a worsening of the V_Z resolution [57].

As recommended by the *QA group* a quality cut on the vertex resolution σ_{V_Z} <0.25 cm should be applied.

The additional selections applied to events for the *multiplicity dependent analysis* are thus:

- $-10 < V_Z^{SPD} < 10$ cm, the position of the primary vertex from the SPD along the Z-axis,
- $\sigma(V_Z^{SPD}) < 0.25$ cm, the resolution on the primary vertex from the SPD.

Events must also pass the opposite-sign or the like-sign dimuon trigger (respectively CMUL7 or CMLL7). These triggers are activated when at least two opposite-charge (CMUL7) or two same-charge (CMLL7) tracks, each with a transverse momentum threshold set at $p_T^{\mu} \gtrsim 0.5$ GeV/*c*, fire the muon trigger chambers as described in 2.4.1.

3.1.3 Integrated Luminosity

The events considered in the analysis are the ones that fire the dimuon trigger. As they do not represent the full number of minimum bias events, the number of dimuon triggered events is corrected to correspond to the number of minimum bias events. The integrated luminosity is evaluated from the Minimum Bias (MB) events as:

$$L_{int} = \frac{N_{MB}}{\sigma_{MB}} = \frac{F_{Norm} \cdot N_{CMUL}}{\sigma_{MB}} \ . \tag{3.1}$$

N_{MB} is the number of MB events for the analysed triggered events, F_{Norm} is the normalisation factor that allows for rescaling the number of CMUL7 (N_{CMUL}) to the number of MB triggered events (N_{MB}) and σ_{MB} is the MB cross section estimated using a Van Der Meer scan [58].

The number of Minimum Bias events N_{MB} is obtained as

$$N_{MB} = \sum_{irun=1}^{n_{run}} F_{Norm}^{irun} \cdot N_{CMUL}^{irun} \ , \tag{3.2}$$

where N_{CMUL}^{irun} is the number of events satisfying the CMUL7 requirements in the run *irun* and F_{Norm}^{irun} is the normalisation factor to rescale the number of CMUL7 events to the number of Minimum Bias events in each run.

To evaluate the value of F_{Norm}^{irun}, first one has to take into account the correction due to the pile-up rejection. The pile-up correction factor (PU^{irun}) can be evaluated in each run according to the equation:

$$PU^{irun} = \frac{\mu^{irun}}{1 - e^{\mu^{irun}}} \ , \tag{3.3}$$

where

$$\mu^{irun} = -ln\left(1 - \frac{F_{purity}^{MB,irun} \cdot L0b_{MB}^{irun}}{D^{irun} \cdot N_{colliding}^{irun} \cdot f_{LHC}}\right) \ , \tag{3.4}$$

is obtained using [2] :

- f_{LHC}: the bunch frequency in the LHC (11245 Hz),
- $N_{colliding}^{irun}$: the number of colliding bunches,
- D^{irun}: the run duration given by the Central Trigger Processor (CTP),
- $L0b_{MB}^{irun}$: the scaler input of the level-0 trigger for the considered MB condition,
- $F_{purity}^{MB,irun}$: the purity factor for the MB trigger, as defined as

$$F_{purity}^{MB,irun} = \frac{N_{MB}^{irun}(PS)}{N_{MB}^{irun}(All)} \ , \tag{3.5}$$

  where $N_{MB}^{irun}(PS)$ is the number of Physics-Selected and MB triggered events, and $N_{MB}^{irun}(All)$ all the Minimum Bias events. In this case where the number of MB events is estimated from the number of CMUL events, the technique will be denoted as the *direct method*.

As the number of $MUL\&MB$ triggered events can be limited and lead to high statistical uncertainties on the normalisation factor, the evaluation of the latest can be performed using the relative rate of the number of $MB\&OMSL$ events to the number of $MSL\&OMUL$. To calculate F_{Norm}^{irun} an *indirect method* is used, given:

[2] The following values can be obtained for each run in the *ALICE logbook* as introduced in 2.4.3 as for the run 282343: `https://alice-logbook.cern.ch/logbook/dateonline.php?pcont=rund&prun=282343&ptab=trg&psubtab=tti`

$$F_{Norm}^{irun} = PU^{irun} \cdot \frac{MB^{irun}}{(MB\&OMSL)^{irun}} \cdot \frac{MSL^{irun}}{(MSL\&OMUL)^{irun}} \tag{3.6}$$

In this equation, the different terms correspond to:

- MSL^{irun} is the number of events passing the single-muon trigger conditions. The single muon trigger is satisfied when at least one segment is present in the muon-trigger, and the Minimum Bias conditions (from the V0) are satisfied.
- $(MB\&0MSL)^{irun}$ is the number of physics-selected MB events also satisfying the MSL trigger condition at level 0.
- $(MSL\&0MUL)^{irun}$ is the number of physics-selected MSL events also satisfying the CMUL7 trigger condition at level 0.

The integrated luminosity has been estimated for the LHC17p and LHC17q periods to be $L_{int} = 1222.6$ nb^{-1}, with an uncertainty of 2.1% as presented in [59] and with a MB cross-section measured from the V0 of σ_{MB} =(50.77$\pm$0.05$\pm$1.8%) mb. Figure 3.4 represents the integrated luminosity collected by ALICE during RUN2 data taking period in pp collisions at $\sqrt{s}$ =5.02 TeV.

Following the same idea, the correction factor $F_{Norm.}^{jmult}$ was estimated for each *jmult* multiplicity interval in the *multiplicity dependent analysis*. Thus, the normalisation factor is calculated separately for each multiplicity interval as:

$$F_{Norm}^{jmult} = \frac{1}{N_{MUL}^{irun}} \sum_{irun=run} F_{Norm}^{irun} \cdot N_{MUL}^{irun} \frac{N_{MB}^{irun,jmult}}{N_{MB}^{irun}}. \tag{3.7}$$

In equation 3.7 in each $N_{MB}^{irun,jmult}$ denotes the number of MB events for each $irun$ in each $jmult$ multiplicity interval. The different values of F_{Norm}^{jmult} are presented in table 3.1.

3.1.4 Single track and pair selections

A set of cuts was applied to the muon tracks reconstructed in the muon arm (as described in 2.3.3), both on single muons and on muon pairs. The selections applied in this analysis are the following:

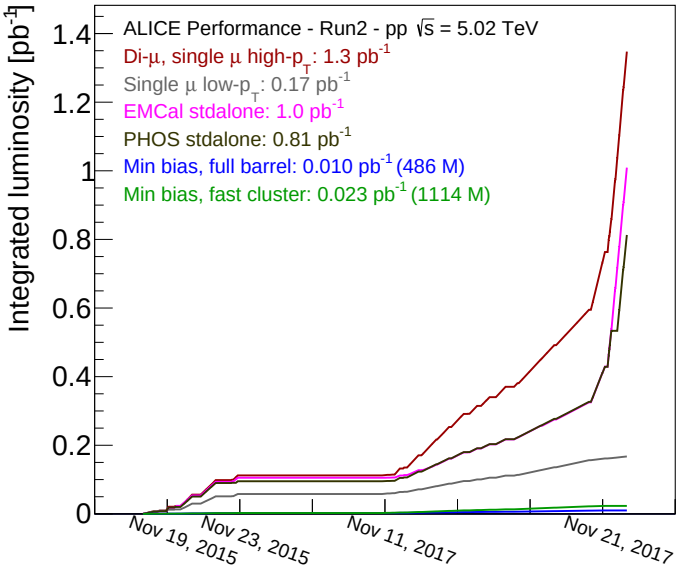

Figure 3.1: Integrated Luminosity measured by the ALICE collaboration in pp collisions at $\sqrt{s}$ =5.02 TeV for different triggers.

		F_{Norm}^{jmult}		
$N_{SPD,Trk}^{Cor.}$	Mult. Percentile	Indirect	Direct	Systematic uncertainty
[1-7]	50-100%	5920.19 ± 0.05	5898 ± 55	0.37 %
[8-15]	20-50%	2945.88 ± 0.04	2934 ± 42	0.38 %
[16-21]	10-20%	1923.73 ± 0.03	1916 ± 36	0.37 %
[22-105]	0-10%	1247.78 ± 0.03	1241 ± 39	0.38 %
[1-105]	0-100%	3225.19 ± 0.06	3213 ± 58	0.37 %

Table 3.1: Summary of the different correction factors F_{Norm}^{jmult}, obtained either with the direct and the indirect method and the resulting systematic uncertainty.

- the muon track reconstructed in the muon tracker must match a tracklet reconstructed in the muon trigger at the low-p_T level ($p_T^{\mu} \gtrsim 0.5$ *GeV/c*);
- $-4 < \eta_{\mu} < -2.5$ [3] to ensure that the track has been reconstructed in the active part of the muon arm and to avoid edge effects;

[3] In the ALICE reference frame the muon spectrometer covers negative η. However, positive values are used when referring to y.

After selecting tracks, a cut is applied at the pair level to select reconstructed pairs in the phase space domain covered by this analysis:

- $2.5 < y_{\mu\mu} < 4$;
- $p_{\mathrm{T}}^{\mu\mu} > 0.75$ *GeV/c*;
- the muon pairs are required to hit different local boards (presented in section 2.3.3.4). This selection has been introduced to avoid correlations introduced by the trigger when two muons cross the same local board, thus giving a single muon trigger signal.

Both single track and pair selections are summarised in table 3.2.

Cut Selection Summary	
Track Level	
Quality Cut	track matches a tracklet in the trigger
Kinematic Cut	$p_{\mathrm{T}}^{\mu} \gtrsim 0.5$ GeV/c $-4 < \eta_{\mu} < -2.5$
Pair Level	
Quality Cut	muons cannot hit the same local board
Kinematic Cut	$2.5 < y_{\mu\mu} < 4$ $p_{\mathrm{T}}^{\mu\mu} > 0.75$ *GeV/c*

Table 3.2: Summary of the pair selection

3.1.5 Opposite-sign mass spectra and raw signal

The signal in the low-mass region is composed of opposite-sign pairs coming from either the same mother particle, in the case of light flavours, or originating from a pair of correlated open-heavy flavour hadrons decaying semi-leptonically (creating a continuum). As experimentally the origin of muons cannot be known, all tracks passing the previously described selection (presented in 3.1.4) in the same event are paired together. This pairing gives rise to two types of pairs: the opposite-sign(OS) and the like-sign(LS) pair. From the OS pairs, one has to separate the signal from correlated muon pairs(S), and combinatorial pairs that create an uncorrelated

background(B), where uncorrelated muons coming from the weak decays of kaons and pions are the main contributors.

The combinatorial background was evaluated using the *event mixing* technique. This technique consists of pairing single muons taken from different events and passing the different selections. Thus, the created muon pairs are uncorrelated by construction, and their total amount is normalised using the total number of LS pairs from data and correcting for possible biases introduced by the detector. The like sign yield is taken as the geometrical mean of both $N^{data}_{\mu^+\mu^+}$ and $N^{data}_{\mu^-\mu^-}$ measured in data.

To correct for bias effects introduced by the detector, a multiplicative factor, the correction factor R defined as:

$$R = \frac{A_{\mu^+\mu^-}}{\sqrt{A_{\mu^+\mu^+} \cdot A_{\mu^-\mu^-}}} \,, \tag{3.8}$$

is applied. $A_{\mu^+\mu^-}$, $A_{\mu^+\mu^+}$ and $A_{\mu^-\mu^-}$ respectively stand for the acceptance for OS, $++$ and $--$ pairs. The latest are mixed among the events showing similar features to obtain a coherent description of the uncorrelated signal. Hence in the *multiplicity dependent analysis*, only muons coming from the same multiplicity interval are mixed together. In this particular case, ten multiplicity intervals matching the edges of the intervals in the analysis are considered. The R-factor is evaluated as:

$$R = \frac{N^{mixed}_{\mu^+\mu^-}}{2\sqrt{N^{mixed}_{\mu^+\mu^+} \cdot N^{mixed}_{\mu^-\mu^-}}} \,, \tag{3.9}$$

where $N^{mixed}_{\mu^+\mu^-}$, $N^{mixed}_{\mu^+\mu^+}$ and $N^{mixed}_{\mu^-\mu^-}$ correspond to the number of OS, $++$ and $--$ pairs obtained by event mixing.

This finally allows us to estimate the combinatorial background

$$B(m) = N^{mixed}_{\mu^+\mu^-}(m) \cdot S_f \,, \tag{3.10}$$

where the number of OS-mixed pairs ($N^{mixed}_{\mu^+\mu^-}(m)$) is scaled to the number of pairs obtained in data as defined in equation 3.11

$$S_f = \frac{2 \cdot R \cdot \sqrt{N^{data}_{\mu^+\mu^+} N^{data}_{\mu^-\mu^-}}}{N^{mixed}_{\mu^+\mu^-}} \tag{3.11}$$

Finally, the estimation of correlated pairs, here denoted as signal, is obtained:

$$S(m) = N^{data}_{\mu^+\mu^-}(m) - B(m) \tag{3.12}$$

Figure 3.2 shows the overall opposite-sign mass spectra together with the background (evaluated via event-mixing) for $0.75 < p_{\mathrm{T}} < 8$ GeV/c obtained in the *multiplicity integrated analysis*.

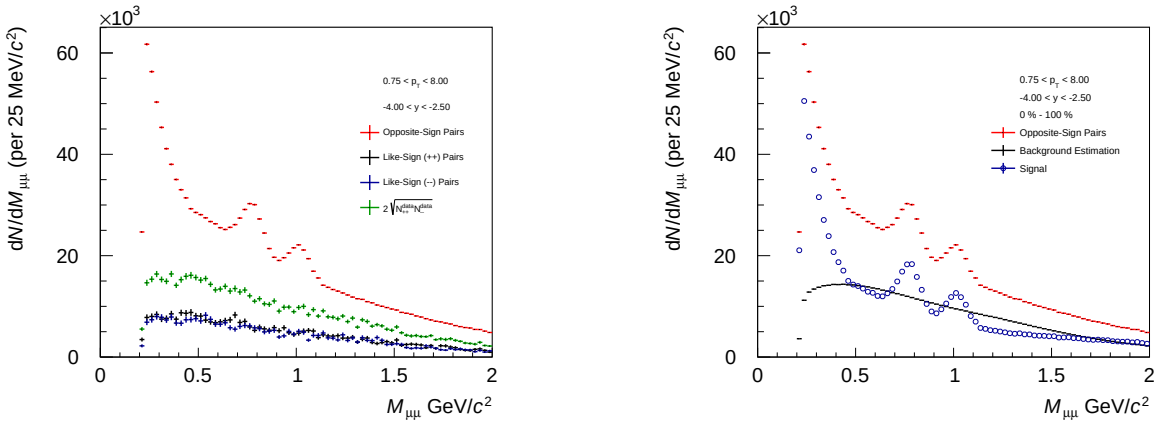

(a) Invariant mass spectra from LS and OS muon pairs obtained from data for $0.75 < p_{\mathrm{T}} < 8$ GeV/c and $2.5 < y_{\mu\mu} < 4$ at $\sqrt{s} = 5.02$ TeV

(b) Invariant mass spectra from OS, combinatorial estimation and correlated muon pairs obtained from data after background subtraction for $0.75 < p_{\mathrm{T}} < 8$ GeV/c and $2.5 < y_{\mu\mu} < 4$ at $\sqrt{s} = 5.02$ TeV

Figure 3.2: OS and uncorrelated pairs allowing the estimation of signal integrated over $0.75 < p_{\mathrm{T}} < 8$ GeV/c and $2.5 < y_{\mu\mu} < 4$

As shown in fig. 3.2(a) the number of like-sign muon pairs is suffering from statistical uncertainties that would be propagated to signal if they would be used directly for the estimation of combinatorial background. The use of mixed events removes this dependency on the statistics of like-sign pairs measured in data but blinds the physics encoded in these pairs such as correlated like-sign pairs coming from open-beauty pairs. Thus starting from the overall OS yield and background estimation as in Figure 3.2(b), one can obtain the estimate of correlated muon pairs. From this figure, it can already be noticed the four main contributors to the invariant mass spectrum: the $\eta \rightarrow \mu^+\mu^-\gamma$ Dalitz-decay at low masses, the $\omega \rightarrow \mu^+\mu^-$ and

the $\phi \rightarrow \mu^+\mu^-$ two-body decays peaking at their respective masses, and finally, the correlated continuum mostly composed of open $c\bar{c}$ decaying semi-leptonically present all along the studied mass range.

Figure 3.3(a) shows the ratio of the estimated correlated pairs over combinatorial background pairs. This ratio shows a maximum at low invariant masses due to the low combinatorial background contribution at these values and to the high contribution from the η Dalitz-decay. The ratio maximises at the level of the 2-body decays of the ω and the ϕ, increasing respectively up to 1.55 and 1.40. Similar behaviour is observed for statistical significance $\sigma = S/\sqrt{B+S}$ in Figure 3.3(b), but statistically dependent, where it maximises at low $M_{\mu\mu}$ and is of 110 for ω and 85 for ϕ.

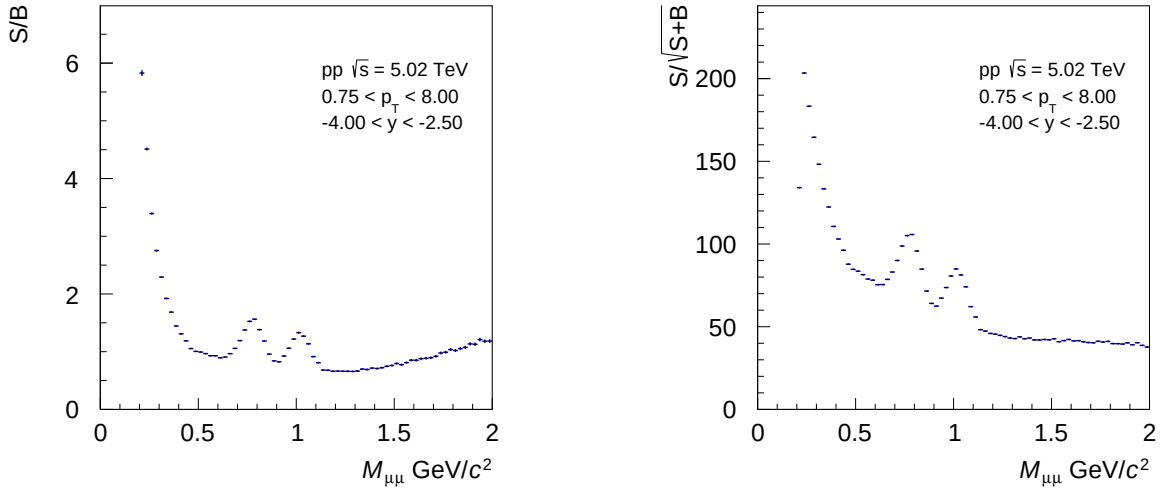

(a) Signal over Background as a function of invariant mass

(b) Statistical significance (σ) defined as $\sigma = S/\sqrt{B+S}$ as a function of invariant mass

Figure 3.3

3.2 Monte Carlo simulation of the dimuon sources

To extract the contribution from the various components of the dimuon signal, a phenomenological fit based on simulations is used. These simulations encode two crucial pieces of information: first, at the generation level, the relative contributions from particles decaying into

dimuons with their associated kinematic; second when simulating the propagation of the particles through the ALICE detectors using a transport code. This step allows the estimation of the distortion introduced by the detector and the various selections applied to the signal.

3.2.1 The generation of the hadronic cocktail

As discussed in section 1.3, the signal is provided by two main components, the decay of light hadrons resonances (the so-called hadronic cocktail) and heavy-flavour hadrons. Their generation is performed using the AliROOT framework. The light resonances generation is performed using the *AliGenMUONLMR* generator, while for heavy-flavours the *AliGenCorrHF* parametrisation is used.

3.2.1.1 The hadronic cocktail

The processes entering the dimuon signal in the low mass region via their electromagnetic decays are:

- $\eta \to \mu^+\mu^-$, - $\eta \to \gamma\mu^+\mu^-$, - $\rho \to \mu^+\mu^-$, - $\omega \to \mu^+\mu^-$,
- $\omega \to \pi^0\mu^+\mu^-$, - $\eta' \to \gamma\mu^+\mu^-$, - $\phi \to \mu^+\mu^-$

The generated kinematics of the hadrons include crucial information on the process. First, the mass widths of the mesons are parametrised. This is particulary important for the ρ meson which has a short lifetime of 1.3 fm/*c*. Then come the p_{T} and rapidity distributions of the different mesons, and finally, the form factors of the Dalitz decays for the η, η' and ω.

Two-body decay and ρ mass shape Due to its short lifetime of 1.3 fm/*c*, the ρ meson presents a significantly large mass width. Contrarily to the other mesons that have a larger lifetime, leading to smaller mass-widths which can be generated as δ-functions at their pole-mass, the mass width of the ρ must be parametrised. In accordance with the results obtained by NA60 [60] [61], the following parametrisation of the ρ is used:

$$\frac{dN(M)}{dM} = \frac{\alpha^2 m_\rho^4}{3(2\pi)^4} \frac{\sqrt{1-\frac{4m_\mu^2}{M^2}}\left(1+\frac{2m_\mu^2}{M^2}\right)\left(1-\frac{4m_\pi^2}{M^2}\right)^{3/2}(MT)^{3/2}e^{-M/T_\rho}}{(m_\rho^2-M^2)^2+m_\rho^2\Gamma_\rho^2(M)}\,, \tag{3.13}$$

where the width $\Gamma_\rho(M)$ is also mass dependent and taken as:

$$\Gamma_\rho(M) = \Gamma_{0\rho}\frac{m_\rho}{M}\left(\frac{M^2/4 - m_\mu^2}{m_\rho^2/4 - m_\mu^2}\right)^{3/2} \quad . \tag{3.14}$$

In these equations, the muon m_μ and pion m_π masses, just like the nominal width $\Gamma_{0\rho}$, are fixed to the PDG values while m_ρ (the pole mass) and T_ρ were obtained from NA60 data [61].

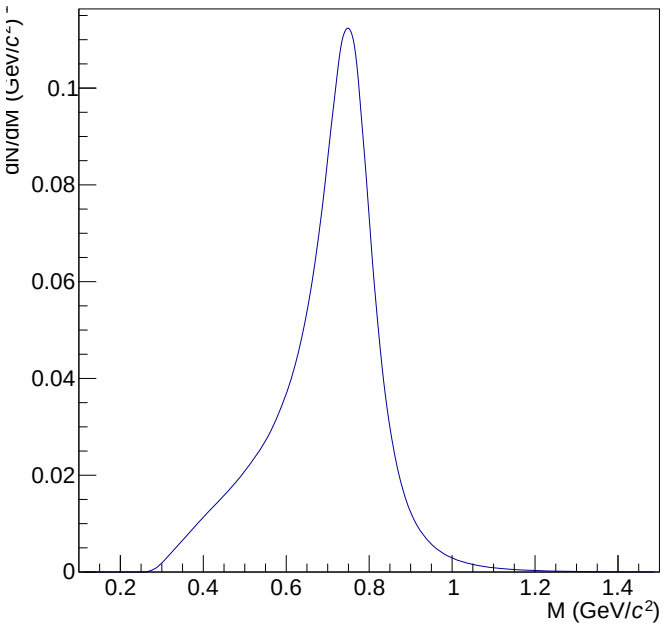

Figure 3.4: Mass shape of the generated ρ meson

Dalitz decay and form factors Part of the dimuon signal observed at low mass is coming from the Dalitz decays of the η, η' and ω. In this case, the particles decay into a virtual photon γ^* of mass M that converts into a muon pair and a third party (either a real photon or a π^0). From these decays, only the correlated muon pair is detected, meaning that the reconstructed invariant mass of the pair is the one of the virtual photon that created it. This requires knowledge of the mass shape of such processes. This is actually provided by the so-called *form factors* ($|F(M^2)|^2$) which can be evaluated using QED calculations or parametrisations from measurements. The obtained dimuon invariant mass distributions can be expressed for the different contributors to the low-mass spectrum as

$$\frac{d\Gamma(\eta \to \mu\mu\gamma)}{dM} = 2M\frac{2}{3}\frac{\alpha}{\pi}\frac{\Gamma(\eta \to \gamma\gamma)}{M^2}\left(1-\frac{M^2}{m_\eta^2}\right)^3\left(1+\frac{2m_\mu^2}{M^2}\right)\sqrt{1-\frac{4m^2}{M^2}}|F_\eta(M^2)|^2\,, \tag{3.15}$$

$$\begin{aligned}\frac{d\Gamma(\omega \to \mu\mu\pi^0)}{dM} &= 2M\frac{2}{3}\frac{\alpha}{\pi}\frac{\Gamma(\omega \to \gamma\pi)}{M^2}\left(1+\frac{2m_\mu^2}{M^2}\right)\sqrt{1-\frac{4m_\mu^2}{M^2}} \\ &\times\left[\left(1+\frac{M}{m_\omega^2-m_{\pi^0}^2}\right)^2-\frac{4m_\omega^2M^2}{(m_\omega^2-m_{\pi^0}^2)^2}\right]^{3/2}|F_\omega(M^2)|^2\,, \text{ and}\end{aligned} \tag{3.16}$$

$$\frac{d\Gamma(\eta' \to \mu\mu\gamma)}{dM} = 2M\frac{2}{3}\frac{\alpha}{\pi}\frac{\Gamma(\eta' \to \gamma\gamma)}{M^2}\left(1+\frac{2m_\mu^2}{M^2}\right)\left(1-\frac{M}{m_{\eta'}^2}\right)\sqrt{1-\frac{4m_\mu^2}{M^2}}|F_{\eta'}(M^2)|^2\,, \tag{3.17}$$

where all the different masses used as input are taken from the PDG [8]. Concerning the form factors they are given as a pole-parametrisation for the η and the ω mesons while for the η' a Breit-Wigner is considered as described below:

$$|F_\eta(M^2)|^2 = \frac{1}{\left(1-\frac{M^2}{\Lambda_\eta^2}\right)^2}\,, \tag{3.18}$$

$$|F_\omega(M^2)|^2 = \frac{1}{\left(1-\frac{M^2}{\Lambda_\omega^2}\right)^2}\,, \text{ and} \tag{3.19}$$

$$|F_{\eta'}(M^2)|^2 = \frac{m_0^4}{(m_0^2-M^2)^2+m_0^2\Gamma_0^2}. \tag{3.20}$$

The form factors of the η and the ω are taken from the NA60 results in [61] and the parameters for the η' are taken from the Lepton-G data [62].

All the equations describing the Dalitz-Decay of light mesons in 3.15-3.20 are implemented in the *AliGenMUONLMR* generator. The generated dimuon invariant mass distributions of the Dalitz decay processes are shown in figure 3.5.

p_{T} and *y* distributions The kinematic properties (p_{T} and rapidity) of part of these hadrons and their relative abundances have already been measured. Based on the previous measurements performed with the low-statistics LHC15n sample, the achieved knowledge was used

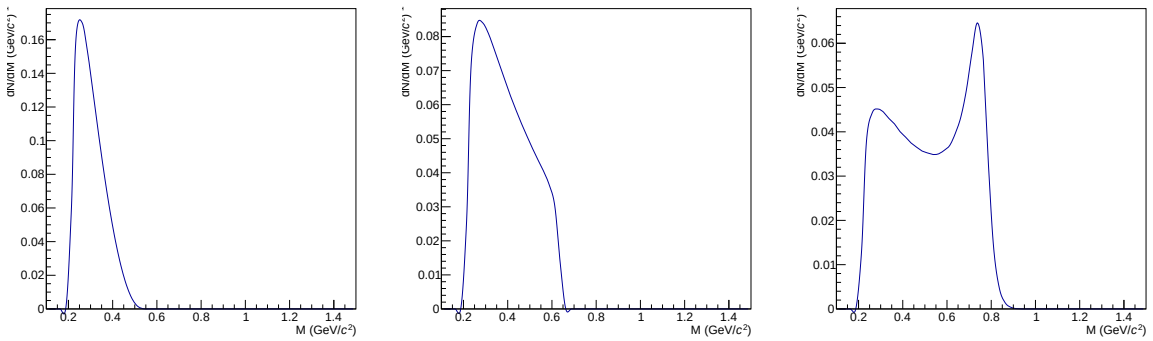

Figure 3.5: Invariant mass distributions of the generated muon pairs from the Dalitz decay of the η (**left**), ω (**center**), η' (**right**)

to parametrise the kinematic distributions of the ϕ and ω mesons. These were used as input for the simulation of the hadronic cocktail, as done in previous low-mass dimuons analyses [63][64]. The input rapidity and p_{T} distributions of the other mesons are based on a parametrisation of PYTHIA 6.4 with the Perugia-0 tune [65]. The input p_{T} distribution is described with a power-law function:

$$\frac{dN}{dp_{\mathrm{T}}} = C\frac{p_{\mathrm{T}}}{[1+(p_{\mathrm{T}}/p_0)^2]^n} \,. \tag{3.21}$$

The rapidity distributions show a plateau centered around $y = 0$ and gaussian tails as described in the equation:

$$\frac{dN(y)}{dy} = \begin{cases} N_0, & \text{if } y < |y_0| \\ N_0 e^{-((y-a)/b)^2/2}, & \text{if} y \geq y_0 \\ N_0 e^{-((y+a)/b)^2/2}, & \text{if} y \leq y_0 \end{cases} \,. \tag{3.22}$$

3.2.1.2 Heavy flavour simulation

The heavy flavour contribution to the correlated signal corresponds to the semileptonic decays of open charm ($D \rightarrow X + \mu$) and beauty hadrons ($B \rightarrow X + \mu$). As the c and $\bar{c}$ (or b and $\bar{b}$) are always created in pairs and hadronise separately (creating open heavy flavours), their correlation propagates to the muons which are the products of their semimuonic decays. This results in correlated muon pairs creating a continuum in the invariant mass spectrum.

Differently to light flavour mesons (sec. 3.2.1.1) this contribution was generated using a PYTHIA 6.4 parametrisation implemented in the *AliGenCorrHF* code from the AliRoot framework. The contribution from open beauty is computed separately from open charm and considering only one pair per event (in each case).

3.2.2 Simulation and reconstruction

Once generated the simulation process uses a transport code based on the GEANT3 [66] to reproduce the effect of the ALICE detector, and especially of the muon arm. As the bias introduced by the detector depends on the dimuon kinematic hitting it, the accurate knowledge about the later is crucial.

3.2.2.1 Dimuon Reconstruction

Once the various processes are simulated, the distortions introduced by the apparatus can be reproduced by transport codes. Two of them are considered here: GEANT3[66] and GEANT4[67]. Once propagated through the different parts of the detector, different impacts (hits) are produced by the particles interacting within the active part of the detector. These hits are digitised first into SDigit to consider the detector response function and then into Digits to account for the detector electronic noise and calibration. During this last step, the response of the muon trigger is also simulated. Finally, the produced Digits are processed using the same reconstruction algorithm as for data, and the events are saved in the AOD/ESD format keeping information on the different generated "true" particles. A sketch of the full process in the ALICE framework is presented in figure 3.6.

3.2.2.2 Acceptance and efficiency correction

The acceptance times efficiency ($\mathcal{A} \times \epsilon$) factor accounts for the bias introduced by the limited detector geometry coverage (the acceptance) and the selection criteria applied to the different events together with the actual efficiency of the detector (efficiency). The $\mathcal{A} \times \epsilon$ for the $\phi \rightarrow \mu^+\mu^-$ and the $\omega \rightarrow \mu^+\mu^-$ decays is

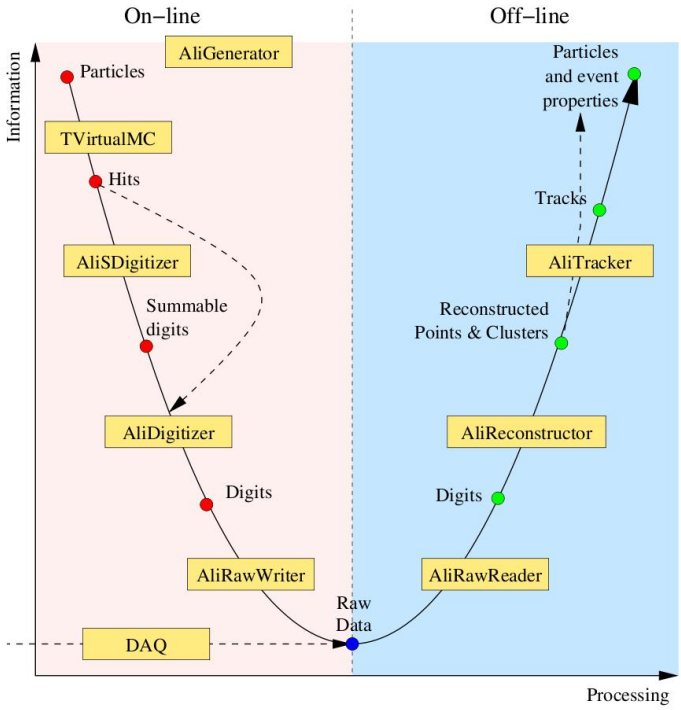

Figure 3.6: ALICE simulation and reconstruction sketch, the left part represents the simulated, and digitalised signal until their transformation into the raw data format. The right part of the sketch represents the reconstruction process in the ALICE framework used both for simulated and real signal.

$$\mathcal{A} \times \epsilon(p_T, y) = \frac{N^{rec}_{\phi/\omega\to\mu^+\mu^-}(p_{\mathrm{T}}, y)}{N^{gen}_{\phi/\omega\to\mu^+\mu^-}(p_{\mathrm{T}}, y)}\,, \tag{3.23}$$

In equation 3.23, $N^{rec}_{\phi(\omega)\to\mu^+\mu^-}$ is the number of reconstructed $\phi \to \mu^+\mu^-$ ($\omega \to \mu^+\mu^-$) out of the generated $N^{gen}_{\phi(\omega)\to\mu^+\mu^-}$ pairs for a given p_{T} and y bin as shown in Figure 3.7.

On these maps, the $\mathcal{A} \times \epsilon$ is found to show an overall similar trend for the two resonances. The product of acceptance and efficiency ($\mathcal{A} \times \epsilon$) increases with p_{T} both for ω and ϕ with a $\mathcal{A}\times\epsilon$ <10% at low-p_{T} and increasing to about 60% when going to high transverse momenta, as presented in figure 3.8. Due to the low-p_{T} cut introduced by the trigger, the $\mathcal{A}\times\epsilon$ is suppressed at low p_{T}. At low p_{T} and low y, muons are not enough energetic to cross the absorber leading to a smaller $\mathcal{A} \times \epsilon$.

Figure 3.9 shows the $\mathcal{A} \times \epsilon$ as a function of rapidity in various p_{T} intervals. Edge effects can also be noticed around y ∼2.5 and y ∼4, with a decrease of $\mathcal{A} \times \epsilon$ with respect to the

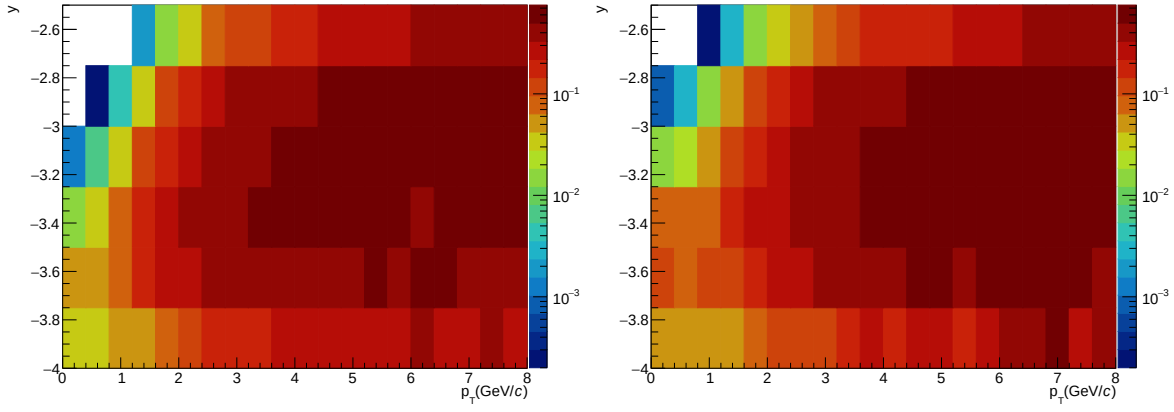

Figure 3.7: $\mathcal{A} \times \epsilon$ for the ω (**left**), ϕ (**right**) in their two body decay

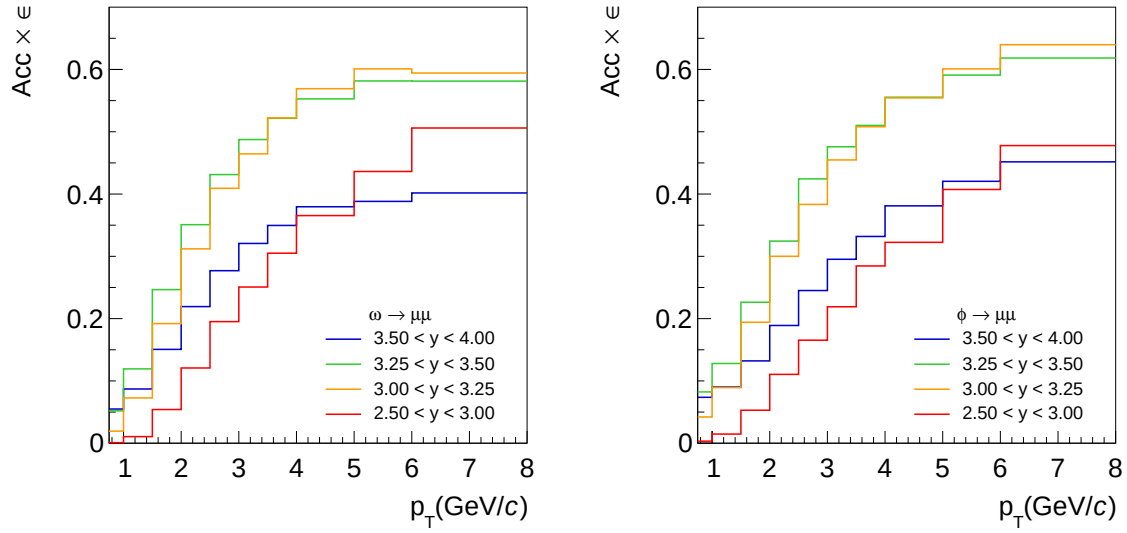

Figure 3.8: $\mathcal{A} \times \epsilon$ for the ω (**left**), ϕ (**right**) in their two body decay as a function of p_{T}

values at $y \sim 3$ also depending on p_{T}. This effect has the consequence that a lower amount of mesons will be reconstructed in this area, requiring a broader rapidity window (at $2.5 < y < 3$ and $3.5 < y < 4$), with respect to the intervals less affected by edge effects(at $3 < y < 3.25$ and $3.25 < y < 3.5$). In this figure the p_{T} dependency is also shown. An increase of $\mathcal{A} \times \epsilon$ with the increasing p_{T} is observed.

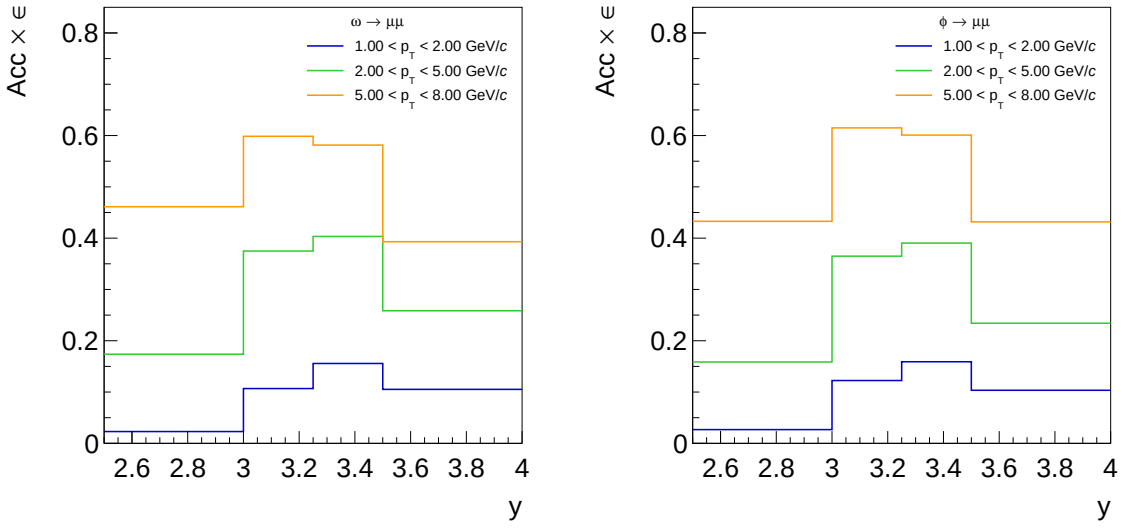

Figure 3.9: $\mathcal{A} \times \epsilon$ for the ω (**left**), ϕ (**right**) in their two body decay as a function of rapidity

3.3 Signal extraction

3.3.1 Signal extraction and continuum regularisation

A phenomenological fit to the different correlated dimuon mass spectra (see Section 3.1.5) is performed considering the different sources of the hadron cocktail. The fit is performed in the mass range $0.2 < M_{\mu\mu} < 2$ GeV/c^2 and takes into account all the processes of interest. The signal is integrated over $0.75 < p_{T,\mu\mu} < 8$ GeV/c as shown in Fig. 3.11. The lowest value is set to 0.75 GeV/c to avoid edge effects coming from the dimuon trigger introducing a non-sharp cut at $p_{T,\mu} \gtrsim 0.5$ GeV/c.

The free parameters of the fit are the normalisations of $\eta \to \mu^+\mu^-\gamma$, $\omega \to \mu^+\mu^-$, $\phi \to \mu^+\mu^-$ processes and of the open heavy-flavour component[4]. An attempt of using the cocktail from heavy-flavour to describe the correlated continuum has been performed but failed to reproduce the data at low mass/low p_{T}. The open-charm and open-beauty contributions are instead considered in an overall correlated continuum represented by an empirical function described below. The other processes were fixed according to their relative branching ratios from the Particle Data Group [8], and from their relative cross sections obtained from the

[4]The ratio $\sigma_{c\bar{c}}/\sigma_{b\bar{b}}$ is taken for the LHCb measurement at $\sqrt{s}$ = 7 TeV [68] [69] and is corrected using FONLL

NA60 [60] experiment (such as $\sigma_\omega = \sigma_\rho$ as in [70]). Due to the lack of measurements, the contribution from the η' is taken from Monte Carlo predictions[5] by fixing the $\sigma_{\eta'}/\sigma_\eta$ ratio in the *multiplicity integrated analysis* and the $\sigma_{\eta'}/\sigma_\phi$ ratio in the *multiplicity dependent analysis*[6]. Comparing the values of the ratios obtained from various generators, a conservative uncertainty of 50% on their values is considered. The inputs for the fit are summarised in table 3.3.

Input type	Input value
Relative branching ratios	$\frac{BR(\eta\to\mu^+\mu^-)}{BR(\eta\to\mu^+\mu^-\gamma)} = 1.87\cdot10^{-2}$ $\frac{BR(\omega\to\mu^+\mu^-\pi^0)}{BR(\omega\to\mu^+\mu^-)} = 1.329$
Relative cross section	$\frac{\sigma_\rho}{\sigma_\omega} = 1$ $\frac{\sigma_{\eta'}}{\sigma_\eta} = 0.28$ $\frac{\sigma_{\eta'}}{\sigma_\phi} = 2.79$

Table 3.3: Input list for the cocktail fitting to the signal

The signal extraction procedure is performed as follows:

- The normalisations of the light flavour resonances and the heavy flavours are fitted to the raw signal spectrum,
- The contribution of all light flavour contributions is subtracted to the raw signal resulting in a continuum contribution as shown in figure 3.10 (brown points),
- The obtained (correlated) continuum is then fitted using an empirical function. As this function is meant to reproduce the correlated continuum, the fit is performed in the mass intervals where the later is dominant. Thus the mass intervals where the resonances (from η, ω and ϕ) dominate the signal are excluded from the fit of the continuum. These intervals are presented in figure 3.10 as shaded areas. Three different empirical function are considered: a polynomial of the N^{th}-order (PolN), a single or double exponential (ExpN), and a Variable Width Gaussian (VWG) defined as:

$$f_{VWG}(m) = N_0 e^{\frac{-(m-\mu)^2}{2\sigma(m)^2}} \tag{3.24}$$

[5]Considering the value obtained using the PYTHIA6.4 generator with the Perugia0 tune

[6]The change was made in order to have similar extraction technique with a similar analysis performed on the 13 TeV data.

where

$$\sigma(m) = \sigma_0(1.01 - e^{-\alpha m}) \; . \tag{3.25}$$

The VWG-function has three free parameters: the normalisation N_0, μ encoding the maximum of the function, and α encoding the hardening of the function at high masses ($\mu < m$) and part of the growth at low-masses ($m < \mu$).

To account for the presence of the threshold in the dimuon mass spectrum, all these functions are multiplied by an error function defined as:

$$f_{Err.}(m) = \frac{1}{\sqrt{\pi}} \int_0^{200(m-0.2)} e^{-t^2} dt \tag{3.26}$$

Thus, in the case of the VWG, the fitting function becomes:

$$f_{VWG}^{Fit}(m) = f_{Err.}(m) \times f_{VWG}(m) \tag{3.27}$$

- The fitting procedure of the light flavour resonances is repeated considering the regularised correlated continuum contribution,
- Then a new subtraction of the resonances is performed, from which a new continuum can be obtained.

The last two steps are repeated three times in order to converge to an accurate description of the overall signal.

As described in the previous part, the *continuum regularisation* can be performed considering three different empirical functions: VWG, PolN, expN. For the PolN, N can either be 3, 4, or 5, and for expN, N can be either 1 or 2. The order of the function is chosen by means of an F-Test. The degree of the polynomial is chosen to be the lowest one that satisfactorily fits the data, according to a statistical criterion based on the F-test, which can be briefly described as follows. The correlated continuum is first fitted with two polynomials of degree n and $n+1$ respectively. The null hypothesis is that the continuum is equivalently described by the lower and the higher degree functions. This hypothesis is tested by applying the F-test to the results of the fit. If the resulting P-value is larger than 5%, the lowest degree polynomial

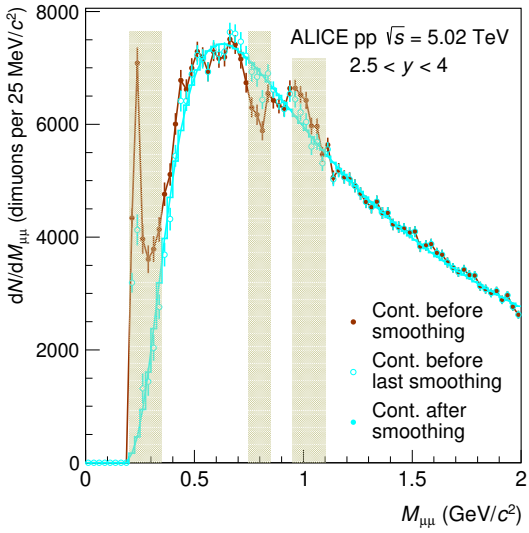

Figure 3.10: Correlated continuum for $0.75 < p_{\mathrm{T}} < 8$ GeV/c, $2.5 < y < 4$ integrated in multiplicity regularised using a VWG. The shaded areas represent the intervals where the data is not considered in the fit of the continuum

is used, otherwise the null hypothesis is rejected and the higher degree polynomial is chosen. The procedure is iterated starting from $n = 3$ to the maximum value allowed by the F-test, typically $n = 4$. The F-test criterion is also applied, properly adapted, to choose among the single or double exponential options.

For all the three different empirical functions, the interpolation of the continuum gives reasonable reduced-χ^2 values. For this reason, no preference on the empirical function is made, meaning that the value of raw ω (ϕ) obtained from the template fit procedure is taken as the mean of the values obtained with the three different empirical continuum functions. The resulting fit using a VWG to regularise the continuum is shown in Fig. 3.11.

3.3.2 Cross section extraction

The cross section of a particle in a given $(\Delta p_{\mathrm{T}} - \Delta y)$ interval is evaluated through the formula:

$$\frac{d^2\sigma_{\phi,\omega}}{\Delta y \Delta p_{\mathrm{T}}} = \frac{N^{\mathrm{raw}}_{\phi,\omega}(\Delta p_T, \Delta y)}{A \cdot \epsilon(\Delta p_T, \Delta y) BR_{\phi,\omega\to e^+e^-} L_{\mathrm{INT}}} \,, \tag{3.28}$$

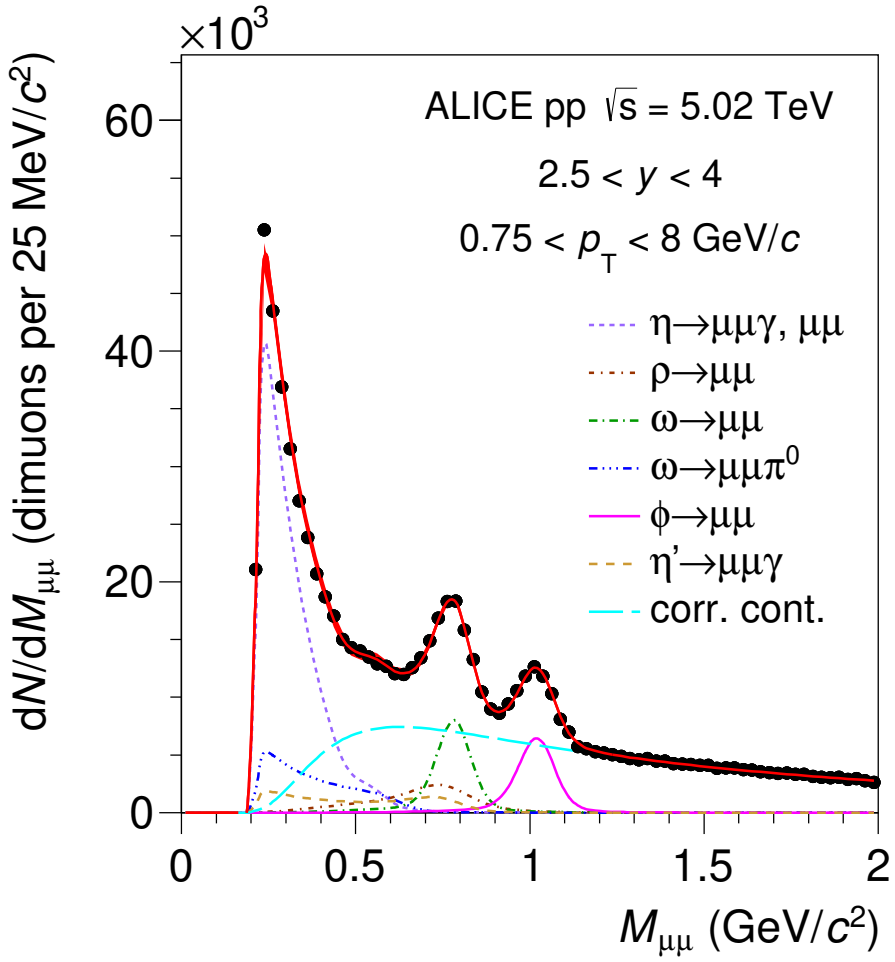

Figure 3.11: Fit of the dimuon invariant mass spectrum to the hadronic cocktail in pp collisions at $\sqrt{s} = 5.02$ TeV in $2.5 < y < 4$ for $0.75 < p_{\mathrm{T}} < 8$ GeV/c. In this interpolation the correlated continuum is fitted with a variable-width Gaussian function. The red band represents the total fit of the invariant mass spectrum.

where $N^{\mathrm{raw}}_{\phi,\omega}(\Delta p_{\mathrm{T}}, \Delta y)$ is the raw number of ϕ or ω for a given Δp_T and Δy interval, $BR_{\phi\to e^+e^-}$ = (2.973 $\pm$ 0.034)$\times 10^{-4}$ and $BR_{\omega\to e^+e^-}$ = (7.36 $\pm$ 0.15)$\times 10^{-5}$ are the branching ratios for the ϕ and the ω decays into dielectrons. These branching ratios are used instead of the ones of the dimuons as they are expected to be equal assuming lepton universality, and have been more precisely measured. As a reminder, the integrated luminosity $L_{INT} = 1222.6$ nb^{-1} as described in 3.1.3.

3.3.3 Systematic uncertainties on $N_{\omega,\phi}$

The systematic uncertainties on the signal extraction can be categorised into two main sources: the extraction procedure and the reconstruction efficiency.

3.3.3.1 Systematic uncertainties on the extraction procedure

The systematic uncertainties on the raw number of ω and ϕ mesons $N^{raw}_{\omega/\phi}$ extracted were evaluated by changing the different values used as input for the fitting procedure. Are considered for the systematic variation:

- The empirical function: VWG, PolN, expN ($\times 3$)
- The upper value of the invariant mass interval for the fit to the mass spectrum: 1.8, 2.0, 2.2 GeV/c^2 ($\times 3$),
- The different relative branching ratios and cross sections used to fix the contributions from the non-extracted resonances as listed in table 3.4 ($\times 3^4$)

Process	Input value	Source of the uncertainty
$Br(\eta \to \mu^+\mu^+)$	$(5.8 \pm 0.8) \times 10^{-6}$	PDG [8]
$Br(\eta \to \mu^+\mu^+\gamma)$	$(1.09 \pm 0.27) \times 10^{-4}$	PDG [8]
$Br(\omega \to \mu^+\mu^+\pi)$	$(1.34 \pm 0.18) \times 10^{-4}$	PDG [8]
$\frac{\sigma_\rho}{\sigma_\omega}$	1.0 ± 0.1	NA60 [71]
$\frac{\sigma_{\eta'}}{\sigma_\eta}$	0.28 ± 0.14	MC-models [72] [73, 74] [75] [76]
$\frac{\sigma_{\eta\prime}}{\sigma_\phi}$	2.79 ± 1.4	MC-models [72] [73, 74] [75] [76]

Table 3.4: Input branching ratios and relative cross sections with their relative errors and their corresponding source

All combinations considered together represent a total of 3^6=729 variations per kinematic interval considered. The systematic value on the $N^{raw}_{\omega/\phi}$ is taken as the RMS of these 729 different estimations on the mean value. The systematic uncertainties obtained for the ω and the ϕ are taken as the mean of the relative uncertainty along p_{T} and are at the level of 3.7% for the ϕ and 4.0% for the ω. The main contributor to the systematic uncertainty comes from the

choice of the empirical function, then comes the choice of the fitting interval, and then the relative cross-section $\sigma_\rho/\sigma_\omega$. An example of the estimation of the systematic uncertainty on the extracted value of the ω meson for $0.75 < p_{\mathrm{T}} < 1$ GeV/c is shown in figure 3.12.

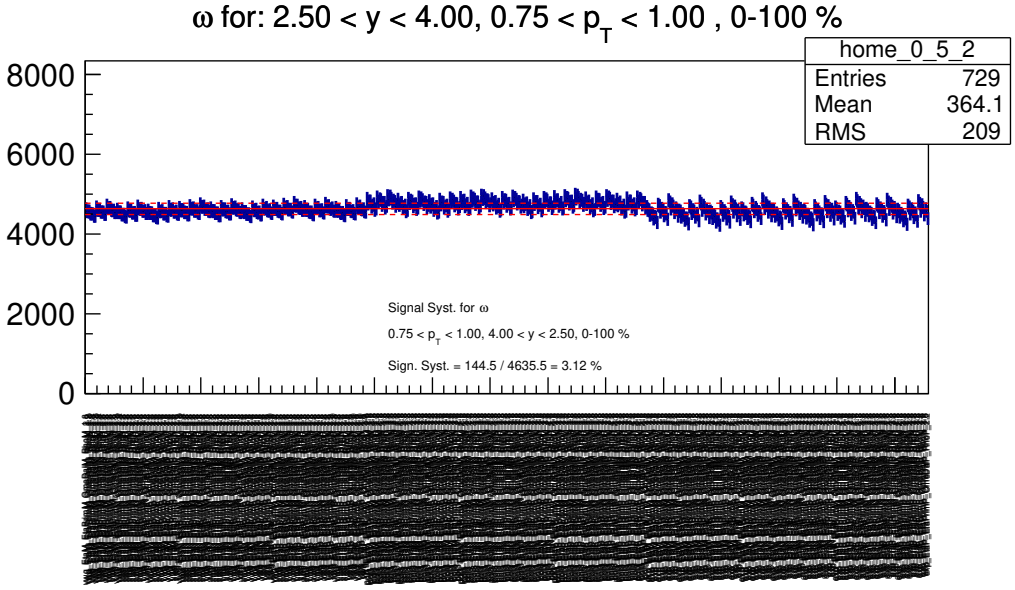

Figure 3.12: N_{ω}^{raw} for the different combination multiplicity integrated. The continuous red line represent the mean value obtained out of the 729 combinations and the dotted red line $\pm$ 1 RMS.

3.3.3.2 Systematic uncertainties on the reconstruction efficiency

The uncertainty on the reconstruction efficiency comes from three different sources:

- The matching efficiency: this contribution was determined by the ALICE group analysing J/ψ [77] for the selected periods (LHC17p and LHC17p) and is related to the choice of the χ^2 cut used in defining the matching between the tracks reconstructed by the tracking chambers and the tracklets reconstructed by the trigger chambers. In the current analysis, a track in the muon chamber and a tracklet in the trigger must match with a χ^2 <36, corresponding to 6σ. The systematic uncertainty is evaluated at the single muon level, changing the χ^2 upper-value between 16 and 36. This uncertainty amounts to 1%.

- The trigger efficiencies are given by the sum of two contributions: one on the description of the absorbers (the iron wall and the hadronic absorber), and the other on the description of the trigger chambers background in the MC. The absorber description has been done comparing the acceptance times efficiency using two different transport codes, namely GEANT4 [67], and GEANT3. The uncertainty on the occupancy of the trigger chambers was evaluated comparing $A \times \varepsilon$ resulting from simulations where the MC signal was simulated either as generated or by embedding[7] it in the environment of a real event. For both pure and embedded simulations, the samples used to estimate the $\mathcal{A} \times \epsilon$ are weighted to reproduce the trigger effect obtained in data. This weight is based on the ratio of the number of all reconstructed muons passing the low-p_{T} trigger threshold over all reconstructed muons. This procedure follows the one presented, and developed in the analysis at 13 TeV[78]. At high-p_{T}, for $p_{\mathrm{T}} > 2.5$ GeV/c, the systematic uncertainty is taken as a constant as the effect becomes negligible with the increase of p_{T} and allows to get rid of the fluctuations arising from the MC sample which become large at high-p_{T}. The systematic uncertainty coming from the trigger has been estimated to range from 2.4 to 10.5% depending on the muon pair $p_{\mathrm{T}} - y$.

- Tracking efficiency: it was evaluated both from data and MC simulations. To this purpose, the MC was tuned to the detector condition during data taking, in order to reproduce the uncertainties arising from correlated and anti-correlated dead areas in the muon tracker. As the same tracking algorithm is applied on MC and data, the difference observed between the two estimates is assumed as the systematic uncertainty on the tracking efficiency. In this case, the correlations over p_{T} and y are found to be negligible, and the uncertainty due to the tracking efficiency amounts to 2.0%.

3.3.4 Systematic uncertainties on the cross sections

The systematic uncertainty on the ϕ and ω differential cross sections can come from four different sources:

[7] An embedded simulation is obtained superimposing the hits of a simulated signal event to the hits of a real event

- The number of N_{ϕ}^{raw} (see Sec. 3.3.3).

- The uncertainty on the input kinematic distributions used to generate the ϕ and ω mesons. In this analysis, the p_{T} and y distributions of the generated particles had already been tuned on data. The resulting uncertainty obtained changing the parameters of the input functions was found to be negligible.

- The uncertainty of the branching ratios into dielectrons of the ϕ ($\sim$2.0%) and the ω ($\sim$2.0%) [8], correlated as a function of p_{T}.

- The uncertainty on the integrated luminosity, correlated as a function of p_{T}. It is taken from the resulting value obtained with the Van Der Meer scan [58] and is found to be 2.1% for the *multiplicity integrated analysis*, basing the result on the measured σ_{MB}.

- The uncertainty on the event correction, only in the case of the *multiplicity dependent analysis*, evaluated comparing the results obtained using two different MC generators, namely PYTHIA8 and EPOS-LHC (developed in 5.2.2). This uncertainty is found to be less than 1% in all multiplicity intervals considered.

Chapter 4

Production of ϕ and ω mesons in inelastic pp collisions at $\sqrt{s} = 5.02$ TeV

The measurement of light vector meson production in pp collisions at $\sqrt{s} = 5.02$ TeV is required to provide a baseline to the yields obtained in other collision systems, namely p-Pb and Pb-Pb at the same centre-of-mass energy. On top of being a baseline, pp collisions at this energy allow a direct comparison to measurements in the same collision system at different centre-of-mass energies. The statistics available in 2017 allows the measurement of double-differential cross sections for the ϕ and ω mesons as a function of p_{T} and y. It has to be pointed out that pp collisions at $\sqrt{s} = 5.02$ TeV have also been collected by ALICE in 2015. The data collected in 2017 represent ten times the statistics collected in 2015.

4.1 Signal extraction

4.1.1 Signal selection

Following the procedure described in chapter 3 the events, tracks and pairs were selected according to the requirements presented in table 4.1.

The background estimation is performed using mixed events, where the mixed events were categorised into ten different V_Z intervals.

Selection Summary	
Event Level	
Trigger	CMUL or CMLL
Quality cut	Physics Selection SPD pile-up rejection $N^{vtx}_{Contrib.} \geq 1$ -20< V_Z <20 cm
Track Level	
Quality Cut	track matches a tracklet in the trigger
Kinematic Cut	$p^{\mu}_{\mathrm{T}} \gtrsim 0.5$ *GeV/c* $-4 < \eta_{\mu} < -2.5$
Pair Level	
Quality Cut	muons cannot hit the same local board
Kinematic Cut	$2.5 < y_{\mu\mu} < 4$ $p^{\mu\mu}_{\mathrm{T}} > 0.75$ *GeV/c*

Table 4.1: Summary of the selections

4.1.2 Signal extraction

Using the simulations of the signal at low-masses, the reconstructed invariant mass spectra forming the cocktail are used for a phenomenological fit and to estimate $\mathcal{A} \times \epsilon$. The phenomenological fit of the mass spectrum is performed in twelve p_{T} intervals, starting from 0.75 GeV/*c*. The different fits are presented in figure 4.2[1].

The resulting order of the polN and expN functions obtained using the F-test are presented in figure 4.1(a). From this figure it can be pointed out that the intervals with more statistics require a higher order of the empirical function to describe it.

The fit of the mass spectrum gives reasonable reduced-χ^2 values for each of the three possible choices for the continuum description, as shown in figure 4.1(b). For this reason, no preference on the empirical function is made, meaning that the values of raw ω and ϕ are taken as the mean of the results from the fits obtained considering the three different functions.

[1]In these fits, the VWG is chosen for the description of the correlated continuum. The fits obtained when considering other functions for the continuum are presented in the Appendices F.1 and F.1

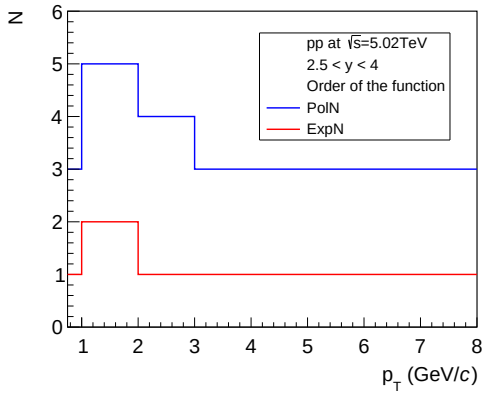

(a) Order of the PolN and ExpN functions used for the continuum regularisation in the studied p_{T} bins

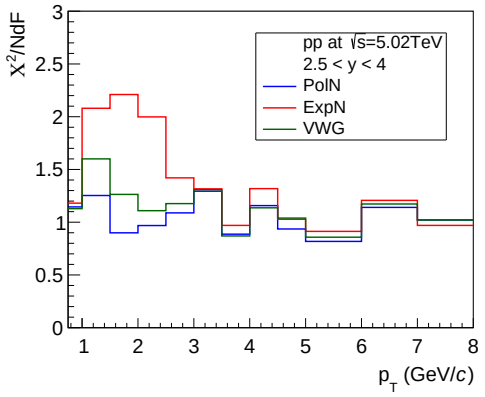

(b) Reduced-χ^2 of the phenomenological fit to the correlated mass spectrum

Figure 4.1

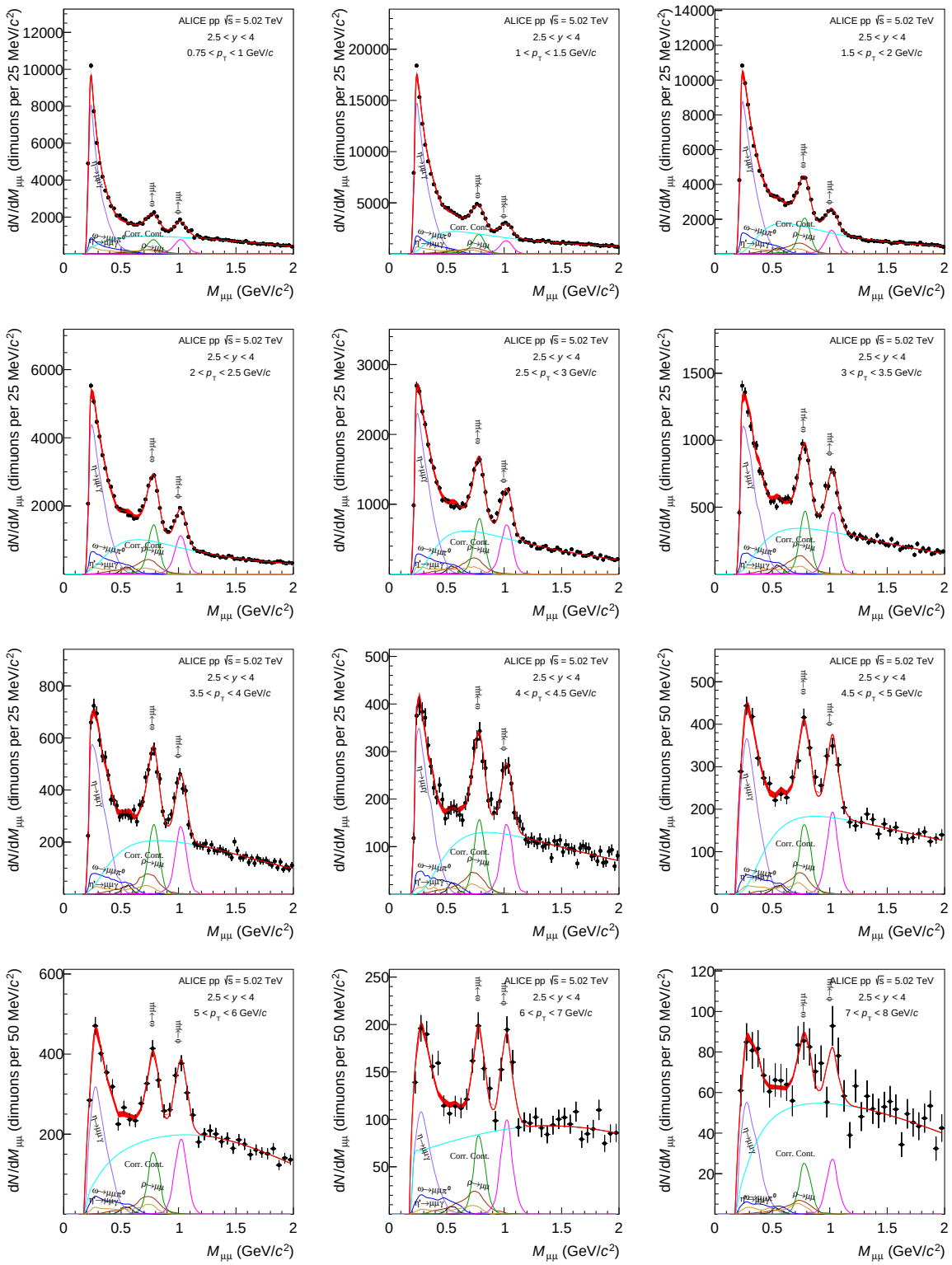

Figure 4.2: Fits to the invariant dimuon mass spectra of the hadronic cocktail in pp collisions at $\sqrt{s} = 5.02$ TeV in $2.5 < y < 4$ for twelve p_{T} intervals from 0.75 to 8 GeV/c. In these interpolations the correlated continuum is fitted with a variable-width Gaussian function. The red band represents the total fit of the invariant mass spectrum.

The raw number of resonances has then to be corrected for the acceptance and efficiency. The $\mathcal{A}\times\epsilon$ is evaluated in all the different p_{T} intervals considered both for ω and ϕ. The resulting $\mathcal{A} \times \epsilon$ is presented in figure 4.3.

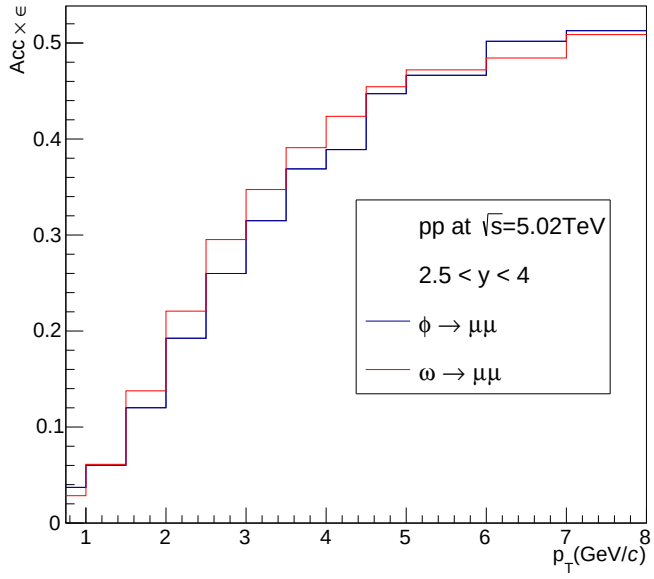

Figure 4.3: $\mathcal{A} \times \epsilon$ as a function of p_{T} for ϕ and ω mesons estimated via their dimuon decay channel

4.1.3 Systematic uncertainties on the ω and ϕ production

As previously discussed in section 3.3.4, the systematic uncertainties on the signal can be categorised into two main sources: the extraction procedure and the reconstruction efficiency. The different contributions are listed in table 4.2.

4.1.4 ϕ and ω differential cross section

Following the procedure developed in section 3.3.2 and especially the equation 3.28, the cross-sections of the ω and ϕ mesons were extracted. The cross-sections obtained in the different p_{T}-intervals, in the forward rapidity region $2.5 < y < 4$ are listed in the table 4.3. The integrated cross sections for $0.75 < p_{\mathrm{T}} < 8$ GeV/c and $2.5 < y < 4$ are found to be $\sigma_{\omega} =$

Source	Relative systematic uncertainty	
	ω	ϕ
Uncorrelated systematic		
N^{raw}	3.8%	3.7%
Tracking efficiency	2.0%	2.0%
Trigger efficiency	2.2-10.8%	2.4-10.5%
Matching efficiency	1.0%	1.0%
Correlated systematic		
BR($X \to e^+e^-$)	2.0%	1.0%
$L_{\rm INT}$	2.1%	2.1%

Table 4.2: Systematic uncertainties for the ω and ϕ differential cross section for $2.5 < y < 4$

$6.185 \pm 0.198(\text{stat}) \pm 0.138(\text{syst})$ mb $\sigma_\phi = 1.053 \pm 0.047(\text{stat}) \pm 0.024(\text{syst})$ mb. As a reminder, the is the integrated luminosity $L_{\rm INT} = 1222.6\ nb^{-1}$ as described in 3.1.3.

$p_{\rm T}$ (GeV/c)	$d^2\sigma/dydp_T \pm$ stat. $\pm$ uncorr. syst. $\pm$ corr. syst. [mb/(GeV/c)]	
	ω	ϕ
0.75–1	$5.86 \pm 0.12 \pm 0.35 \pm 0.13$	$(9.93 \pm 0.57 \pm 1.51 \pm 0.23).10^{-1}$
1–1.5	$3.08 \pm 0.04 \pm 0.18 \pm 0.07$	$(5.44 \pm 0.22 \pm 0.70 \pm 0.13).10^{-1}$
1.5–2	$1.28 \pm 0.01 \pm 0.08 \pm 0.03$	$(2.35 \pm 0.073 \pm 0.13 \pm 0.055).10^{-1}$
2–2.5	$(5.21 \pm 0.05 \pm 0.31 \pm 0.12).10^{-1}$	$(1.23 \pm 0.032 \pm 0.059 \pm 0.029).10^{-1}$
2.5–3	$(2.05 \pm 0.03 \pm 0.12 \pm 0.05).10^{-1}$	$(5.65 \pm 0.16 \pm 0.25 \pm 0.13).10^{-2}$
3–3.5	$(1.03891 \pm 0.02 \pm 0.06 \pm 0.02).10^{-1}$	$(2.94 \pm 0.096 \pm 0.15 \pm 0.069).10^{-2}$
3.5–4	$(5.17 \pm 0.11 \pm 0.31 \pm 0.12).10^{-2}$	$(1.56 \pm 0.067 \pm 0.068 \pm 0.036).10^{-2}$
4–4.5	$(2.89 \pm 0.08 \pm 0.17 \pm 0.06).10^{-2}$	$(7.99 \pm 0.44 \pm 0.37 \pm 0.19).10^{-3}$
4.5–5	$(1.48 \pm 0.06 \pm 0.09 \pm 0.03).10^{-2}$	$(4.65 \pm 0.32 \pm 0.23 \pm 0.11).10^{-3}$
5–6	$(6.22 \pm 0.27 \pm 0.37 \pm 0.14).10^{-3}$	$(2.30 \pm 0.16 \pm 0.11 \pm 0.054).10^{-3}$
6–7	$(3.34 \pm 0.27 \pm 0.19 \pm 0.08).10^{-3}$	$(1.05 \pm 0.12 \pm 0.085 \pm 0.025).10^{-3}$
7–8	$(9.72 \pm 1.23 \pm 0.57 \pm 0.22).10^{-4}$	$(3.38 \pm 0.73 \pm 0.19 \pm 0.078).10^{-4}$

Table 4.3: ω and ϕ $p_{\rm T}$-differential cross section for $2.5 < y < 4$ and their relative uncertainties (statistical, uncorrelated and correlated systematic).

The cross-sections of the ω and ϕ mesons as a function of their transverse momentum are

shown in figure 4.4. The p_{T} distributions are fitted using a Lévy-Tsallis function as it derives from a Boltzmann distribution function and succeeds in interpolating the full spectrum.

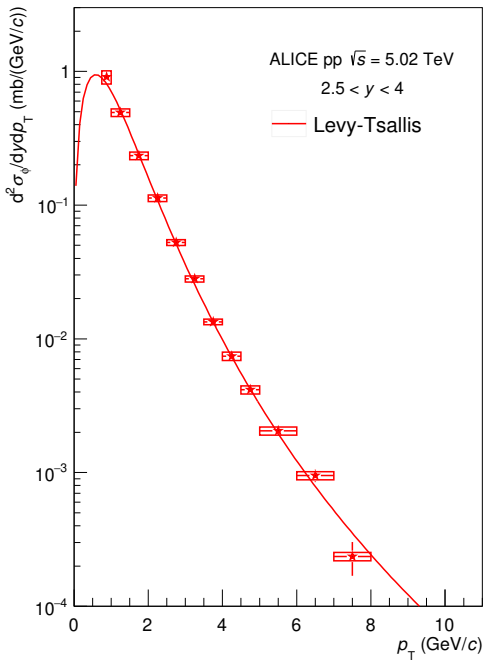

(a) ϕ differential cross section as a function of p_{T} in pp collisions at $\sqrt{s} = 5.02$ TeV at $2.5 < y < 4$ fitted by a Lévy-Tsallis function.

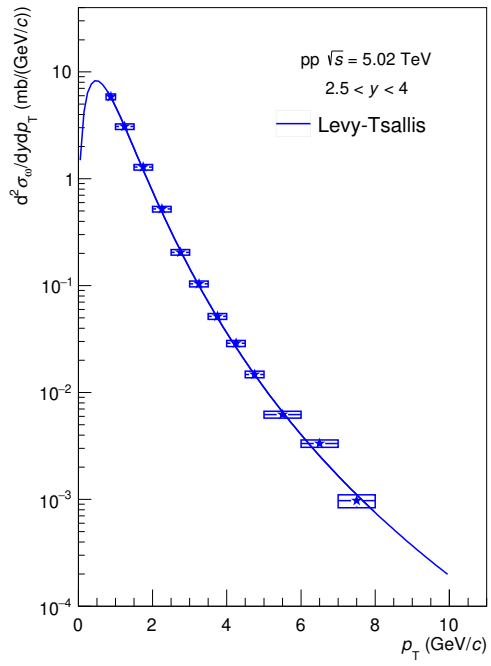

(b) ω differential cross section as a function of p_{T} in pp collisions at $\sqrt{s} = 5.02$ TeV at $2.5 < y < 4$ fitted by a Lévy-Tsallis function.

Figure 4.4

Table 4.4 summarises the results of the interpolation of data with a Lévy-Tsallis. Both for the ω and the ϕ mesoon production, a value of the parameter n is found to be consistent with the expected value for mesons produced by a q+meson $\rightarrow$ q+meson process of $n = 8$ [79]. The inverse slope parameter T is found to increase with the mass of the particle as already observed in the K^+K- decay channel by ALICE [80]. For the values obtained, it can be seen looking at the $\langle p_{\mathrm{T}} \rangle$ values that the ϕ spectrum is harder than the one of the ω.

This mass ordering of the p_{T} spectrum hardening can be directly observed when looking at the yield ratio as a function of p_{T}. This is presented in figure 4.5. The ϕ/ω ratio stands at about 0.15 at low-p_{T} where the signal is dominant. When going to higher-p_{T} intervals the

χ^2/NdF	T (GeV)	n	$\langle p_{\mathrm{T}} \rangle$ (GeV/c)
		ω	
1.509	0.235 ± 0.009	8.04 ± 0.30	0.858 ± 0.010
		ϕ	
1.41	0.273 ± 0.011	7.86 ± 0.38	1.031 ± 0.016

Table 4.4: Parameters of the Lévy-Tsallis fits to the differential cross sections at forward rapidity (2.5$<$ y $<$4) at $\sqrt{s}$ = 5.02 TeV. The mean value of p_{T} calculated extrapolating the fit functions is also reported.

ratio increases up to a value of 0.25.

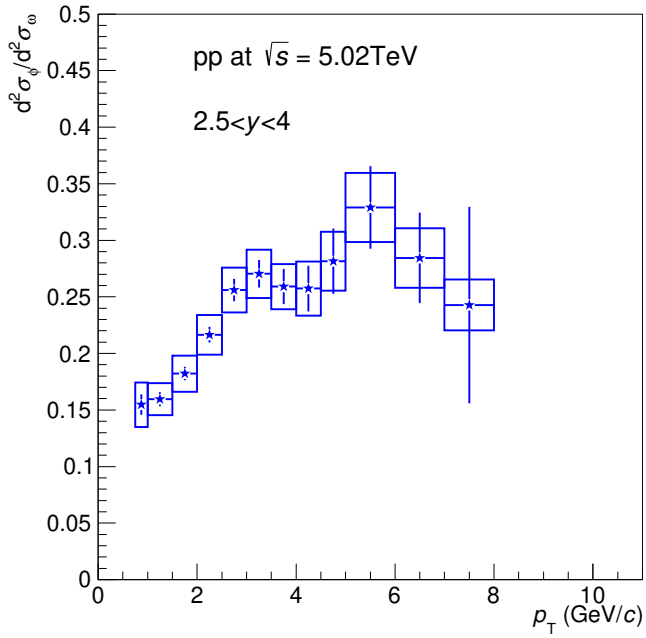

Figure 4.5: Ratio of the ϕ/ω cross sections at forward rapidity for pp collisions at $\sqrt{s}$ =5.02 TeV

4.1.5 Comparison with results at other centre-of-mass energies

This analysis has already been performed for the ϕ meson at other centre-of-mass energies, leading to publications at $\sqrt{s} = 2.76$ TeV [81] and at $\sqrt{s} = 7$ TeV [82] at forward rapidity, but

also at midrapidity ($|y|$<0.5) at 5.02, 8 and 13 TeV [83, 84, 51]. These previous measurements are presented in D.

On top of these published analyses, two new measurements have been performed by the ALICE Collaboration at forward rapidity, one at $\sqrt{s} = 8$ TeV [85] and another one with more statistics at $\sqrt{s} = 13$ TeV [78]. With the exchanges of results among groups from the collaboration, the method used for the signal extraction (the one presented in this analysis) was used in all the three analyses.

In Fig. 4.6, the differential cross sections are compared with the previously published results at $\sqrt{s} = 2.76$ TeV [86] and $\sqrt{s} = 7$ TeV [87], together with work in progress at $\sqrt{s} = 8$ TeV and $\sqrt{s} = 13$ TeV. The ratio to the measurement at $\sqrt{s} = 13$ TeV is also reported in the bottom panel for a direct comparison. A hardening of the p_{T} spectra is observed when increasing the centre of mass energy. The values of the ratio at $p_{\mathrm{T}} \sim 5$ GeV/c change from ~ 0.2 for $\sqrt{s} = 2.76$ TeV to ~ 0.65 for $\sqrt{s} = 8$ TeV.

In Fig. 4.7 data are compared to the calculations performed with the models EPOS 3 [88, 89, 90], PHOJET[2] [73, 74] and the Monash 2013 tune of PYTHIA 8.1 [92] (developed in E). At all collision energies, EPOS 3 underestimates the cross section at low p_{T}, while it describes the data for $p_{\mathrm{T}} > 4$ GeV/c. PHOJET reproduces the low-p_{T} region up to $p_{\mathrm{T}} \sim 2$ GeV/c, but does not describe the spectra shape, predicted to be harder by the model. PYTHIA 8.1 with the Monash 2013 tune reproduces the shape of the differential cross section at all energies. However, it underestimates the measurement at $\sqrt{s} = 5.02$ and 8 TeV while reproduces well the results at $\sqrt{s} = 13$ TeV.

The ϕ meson production cross section has then been integrated in the p_{T} range $1.5 < p_{\mathrm{T}} < 5$ GeV/c, common to the five measurements at different collision energies, and is plotted as a function of $\sqrt{s}$ in Fig. 4.8. Results are compared with EPOS 3, PHOJET and PYTHIA 8.1 with the Monash 2013 tune. In the p_{T} interval considered for this comparison, the evolution of the cross section with the collision energy is satisfactorily described by PHOJET. This indicates that the combination of the Dual Parton Model at low-p_{T} and pQCD for high-p_{T} in the model gives a fair description in the studied p_{T} interval as a function of the centre of mass energy. EPOS 3 and PYTHIA 8.1/Monash 2013 both underestimate the absolute values by a factor

[2]Phojet: model combining the Dual Parton Model [91] for soft-processes and pQCD for hard-processes

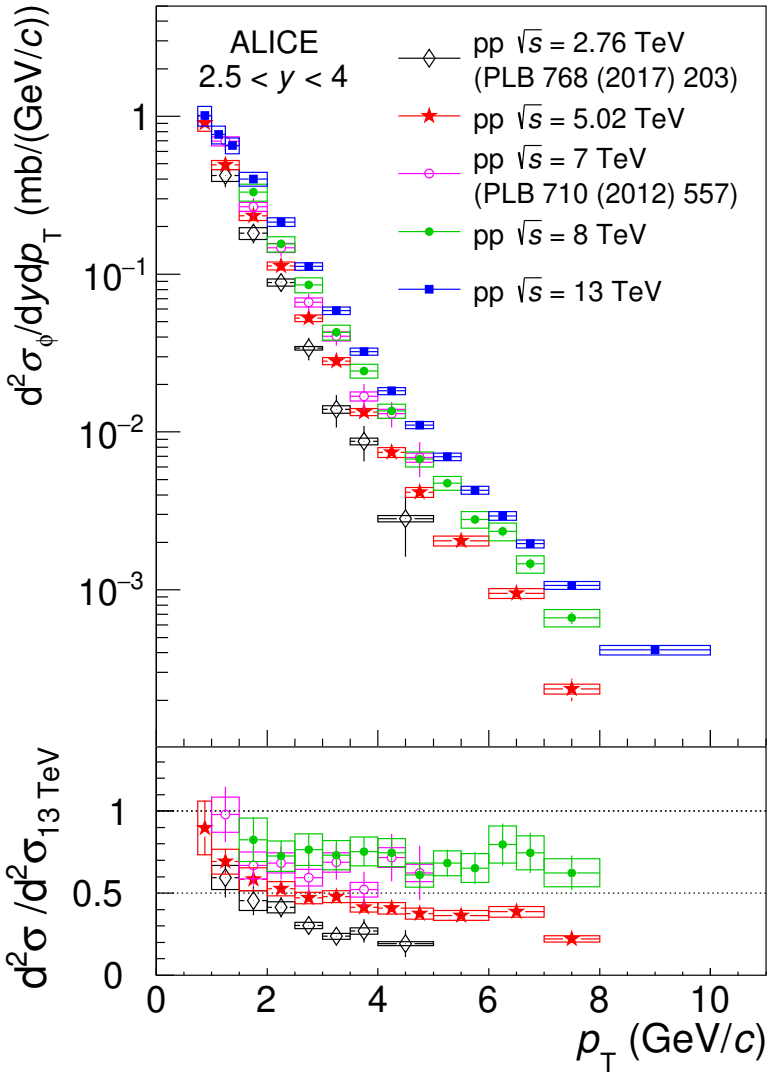

Figure 4.6: Top: differential ϕ meson production cross section $\mathrm{d}^2\sigma/(\mathrm{d}y\mathrm{d}p_\mathrm{T})$ as a function of p_T at $\sqrt{s}$ =2.76, 5.02, 7, 8 and 13 TeV [86] [87]. Bottom: ratio between the measured cross sections at several centre-of-mass energies to the one obtained at $\sqrt{s} = 13$ TeV.

ranging from about 1.2 to 1.7, while reproducing the increase of the ϕ production as a function of the centre-of-mass energy.

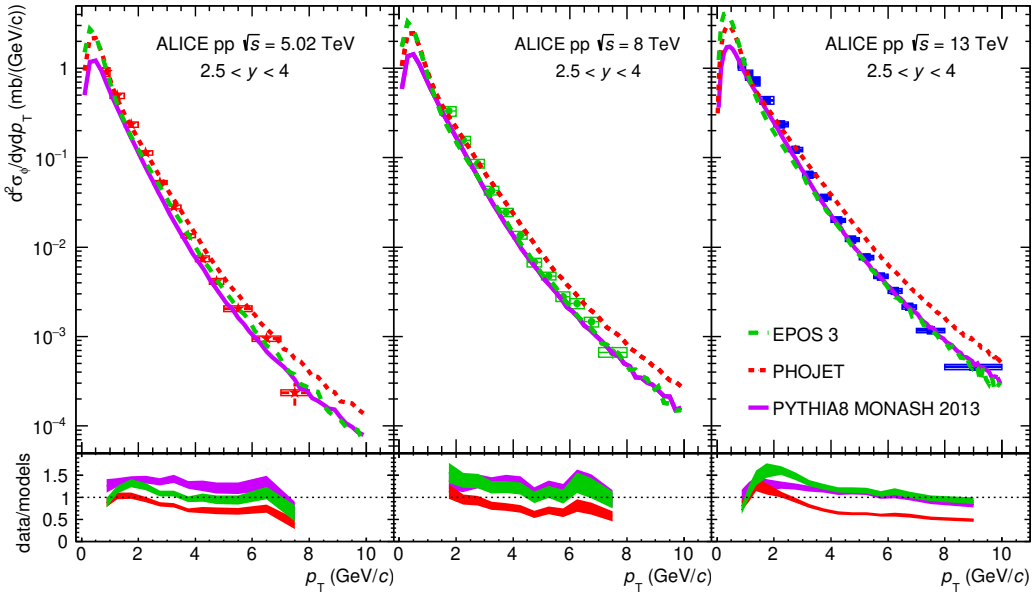

Figure 4.7: Differential ϕ meson production cross section $\mathrm{d}^2\sigma/\mathrm{d}y\mathrm{d}p_\mathrm{T}$ as a function of p_T at $\sqrt{s} = 5.02$ TeV (left), $\sqrt{s} = 8$ TeV (centre) and $\sqrt{s} = 13$ TeV (right) in the rapidity interval $2.5 < y < 4$, compared with EPOS 3 [88, 89, 90], PHOJET [73, 74] and the Monash 2013 tune of PYTHIA 8.1 [92].

4.1.6 Comparison with results obtained at mid-rapidity

The differential ϕ meson production cross sections at $\sqrt{s} = 5.02$, 8 and 13 TeV, measured in the rapidity range $2.5 < y < 4$, are shown in Fig. 4.9 as a function of the transverse momentum. The cross sections are fitted with a Lévy-Tsallis function [45, 46]. While the total systematic uncertainty is shown in the spectra of Fig. 4.9, only the contribution coming from the signal extraction (combined with the statistical uncertainty) is considered when performing the fit, the signal extraction being the only source of systematic uncertainty resulting in bin-to-bin uncorrelated fluctuations (on their dependence on transverse momentum and rapidity) of the measured points.

Still in figure 4.9 the spectra at midrapidity measured by ALICE [83, 84, 51], normalized using the inelastic cross sections reported in [93] are also plotted for comparison. ϕ production has been extracted at midrapidity via its K^+K^- hadronic decay channel. Benefiting from the strong coupling of this decay leading to a high branching ratio of BR($\phi \rightarrow K^+K^-$) = 49.2% (with respect to the dimuon decay channel), the study could profit from a large number of raw

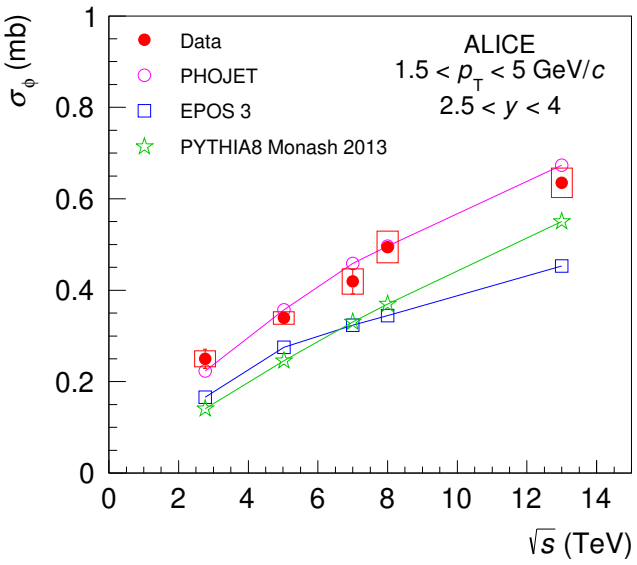

Figure 4.8: ϕ meson production cross section as a function of $\sqrt{s}$ for $1.5 < p_{\mathrm{T}} < 5$ GeV/c and $2.5 < y < 4$, compared with EPOS 3 [88, 89, 90], PHOJET [73, 74] and the Monash 2013 tune of PYTHIA 8.1 [92].

ϕ reconstructed at midrapidity. This higher number of reconstructed ϕ mesons led both to a finer-binning in p_{T} and to a larger p_{T} coverage (0.2$<$ p_{T} $<$16 GeV/c). In the bottom panel of figure 4.9, the ratio between the fit with the Lévy-Tsallis functions at forward rapidity and the data at midrapidity is presented. A hardening of the p_{T} spectrum is observed. The p_{T} spectra are harder at midrapidity. The difference between the slopes at forward and midrapidity is more apparent at the lowest energy considered.

Table 4.7 summarises the results of the fit of data with a Lévy-Tsallis. The mean p_{T} value, calculated using the fit functions, increases by about 20 % when increasing the centre of mass energy from 5.02 to 13 TeV.

$\sqrt{s}$ (TeV)	χ^2/NdF	T (GeV)	n	$\langle p_{\mathrm{T}} \rangle$ (GeV/c)
		ω		
5.02	1.509	0.235 ± 0.009	8.04 ± 0.30	0.858 ± 0.010
		ϕ		
5.02	1.41	0.273 ± 0.011	7.86 ± 0.38	1.031 ± 0.016
8	0.52	0.310 ± 0.045	7.92 ± 1.00	1.132 ± 0.049
13	1.13	0.341 ± 0.005	8.24 ± 0.14	1.206 ± 0.006

Table 4.5: Parameters of the Lévy-Tsallis fits to the differential cross sections at forward rapidity (2.5$<$ y $<$4). The mean value of p_{T} calculated extrapolating the fit functions is also reported.

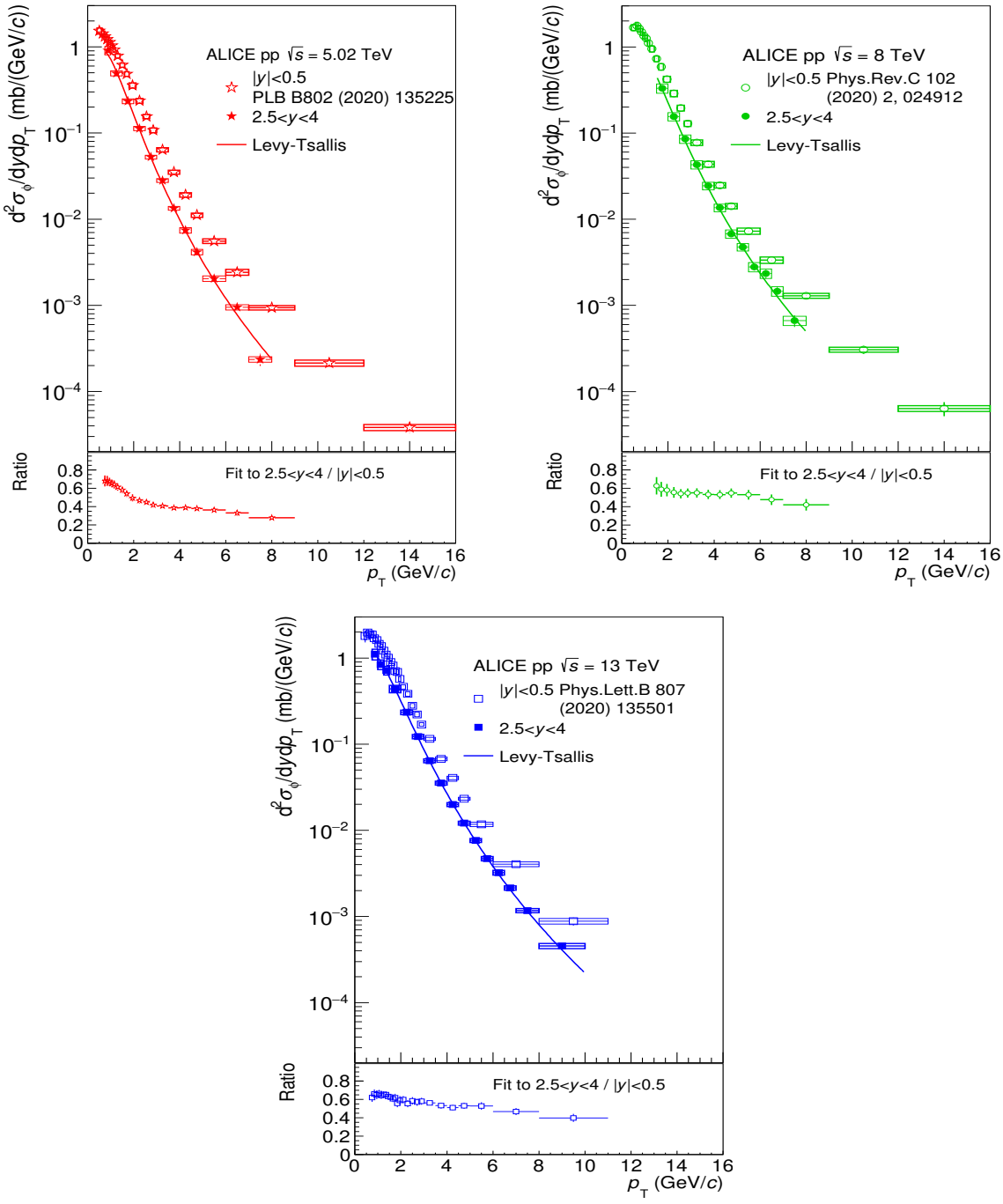

Figure 4.9: Differential ϕ meson production cross section $\mathrm{d}^2\sigma/(\mathrm{d}y\mathrm{d}p_\mathrm{T})$ as a function of p_T at $\sqrt{s}$ =5.02, 8 and 13 TeV measured in the $\mu^+\mu^-$ decay channel in the rapidity interval $2.5 < y < 4$ (full symbols) and in the $\mathrm{K}^+\mathrm{K}^-$ channel at midrapidity (open symbols). The boxes represent the systematic uncertainties, the error bars the statistical uncertainties. The data points are fitted with a Levy-Tsallis function, see Eq. 1.17. The ratio between the fit function at forward rapidity and the data at midrapidity is plotted in the bottom panels.

4.2 Double-differential analysis

As allowed by the large amount of data recorded in 2017, the study of the ω and ϕ meson production can be extended to a double-differential analysis, namely the production as a function of p_T and y into four different rapidity intervals.

4.2.1 Signal extraction

This analysis requires the same event triggering as for the rapidity integrated analysis described in the sections 4.1.1 and 3.1.2 as summarised in table 3.2. The main difference with the rapidity integrated analysis is the limitation in part of the rapidity intervals where acceptance effects do not allow the extraction of the signal.

The signal extraction procedure using the *Continuum Smoothing* as presented in the section 3.3.1 is applied. The various mass spectra obtained for this analysis are reported in Appendix F.2. Regarding the quality of the phenomenological fit performed in these intervals, a verification of the goodness is performed controlling the reduced-χ^2 using the three different empirical functions to describe the continuum as presented on figure 4.10. It can be pointed out that the three different representations of the continuum obtain a fair description of the signal in all considered intervals where the signal is extracted (with 0.7$<\ \chi^2/ndf\ <$ 1.7). Similarly to the analysis performed over the full rapidity range, no preference is made among the different functions, and the raw value of N_ϕ^{raw} and N_ω^{raw} is taken as the mean value of the three different values obtained using the different empirical functions to describe the correlated continuum.

In this double-differential analysis, the $\mathcal{A}\times\epsilon$ for the $\phi \to \mu^+\mu^-$ and the $\omega \to \mu^+\mu^-$ decays is computed for each interval studied. The $p_{\rm T}$ and y difference of the $\mathcal{A}\times\epsilon$ for both mesons can be drawn as in Figure 4.11(a) for ϕ and 4.11(b) for ω. Edge effects are noticed around $y\ \sim 2.5$ and $y\ \sim$4, with a decrease of $\mathcal{A}\times\epsilon$ with respect to the values at $y\ \sim$3 also depending on $p_{\rm T}$. This effect has the consequence that a lower amount of mesons will be reconstructed in this area, requiring a broader rapidity window (at $2.5 <\ y\ < 3$ and $3.5 <\ y\ < 4$), with respect to the intervals less affected by edge effects(at $3 <\ y\ < 3.25$ and $3.25 <\ y\ < 3.5$). Furthermore,

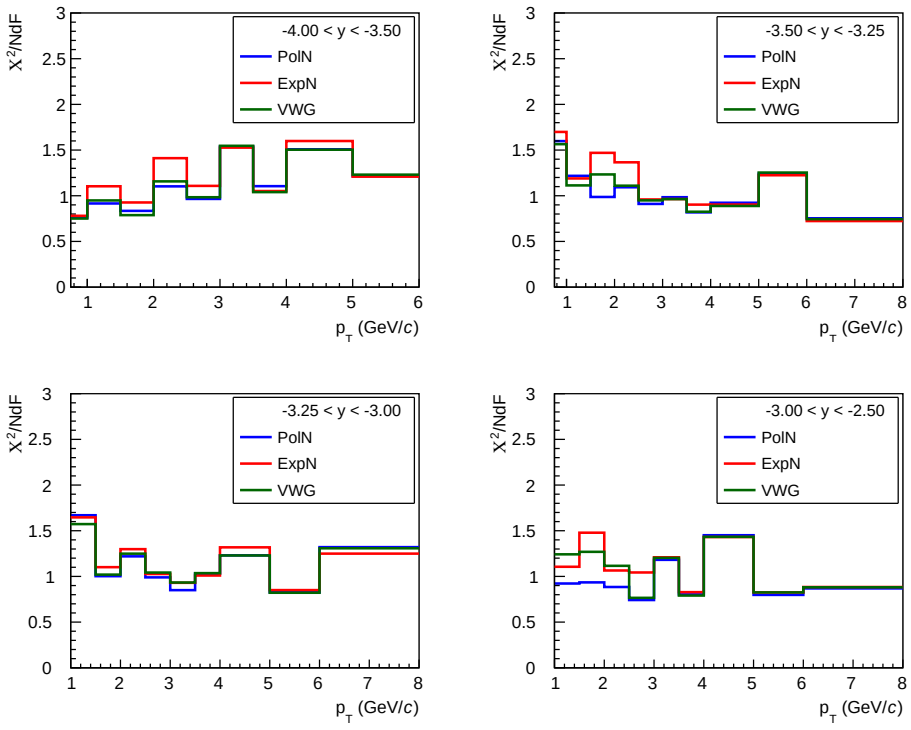

Figure 4.10: Reduced-χ^2 of the phenomenological fit to the correlated mass spectrum for the three different empirical functions considered in the four different rapidity intervals as a function of the studied p_{T} bins

two effects are leading to limitations in the reconstructed signal yield. First at low p_{T} and low-y, decay muons are not enough energetic to cross the absorber, although statistics (at the production level) would not be the issue. Second, at high-p_{T} and high-y the cross section is small, although $\mathcal{A}\times\epsilon$ is large enough to recover the signal, these intervals will not be populated enough.

4.2.2 Systematic uncertainties on the differential cross section

The systematic uncertainties on N_{ϕ}^{raw} and N_{ω}^{raw} is taken as the RMS of the different combinations obtained by varying the different inputs used for the fitting procedure as presented in the section 3.3.3. The only difference in this analysis is that the uncertainty on the raw signal extraction is taken as the mean value of the uncertainty over p_{T} separately in each rapidity window.

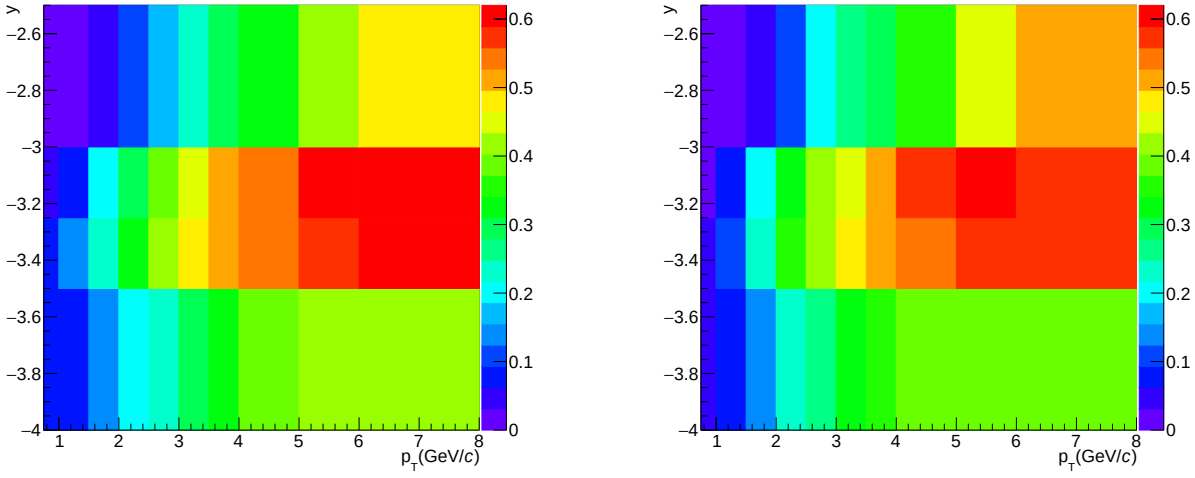

(a) $\mathcal{A}\times\epsilon$ map for the ϕ meson into its dimuon decay channel as a function of p_{T} and y

(b) $\mathcal{A}\times\epsilon$ map for the ω meson into its dimuon decay channel as a function of p_{T} and y

Figure 4.11

Similarly to what was done in the section 3.3.4, the systematic uncertainties on the double-differential cross sections are summarised in the table 4.6.

Source	Relative systematic uncertainty	
Uncorrelated systematic		
Particle	ω	ϕ
N_{ϕ}^{raw}	$4.2-5.1\%$	$3.1-4.2\%$
Matching efficiency	1.0%	1.0%
Tracking efficiency	2.0%	2.0%
Trigger efficiency	$2.9-5.1\%$	$2.4-10.5\%$
Correlated systematic		
BR(ω/ϕ) $\rightarrow e^+e^-$)	2.0%	1.0%
L_{INT}	2.1%	2.1%

Table 4.6: Systematic uncertainties for ω and ϕ double-differential cross section

4.2.3 ϕ and ω differential cross sections

The ϕ and ω differential cross sections are evaluated for each $p_T - y$ interval. The ϕ and ω double-differential cross sections as a function of p_{T} are shown in figure 4.12 in several rapidity intervals.

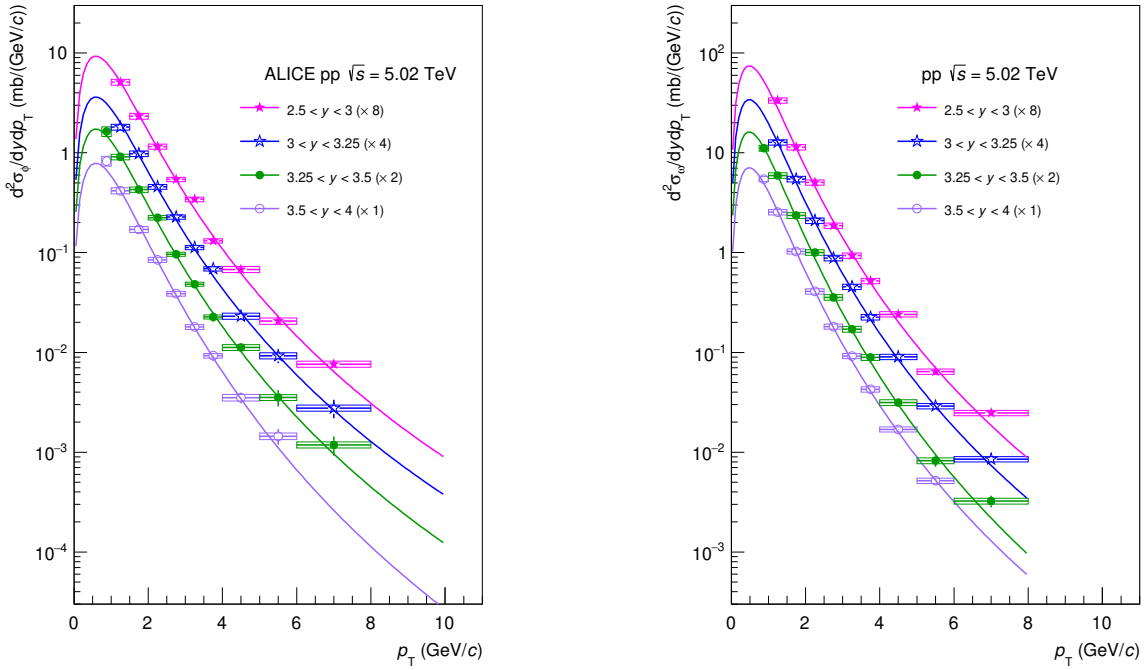

(a) Differential ϕ meson production cross section $\mathrm{d}^2\sigma/\mathrm{d}y\mathrm{d}p_{\mathrm{T}}$ as a function of p_{T} at $\sqrt{s} = 5.02$ TeV. Data are fitted with a Lévy-Tsallis function.

(b) Differential ω meson production cross section $\mathrm{d}^2\sigma/\mathrm{d}y\mathrm{d}p_{\mathrm{T}}$ as a function of p_{T} at $\sqrt{s} = 5.02$ TeV. Data are fitted with a Lévy-Tsallis function.

Figure 4.12

Due to acceptance effects, the number of raw ϕ cannot be extracted over the full p_T range (from 0.75 to 8 GeV/c) in all the four different rapidity intervals. Thus to obtain the expected cross section in these missing intervals, an extrapolation based on a Lévy-Tsallis function as defined in Eq. 1.17 is performed. Results are reported in Tab. 4.7, together with the mean p_{T} values calculated using the fit functions. For both mesons, a moderate decrease of $\langle p_{\mathrm{T}} \rangle$ is observed when rapidity is increased.

To account for the uncertainty coming from the extrapolation, the statistical and system-

Rapidity interval	χ^2/NdF	T (GeV)	n	$\langle p_{\mathrm{T}} \rangle$ (GeV/c)
		ω		
$2.5 < y < 4$	1.509	0.235 ± 0.009	8.04 ± 0.30	0.858 ± 0.010
$2.5 < y < 3$	2.37	0.235 (fixed)	7.73 ± 0.15	0.869 ± 0.005
$3 < y < 3.25$	0.28	0.235 (fixed)	7.93 ± 0.15	0.861 ± 0.005
$3.25 < y < 3.5$	1.00	0.235 (fixed)	8.63 ± 0.18	0.840 ± 0.005
$3.5 < y < 4$	0.76	0.235 (fixed)	8.18 ± 0.16	0.853 ± 0.005
		ϕ		
$2.5 < y < 4$	1.41	0.273 ± 0.011	7.86 ± 0.38	1.031 ± 0.016
$2.5 < y < 3$	1.57	0.273 (fixed)	7.49 ± 0.21	1.045 ± 0.009
$3 < y < 3.25$	0.95	0.273 (fixed)	7.41 ± 0.21	1.050 ± 0.010
$3.25 < y < 3.5$	0.72	0.273 (fixed)	7.85 ± 0.22	1.029 ± 0.009
$3.5 < y < 4$	1.91	0.273 (fixed)	8.74 ± 0.32	0.999 ± 0.009 height

Table 4.7: Parameters of the Lévy-Tsallis fits to the differential cross sections. The mean value of p_{T}, calculated using the fit functions, is also reported.

atic uncertainties are treated separately. The statistical uncertainty on the extrapolated points is taken as a standard deviation of the different values obtained after having performed 1000 fits with points generated according to their statistical uncertainty. Concerning the uncertainty on the extrapolation due to the uncorrelated systematic part, this component is taken as half of the difference between the values obtained performing the extrapolation considering plus or minus the systematic uncertainty on each point.

Finally, three p_{T}-intervals are selected to compare the results as a function of rapidity as shown in figure 4.13. In the bottom panel of figure 4.13(a) the ratio between the rapidity distributions in a given p_{T} interval and in the lowest p_{T} interval are shown, scaled such that the ratio at midrapidity is set to unity. A moderate narrowing of the rapidity distribution is observed when increasing the transverse momentum. For the ω meson in figure 4.13(b), since no measurement of its yield has been performed at midrapidity for this energy, the rapidity distributions are directly compared among themselves. The narrowing of the rapidity distribution is only observed to the highest p_{T} range (for $5 < p_{\mathrm{T}} < 8$GeV/c).

To cross-check the consistency between the results obtained considering the full rapidity range in figures 4.4(a) and 4.4(b) to the ones obtained summing over the four rapidity intervals shown on figures 4.12(a) and 4.12(b), the results obtained in the different rapidity windows were summed together and compared to the integrated values. The differences between the two methods are found to be less than $6\,\%$ in the common p_{T} region.

4.2.4 Results obtained at $\sqrt{s}$ =13 TeV

As mentioned above (in section 4.1.5) the analyses at $\sqrt{s} = 13$ and 8 TeV have been conducted following the same procedure, but only the statistics available at $\sqrt{s} = 13$ TeV allows a double-differential analysis; giving even the possibility to have a fifth rapidity interval for the extraction of the ϕ as shown on figures 4.14(a) (as a function of p_{T}) and 4.14(b) (as a function of y). As for the results obtained at $\sqrt{s} = 5.02$ TeV a slight narrowing of the rapidity distribution is observed when increasing the transverse momentum of the ϕ.

The $< p_{\mathrm{T}} >$ values have been extracted from the Lévy-Tsallis functions fitted to the data. The results, summarised in table 4.8, complete the ones observed at $\sqrt{s} = 5.02$ TeV, with the

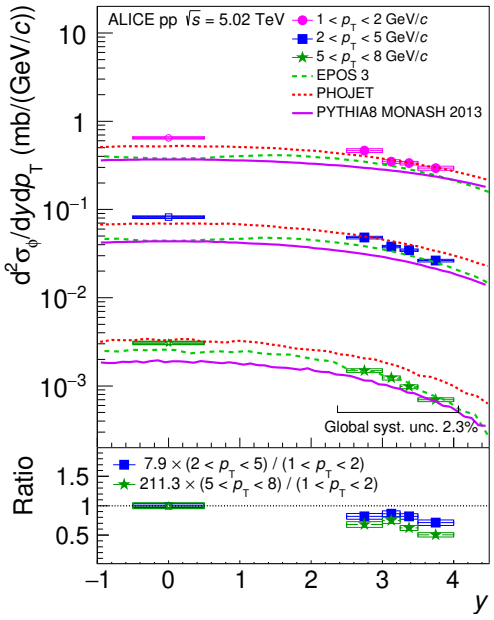

(a) Differential ϕ meson production cross section $\mathrm{d}^2\sigma/\mathrm{d}y\mathrm{d}p_\mathrm{T}$ as a function of rapidity at $\sqrt{s} = 5.02$ TeV. The ratio of the data to the lowest p_T interval is shown in the bottom panel, scaled to the value obtained at mid-rapidity [83, 84, 51]

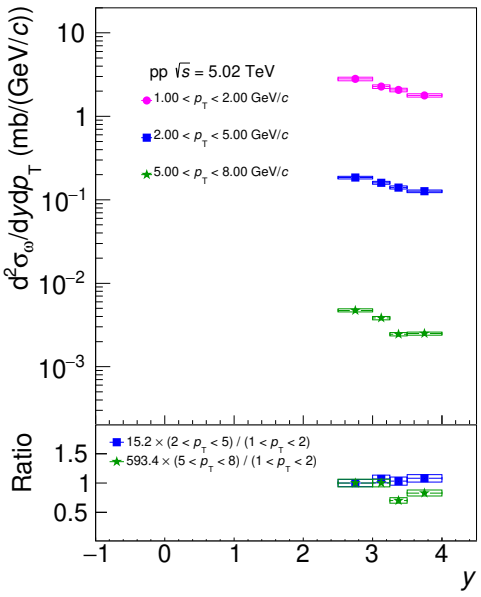

(b) Differential ω meson production cross section $\mathrm{d}^2\sigma/\mathrm{d}y\mathrm{d}p_\mathrm{T}$ as a function of rapidity at $\sqrt{s} = 5.02$ TeV. The ratio of the data to the lowest p_T interval is shown in the bottom panel, scaled to the value obtained in $2.5 < y < 3$.

Figure 4.13

observation of a slight hardening of the p_T distribution when going towards midrapidity.

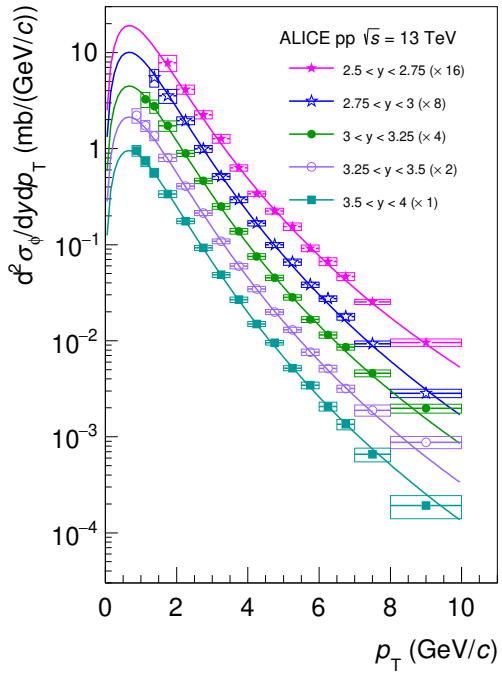

(a) Differential ϕ meson production cross section $\mathrm{d}^2\sigma/\mathrm{d}y\mathrm{d}p_\mathrm{T}$ as a function of p_T at $\sqrt{s} = 13$ TeV. Data are fitted with a Lévy-Tsallis function.

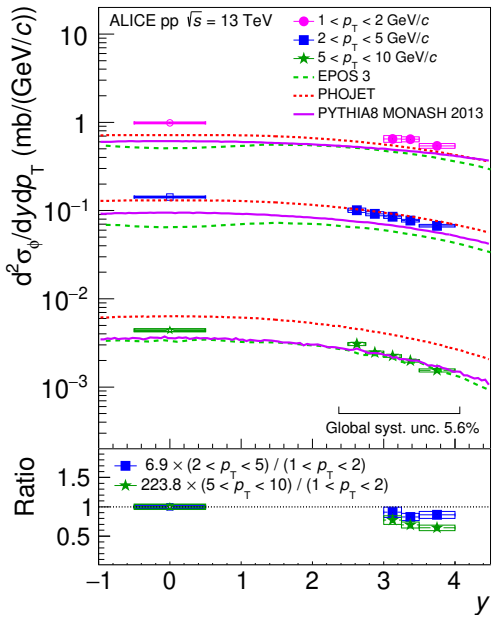

(b) Differential ϕ meson production cross section $\mathrm{d}^2\sigma/\mathrm{d}y\mathrm{d}p_\mathrm{T}$ as a function of rapidity at $\sqrt{s} = 13$ TeV. The ratio of the data to the lowest p_T interval is shown in the bottom panel, scaled to the value obtained at mid-rapidity

Figure 4.14

Rapidity interval	χ^2/NdF	T (GeV)	n	$\langle p_{\mathrm{T}} \rangle$ (GeV/c)
$\sqrt{s} = 13$ TeV				
$2.5 < y < 4$	1.13	0.341 ± 0.005	8.24 ± 0.14	1.206 ± 0.006
$2.5 < y < 2.75$	2.03	0.341 (fixed)	7.71 ± 0.09	1.231 ± 0.005
$2.75 < y < 3$	1.90	0.341 (fixed)	8.45 ± 0.09	1.196 ± 0.004
$3 < y < 3.25$	0.92	0.341 (fixed)	8.26 ± 0.09	1.204 ± 0.004
$3.25 < y < 3.5$	0.61	0.341 (fixed)	8.54 ± 0.11	1.192 ± 0.004
$3.5 < y < 4$	0.75	0.341 (fixed)	8.69 ± 0.12	1.186 ± 0.005

Table 4.8: Parameters of the Lévy-Tsallis fits to the differential cross sections of the ϕ meson. The mean value of p_{T}, calculated using a Lévy-Tsallis function, is also reported.

Chapter 5

Low mass vector meson production as a function of multiplicity

Motivated by recent observations of QGP-like effects in small systems, the choice has been made to study strangeness enhancement in pp collisions at $\sqrt{s}$ = 5.02 TeV. As described in section 1.4, effects such as strangeness enhancement are also observed in small collision systems. Actually, strangeness enhancement is observed to behave independently of the collision system and energy, depending only on the event multiplicity. Performed in parallel to the analysis at 13 TeV in pp collisions, this study focuses on strangeness enhancement as a function of multiplicity at forward rapidity ($2.5 < y < 4$) in pp collisions at $\sqrt{s}$ = 5.02 TeV.

5.1 Multiplicity estimation

The multiplicity of an event is defined as the number of primary charged particles in a collision. Primary particles are all prompt created particles and decay products except for the ones coming from weak decay and photon conversion. The multiplicity can be estimated at different rapidities, but to avoid introducing a bias, its measurement must be performed in a rapidity region which does not overlap to the one of the the signal. Indeed, in the case of single, or double diffractive collisions, particles are produced in the forward region, but not central, leading to a certain multiplicity only observed in a specific rapidity region. Thus to ensure no bias on the multiplicity of an event, its measurement must be performed in a different rapidity

region. Since for low-mass dimuons the signal is measured at forward rapidity, the multiplicity estimation should be performed at midrapidity to avoid any bias when sorting the events in terms of their charged-particle multiplicity. For this reason, the multiplicity estimation is performed using the SPD, which is located at mid-rapidity. The number of tracklets reconstructed in the SPD for $|\eta|<1$ is used to estimate the multiplicity density (per η-unit) $(dN_{ch.}/d\eta)_{|\eta|<1}$. Then, to correct for the SPD efficiency, Monte Carlo models (as listed in section C) are used to obtain the *true* number of primary charged particles and thus the multiplicity. To account for the correction to apply and in order not to introduce a bias on the classification of events used for the signal extraction, the events selected to estimate the multiplicity are the ones triggered by the CINT7 trigger (Minimum-Bias), and passing the event selection described in 3.1.2.

5.1.1 SPD-Tracklets and Multiplicity

In ALICE, the SPD is used as a vertex locator and as a particle tracker. To perform the vertex location the SPD uses the correlation among the different reconstructed clusters in its two layers (details about the reconstruction algorithm can be found in [57]). Two different algorithms are used to locate the vertex. First the 3D-vertexer, which can reconstruct the vertex in the x-y-z coordinates. In the case of low multiplicity events, the 1D-vertexer (also called *SPDZ-vertexer*) can be used to reconstruct the z position of the vertex, but the x and y coordinates will be taken as the run average value. If more than one vertex is found in an event, the vertex having the highest number of contributors to the vertex is kept.

In a second step, SPD-tracklets are reconstructed. To do so, as illustrated in figure 5.1, a segment linking each cluster to the vertex is drawn. To associate two clusters to form a SPD-tracklet, the $\Delta\theta$ and $\Delta\varphi$ values are computed. First a cut-off is applied on both $\Delta\theta$ and $\Delta\varphi$ (cone cut), then a χ^2 is computed based on both segment and the reconstructed SPD-tracklet considering these two clusters. An additional cut on the χ^2 (obtained from the refit of the tracklet to the reconstructed vertex) is then performed to remove combinatorial matches. If there is more than one cluster from the outer layer that can be associated to the inner one, the reconstructed SPD-tracklet returning the lowest χ^2 (still based on the difference between the azimuthal and polar angles) will be taken. Then the reconstruction algorithm links clusters from the first to the second layer which are found to be likely created from the same charged

particle.

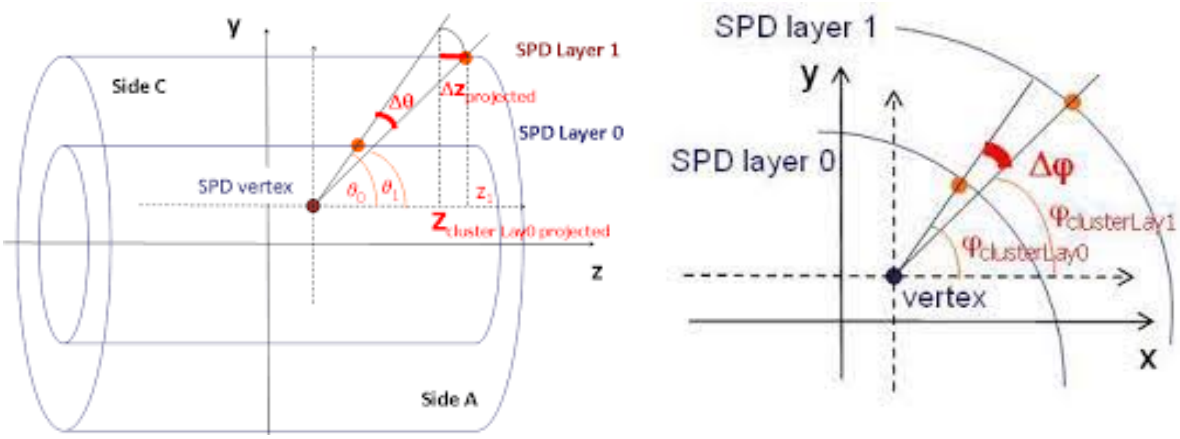

Figure 5.1: Sketch illustrating the calculation of $\Delta\theta$, ΔZ (left figure) and $\Delta\varphi$ (right figure) by use of the two layers of the SPD [94]

5.1.2 V_Z dependence of the multiplicity

Due to noisy and dead pixels, the reconstruction efficiency of the SPD detector can be affected. Noisy pixels returning a signal without any particle hit but also dead pixels which do not return any signal are excluded during data taking. SPD modules suffering from bad cooling performances can also be excluded from data taking during a run. Excluding areas from the detector decreases its total efficiency. The excluded regions of the detector have a direct impact on the number of reconstructed tracks, as can be seen in figure 5.2, where the distribution of tracklets vs Z_V and the ϕ angle (left) and vs η and ϕ (right) in Minimum Bias triggered events is shown. The depleted regions reveal the inactive areas of the detector.

As the efficiency on the reconstruction of SPD-tracklets is affected, it can lead to a bias. Actually the effect can also be observed when looking at the mean number of reconstructed SPD-tracklets ($\langle N_{SPD,trk} \rangle$) as a function of the primary vertex position along the beam axis V_Z as shown in Fig. 5.3. Since there is no reason to expect a dependence of multiplicity on V_Z, this effect has to be corrected. Instead, a relative difference of more than 50% can be observed between $\langle N_{SPD,trk} \rangle$ for V_Z $<$ -9cm and $V_Z \simeq$ 6 cm. To correct for this bias, two different methods are investigated and presented in this analysis:

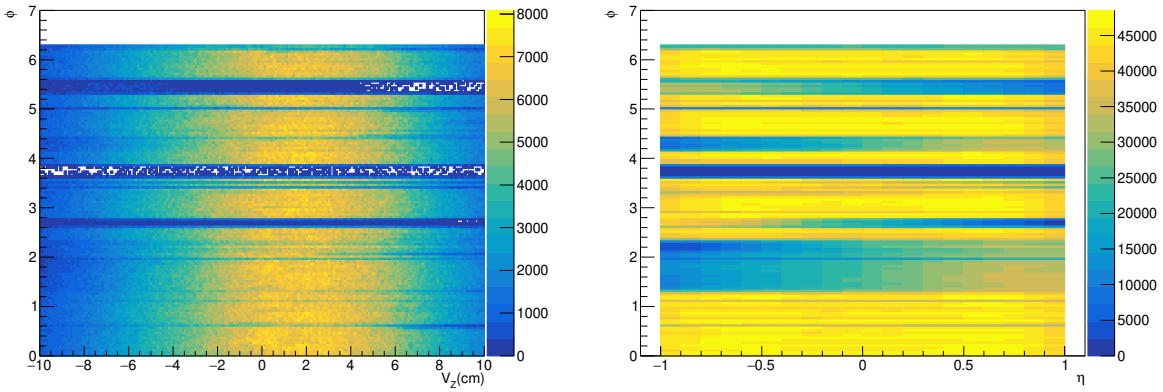

(a) Number of reconstructed SPD tracklets in the $\eta - V_Z$ (b) Number of reconstructed SP tracklets vs ϕ and η for Minimum Bias events

Figure 5.2

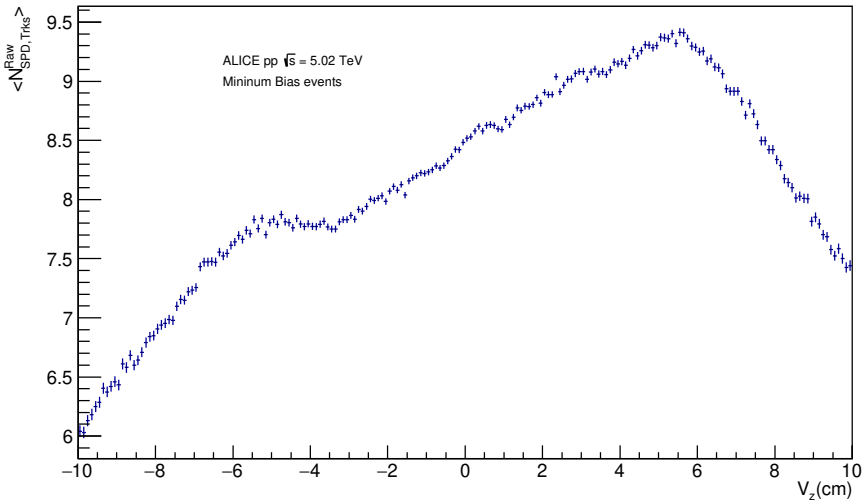

Figure 5.3: $N_{SPD,trk}$ as a function of the primary vertex position along Z, V_Z

- the SPD-equalization method,
- the percentile method.

It has to be noted that the official *AliPhysics* [1] framework is already reporting a value of

[1]General code used by the ALICE collaboration to perform analysis, available at: https://github.com/alisw/AliPhysics

the multiplicity for different multiplicity percentile classes[2]. Unfortunately the current results do not take into account the bias along V_Z.

5.1.3 SPD-equalization method

5.1.3.1 Correction along V_Z

A correction is applied to equalize the V_Z distribution starting from the measured one, shown in Fig.5.3, requiring that it must be flat. This correction is applied on an event-by event basis.

The first step is to choose a reference value $N^{Ref.}_{SPD,Trk}$, which is taken as the maximum value of the measured V_Z distribution ($N^{Ref.}_{SPD,Trk}$ =9.41 in our case). Then, for a given V_Z, the quantity

$$\Delta N(V_Z) = N_{SPD,Trk}(V_Z)\frac{N^{Ref.}_{SPD,Trk} - \langle\, N_{SPD,Trk} \,\rangle\,(V_Z)}{\langle\, N_{SPD,Trk} \,\langle\,(V_Z)} \tag{5.1}$$

is calculated. To account for statistical fluctuations, a smearing is applied extracting a random number distributed as a Poissonian having $\Delta N(V_Z)$ as mean value. The number of corrected SPD tracklets ($N^{Cor.}_{SPD,Trk}$) is then:

$$N^{Cor.}_{SPD,Trk}(V_Z) = N_{SPD,Trk}(V_Z) + Poisson(\Delta N(V_Z)). \tag{5.2}$$

The choice of the reference value as the maximum of the measured V_Z distribution leads to a correction which is always positive and is the least that can be applied, thus limiting the poissonian fluctuations.

Since both periods LHC17p and LHC17q have similar SPD performances, they are considered together to apply the correction. As shown in Figure 5.4 after applying the correction, the number of corrected SPD-tracklets ($N^{Cor.}_{SPD,Trk}(V_Z)$) averages at the $N^{Ref.}_{SPD,Trk}$ value and becomes V_Z-independent.

5.1.3.2 $N^{Cor.}_{SPD,Trk} - N_{Ch}$ Correlation map and multiplicity estimation

The multiplicity is defined as the number of primary charged particles per unit of pseudorapidity with $|\eta| < 1$. To obtain this quantity from the number of tracklets reconstructed in the

[2]These values can be found at: https://alice-notes.web.cern.ch/node/603

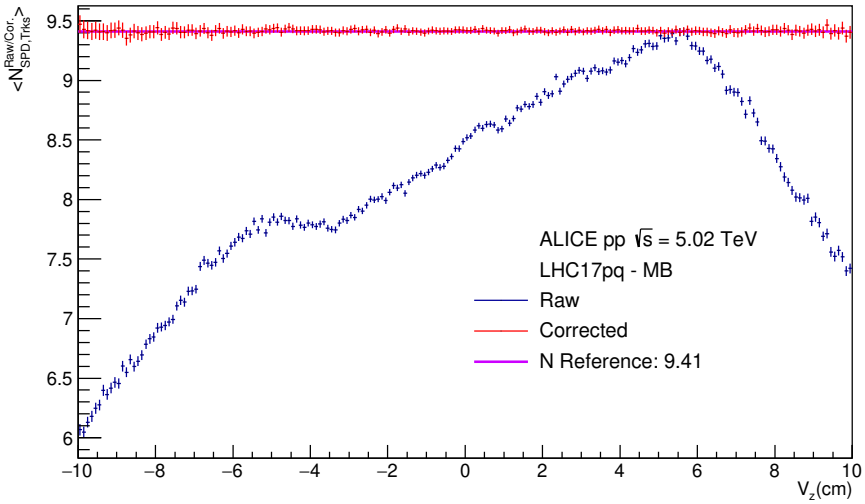

Figure 5.4: $N_{SPD,trk}$ as a function of the primary vertex position along Z, before and after applying the smeared correction

SPD, a Monte Carlo simulation is needed. To do so, the Monte Carlo samples described in section C are used to estimate the correlation between the number of SPD corrected tracklets and the *true* number of charged particles.

As the use of a Monte Carlo sample is required, one has to ensure that it is correctly describing the distribution of SPD tracklets measured in the data. In figure 5.5(a), the distribution of $N^{Cor.}_{SPD,Trk}$ measured in real data and the corresponding distribution obtained from the Monte Carlo are shown. Both are normalised to their respective total number of events. Discrepancies are observed between the two distributions. These discrepancies are within 15% for low multiplicity values ($N^{Cor.}_{SPD,Trk} < 40$), but become large at high multiplicity ($N^{Cor.}_{SPD,Trk} > 40$). This shows that high-multiplicity events in the Monte Carlo are underestimated. To correct for this effect, a weight on Monte Carlo events is applied, depending on their $N^{Cor.}_{SPD,Trk}$. The weight is estimated as:

$$W(N^{Cor.}_{SPD,Trk}) = \frac{N^{MC}_{Evt,Tot}}{N^{Data}_{Evt,Tot}} \frac{N^{Data}_{Evt}(N^{Cor.}_{SPD,Trk})}{N^{MC}_{Evt}(N^{Cor.}_{SPD,Trk})} \ , \tag{5.3}$$

where $N^{MC}_{Evt,Tot}$ is the total number of MC events and $N^{Data}_{Evt,Tot}$ the total number of events in data. The resulting weight applied to Monte Carlo events is shown in figure 5.5(b).

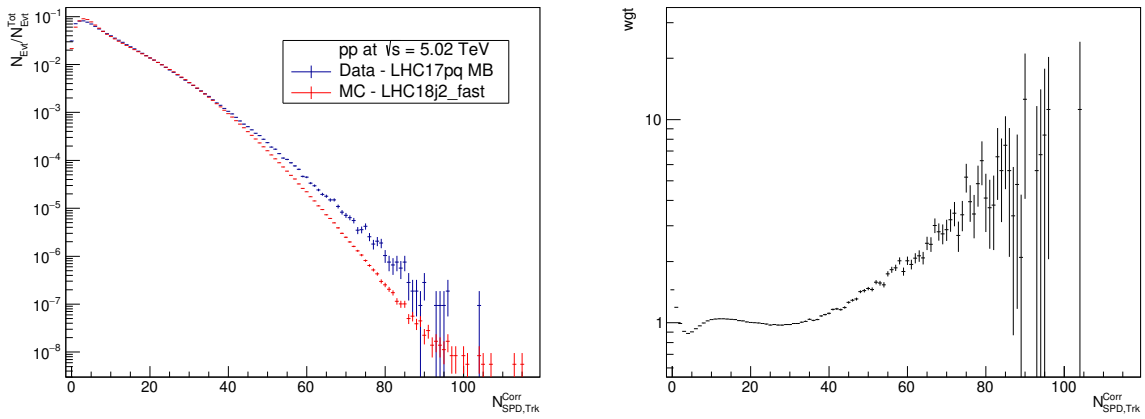

(a) $N^{Cor.}_{SPD,Trk}$ distribution in data and Monte Carlo samples normalised to their total number of events

(b) Weight to apply on Monte Carlo events as a function of the number of corrected SPD-tracklets

Figure 5.5

Once the distribution of SPD-tracklets is corrected applying the weight, its correlation with the number of true charged particles (N_{Ch}) can be extracted. In figure 5.6 the correlation map between the number of true charged particles (N_{Ch}) and the number of corrected SPD-tracklets in Monte Carlo is shown. A strong correlation between the two variables can be noticed, justifying the choice of using SPD-tracklets as a multiplicity estimator.

Events can already be classified from the one showing the lowest multiplicity (low $N^{Cor.}_{SPD,Trk}$) to the highest. After several preliminary studies, the choice of categorising events into four different classes was made. This ensures to have enough statistics to extract the signal in several p_{T} intervals in a second step and to cover a broad multiplicity range. The multiplicity intervals are chosen such that their limits coincide with commonly used percentiles (100, 70, 50, 20, 10, and 0%).

Linear Fit The first attempt to estimate the multiplicity in various intervals is done using a linear interpolation on the mean number of charged particles $\langle\, N_{Ch} \,\rangle$ as a function of $N^{Cor.}_{SPD,Trk}$. The interpolation can be performed over the full $N^{Cor.}_{SPD,Trk}$ range via the α_{Global} factor or limiting it to a i^{th}-multiplicity interval α_i, defined as in equation 5.4.

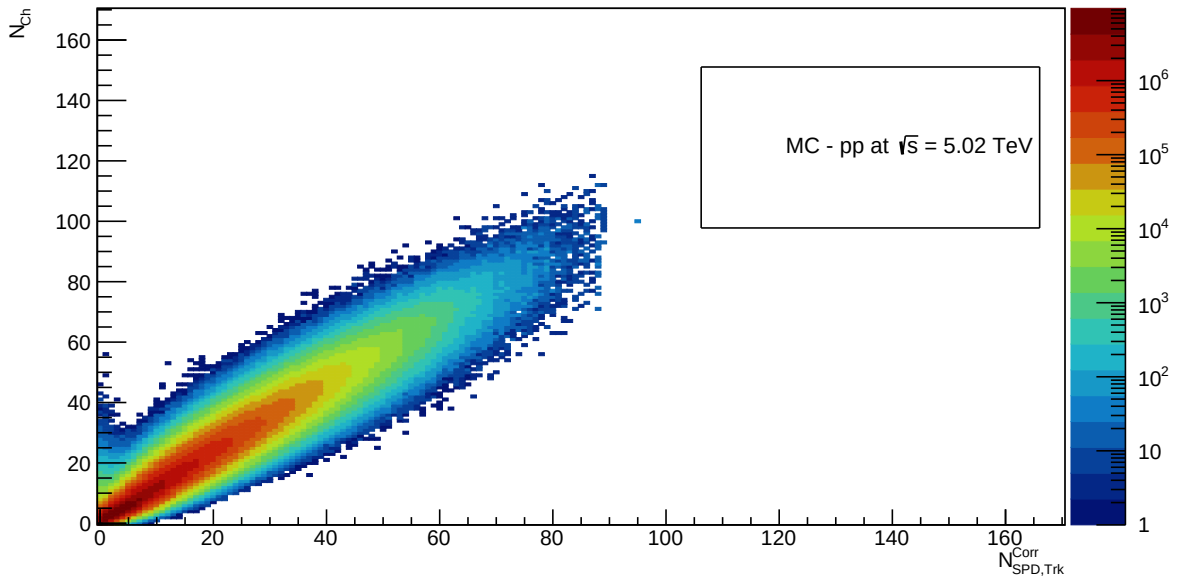

Figure 5.6: Correlation map of N_{Ch} as a function of $N^{Cor.}_{SPD,Trk}$ for $|\eta|<1$ in Monte Carlo

$$< N_{Ch} >= \alpha_{Global/i} \times N^{Cor.}_{SPD,Trk} \, . \tag{5.4}$$

In figure 5.7 the red line indicates the global fit and the violet one the interpolation in all different defined intervals. The global fit shows that an overall linear interpolation gives an overestimation when going to high multiplicities. This overestimation is also observed when limiting the interpolation interval to a smaller extent. As shown in figure 5.8, the differences between the two methods can be as large as 5% at low and high multiplicity. Since the linear fit considers statistical uncertainties, it will tend to be dominated by the lowest multiplicity events in all windows, as they occur more often (see figure 5.5(a)). Once the $\alpha_{Global/i}$ values are extracted, the multiplicity can be estimated in each i^{th}-multiplicity interval as in equation 5.5.

$$\left\langle \frac{dN_{Ch}}{d\eta} \right\rangle_i = \frac{\langle N^{Cor.}_{SPD,Trk} \rangle_i \times \alpha_{Global/i}}{\Delta\eta} \, , \tag{5.5}$$

As the analysis would need both an accurate estimation of the multiplicity over the full multiplicity range and in all the different ranges, another interpolation method has to be found.

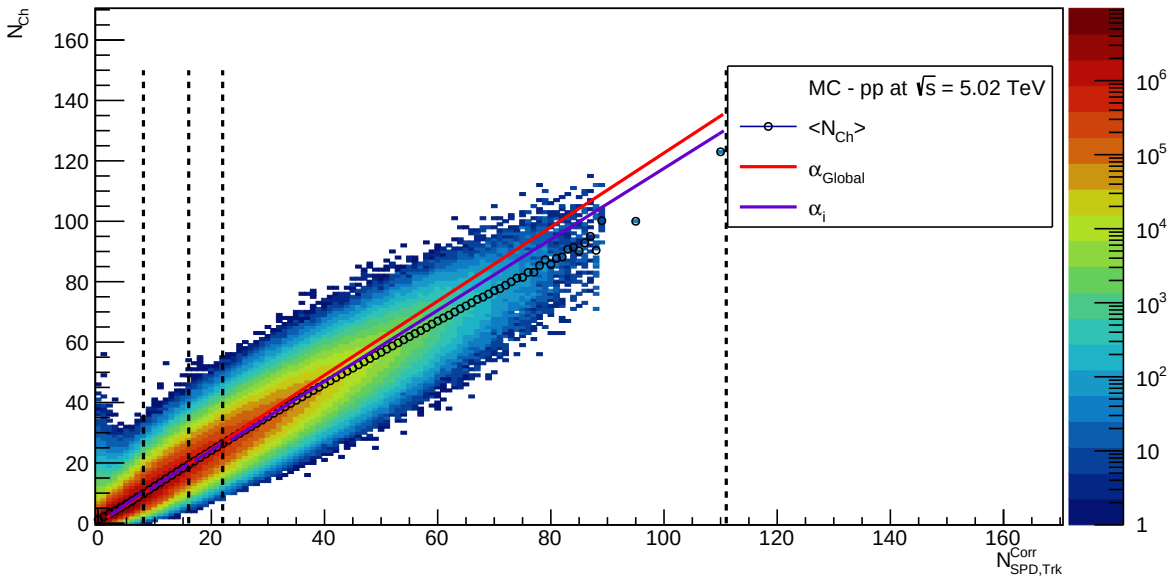

Figure 5.7: Correlation map of N_{Ch} as a function of $N^{Cor.}_{SPD,Trk}$ where the dots represent the $< N_{Ch} >$ values and the dotted lines the limits of the multiplicity intervals

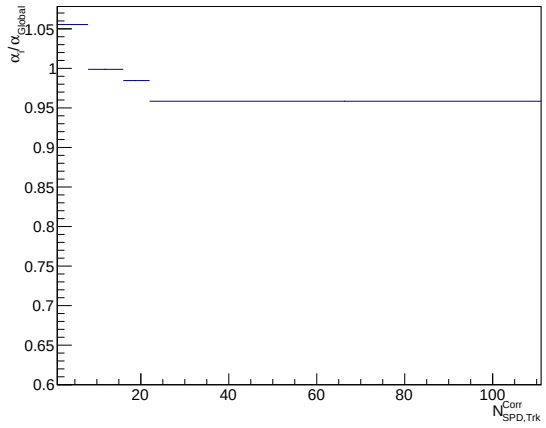

Figure 5.8: Comparison of α_{Global} to α_i as a function of $N^{Cor.}_{SPD,Trk}$ in the different multiplicity intervals

Ad-Hoc polynomial Fit In this case an ad-Hoc polynomial function is used to describe the $\langle N_{Ch} \rangle - N^{Cor.}_{SPD,Trk}$ correlation as defined in equation 5.6, where the x_0 value is left as a free parameter, and the parameters a_i, b_i, c_i must respect the continuity rules defined in equation 5.7.

$$
\begin{aligned}
f(x) &= a_1 x^{c_1} + b_1, \text{for } x \ < \ x_0 \\
f(x) &= a_2 x^{c_2} + b_2, \text{for } x \ \geq \ x_0
\end{aligned}
\tag{5.6}
$$

$$
\begin{aligned}
a_2 &= \frac{a_1 c_1}{c_2} x_0^{c_1 - c_2}, \\
b_2 &= \frac{a_1 c_2 - a_1 c_1}{c_2} x_0^{c_1} + b_1
\end{aligned}
\tag{5.7}
$$

The results of the interpolation obtained using this method are presented in figure 5.9. Contrarily to the linear fits, this method can give an accurate description of the mean number of true charged particles $\langle\ N_{Ch}\ \rangle$ in the full multiplicity range. The multiplicity in the *i*-th multiplicity interval defined between $N^i_{SPD,min}$ and $N^i_{SPD,max}$ is taken as:

$$
\left\langle \frac{dN_{Ch}}{d\eta} \right\rangle_i = \frac{\sum\limits_{j=N^i_{SPD,min}}^{N^i_{SPD,max}} N_j \times f_{ad-Hoc}(N^{Cor.}_{SPD,Trk})}{\Delta\eta \sum\limits_{j=N^i_{SPD,min}}^{N^i_{SPD,max}} N_j} \ . \tag{5.8}
$$

5.1.3.3 Systematic uncertainty estimation

To account for the systematic sources on the evaluation of $\langle\ N_{ch}\ \rangle$ a total of 40 variations were done considering different inputs entering the $\langle\ N_{ch}\ \rangle$ estimation procedure. The different estimations of multiplicity were performed considering the following variations:

- The position of the primary vertex V_Z: [-10, -6[, [-6, -2[, [-2, 2[, [2, 6[, [6, 10] cm
- The generator used: PYTHIA8 or EPOS,
- The profile of reference: taken from data or taken from MC,
- The interpolation method used to represent the correlation between $N^{Cor.}_{SPD,Trk}$ and N_{ch}: ad-hoc polynomial or α_i

The relative systematic uncertainty in each multiplicity bin is taken as the ratio of RMS to the mean value for the different tests.

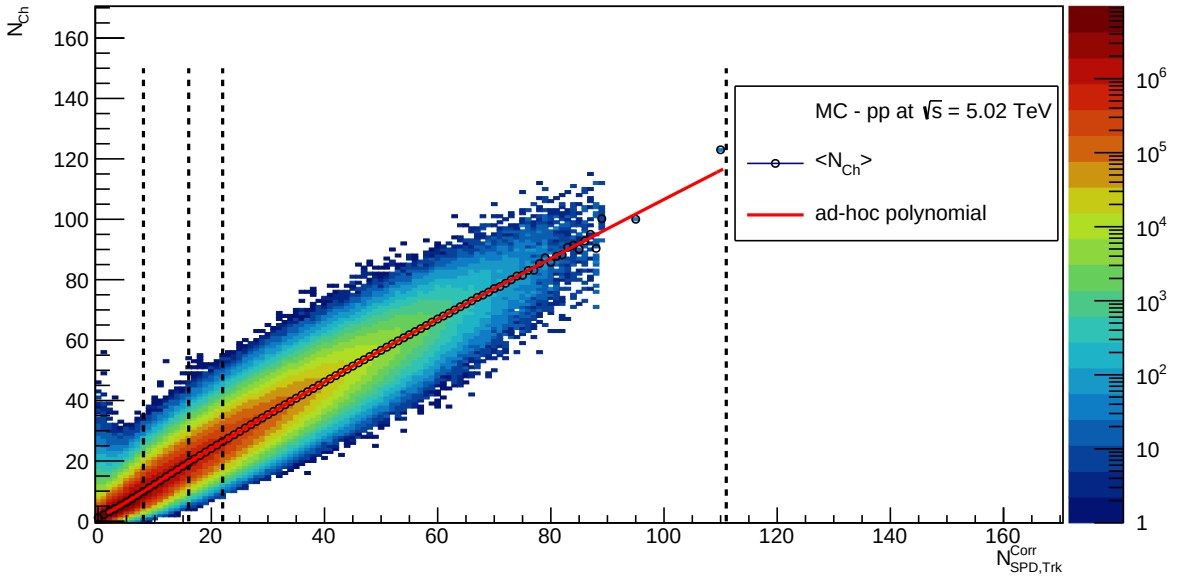

Figure 5.9: Correlation map of N_{ch} as a function of $N^{Cor.}_{SPD,Trk}$ where the dots represent the $\langle\ N_{ch}\ \rangle$ with the ad-hoc polynomial function interpolation

The results of the 40 variations performed on the five different multiplicity windows (the four defined previously and the multiplicity integrated interval) are shown in figure 5.10. The main contributors to the variation of the $<\ N_{Ch}\ >$ estimation are: the profile (data or MC) chosen to correct for the V_Z dependency, and the choice of the MC-generator to obtain the correlation between $N^{Cor.}_{SPD,Trk}$ and N_{Ch}. For what concerns the different V_Z intervals, the differences are negligible compared to the other sources, validating the equalization method to correct the effects on the SPD-performances. The different results are summarised in table 5.1.

For what concerns the systematic on the α_i method, the comparison to the α_{global} is kept to account for the non-linearity aspects of the estimation under the δ-value defined as in equation 5.9

$$\delta = \frac{|\langle\ N_{ch}\ \rangle_{\alpha_{Global}} - \langle\ N_{ch}\ \rangle_{\alpha_i}|}{\langle\ N_{ch}\ \rangle_{\alpha_i}} \tag{5.9}$$

		$\langle N_{Ch} \rangle \pm$ stat. (for $\|\eta\|< 1$)				
$N^{Cor.}_{SPD,Trk}$	Approx. Multiplicity	linear (α_{Global})	linear (α_i)	ad-hoc Pol.	δ	syst.
[1-7]	50-100%	5.13 $\pm$ 0.36	5.57 $\pm$ 0.36	5.574 $\pm$ 0.001	5.5%	4.8%
[8-15]	20-50%	13.86 $\pm$ 0.35	13.85 $\pm$ 0.35	13.847 $\pm$ 0.002	0.13%	0.51%
[16-21]	10-20%	22.77 $\pm$ 0.39	22.42 $\pm$ 0.39	22.451 $\pm$ 0.002	1.16%	0.88%
[22-105]	0-10%	33.32 $\pm$ 0.42	33.85 $\pm$ 0.42	33.92 $\pm$ 0.009	4.2%	2.04%
[1-105]	0-100%	11.92 $\pm$ 0.23	11.88 $\pm$ 0.23	11.99 $\pm$ 0.003	0.25%	0.51%

Table 5.1: Summary of $\langle N_{Ch} \rangle$ obtained within $|\eta|< 1$ with the different interpolation procedures with PYTHIA8 as particle generator

		$\langle N_{Ch} \rangle \pm$ stat. (for $\|\eta\|< 1$)		
$N^{Cor.}_{SPD,Trk}$	Approx. Multiplicity	linear (α_{Global})	linear (α_i)	ad-hoc Pol.
[1-7]	50-100%	5.16 $\pm$ 0.36	5.48 $\pm$ 0.36	5.608 $\pm$ 0.001
[8-15]	20-50%	13.93 $\pm$ 0.35	13.86 $\pm$ 0.35	13.88 $\pm$ 0.002
[16-21]	10-20%	22.87 $\pm$ 0.39	22.47 $\pm$ 0.39	22.483 $\pm$ 0.002
[22-105]	0-10%	35.48 $\pm$ 0.42	34.07 $\pm$ 0.42	34.13 $\pm$ 0.008
[1-105]	0-100%	11.97 $\pm$ 0.23	11.94 $\pm$ 0.23	12.05 $\pm$ 0.003

Table 5.2: Summary of $\langle N_{Ch} \rangle$ obtained within $|\eta|< 1$ with the different interpolation procedures with EPOS as a generator

5.1.4 The Percentile Method

5.1.4.1 $N^{raw}_{SPD,trk} - V_Z$ sorting

An alternative way to to estimate the multiplicity is the *percentile method*. This technique is not meant to apply a correction, but rather to consider the multiplicity of an event independently for each V_Z interval. Thus, the different events are classified in the various multiplicity percentiles based on their raw number of reconstructed SPD-tracklets ($N^{raw}_{SPD,trk}$) in their specific V_Z bins. To consider SPD resolution effects, the percentile in multiplicity in which an event will be classified is estimated in restricted V_Z intervals where the variations of the SPD efficiency can be considered negligible. Taken from the official method of the *ALICE framework*, the multiplicity percentile classification shows discrepancies along the V_Z axis, as shown in

figure 5.11. This figure shows that the intervals in which the mean multiplicity percentile is small (thus corresponding to higher multiplicity events) correspond to the intervals in which the mean number of raw SPD-tracklets is higher, as seen in figure 5.4. Analogously, the intervals in which the mean multiplicity percentile is higher correspond to intervals in which the mean number of raw SPD-tracklets is lower.

As the classification of events is based on data, thus affected by limited statistics, the percentile limits are defined in 20 different V_Z intervals of 1 cm. This fine binning allows neglecting SPD effects along V_Z in each interval. Figure 5.12 shows the limits on the number of $N^{raw}_{SPD,trk}$ to define a multiplicity percentile as a function of V_Z. Hence, in each V_Z interval the events are sorted in their multiplicity percentile, where each multiplicity interval can be defined based on an upper ($N^{Max}_{SPD,trk}(V_Z)$) and lower limit ($N^{Min}_{SPD,trk}(V_Z)$) on the number of $N^{raw}_{SPD,trk}(V_Z)$. In Figure 5.12 the $N^{Min}_{SPD,trk}(V_Z)$ values (z-axis) are drawn as a function of V_Z (x-axis) defining the specific multiplicity percentiles (y-axis). In this case the V_Z dependence on $N^{raw}_{SPD,trk}$ is also observed. This dependence is translated in the classification procedure where the edges of the bins in $N^{raw}_{SPD,trk}$ are found to be lower for negative V_Z. Accounting for the correction with this technique allows to be less dependent among the SPD performances in the different periods considered. This is particularly important for analyses of data taken over a long time, as for the analysis performed in pp collisions at $\sqrt{s}$=13 TeV.

Once the different limits on the $N_{SPD,Trk}$ values defining the multiplicity intervals as a function of V_Z are found, the multiplicity classification can be applied to Monte Carlo. As performed with the *equalization method*, the Monte Carlo events must be corrected in order to describe the $N_{SPD,Trk}$ spectrum observed in data. As shown in figure 5.13 the distribution mostly shows discrepancies at high multiplicity.

Thus, a weight is applied for each Monte Carlo event based on its $N_{SPD,Trk}$. The Monte Carlo events are then sorted in their respective multiplicity intervals depending both on their $N_{SPD,Trk}$ and V_Z values accordingly to the limits obtained in Fig. 5.12.

The $N_{SPD,Trk}$ distribution is shown in figure 5.14. From this figure, the ordering of the multiplicity of the events depending on their multiplicity interval is retrieved.

The mean number of charged particles $\langle N_{Ch} \rangle$ within $|\eta| < 1$ can be obtained as a function of V_Z as shown in figure 5.15. From this figure, no dependence on V_Z is observed, and the

$\langle N_{Ch} \rangle$ value for a specific interval is taken fitting the $\langle N_{Ch} \rangle (V_Z)$ with a constant. The uncertainty on the obtained value is taken as the RMS over the different estimations along V_Z. The results obtained are listed in table 5.3.

5.1.4.2 Systematic uncertainty estimation

The systematic uncertainty on the $\langle N_{Ch} \rangle$ value is taken as the quadratic sum of two main contributors. The first and main source is the V_Z dependence: to account for this one, the RMS over the 20 different $\langle N_{Ch} \rangle$ values obtained in each multiplicity interval is taken. The second source comes from the choice of the generator used to obtain the *true* number of charged particles. To account for this term, the procedure for the multiplicity estimation was performed using the EPOS-LHC generator. The different contributions are listed in table 5.3.

		$\langle N_{Ch} \rangle \pm$ stat. (for $\|\eta\| < 1$)		
Approx. Multiplicity	PYTHIA 8	EPOS-LHC	δ (expressed in %)	Tot. Syst. (expressed in %)
50-100%	5.40 $\pm$ 0.21	5.37 $\pm$ 0.23	0.03 (0.5%)	0.21 (3.9%)
20-50%	13.97 $\pm$ 0.33	13.97 $\pm$ 0.31	0.00 (0.0%)	0.33 (2.4%)
10-20%	22.47 $\pm$ 0.36	22.52 $\pm$ 0.37	0.05 (0.2%)	0.36 (1.6%)
0-10%	34.36 $\pm$ 0.56	34.58 $\pm$ 0.49	0.28 (0.8%)	0.63 (1.8%)
0-100%	12.08 $\pm$ 0.06	12.12 $\pm$ 0.12	0.04 (0.3%)	0.07 (0.6%)

Table 5.3: Summary of $\langle N_{Ch} \rangle$ obtained within $|\eta| < 1$ with the different interpolation procedures with PYTHIA8, EPOS-LHC, their differences (here denoted as δ) and the total systematic uncertainty

5.1.5 Multiplicity estimator choice

Table 5.4 summarises the multiplicity estimation obtained with the two techniques described above. Both techniques show consistent results within uncertainties.

None of the methods described above requires a specific additional selection, so the choice of the multiplicity estimator does not affect the data selection.

The analysis of low-mass dimuons was also performed in pp collisions at $\sqrt{s}$ =13 TeV where 22 data periods were considered. These data were recorded from 2016 to 2018. During

	$\langle N_{Ch} \rangle \pm$ syst. (for $\lvert\eta\rvert < 1$)	
Approx. Multiplicity	SPD percentile method	Equalization method
50-100%	5.40 $\pm$ 0.21	5.57 $\pm$ 0.41
20-50%	13.97 $\pm$ 0.33	13.84 $\pm$ 0.07
10-20%	22.47 $\pm$ 0.36	22.45 $\pm$ 0.33
0-10%	34.36 $\pm$ 0.63	33.92 $\pm$ 1.58
0-100%	12.08 $\pm$ 0.07	11.99 $\pm$ 0.07

Table 5.4: Summary of the $\langle N_{Ch} \rangle$ values obtained within $|\eta| < 1$ for pp collisions at $\sqrt{s} = 5.02$ TeV with the two different multiplicity estimation techniques with the use of the PYTHIA8 model

this period of time, the SPD detector efficiency varied. As the SPD percentile method showed less period dependency, this method was preferred. Thus in order to compare the results obtained at forward-rapidity at both centre-of-mass energies, the SPD percentile method was chosen.

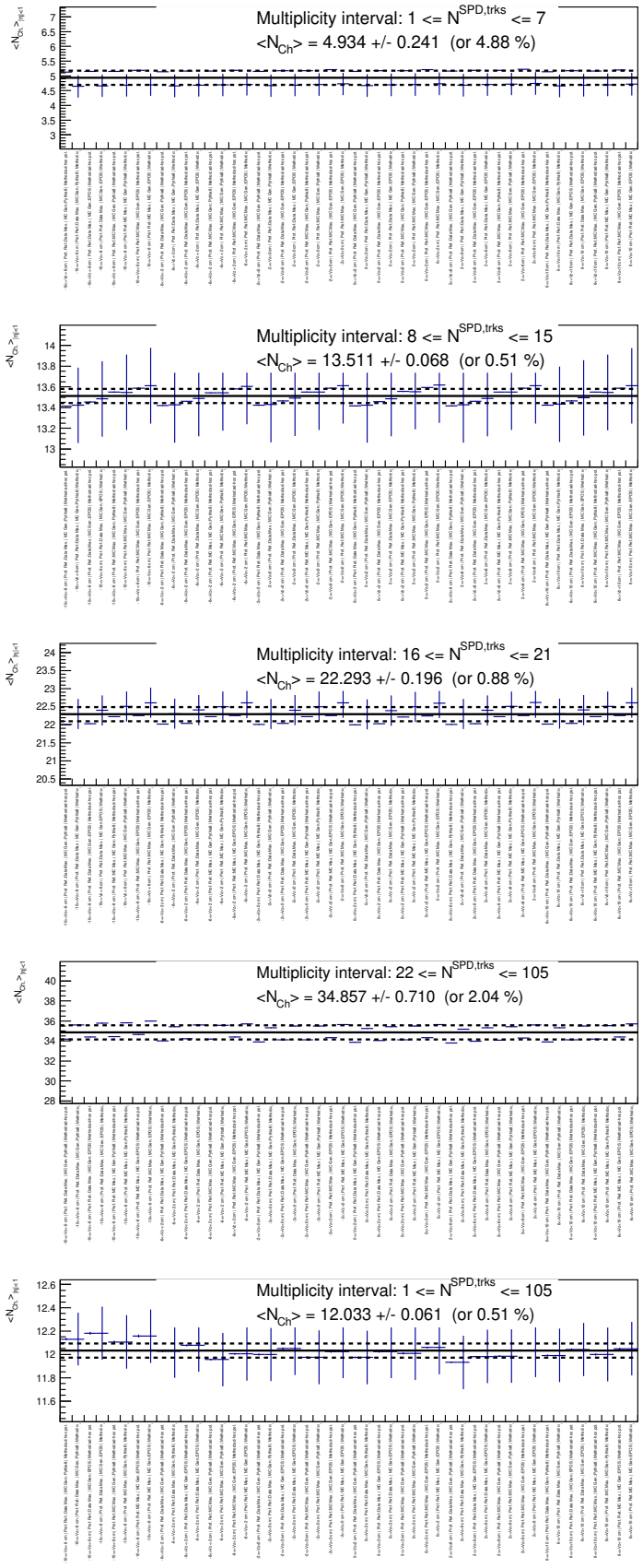

Figure 5.10: Results of the different tests on the $\langle N_{Ch} \rangle$ estimation for $|\eta| < 1$, with the dotted line representing one RMS deviation of the mean value

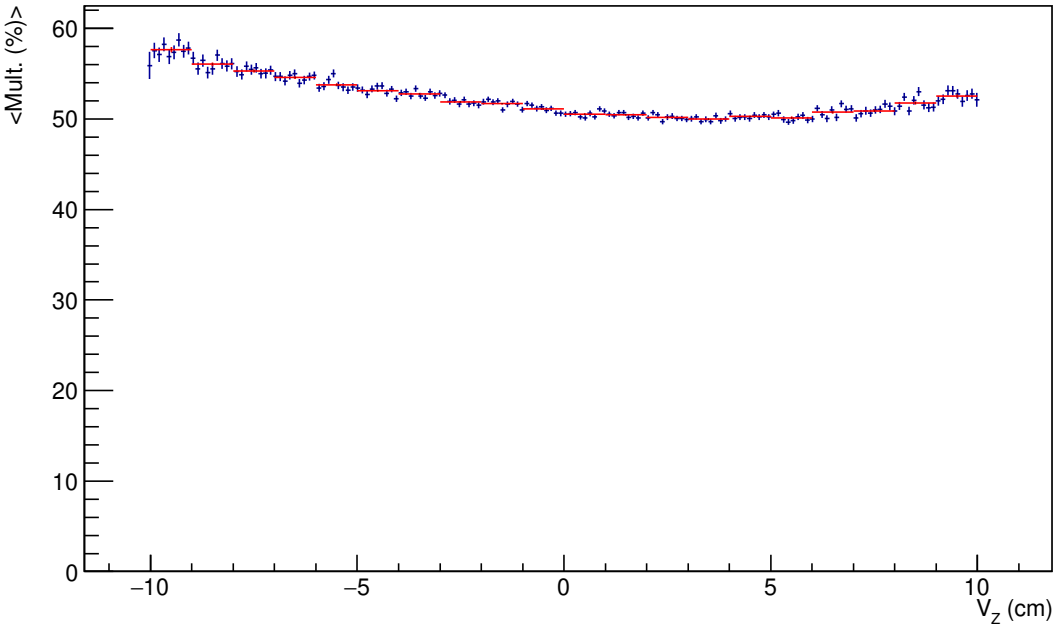

Figure 5.11: Mean Percentile value obtained from the ALICE official framework using SPDtracklets as estimator as a function of the interaction vertex position V_Z

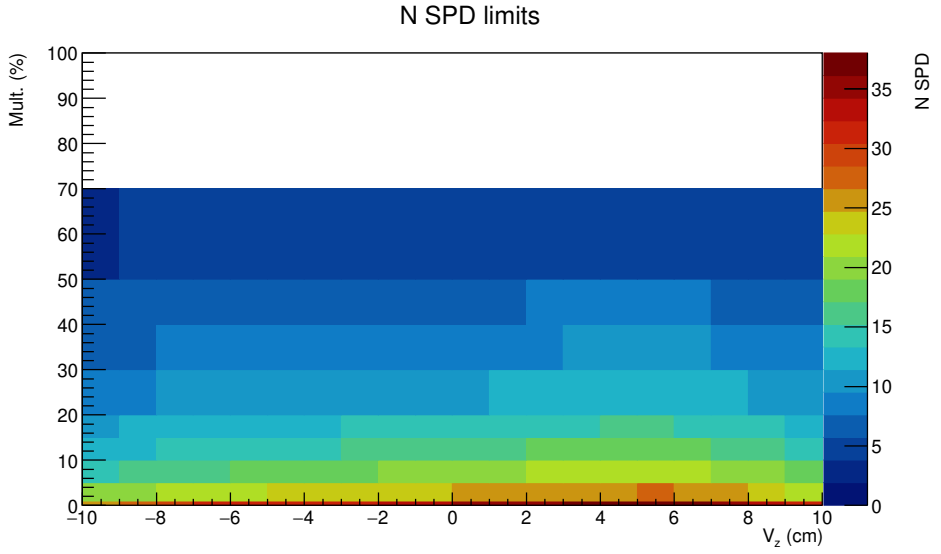

Figure 5.12: Lower limit on the number of $N^{raw}_{SPD,trk}$ (Z-axis) to classify a event in a multiplicity percentile (Y-axis) as a function of V_Z in pp collisions at $\sqrt{s}$ = 5.02 TeV in Minimum Bias triggered data

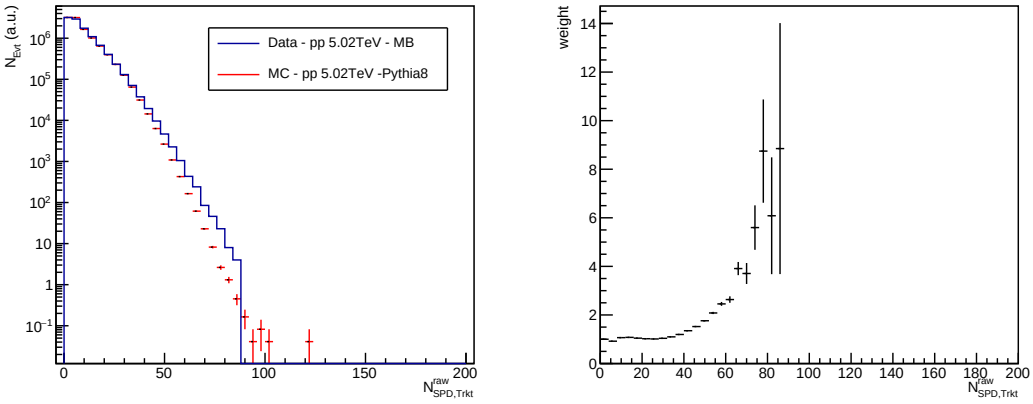

Figure 5.13: **Left:** $N_{SPD,Trk}$ distribution in data and Monte Carlo samples normalised to their total number of events obtained in MB events in pp collisions at $\sqrt{s}$ = 5.02 TeV. **Right:** Weight to apply on Monte Carlo events as a function of the number of corrected SPD-tracklets

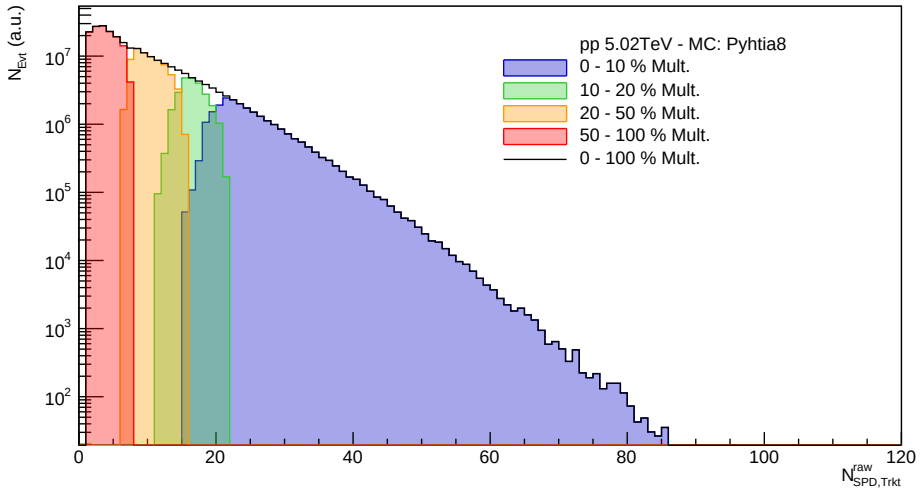

Figure 5.14: $N_{SPD,Trk}$ distribution of Monte Carlo events obtained using PYTHIA8 for the different multiplicity intervals considered

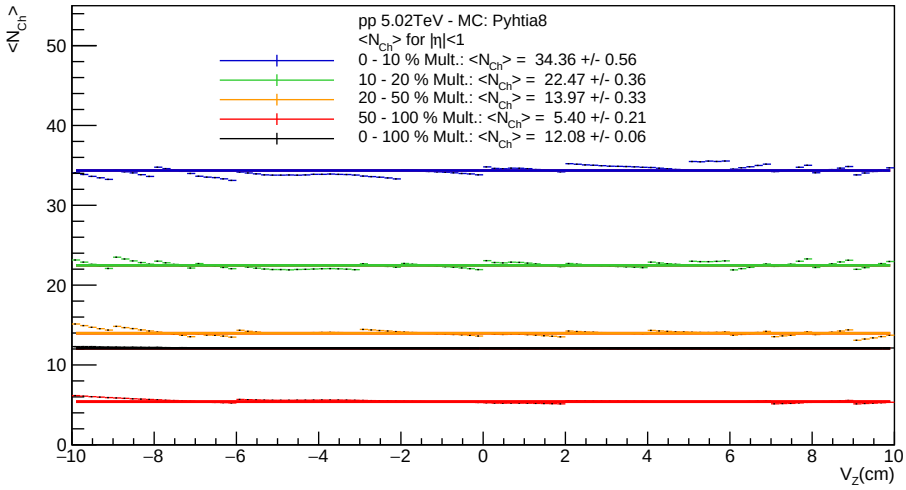

Figure 5.15: $\langle\ N_{Ch}\ \rangle$ for $|\eta|< 1$ as a function of V_Z for the different multiplicity intervals. The $\langle\ N_{Ch}\ \rangle$ values obtained as their RMS for each intervals are given.

5.2 Event Correction

5.2.1 Normalisation factor

To obtain the number of Minimum Bias events from the CMUL7 triggered events where the opposite-sign (OS) pairs are recorded, a normalisation factor must be estimated. To convert from the number of OS triggered events to MB events, the normalisation factor $F_{Norm.}$ (already discussed in the section 3.1.3) is calculated for each multiplicity interval. The corresponding values are presented in table 3.1.

		F_{Norm}		
$N^{Cor.}_{SPD,Trk}$	Mult. Percentile	Indirect	Direct	Systematic uncertainty
[1-7]	50-100%	5920.19 $\pm$ 0.05	5898 $\pm$ 55	0.37 %
[8-15]	20-50%	2945.88 $\pm$ 0.04	2934 $\pm$ 42	0.38 %
[16-21]	10-20%	1923.73 $\pm$ 0.03	1916 $\pm$ 36	0.37 %
[22-105]	0-10%	1247.78 $\pm$ 0.03	1241 $\pm$ 39	0.38 %
[1-105]	0-100%	3225.19 $\pm$ 0.06	3213 $\pm$ 58	0.37 %

Table 5.5: Summary of the different event correction F_{Norm} values obtained, either with the direct and the indirect method and the resulting systematic uncertainty

5.2.2 Event efficiency

The Minimum Bias trigger does not collect all inelastic collisions. To consider this effect, the efficiency of this trigger is estimated using Monte Carlo simulations. The efficiency is defined as follows:

$$\epsilon^{MB}_{INEL>0} = \frac{N^{MB,INEL>0}_{Evt}}{N^{INEL>0}_{Evt}} \ , \tag{5.10}$$

where $N^{MB,INEL>0}_{Evt}$ is the number of events passing the MB trigger and the requirement to have at least one reconstructed charged particle within $|\eta|< 1$ (INEL>0).

Similarly, the efficiency of the QA selection is

$$\epsilon^{QA}_{INEL>0} = \frac{N^{QA,INEL>0}_{Evt}}{N^{INEL>0}_{Evt}} \ , \tag{5.11}$$

where $N^{QA,INEL>0}_{Evt}$ is the number of events passing both the $INEL > 0$ requirement and the event QA selection. These effects are considered together in a single efficiency term ϵ_{evt} defined for each multiplicity interval as:

$$\epsilon^{mult}_{Evt} = \frac{N^{MB,QA,INEL>0}_{Evt}}{N^{INEL>0}_{Evt}} \ . \tag{5.12}$$

All the different contributions to the correction of the number of events are presented in figure 5.16. The MB trigger efficiency is lower for low multiplicity events and affects mostly events with a low number of $N^{Cor.}_{SPD,Trk}$. Similarly, the effect of the event QA is mostly observed for events with a low number of vertex contributors. Limitation on contributors to the vertex leads to a worsening on the vertex resolution, possibly causing to the rejection of these events. Results are summarised in table 5.6.

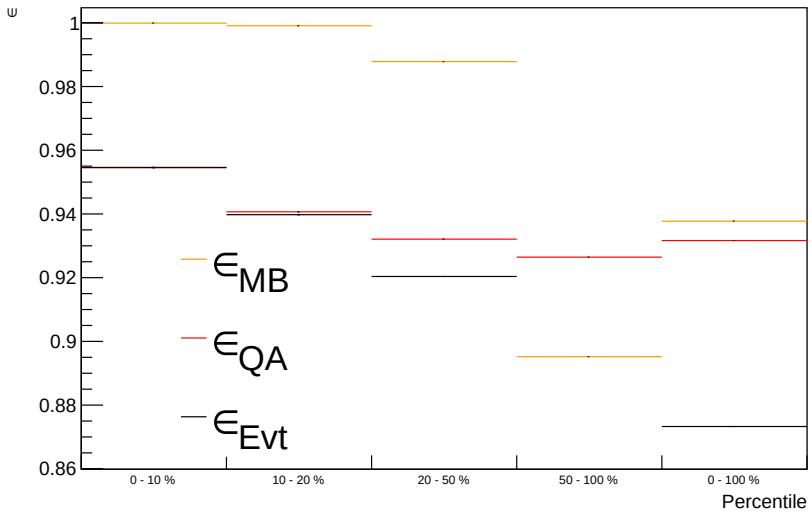

Figure 5.16: Event efficiency due to the MB trigger effects, and to the event selection in the different multiplicity intervals

	ϵ_{evt}						
	PYTHIA8			EPOS			
Mult. Percentile	$\epsilon^{MB}_{INEL>0}$	$\epsilon^{QA}_{INEL>0}$	ϵ_{Evt}	$\epsilon^{MB}_{INEL>0}$	$\epsilon^{QA}_{INEL>0}$	ϵ_{Evt}	$\delta(\epsilon_{Evt})$
50-100%	0.8952	0.9216	0.8283	0.8946	0.9179	0.8197	0.0086 (1.0%)
20-50%	0.9878	0.9320	0.9204	0.9938	0.9247	0.9189	0.0015 (0.2%)
10-20%	0.9990	0.9407	0.9398	0.9996	0.9341	0.9337	0.006 (0.7%)
0-10%	0.9999	0.9546	0.9545	0.9999	0.9487	0.9486	0.006 (0.6%)
0-100%	0.9377	0.9377	0.8733	0.9409	0.9241	0.8690	0.004 (0.5%)

Table 5.6: Summary of the different event corrections obtained with PYTHIA and EPOS and the resulting systematic uncertainty ($\delta(\epsilon_{Evt})$)

5.3 Signal extraction

5.3.1 Signal selection

Following the procedure described in chapter 5.3.2, the events, tracks and pairs were selected according to the requirements presented in table 5.7.

The background estimation is performed using the event mixing technique, where mixed events are categorised into ten different V_Z intervals and ten different multiplicity intervals. The resulting OS and background mass spectra are reported in Fig. fig:SandB˙mult in the different multiplicity bins, while the corresponding ratios between correlated and uncorrelated pairs mass spectra are shown in Fig. 5.18. A moderate decrease of this ratio is observed in the highest multiplicity intervals.

5.3.2 Signal extraction

For signal extraction, the technique developed in section 5.3.2 is used. The χ^2 resulting from the different fits to the continuum is presented in figure 5.19. It can be seen that, for all the three different empirical functions described in chapter 3, the interpolation of the continuum gives reasonable reduced-χ^2 values around 1. For this reason, no preference on the empirical function is made, meaning that the extracted values of raw ω and ϕ obtained from the template fit procedure is taken as the mean of the values obtained considering the three different

Selection Summary	
Event Level	
Trigger	CMUL or CMLL
Quality cut	Physics Selection SPD pile-up rejection $N^{vtx}_{Contrib.} \geq 1$ -10 $< V_Z <$ 10 cm $N_{SPD,trkl} \geq 1$ within $\|\eta\| < 1$
Track Level	
Quality Cut	track matches a tracklet in the trigger
Kinematic Cut	$p^{\mu}_{\mathrm{T}} \gtrsim 0.5$ *GeV/c* $-4 < \eta_{\mu} < -2.5$ 17.6 $< R_{Abs} <$ 89.5 cm
Pair Level	
Quality Cut	muons cannot hit the same local board
Kinematic Cut	$2.5 < y_{\mu\mu} < 4$ $p^{\mu\mu}_{\mathrm{T}} > 0.75$ *GeV/c*

Table 5.7: Summary of the selections

empirical functions that describe the correlated continuum.

In figure 5.20 the order of the polynomial and the number of exponentials used (single or double) are plotted.

The fits to the mass spectra performed in several p_{T} intervals are shown in Fig. 5.21 and 5.22 for high-multiplicity and inelastic collisions, respectively. In these figures the VWG function is used for the description of the correlated continuum.

5.3.2.1 Systematic uncertainties on signal extraction

All together there is a total of 729 variations of the fitting parameters for the signal extraction for each interval. The systematic uncertainty on $N^{\mathrm{raw}}_{\omega/\phi}$ is then taken as the RMS of these 729 different estimations on the mean value.

The p_{T} dependence of the systematic uncertainty on the raw number of ω and ϕ are shown in Fig.5.23 and Fig.5.24 respectively, in the multiplicity intervals considered in this analysis.

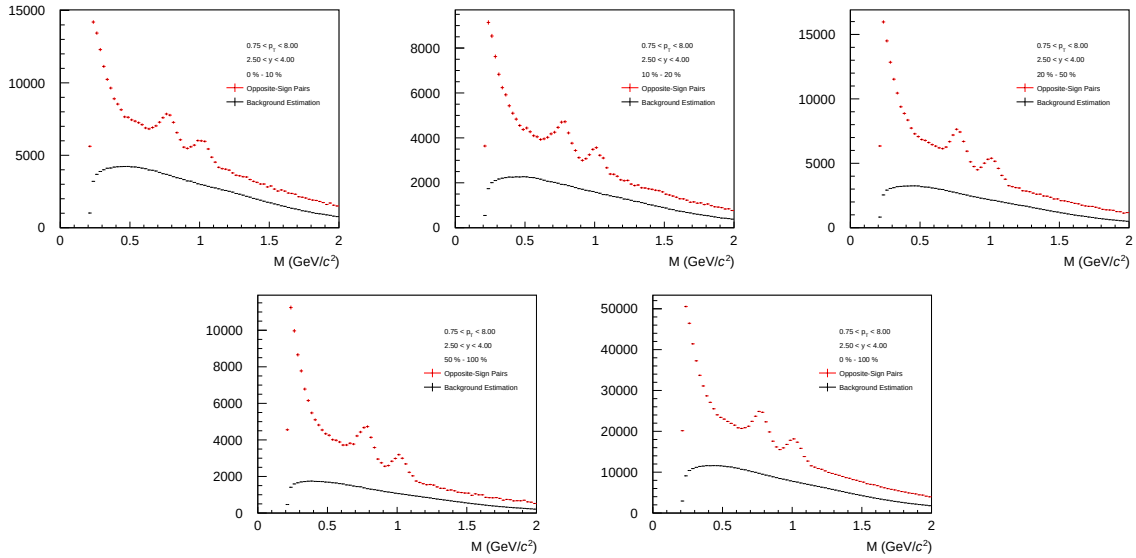

Figure 5.17: Dimuon invariant mass spectrum in pp collisions at $\sqrt{s} = 5.02$ TeV for all the multiplicity intervals studied for $0.75 < p_{\mathrm{T}} < 8$ GeV/c and $2.5 < y < 4$

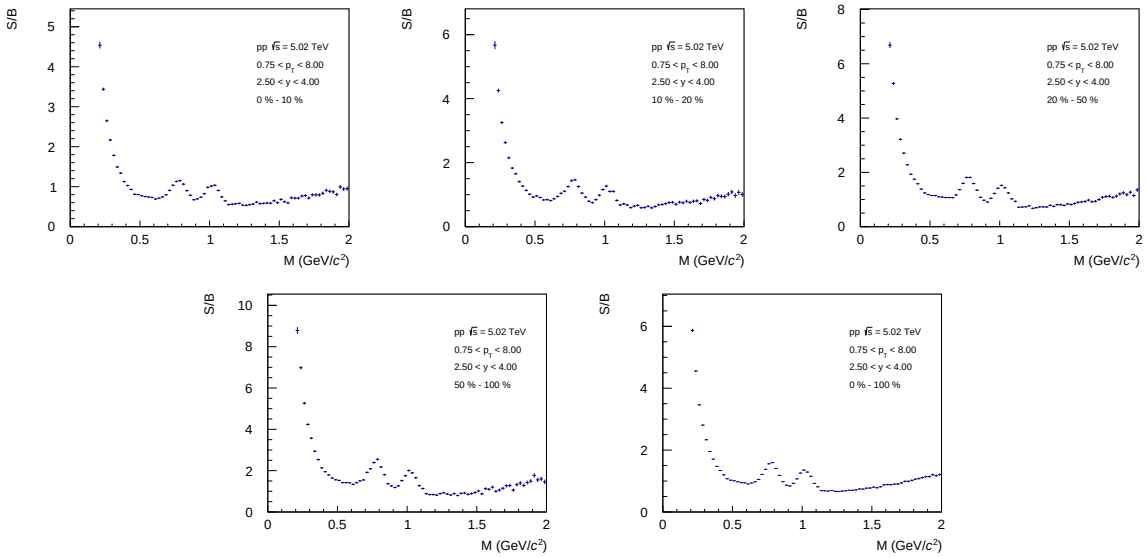

Figure 5.18: Correlated over Uncorrelated (S/B) as a function of invariant mass in pp collisions at $\sqrt{s} = 5.02$ TeV for all the multiplicity intervals studied for $0.75 < p_{\mathrm{T}} < 8$ GeV/c and $2.5 < y < 4$

The main contributors to the systematic uncertainty come from the choice of the empirical function, then comes the choice of the fitting interval and then the variation in the value of the parameter $\sigma_\rho/\sigma_\omega$ fixed in the fit. This uncertainty does not exceed 10%.

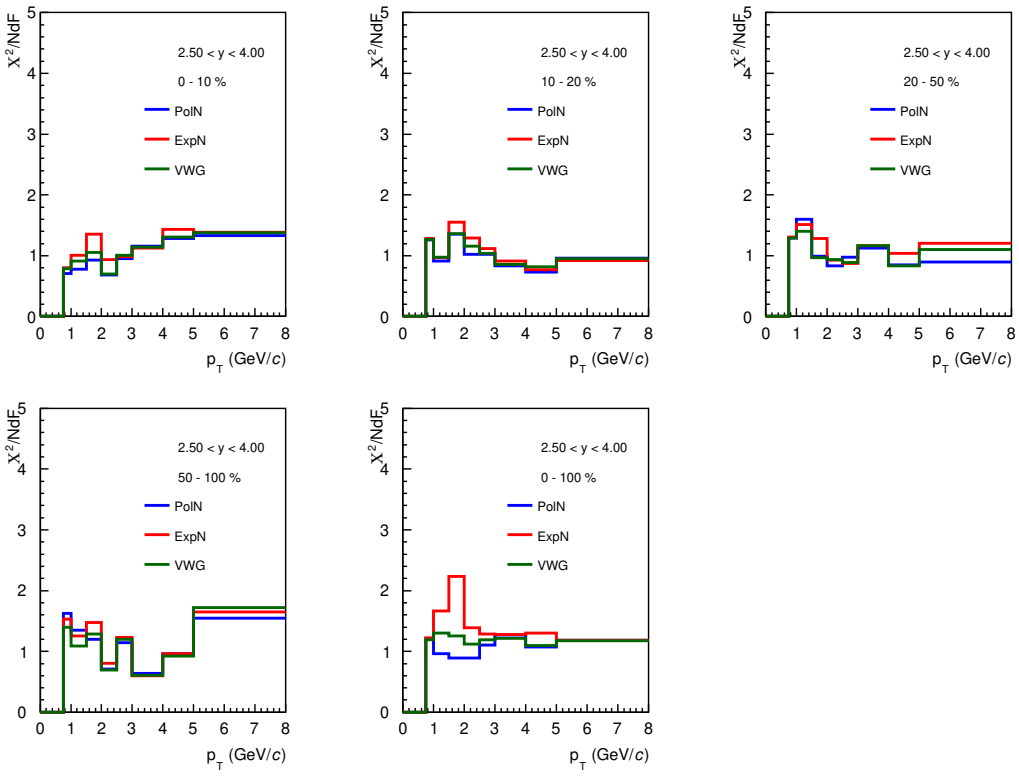

Figure 5.19: Reduced-χ^2 for the three different empirical function in all the different multiplicity intervals

The systematic uncertainty coming from the trigger efficiency is assumed to be multiplicity independent. Results are shown in figure 5.25. For $p_{\mathrm{T}} > 2.5$ GeV/c the systematic uncertainty is taken as a constant, as the effect becomes negligible with the increase of p_{T}. This assumption allows to get rid of the fluctuations arising from the MC sample.

The total systematic uncertainty has been obtained summing in quadrature the different contributions. These values are summarised in table 5.8.

5.3.3 ω and ϕ corrected yield

5.3.3.1 Corrected yield

To obtain the corrected number of ω and ϕ per inelastic events in specific *imult*-multiplicity bin, the following equation is used:

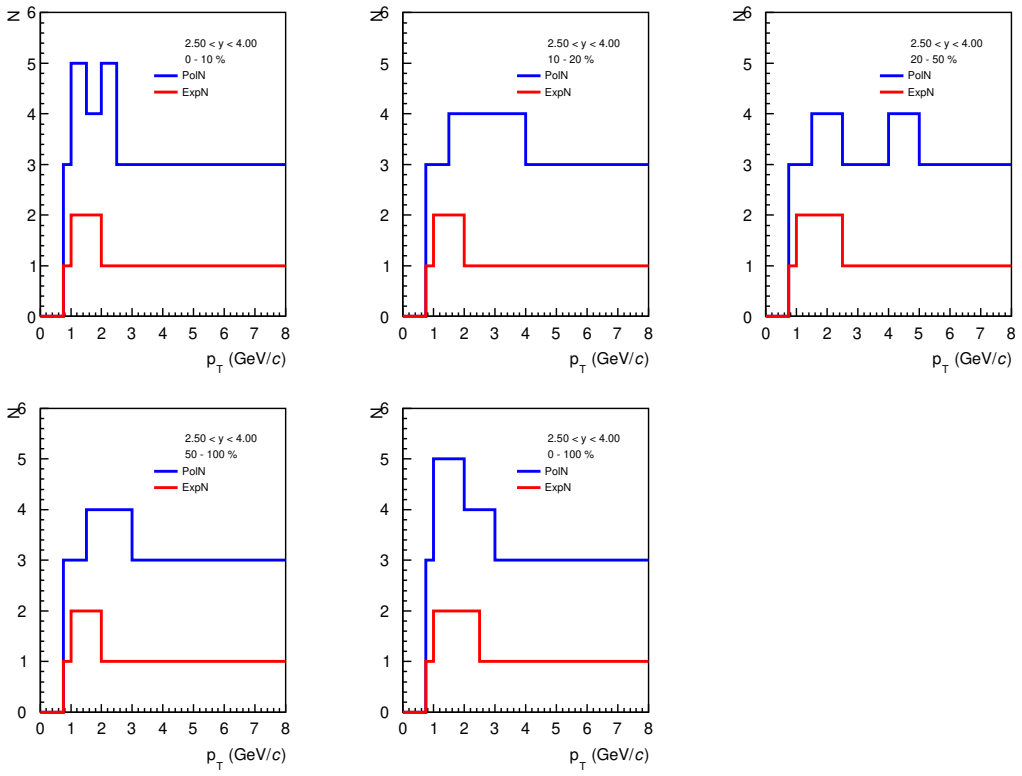

Figure 5.20: Order of the polynomial and number of exponentials (single or double) used as empirical functions for the continuum description, obtained from the F-test in the multiplicity intervals considered in this analysis

$$\frac{1}{N^{imult}_{INEL>0}} \frac{d^2 N^{imult}_{\omega/\phi}}{dy dp_T} = \frac{F^{imult}_{Norm} \cdot \epsilon_{evt}}{N_{INEL>0}} \frac{N^{\rm raw}_{\omega/\phi}(\Delta p_T, \Delta y)}{A \cdot \epsilon(\Delta p_T, \Delta y) \Delta p_T \Delta y B R_{\omega/\phi \to e^+e^-}} \,. \tag{5.13}$$

In this equation $N^{raw}_{\omega/\phi}(\Delta p_T, \Delta y)$ is the raw number of ω (or ϕ) for a given p_T bin in the rapidity range Δy defined as $2.5 < y < 4$, $A \cdot \epsilon(\Delta p_T, \Delta y)$ is the corresponding acceptance $\times$ efficiency obtained as in the *multiplicity integrated analysis* it is considered to not change with multiplicity.

The different results as a function of $p_{\rm T}$ in the different multiplicity intervals are shown in figure 5.26 for the ω and in figure 5.27 for the ϕ. All the distributions are fitted using a Lévy-Tsallis function representing the distributions over the full $p_{\rm T}$-range for both particles.

Multiplicity-dependent $p_{\rm T}$-spectra are compared to the multiplicity-integrated one in figure 5.28. The ratio, plotted in the bottom panel, shows a hardening of the $p_{\rm T}$-spectra with

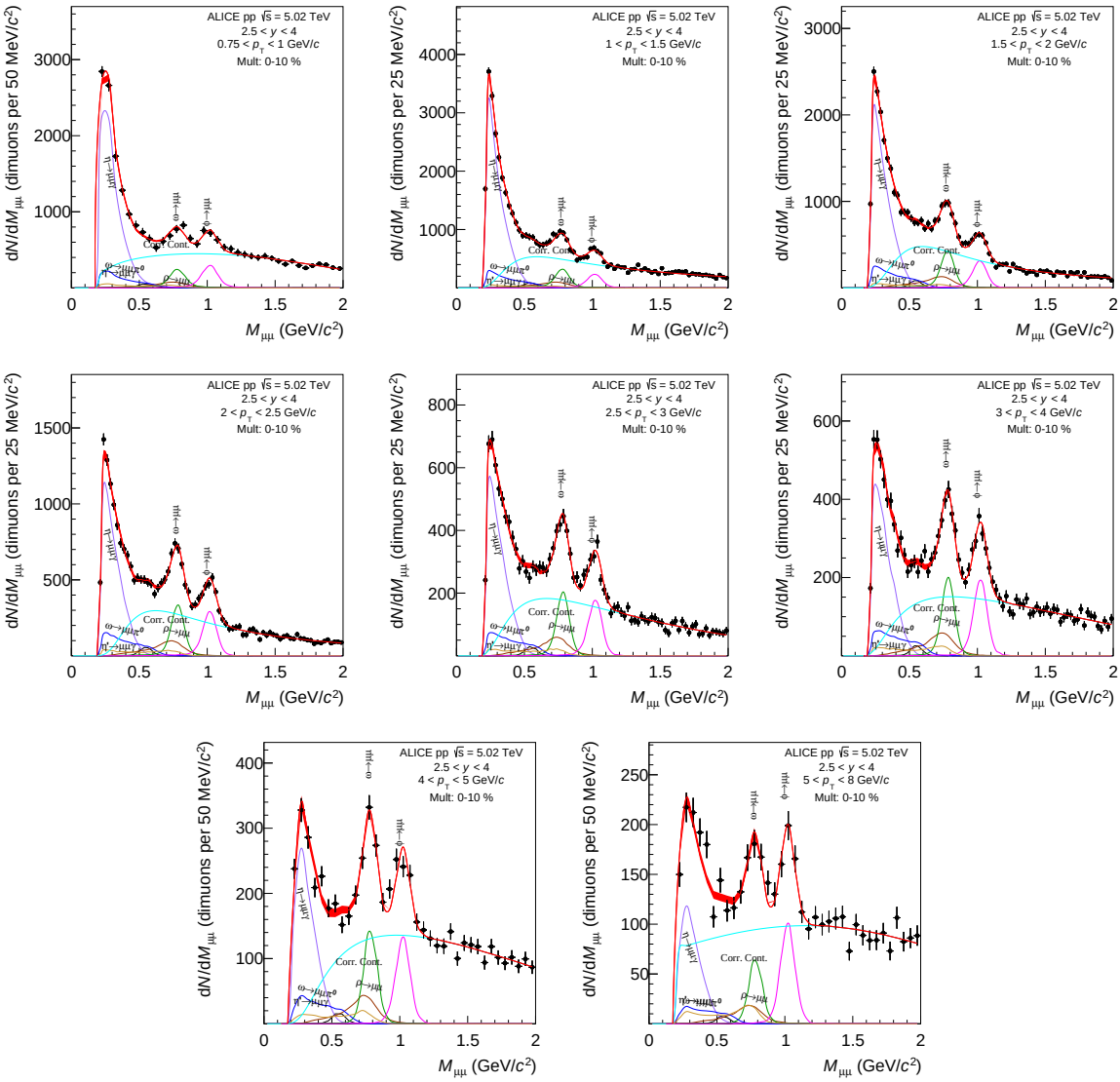

Figure 5.21: Dimuon invariant mass spectrum in pp collisions at $\sqrt{s} = 5.02$ TeV for the 0-10 % multiplicity interval; in these spectra a VWG was used to describe the continuum

increasing multiplicity. This effect is observed for both ω and ϕ.

When taking the ratio of the p_{T}-spectra it has to be noted that most of the contributions to the systematic uncertainties cancel out. This is the case for the contribution due to the detector description. Therefore in the ratio as a function of p_{T}, the systematic uncertainty considered are the ones coming from F_{Norm}^{imult}, ϵ_{evt}^{inorm}, and $N_{\omega/\phi}^{raw}$.

The corrected spectra are fitted using a Lévy-Tsallis giving the possibility to extrapolate the signal down to 0 p_{T} and to extract the $\langle\, p_{\mathrm{T}} \,\rangle$ value in this range. The $\langle\, p_{\mathrm{T}} \,\rangle$ of the ω meson is

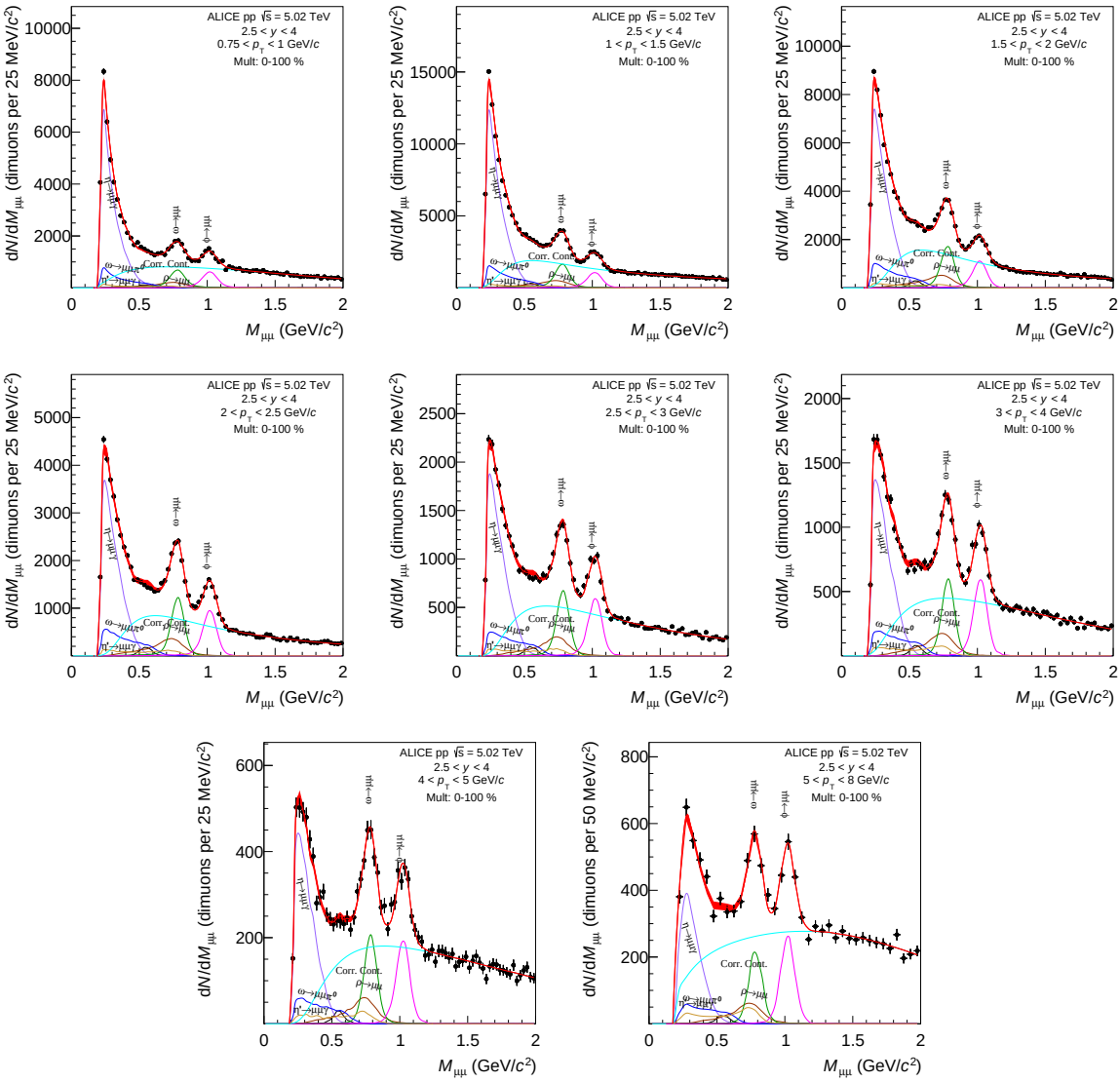

Figure 5.22: Dimuon invariant mass spectrum in pp collisions at $\sqrt{s} = 5.02$ TeV for the 0-100 % multiplicity (integrated) interval; in these spectra a VWG was used to describe the continuum

then computed as a function of multiplicity and showed in figure 5.29. An increase of $\langle\, p_{\mathrm{T}} \,\rangle$ as a function of multiplicity is observed, which is expected from the previous observation of the hardening of the p_{T}-spectra in the bottom panel of figure 5.28(a). The comparison to models show that both EPOS and PYTHIA8 predict the increase of p_{T} but both underestimate the observed value by $\sim 20\%$.

The $\langle\, p_{\mathrm{T}} \,\rangle$ distribution as a function of multiplicity of the ϕ meson is showed in figure 5.30. An increase of $\langle\, p_{\mathrm{T}} \,\rangle$ as a function of multiplicity is observed, also expected from the previous

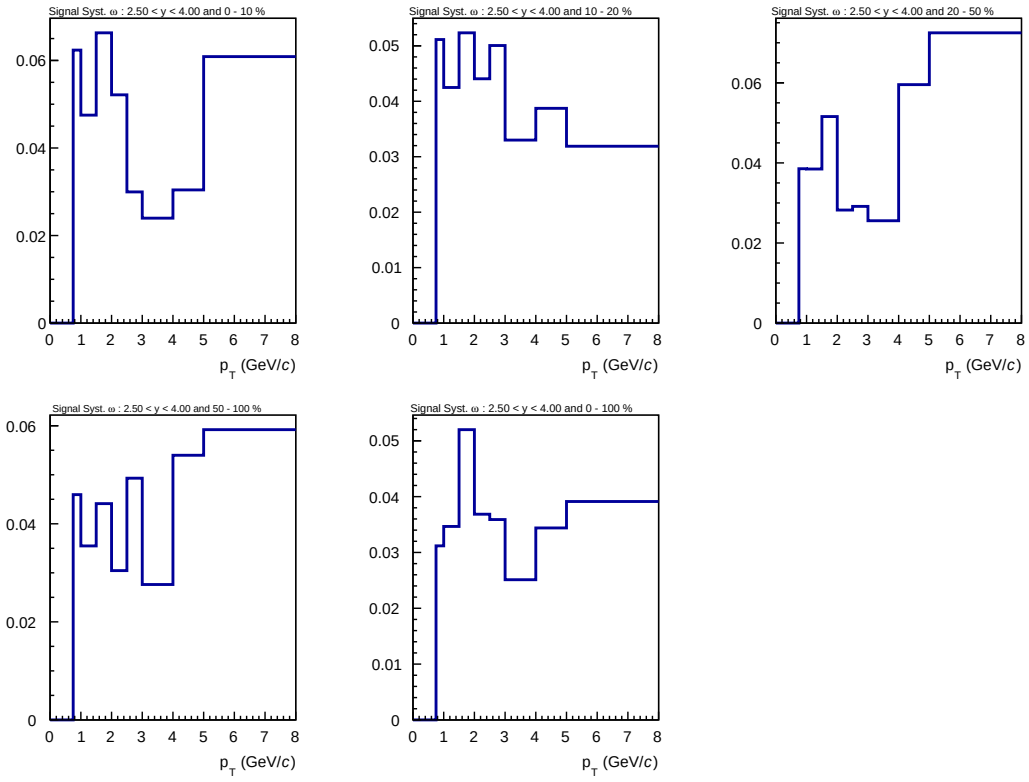

Figure 5.23: Relative systematic uncertainty on N_{ω}^{raw} in all multiplicity intervals

Source	Relative systematic uncertainty	
	ω	ϕ
Uncorrelated systematic		
N^{raw}	2-10%	2-10%
Tracking efficiency	2.0%	2.0%
Trigger efficiency	2-5%	1-10%
Matching efficiency	1.0%	1.0%
Event Correction	1.0%	1.0%
Correlated systematic		
BR($X \rightarrow e^+e^-$)	2.0%	1.0%
L_{INT}	2.1%	2.1%

Table 5.8: Systematic uncertainties on the extraction of ω and ϕ for $2.5 < y < 4$

observation of the hardening of the p_{T}-spectra in the bottom panel of figure 5.28(b). Comparison to models show that PYTHIA8 predicts the increase of p_{T} but underestimates the observed

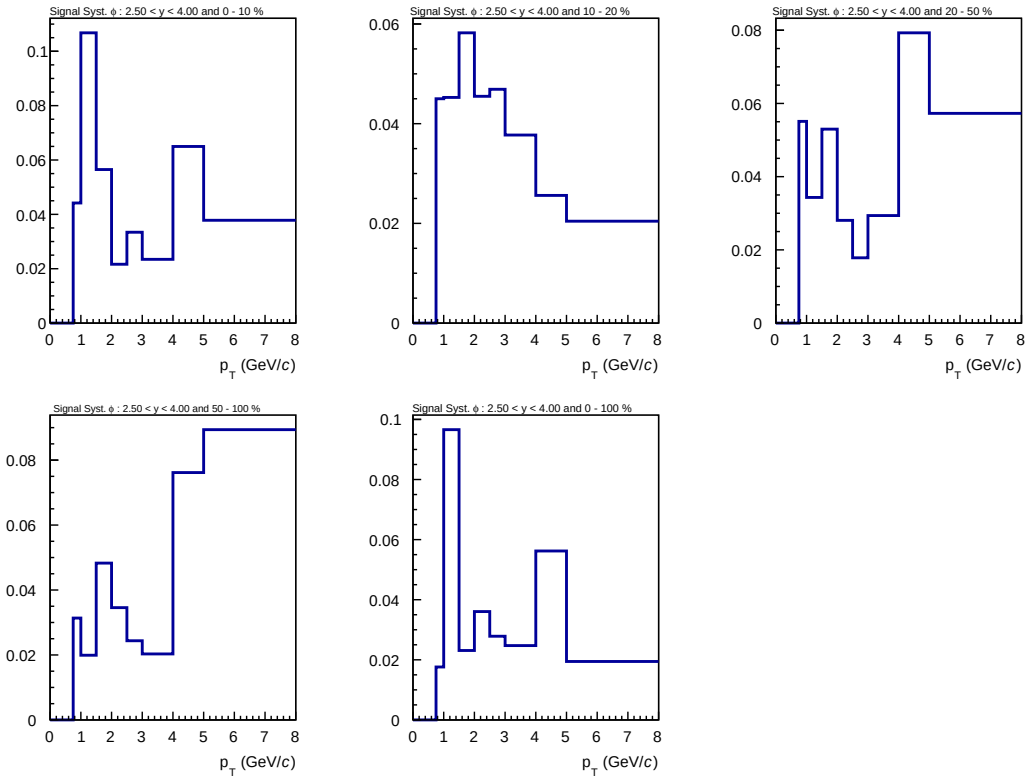

Figure 5.24: Relative systematic uncertainty on N_{ϕ}^{raw} in all multiplicity intervals

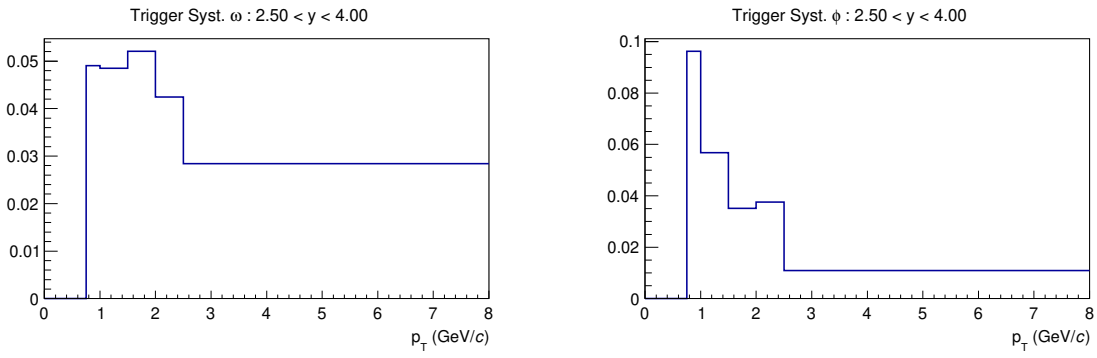

(a) Systematic uncertainty on the trigger response for ω (b) Systematic uncertainty on the trigger response for ϕ

Figure 5.25

value by $\simeq 15\%$. Instead, the EPOS model reproduces the evolution as a function of multiplicity. The model succeeds to describe the values obtained at high multiplicity, but underestimates it in the two lowest measured points.

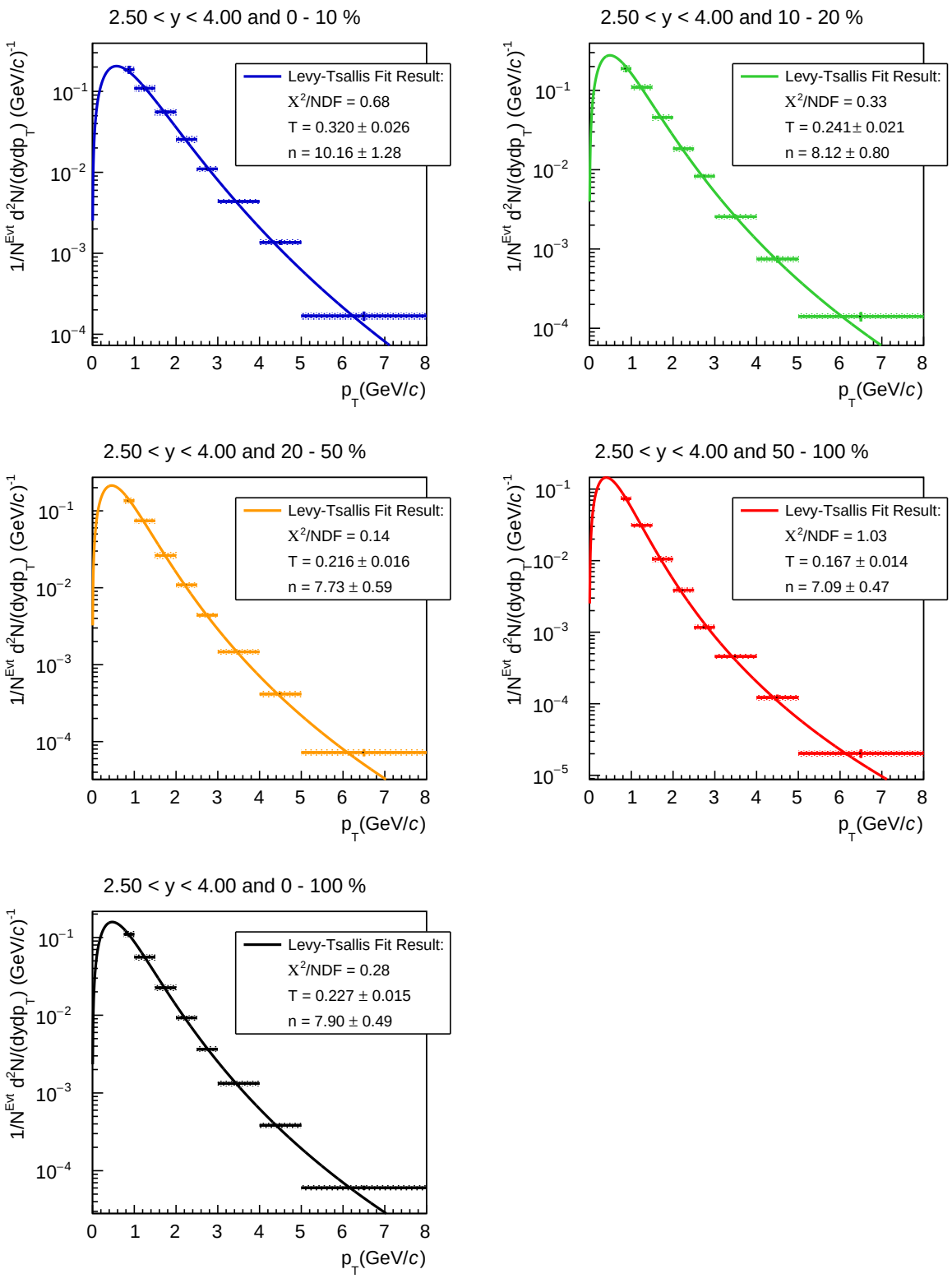

Figure 5.26: Corrected Yield of the ω in the different multiplicity intervals fitted by a Levy-Tsallis

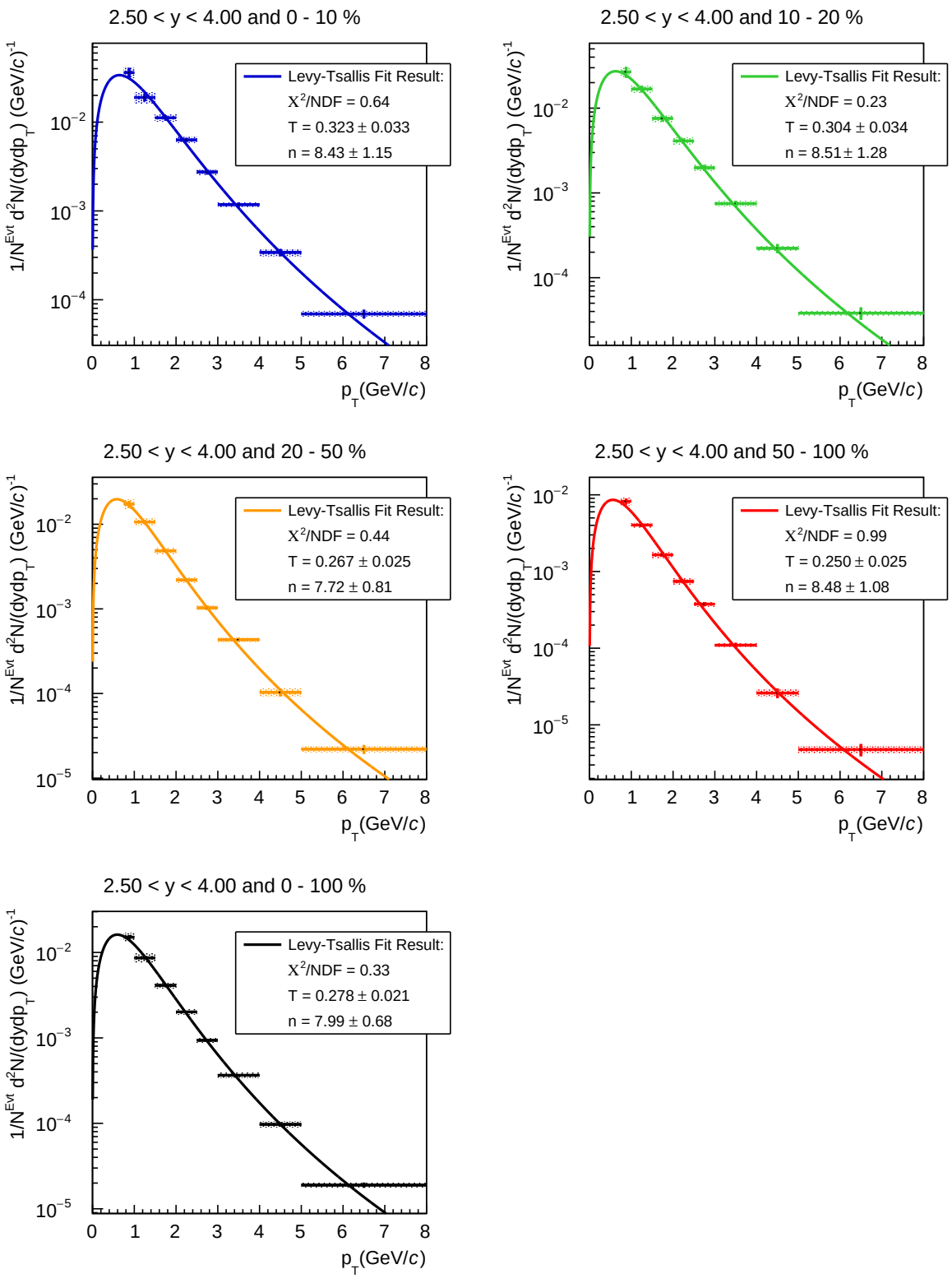

Figure 5.27: Corrected Yield of the ϕ in the different multiplicity intervals fitted by a Levy-Tsallis

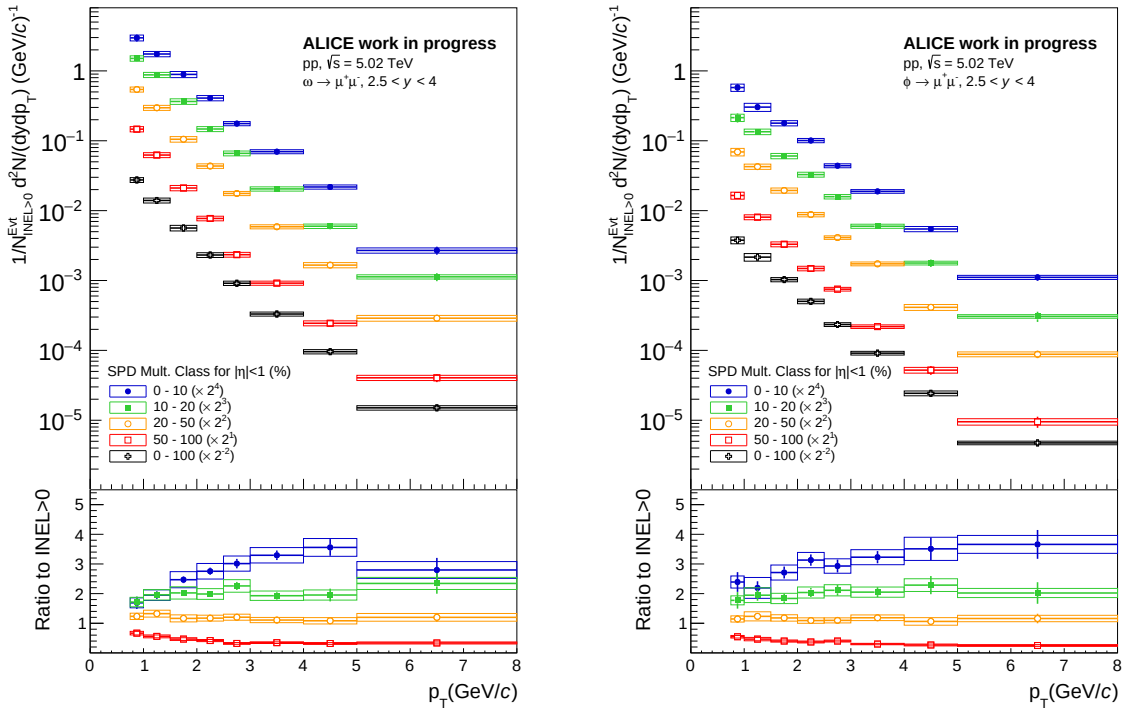

(a) Corrected Yield of the ω in the different multiplicity intervals ratio to all INEL>0 events, the boxes represent the systematic uncertainty and the crosses the statistical uncertainties

(b) Corrected Yield of the ϕ in the different multiplicity intervals ratio to all INEL>0 events , the boxes represent the systematic uncertainty and the crosses the statistical uncertainties

Figure 5.28

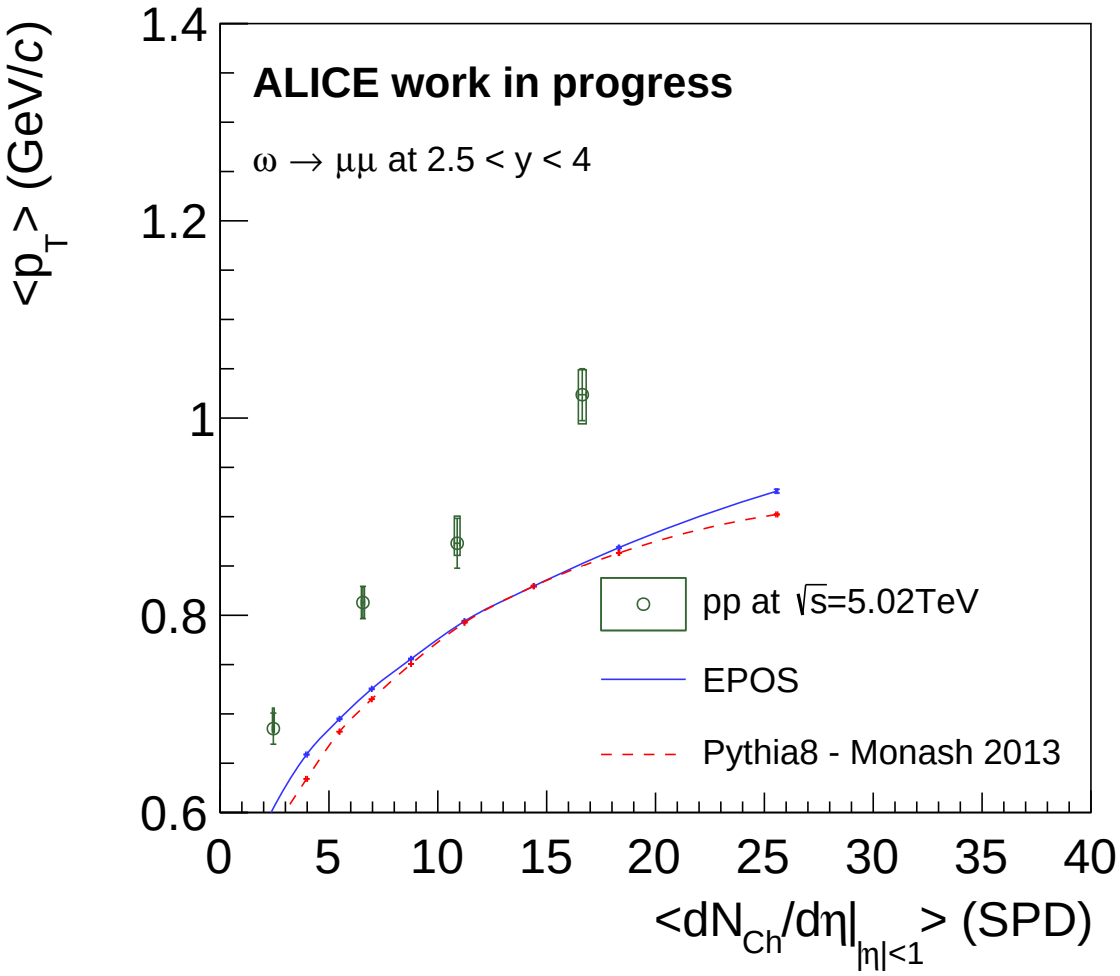

Figure 5.29: $\langle\, p_{\mathrm{T}} \,\rangle$ of the ω meson as a function of multiplicity estimated for $0 < \ p_{\mathrm{T}} \ < 8$ GeV/c and comparison to models

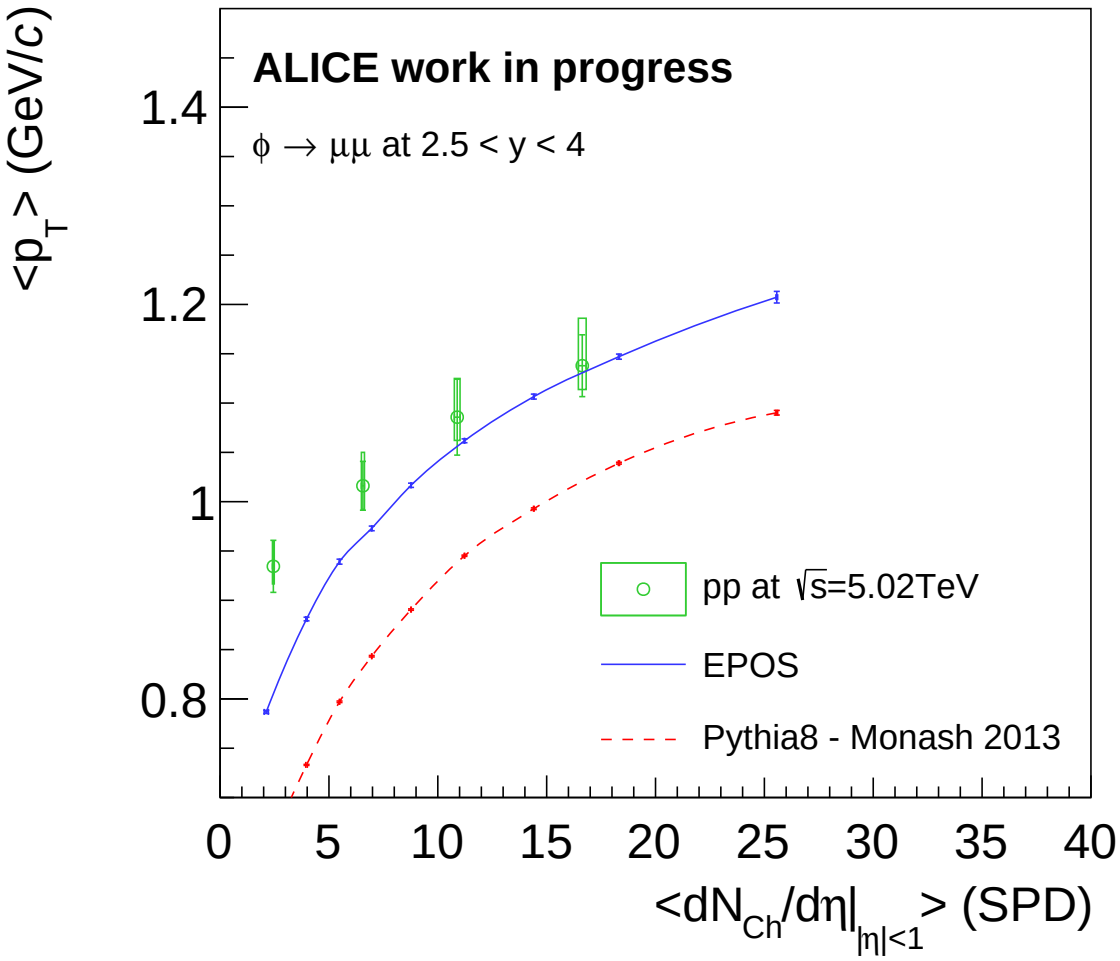

Figure 5.30: $\langle\, p_{\mathrm{T}} \,\rangle$ of the ϕ meson as a function of multiplicity estimated for $0 < \ p_{\mathrm{T}} \ < 8$ GeV/c and comparison to models

5.3.4 Self-normalised yield

To observe if the increase of the ω and ϕ yields is scaling with the multiplicity, their relative self-normalised yields are studied. The self-normalised yield in a given multiplicity bin $imult$ is taken as

$$\frac{N^{imult}_{INEL>0}/dydp_T}{N_{INEL>0}/dydp_T} \,. \tag{5.14}$$

Results are shown in figure 5.31 for the ω and in figure 5.32 for the ϕ. The study is then performed in the 8 different $p_{\rm T}$-intervals and a linear line representing the exact scaling of particle yield with multiplicity is drawn to guide the eye. Both results obtained for the ω and the ϕ are compared to the expectations from two models, namely PYTHIA8 (Monash2013 tune) [72] and EPOS-LHC [95].

For the ω meson, a deviation from the scaling with multiplicity is observed at low-$p_{\rm T}$. Indeed, in the two lowest $p_{\rm T}$ intervals, when increasing the multiplicity the ω yield scales slower than multiplicity. Even if both models used for comparison are also predicting such a behavior, none of them successfully reproduces the trend at low-$p_{\rm T}$. Looking at intermediate $p_{\rm T}$ intervals, the production of the meson scales with multiplicity, while in two of three highest $p_{\rm T}$-intervals ($3 < \ p_{\rm T} \ < 4$ and $4 < \ p_{\rm T} \ < 5$ GeV/c) the production tends to scale faster than multiplicity. The PYTHIA8 model overestimates the ω production in the highest multiplicity interval, but gives a fair description below. The EPOS model gives a better description for intermediate and high-$p_{\rm T}$ ranges over the whole multiplicity range which could be interpreted as an effect of collective radial expansion. This confirms the first observations made at mid-rapidity and extended the basis to understand this phenomenon also at forward rapidity.

The normalised yield of the ϕ meson is presented in figure 5.32. No strong deviation from a multiplicity scaling of the ϕ meson production is found considering the resolution of the measurement. The EPOS model reproduces the self-normalisation of the ϕ over the full $p_{\rm T}$ range considered. PYTHIA8 agrees with the measurement at low and high-$p_{\rm T}$ in the full multiplicity coverage. However, there is a hint for an overestimation of the ϕ yield in the highest multiplicity interval for $1.5 < \ p_{\rm T} \ < 4$ GeV/c by more than one standard deviation (considering both the systematical and statistical uncertainties).

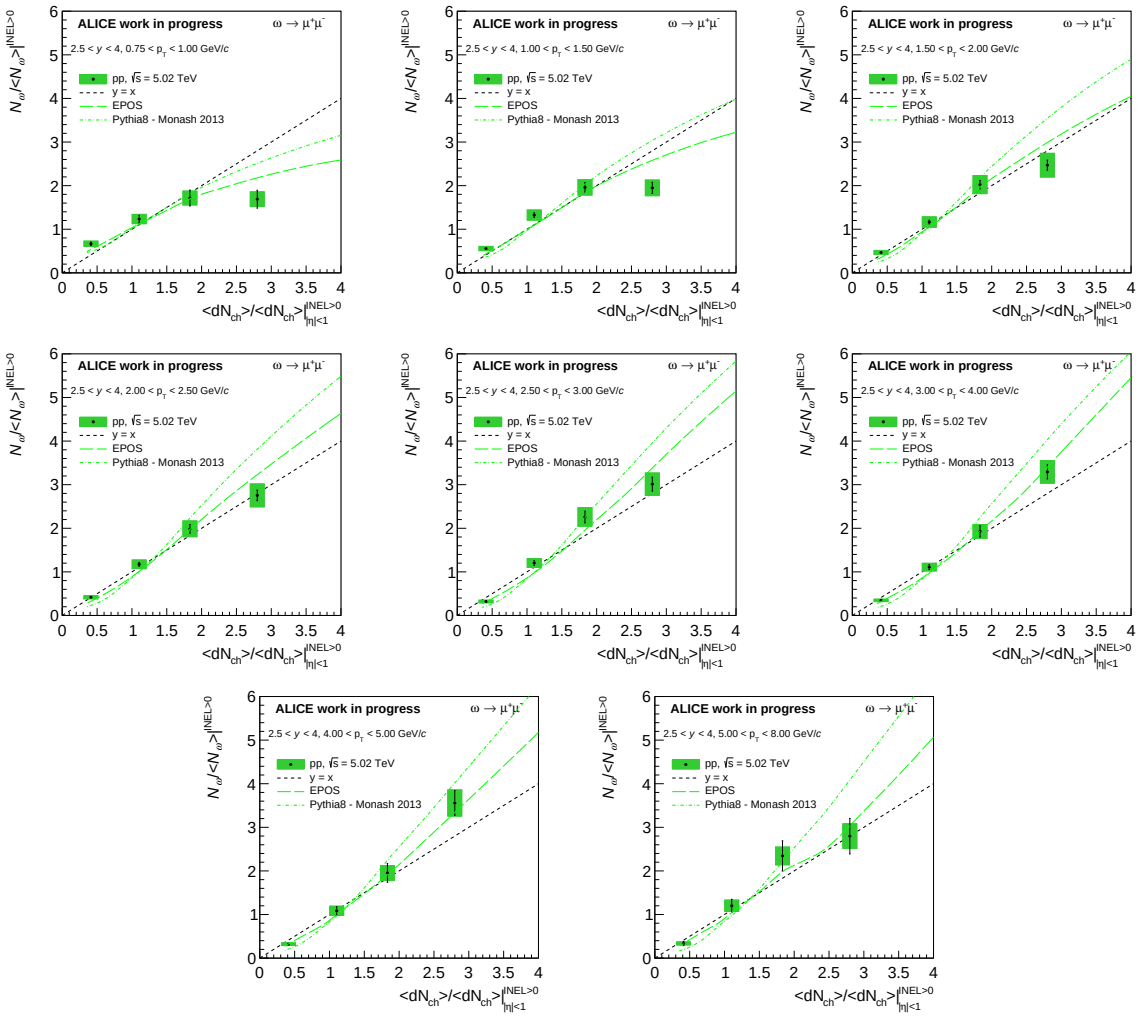

Figure 5.31: Self-normalised yield of the ω meson in various p_{T} intervals

5.3.5 ϕ to ω ratio

As discussed in the previous parts, the strangeness enhancement can be studied at forward rapidity in ALICE comparing the production of the ϕ (with hidden strangeness content) to the ω (light-flavour content). Thus, the yield of both mesons is extracted in the various multiplicity intervals and then compared. As the extraction of the signal was performed in the $0.75 < \ p_{\mathrm{T}} \ < 8$ GeV/c range, an extrapolation using a Lévy-Tsallis is used to obtain the estimated value for $0 < p_{\mathrm{T}} < 0.75$ GeV/c. The extrapolation account for 25 to 35% of the total signal in the $0 < \ p_{\mathrm{T}} \ < 8$ GeV/c interval.

First the ω production in INEL>0 is extracted in the $0 < p_{\mathrm{T}} < 8$ GeV/c interval at forward

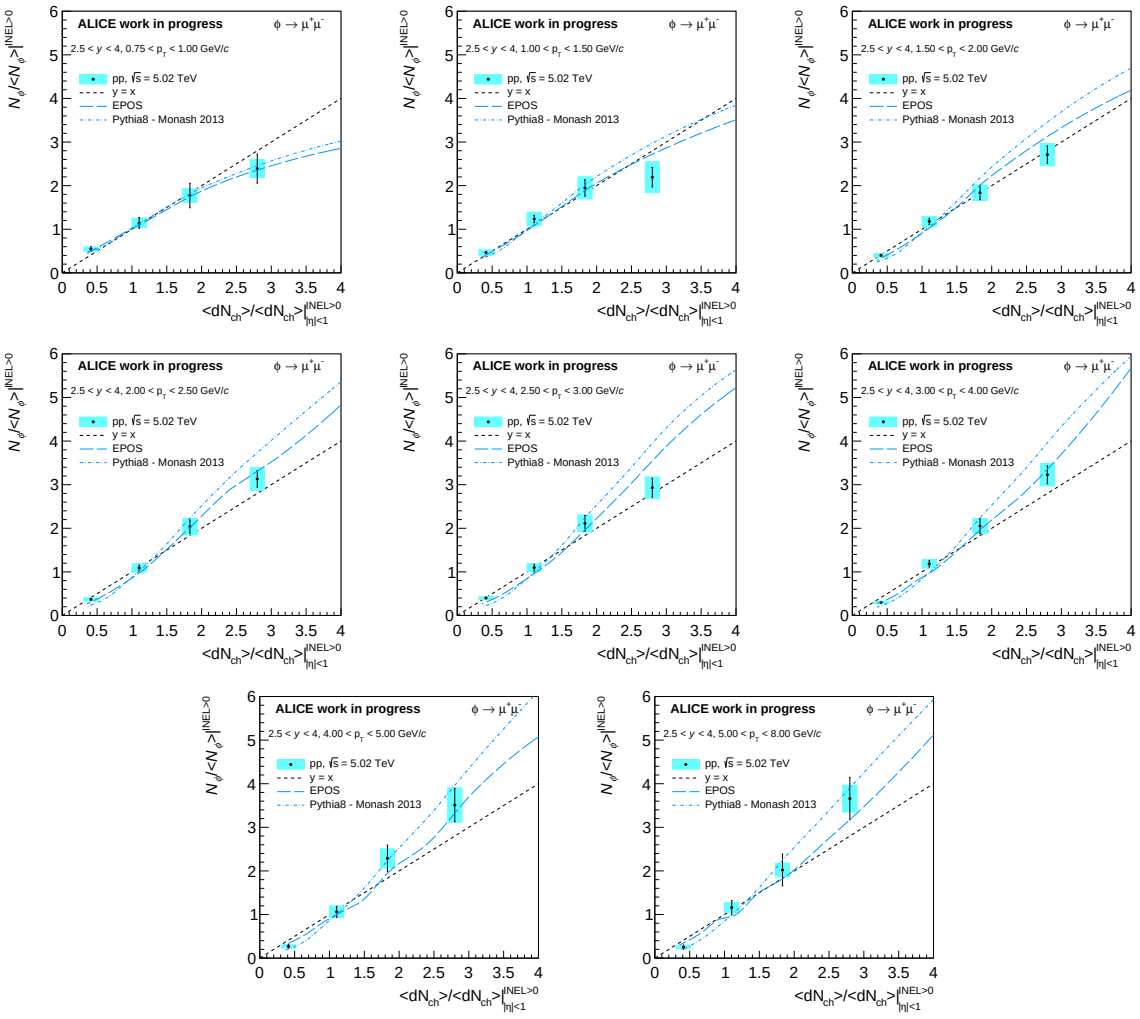

Figure 5.32: Self-normalised yield of the ω meson in various p_{T} intervals

rapidity. Figure 5.33 shows the results obtained in the four different multiplicity intervals and comparison to the EPOS and PYTHIA8 models. An enhancement of the ω production is observed as a function of multiplicity, both in data and models. Even if both models reproduce an enhancement, they overestimate the ω production by at least a factor 2 at low multiplicity and a factor 3 and even 4.5 for the highest multiplicity interval considered for PYTHIA8.

The ϕ production in INEL>0 is extracted in the $0< p_{\mathrm{T}} <8$ GeV/c interval at forward rapidity. Figure 5.34 shows the results obtained and the comparison to the same models as for the ω. An increase of the ϕ production is observed as a function of multiplicity, both in data and models. Both models overestimate the ϕ production, but while EPOS overestimates it by a factor 2.5 at high multiplicity, PYTHIA8 overestimates it by a factor that does not exceed 25%.

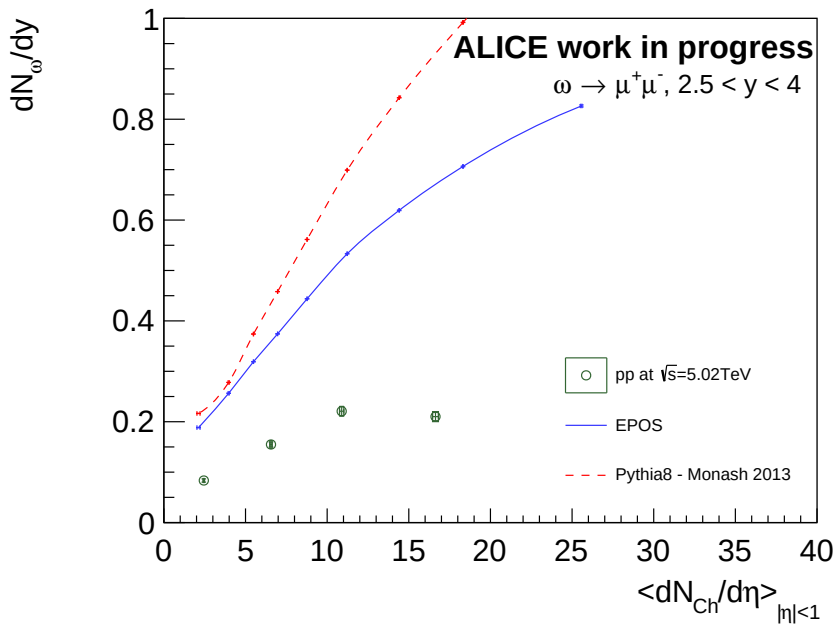

Figure 5.33: Measured ω-yield dN_ω/dy at forward rapidity as a function of multiplicity in INEL$>$0 events for 0$<$ p_{T} $<$8 GeV/c

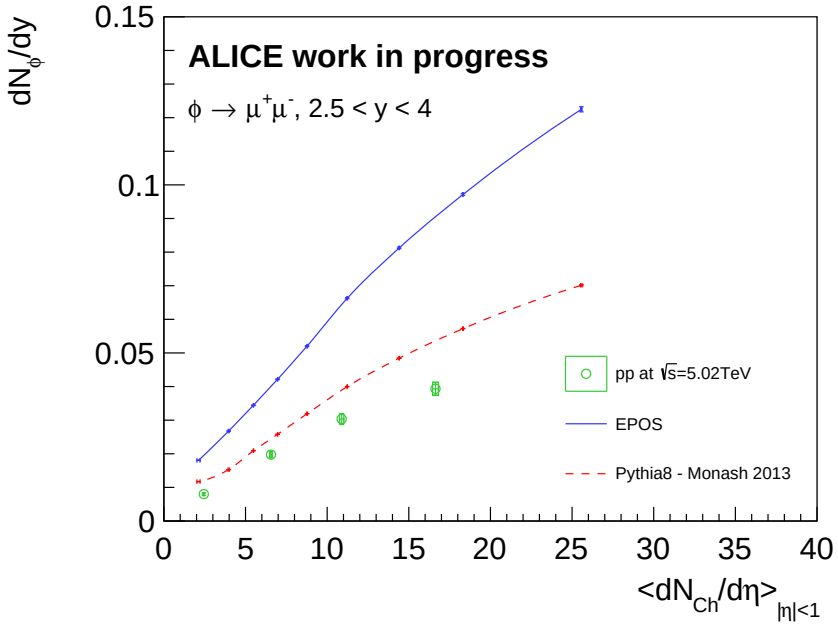

Figure 5.34: Measured ϕ-yield dN_ϕ/dy at forward rapidity as a function of multiplicity in INEL$>$0 events for 0$<$ p_{T} $<$8 GeV/c

The ϕ/ω ratio is calculated and presented in figure 5.35. An increase of this ratio is observed as a function of multiplicity. This increase is only predicted by the EPOS model, which underestimates the ratio by less than two standard deviations in the first three multiplicity intervals. Instead, the PYTHIA8 model does not predict an increase of the ϕ/ω ratio, and underestimates the values obtained over all the multiplicity range by a factor that ranges from 2 to 3, depending on the multiplicity.

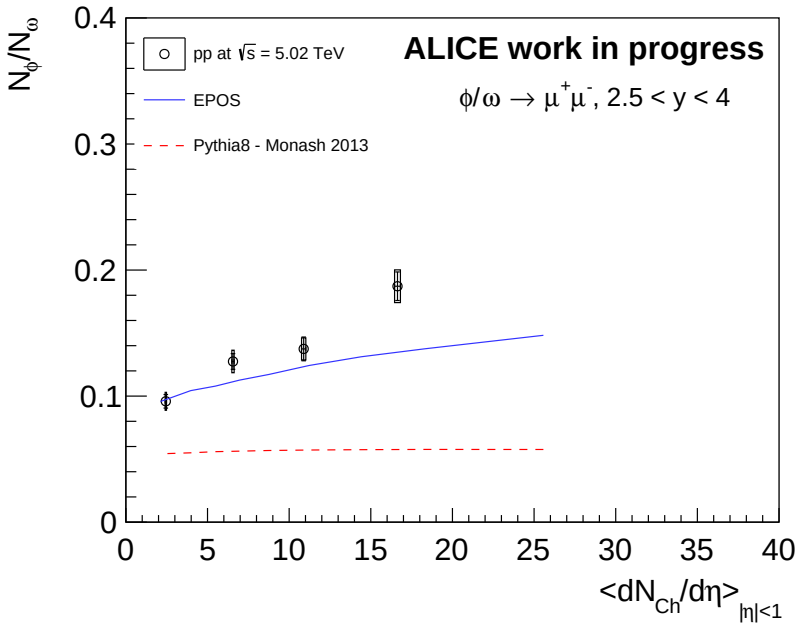

Figure 5.35: ϕ/ω ratio obtained in pp collisions at $\sqrt{s}$=5.02 TeV at forward rapidity for 0< p_{T} <8 GeV/c using the SPD-percentile multiplicity estimation

5.3.6 Comparison to other measurements

5.3.6.1 Comparison to results at 13 TeV

The extraction of the ω and the ϕ production has also been performed in pp collisions at $\sqrt{s}$ = 13 TeV at forward rapidity in an independent previous analysis. Following the same techniques for the signal extraction, the analysis of low-mass dimuons at 13 TeV was also performed to study the strangeness enhancement in small collision systems.

In this analysis, the multiplicity estimation was performed using the *SPD percentile* method,

just like in the 5.02 TeV analysis. The main feature of this multiplicity estimator is that it avoids the use of a correction factor which is period-dependent and which was found to lead to discrepancies at high multiplicity (at 13 TeV). Furthermore this method links directly the number of measured SPD-tracks to the number of true charged particles instead of using a smeared correction. As this analysis was performed on data taken over 14 different periods (recorded between 2016 and 2018), this technique of multiplicity estimation was preferred. The mean multiplicity in the multiplicity integrated window was estimated to be: $< dN_{Ch}/d\eta >^{INEL>0}_{|\eta|<1}$=7.0780$\pm$0.0004, so $\sim$ 20% higher than at 5.02 TeV.

Benefiting from a large data sample, the analysis was performed in eight multiplicity intervals (plus one for the multiplicity integrated window). The normalised ratio (as introduced in 5.14) of the ω obtained in pp collisions at $\sqrt{s}$ = 13 TeV is shown in figure 5.36. In this study, results were compared to the PYTHIA8 model with the Monash2013 tune, considering either the possibility of hadron scattering or color rope with a parametrisation based on previous LHC results (more details in App. E). At low p_{T} the ω production is found to scale slower than multiplicity just like at 5.02 TeV. At this energy, the different tunes of PYTHIA8 (produced at $\sqrt{s}$ = 13 TeV) both predict a scaling slower than multiplicity in the 0.5 $< p_{\mathrm{T}} <$ 1 GeV/c interval. Nevertheless, both models fail to reproduce data in the highest multiplicity intervals. At intermediate transverse momentum, the production shows to scale *slightly* faster than multiplicity. This behaviour is predicted in both models, but they all overestimate the increase with respect to multiplicity. In the highest p_{T} interval, the ω production shows to scale faster than multiplicity. Also the models reproduce the trend, but only the tune considering hadron scattering successfully reproduces the data over the full multiplicity range.

The ϕ self-normalised yield is presented in figure 5.37 as a function of self-normalised multiplicity. At low-p_{T}, the ϕ scales slower than multiplicity just like the ω meson. In this p_{T} range, the color rope tune of the PYTHIA8 model predicts a linear scaling of the ϕ production with multiplicity, while the hadron scattering implementation reproduces data in the 0.5 $< p_{\mathrm{T}} <$ 1 GeV/c interval. For 2.5 $< p_{\mathrm{T}} <$ 3 GeV/c, the self-normalized yield scales faster than multiplicity. Both models predict this behaviour. The color rope setup on, reproduces the data in the lowest multiplicity intervals but fails to reproduce it in the highest. However, the hadron scattering tune gives a fair description of the data. In the highest p_{T}-interval, the ϕ

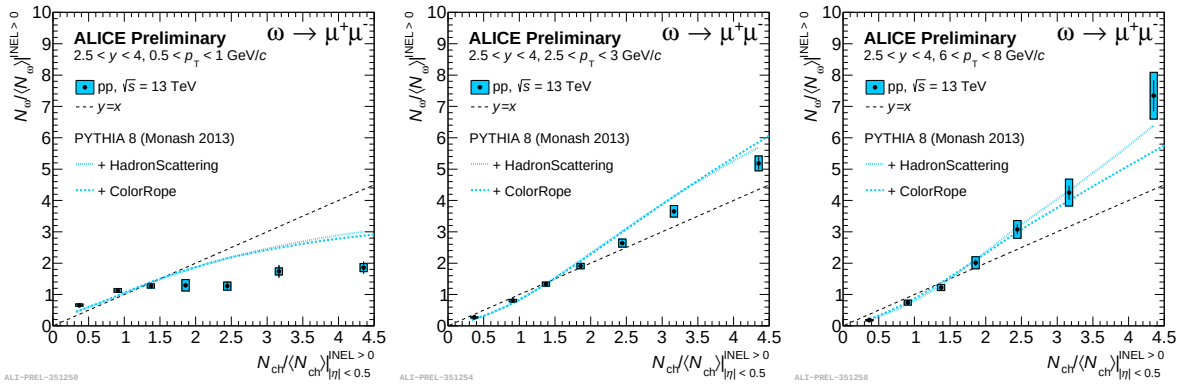

Figure 5.36: Self-normalised yield of the ω meson as a function of relative multiplicity at low (**left**), intermediate (**middle**) and high-p_{T} (**right**), in pp collisions at $\sqrt{s}$ =13 TeV

production scales faster than multiplicity. Both tunes of PYTHIA8 show similar predictions and give a reasonable description of the data.

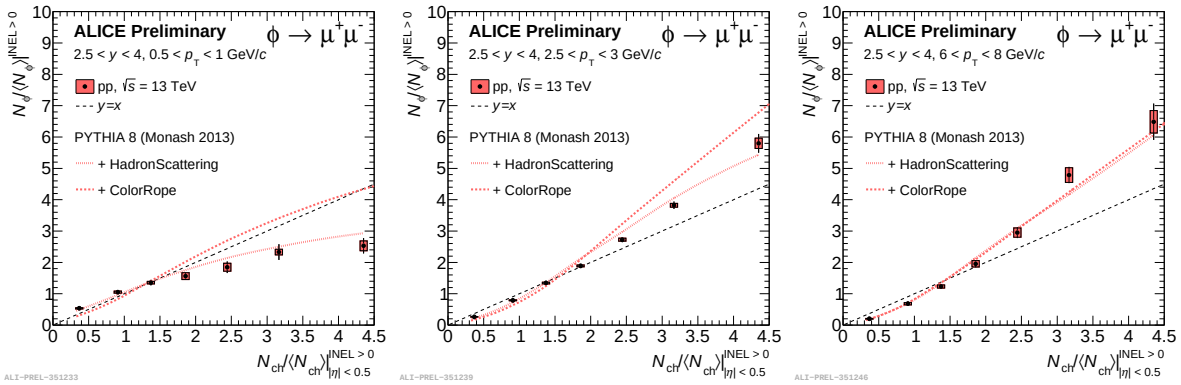

Figure 5.37: Self-normalised yield of the ϕ meson as a function of relative multiplicity at low (**left**), intermediate (**middle**) and high-p_{T} (**right**), in pp collisions at $\sqrt{s}$ =13 TeV

The ϕ/ω ratios versus multiplicity at $\sqrt{s}$ = 5.02 and 13 TeV are compared in figure 5.38. The results from the models studied at $\sqrt{s}$ = 5.02 TeV are also plotted. The extraction of the ω and ϕ mesons at 13 TeV was performed in the 0.5 $<$ p_{T} $<$ 8 GeV/c interval, and their yield was extrapolated down to 0-p_{T} using Lévy-Tsallis functions. Here, the extrapolated interval corresponds to 15 to 25% of the signal. The ϕ/ω ratio at 13 TeV shows to be compatible with the results obtained at 5.02 TeV. Thus, the ϕ/ω ratio shows to be independent of the centre-of-mass energy of the collision, but to depend on the event multiplicity. Being consistent with the previously presented results in section 5.3.5, the comparison to models remains unchanged.

The EPOS model predicts an increase of strangeness production, but underestimates the ratio in the different multiplicity intervals.

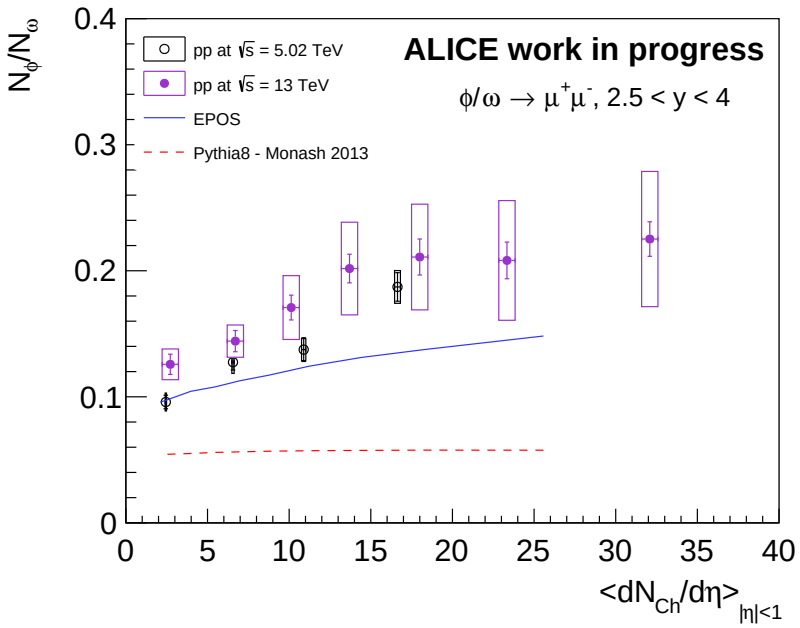

Figure 5.38: ϕ/ω ratio obtained in pp collisions at $\sqrt{s}$=5.02 and 13 TeV at forward rapidity for 0< p_{T} <8 GeV/c using the SPD-percentile multiplicity estimation

5.3.6.2 Comparison to results at mid-rapidity

The extraction of the ϕ meson has been performed at $\sqrt{s}$ = 5.02 TeV at midrapidity ($|\eta| < 0.5$) via its K^+K^- decay channel by ALICE. As the signal is measured at midrapidity, the multiplicity estimator is taken in another rapidity interval, namely using the multiplicity recorded by the V0M.

The V0M multiplicity estimator is based on the sum of the signal received both in the V0A and the V0C detectors (described in 2.3.2). As the signal detected in the V0M is not the same as in the SPD, the multiplicity estimation was performed using a different classification (see details in [96]) of the events than the one for the studies at forward rapidity. In this case, the events are required to be Minimum Bias triggered.

As the event classification is not the same as in the analyses at forward rapidity, the extraction of the ϕ meson at forward rapidity was re-performed considering the V0M multiplicity

classification of events. Following the logic of the previous analysis as a function of multiplicity, the same selection was applied (except from requiring the MB trigger instead of the INEL>0 requirement). The ϕ yield was extracted in four different multiplicity intervals (plus the multiplicity integrated interval).

The mean-p_{T} was calculated in both analyses and results are shown in figure 5.39. As at forward rapidity, the extraction at mid-rapidity can not be performed down to 0 p_{T} and actually starts at 0.5 GeV/c. To obtain the $< p_{\mathrm{T}} >$ over the $0 < \ p_{\mathrm{T}} \ < 8$ GeV/c range, the extrapolation of the signal is performed using a Lévy-Tsallis. As shown in figure 5.39, an increase of $\langle\, p_{\mathrm{T}\phi} \,\rangle$ is observed both at forward and mid-rapidity. However the results obtained at mid-rapidity tend to show higher values of $\langle\, p_{\mathrm{T}\phi} \,\rangle$.

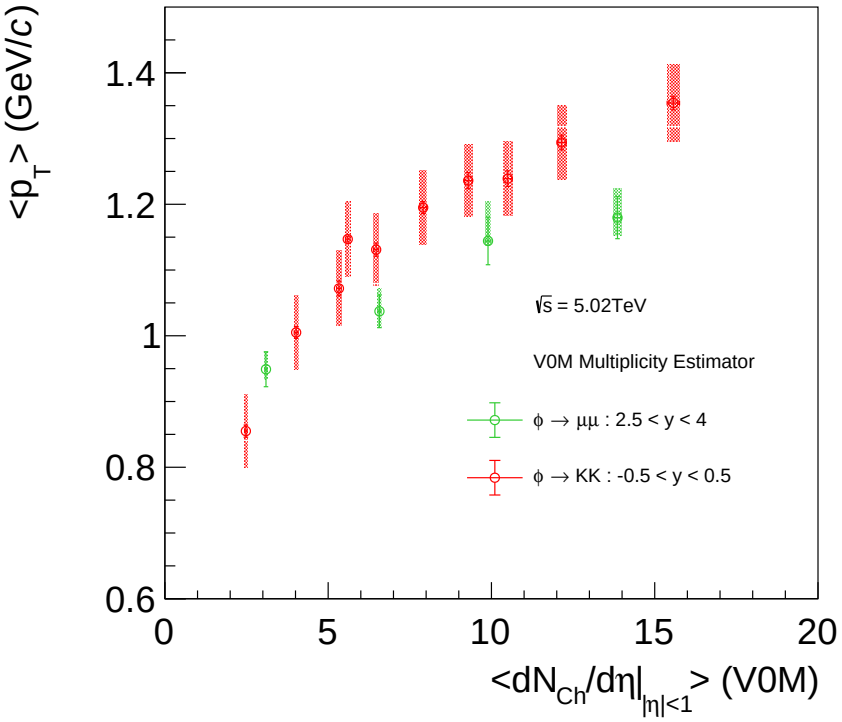

Figure 5.39: $< p_{\mathrm{T}} >$ of the ϕ meson obtained in pp collisions at $\sqrt{s} = 5.02$ TeV using the extrapolation of a Lévy-Tsallis to cover the $0< p_{\mathrm{T}} <8$ GeV/c interval

The total yield was also measured for $0< p_{\mathrm{T}\phi} <8$ GeV/c and is presented in figure 5.40. As for the measurement at forward rapidity, an increase of ϕ production is observed as a function of multiplicity. Nonetheless, the increase is more pronounced at mid-rapidity.

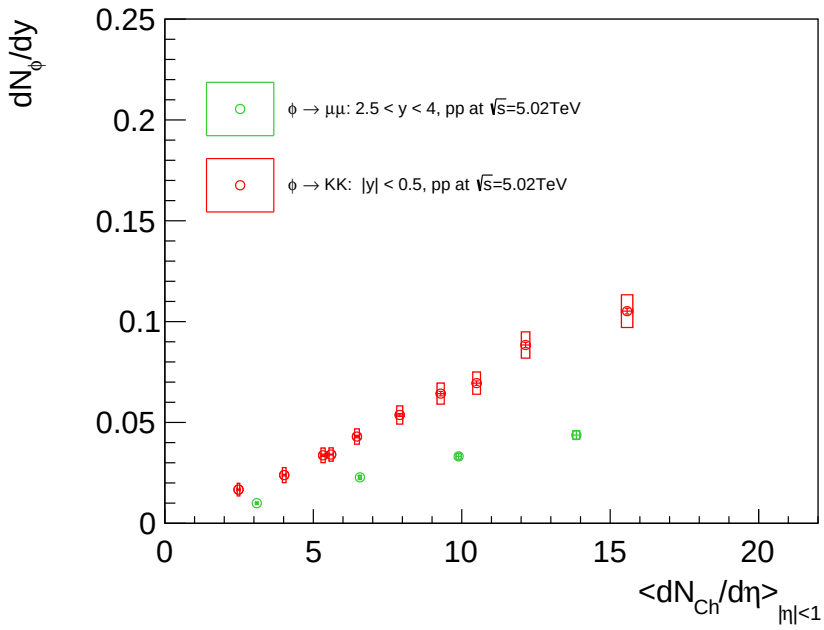

Figure 5.40: Total yield of the ϕ meson measured at forward and mid-rapidity as a function of multiplicity estimation obtained from the V0M

Conclusions

This work has presented the ω and ϕ production in ALICE at forward rapidity (2.5$<y<$4) in pp collisions at $\sqrt{s}$ =5.02 TeV in the dimuon channel. Over the accessible phase-space and using the integrated luminosity $L_{\rm INT} = 1222.6\ nb^{-1}$ provided by the LHC, the cross sections of the ω and ϕ mesons have been measured in $0.75 < p_{\rm T} < 8$ GeV/c and $2.5 < y < 4$:

$$\sigma_{\omega} = 6.185 \pm 0.198(\rm stat) \pm 0.138(\rm syst)\ \rm mb$$
$$\sigma_{\phi} = 1.053 \pm 0.047(\rm stat) \pm 0.024(\rm syst)\ \rm mb$$

The $p_{\rm T}$ spectra are well described by a Lévy-Tsallis function. The ϕ meson shows a harder $p_{\rm T}$ spectrum with respect to the one of the ω, which is expected due the heavier mass of the ϕ. A hardening of the $p_{\rm T}$-differential cross section with the collision energy is observed, as is evinced from the comparison between the average values of the transverse momentum or from the ratios between the differential cross sections as a function of $p_{\rm T}$. For each energy, the $p_{\rm T}$ spectra at midrapidity are harder than the corresponding ones at forward rapidity. Results were compared with the predictions from PYTHIA 8.1-Monash 2013, EPOS 3 and PHOJET. PHOJET reproduces the cross section at low $p_{\rm T}$, while EPOS 3 better approaches the data for $p_{\rm T} > 4$ GeV/c. PYTHIA 8.1 with the Monash 2013 tune properly describes the shape of the differential cross section at all energies and reproduces the results at $\sqrt{s} = 13$ TeV, but underestimates the measurement at lower energies. At $\sqrt{s} = 5.02$ and 13 TeV, a double differential study of the ϕ meson production cross section was performed as a function of $p_{\rm T}$ and rapidity. A small decrease of $\langle p_{\rm T} \rangle$ value was observed with increasing rapidity, although with relatively large uncertainties. Analogously, the cross section as a function of rapidity shows a slight narrowing going towards higher $p_{\rm T}$ values.

For the multiplicity estimation using the SPD, two different methods have been presented,

leading to consistent results. At $\sqrt{s} = 5.02$ TeV a hardening of the p_{T} spectrum was found both for the ϕ and ω mesons when going toward higher multiplicities. This hardening of the p_{T} spectrum can actually be qualitatively reproduced by models such as EPOS-LHC and PYTHIA8. Both models undershoot the $\langle\, p_{\mathrm{T}} \,\rangle$ value measured in the four multiplicity intervals studied for the ω mesons by $\simeq$ 15%. For the ϕ meson, PYTHIA8 underestimates the measured $\langle\, p_{\mathrm{T}} \,\rangle$ values. Instead, the EPOS model is successful in describing the values obtained in the two highest multiplicity intervals for the ϕ meson, but underestimates it in the two lowest measured points.

Looking at the self normalised yield of the ω meson, its production is found not to scale with multiplicity at low-p_{T} (for 0.75 $< p_{\mathrm{T}} <$ 1.5 GeV/c). For higher p_{T} values, the production of the meson scales with multiplicity. The PYTHIA8 and EPOS-LHC models predict a scaling slower than multiplicity at low-p_{T} but none of them successfully reproduce the trend observed in data. The PYTHIA8 model overestimates the ω production in the highest multiplicity interval, but gives a fair description for the three lowest intervals. The EPOS model reproduces the self-normalisation of the ω production in the intermediate and high-p_{T} ranges (for 1.5 $< p_{\mathrm{T}} <$ 8 GeV/c).

No strong deviation from a multiplicity scaling of the ϕ meson production is found considering the resolution of the measurement. The EPOS model reproduces the self-normalisation of the ϕ over the full p_{T} range considered. PYTHIA8 agrees with the measurement at low and high-p_{T} in the full multiplicity coverage. However, there is a hint for an overestimation of the ϕ yield in the highest multiplicity interval for 1.5 $< p_{\mathrm{T}} <$ 4 GeV/c by more than one standard deviation.

Considering the integrated yield of the ω and ϕ mesons for 0 $< p_{\mathrm{T}} <$ 8 GeV/c at forward rapidity, an increase of their production as a function of multiplicity is observed. In both cases the EPOS-LHC and PYTHIA8 models also predict such behavior but overestimate their magnitude.

When comparing directly the ϕ and the ω production, the observation of an increase of the ϕ with respect of the ω as a function of multiplicity is observed. This observation is also made considering collisions at $\sqrt{s} = 13$ TeV. The results at the two energies are consistent for the same values of event multiplicities. This confirms the previous measurements performed at

mid-rapidity on strangeness enhancement where this effect can be observed in small collision systems. Furthermore this shows that also at forward rapidity strangeness enhancement is not related to the centre-of-mass energy, but rather on the multiplicity of the event. PYTHIA8 does not predict strangeness enhancement in such collisions and thus returns a multiplicity independent ϕ/ω ratio underestimating the observed value. However, the EPOS-LHC model, which considers a core-corona initialisation, allows strangeness enhancement in pp collisions and predicts an enhancement of the ϕ/ω ratio. Nethertheless, the EPOS-LHC model underestimates the ratio over all the multiplicity range, but by less than two standard deviations.

Appendix A

Kinematic variables

In high energy physics, a set of variables are commonly to describe the processes. If not state explicitly, the natural units$c = \hbar = k_B$ =1 are used.

In general, any particle can be expressed in terms of its 4-momentum vector as

$$P = (E, \vec{p}) = (E, p_x, p_y, p_z) \tag{A.1}$$

where x, y and z denotes the coordinate system. In ALICE, the natural choice of defining the z-axis as the beam axis is made. Thus, the transverse momentum, transverse to the beam axis becomes $\vec{p_{\mathrm{T}}} = (p_x, p_y)$ taking the absolute value

$$p_{\mathrm{T}} = \sqrt{p_x^2 + p_y^2} \tag{A.2}$$

following this idea a pseudo-mass, the transverse-mass of a massive particle can be defined as $m_T = \sqrt{m^2 + p_{\mathrm{T}}^2}$.

The Lorentz transformation between two frames with relative velocity v along z (beam-axis in ALICE) leads to a change in the particle's 4-momentum such that $P = (E, p_{\mathrm{T}}, p_z) \rightarrow P' = (E', p'_{\mathrm{T}}, p'_z)$ where

$$\begin{aligned} E' &= \gamma(E - \beta p_z), \\ p'_z &= \gamma(p_z - \beta E), \\ \vec{p'_{\mathrm{T}}} &= \vec{p_{\mathrm{T}}} \end{aligned} \tag{A.3}$$

with $\beta = v/c$ and $\gamma = 1/\sqrt{1-\beta^2}$ the Lorentz factor. In this case of a longitudinal transformation along z, it can be noted that p_{T} is invariant (so is m_T). An other variable invariant in this type of transformation which can be defined for each particle is the rapidity y defined as

$$y = \frac{1}{2}\frac{E + p_z}{E - p_z} \tag{A.4}$$

this variable as the feature that for a Lorentz transformation $y \to y'$, such that in a system S and a system S moving along the z-axis with a relative velocity β_S and a particle with rapidity y' measured in S', its rapidity in S simply becomes $y = y' + y_S$.

In experiment the position of a particle in the detector is expressed in terms of its azimuthal angle φ (defined in the xy-plane in ALICE) and its polar angle θ (defined along z in ALICE) from which an other variable, its pseudo-rapidity η can be defined as

$$\eta = -ln\left(tan\left(\frac{\theta}{2}\right)\right) \tag{A.5}$$

Thus for particles with $\theta = \pi/2$ which would correspond to the central part of the ALICE detector, then $\eta = 0$. An interesting feature of this variable is that for massless particles $\eta = y$, which is also approximately true for $p \gg m$ (explaining this way the etymology of η).

In the collisions of two particles with $\vec{P_1} = (E_1, \vec{p_1})$ and $\vec{P_2} = (E_2, \vec{p_2})$, the natural choice of choosing a frame where $\vec{p_1} = -\vec{p_2}$, also called the centre-of-mass (CM) can be made. The Lorentz-invariant Mandelstam variable s is defined as

$$s = (p_1 + p_2)^2 = (E_1^{CM} + E_2^{CM})^2 \tag{A.6}$$

hence, $\sqrt{s}$ represents the total energy in the centre-of-mass. In the case of pp collisions as discussed as in this thesis then $\sqrt{s} = 2E_1 = 2E_2$. For a direct comparison with heavy-ions a similar notation can be adopted, where $\sqrt{s_N N} = \sqrt{s}/A$ with A the number of nucleons in a nucleus (A=208 for Pb).

An other interesting variable used in high energy physics is the invariant mass: m_{inv}. This mass is taken from two particles, assuming they have been produced by the decay of the same mother particle such that

$$m_{inv}^2 = m_1^2 + m_2^2 + 2E_1E_2 - 2\vec{p_1} \cdot \vec{p_2} \tag{A.7}$$

and similarly the p_{T} of the mother particle can also be obtained as

$$p_{\mathrm{T}}{}_{inv}^2 = (p_{x,1} + p_{x,2})^2 + (p_{y,1} + p_{y,2})^2 \tag{A.8}$$

It must be also noted that in ALICE, the muon arm is located at forward rapidity at -2.5$<\eta<$-4, however by convention we use positive values when referring to rapidity (y).

Appendix B

List of analyzed runs

All runs were taken in pp collisions at $\sqrt{s} = 5.02$ TeV in 2017. Runs passing the selection are:

- for LHC17p (38 runs):

  282343, 282342, 282341, 282340, 282314, 282313, 282312, 282309, 282307, 282306, 282305, 282304, 282302, 282247, 282230, 282229, 282227, 282224, 282206, 282147, 282146, 282127, 282126, 282123, 282122, 282120, 282119, 282118, 282099, 282098, 282078, 282051, 282050, 282031, 282025, 282021, 282016, 282008

- for LHC17q (13 runs):

  282441, 282440, 282439, 282437, 282415, 282411, 282402, 282398, 282392, 282391, 282367, 282366, 282365

Appendix C

List of Monte Carlo samples

Three general purpose MC sample anchored to the LHC17pq periods have been created and are used in this analysis:

- LHC18j2_fast: PYTHIA8 with Monash 2013 tune as generator, Geant3 for particle propagation, anchored to LHC17p and LHC17q runs with TPC and TOF included, details about its production can be found under the ALIROOT-8017 JIRA ticket: `https://alice.its.cern.ch/jira/browse/ALIROOT-8017`
- LHC20a1: PYTHIA8 with Monash 2013 tune as generator, Geant3 for particle propagation, anchored to LHC17q runs without TPC and TOF included. This MC-sample has been produced in order to add the extra 10 runs of the LHC17q period running without TPC and TOF which were not produced in the LHC18j2_fast sample. Details about its production can be found under the ALIROOT-8391 JIRA ticket: `https://alice.its.cern.ch/jira/browse/ALIROOT-8391`
- LHC20a1: EPOS as generator, Geant3 for particle propagation, anchored to all LHC17p and LHC17q runs, details about its production can be found under the ALIROOT-8392 JIRA ticket: `https://alice.its.cern.ch/jira/browse/ALIROOT-8392`

Appendix D

Results in low-mass dimuons in pp collisions from ALICE

In pp collisions the extraction of the vector mesons has been performed in all the available center-of-mass energies provided by the LHC. Figure D.1 shows the extracted dimuon signal integrated over transverse momentum p_T and rapidity y. In these low-mass interval ($2m_\mu < m_{\mu\mu} < 1.5\ GeV/c^2$) the estimation of the signal from unlike-sign muon pairs is extracted using an hadronic cocktail considering the various sources of the signal.

In these various collisions systems the p_T-differential measurement of the ϕ at all energies and of the ω was performed. As this part will be detailled later in this thesis, we can here give a first insight with the ϕ p_T-differential cross section at 2.76 TeV on figure D.3(a). On the latest, results are compared to phenomenological models and is interpolated by Lévy-Tsallis function. It can be noted that the D6T tune of the PYTHIA generator gives a good description of the ϕ production while other models undershoot its production, for $p_T < 2.5\ GeV/c$ in the case of the PHOJET generator, or over the full covered p_T range.

At $\sqrt{s}$ =7 TeV[97] the ω production at as a function of p_T which can also be interpolated with a Lévy-Tsallis function as represented on D.3(b). The vector meson production can be described over the presented range using the PERUGIA-0 and ATLAS-CSC models, while the other models tend to overestimate its production. Still at this energy the ϕ meson was extracted in 1< p_{T} <5 GeV/c. Comparison to models show that the ATLAS-CSC tune of PYTHIA gives the best description on its production, while the Perugia-0 and 11 tend to underestimate it,

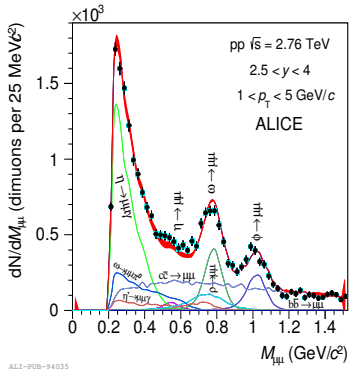

(a) Invariant dimuon mass spectra after combinatorial background substraction obtained in pp collisions at $\sqrt{s}$ = 2.76 GeV

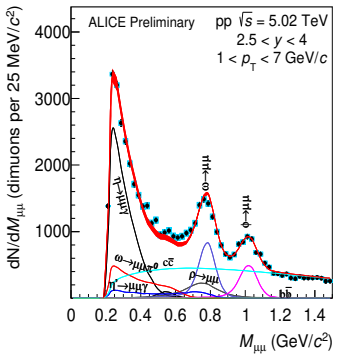

(b) Invariant dimuon mass spectra after combinatorial background substraction obtained in pp collisions at $\sqrt{s}$ = 5.02 GeV

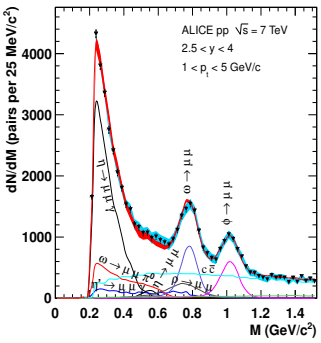

(c) Invariant dimuon mass spectra after combinatorial background substraction obtained in pp collisions at $\sqrt{s}$ = 7 GeV

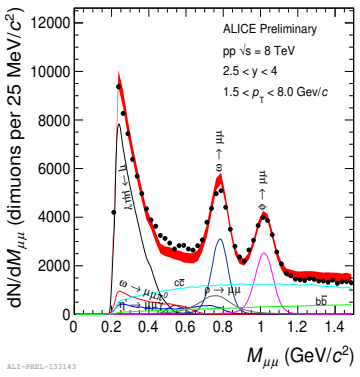

(d) Invariant dimuon mass spectra after combinatorial background substraction obtained in pp collisions at $\sqrt{s}$ = 8 GeV

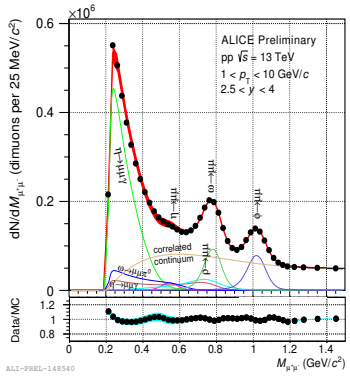

(e) Invariant dimuon mass spectra after combinatorial background substraction obtained in pp collisions at $\sqrt{s}$ = 13 GeV

Figure D.1: Invariant dimuon mass spectra after combinatorial background subtraction obtained in pp collisions with the ALICE collaboration

and the D6T tune and PHOJET would overestimate it.

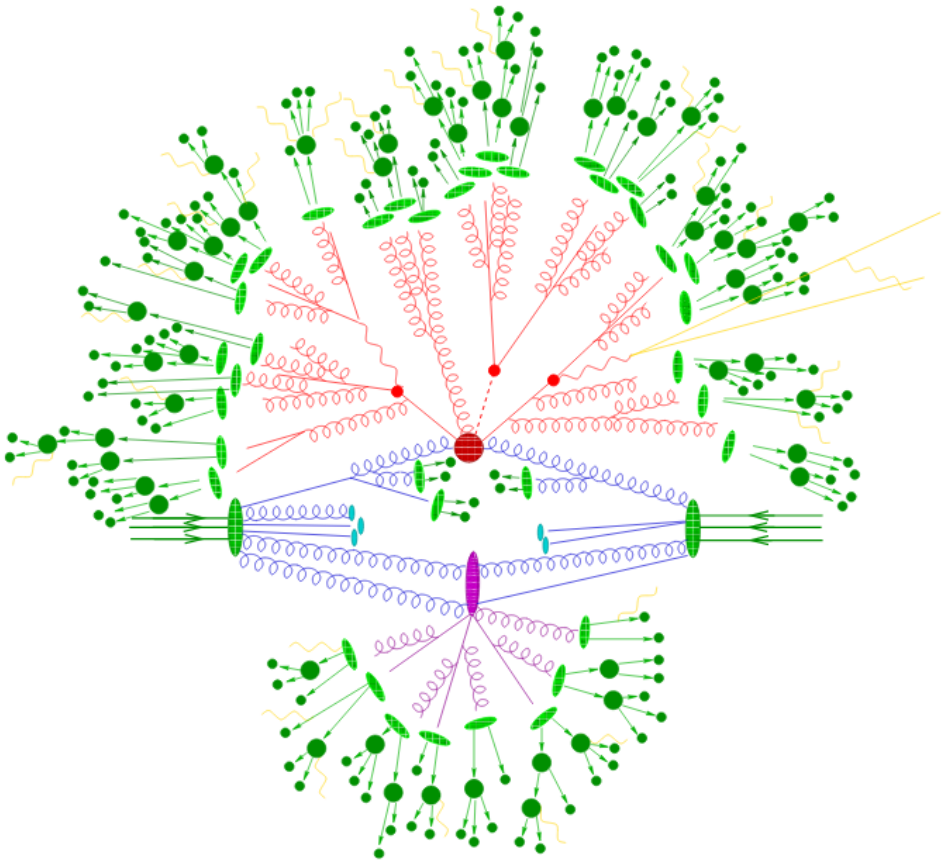

Figure D.2: p_T-differential cross section of the ϕ for $2.5 < \quad y \quad < 4$ in pp collisions at $\sqrt{s} \ = 2.76$ GeV

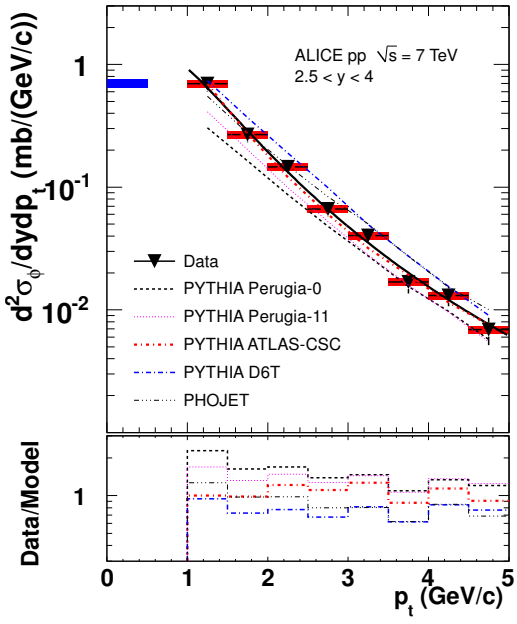

(a) p_T-differential cross section of the ϕ for $2.5 < y < 4$ in pp collisions at $\sqrt{s} = 7$ GeV compared to PYTHIA6 tunes and Phojet models

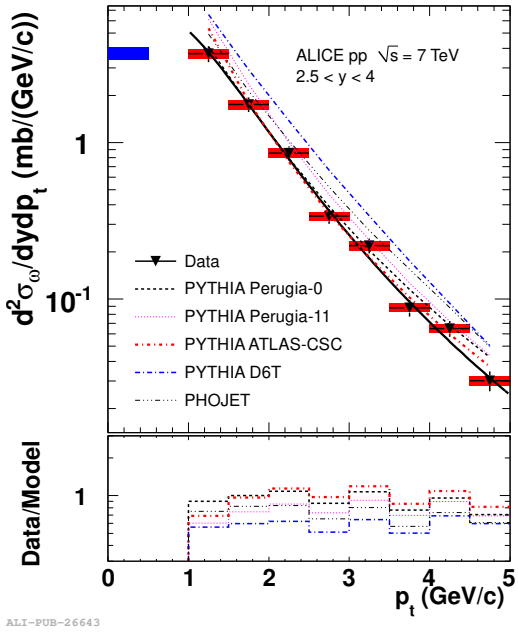

(b) p_T-differential cross section of the ω for $2.5 < y < 4$ in pp collisions at $\sqrt{s} = 7$ GeV[97] compared to PYTHIA6 tunes and Phojet models

Figure D.3

Appendix E

Monte Carlo generators

Tn the following sections, we will explain the event generators physics and theoretical models which are compared to experimental results. While all simulating hadron-hadrons collisions, the generators can choose to involve certain physics mechanism, and to tune the parameter on different data. In figure E.1 a pp collision is represented leading to several final-state particles.

The understanding of a complete pp collision require the knowledge of the hard and soft-components of the collision. The main components are:

- The hard process is characterised by the highest momentum transferred (e.g. production of jets or heavy quarks) in a hadron-hadron collision. Each of them consists of many partons (quarks, antiquarks, and gluons) whose distribution can be characterised by Parton Distribution Functions (PDFs). The PDF $f_{PDF}(x, Q^2)$ describes the probability of finding a parton with the momentum fraction x of the total momentum of the particle probed at an energy scale Q^2.

- An initial-state shower (or initial state radiation) is the radiation that develops from incoming partons.

- A final-state shower (or final state radiation) is the radiation that develops from an outgoing parton of the hard subprocess. This process is especially important for higher energies.

- Multiple parton interactions (MPI) describes the possibility to have more than one dis-

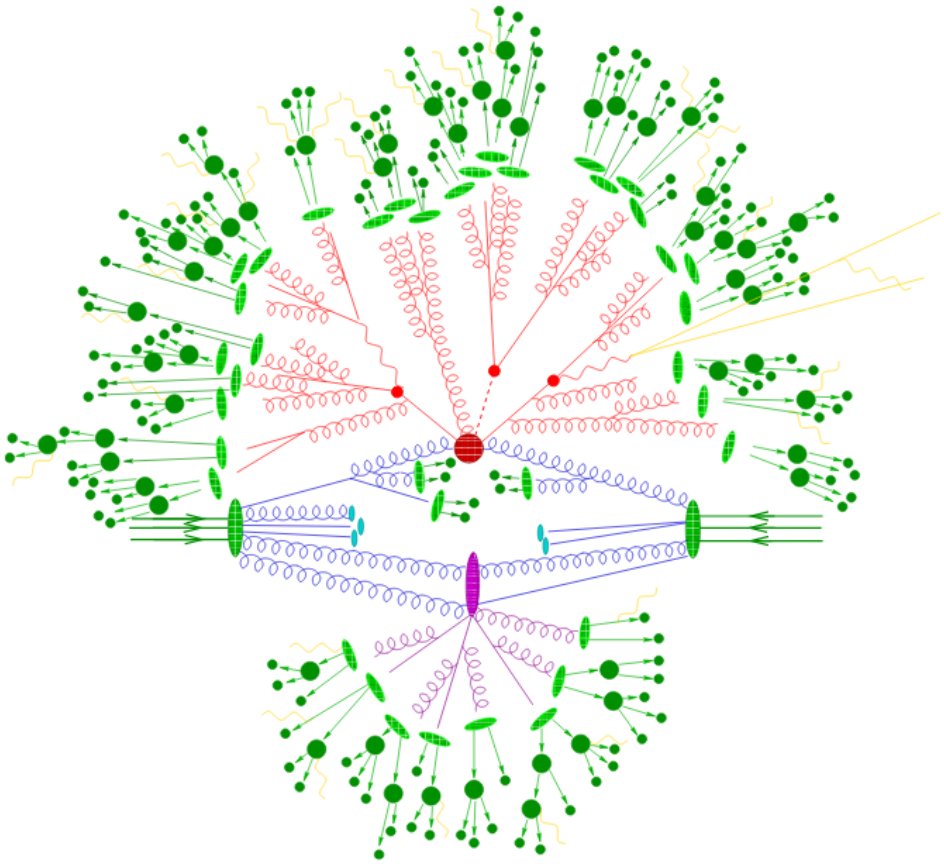

Figure E.1: A sketch of a hadron-hadron collision in PYTHIA event generation. Thered blob in the center represents the hard collision, surrounded by a tree-like structurerepresenting Bremsstrahlung as simulated by parton showers. The purple blob indicatesa secondary hard scattering event. Parton-to-hadron transitions are represented by lightgreen blobs, dark green blobs indicate hadron decays, while yellow lines signal soft photonradiation. [98]

tinct and simultaneous parton interaction inside the same hadronic collision.

E.1 PYTHIA8 and Monash2013 tune

In the default parametrisation of the PYTHIA8 model is based on the Lund model, and on the string fragmentation model. PYTHIA8 [72] includes improved Multiple parton interactions (MPI) and **color reconnection (CR)** [99] which were not present in PYTHIA6. Multiple parton interactions describe the possibility to have more than one distinct and simultaneous

parton interaction inside the same hadronic collision. In a color reconnection scenario, color strings from independent parton interactions do not hadronise independently, but fuse prior to hadronisation. Each further MPI brings less and less additional N_{ch}, while still providing an equally big p_T boost from the interaction itself, to be shared among the produced hadrons. This leads to fewer hadrons, but more energetic.

E.1.1 the Monash2013 tune

The Monash2013 tune of PYTHIA8 [92] parametrise uses updated fragmentation parameters with a new NNPDF2.3 LO Partition Distribution Function (PDF) set. Data from the LHC have been used to constrain the initial-state-radiation and multi-parton interaction parameters, combined with data from SPS and the Tevatron to constrain the energy scaling.

E.1.2 DIPSY

DIPSY is a MC event generator, using PYTHIA8 for hadronisation [100]. In models for hadron collisions based on string hadronisation (such as PYTHIA models), the strings are usually treated as independent, allowing no interaction between the confined colour fields. Based on recent results it has been suggested that strings close in space can fuse to form **colour ropes** [101] [102]. This effect is expected to occur at the LHC where the density of strings is quite high. In this model, strings are allowed to combine into higher multiplets, giving rise to increased production of baryons and strangeness, or recombine into singlet structures and vanish. Furthermore, a model for strings recombining into junction structures is considered, again giving rise to increased baryon production.

E.2 EPOS

EPOS is a universal generator for pp, p-Pb and Pb-Pb collisions [88, 89, 90] . In EPOS, the MPIs are treated via the Gribov-Regge multiple scattering framework [103] combined with pQCD.The scattering is expressed through parton ladders associated to the so-called Pomerons.The number of such Pomeron exchanges characterises the geometry of the colli-

sion. Each parton ladder is associated to a flux tube. This will eventually breaks into individual string and later into hadrons and jets. Parton saturation effects in the nucleus are summarized by a saturation scale Q_s for each Pomeron individually. The scale Q_s depends on the mass number A and can be expressed in function of the momentum fraction x, or as dependent on the number of participants N_{part} (and therefore centrality). This approach gives a different scaling at low and high transverse momenta, corresponding to a soft component scaling with N_{part} and a hard component scaling with the number of binary collisions N_{coll}.In high multiplicity pp, the high density of strings will result in a creation of a thermalised, collectively expanding bulk matter. Such bulk is referred to as *core*. The string close to the surface of the bulk and/or with high p_T will escape the bulk and produce hadrons and jets. These segments are referred to as *corona*. The *core-corona* separation is a dynamical process, which provides the initial conditions for the subsequent **collective radial expansion**.

EPOS-LHC the *-LHC* parametrisation of the EPOS generator considers the results obtained at the LHC to constrain the effects of the flow and core-corona observed according to data.

EPOS-3 is an evolution of EPOS-LHC, considering introducing a variable non-perturbative scale Q_0^2 to recover factorisation and binary scaling for inclusive hard processes above Q_0^2. EPOS-3 is also considering the latest results from the NA61 experiment used to introduce a new diffraction including multiple scattering and new channel for pion exchange.

E.3 PYTHIA6 and Perugia0

PYTHIA6 provides a representation of event properties in a wide range of reactions, within and beyond the Standard Model, with emphasis on those where strong interactions play a role, directly or indirectly, and therefore multi-hadronic final states are produced [104]. The program is based on a combination of analytical results and various QCD-based models. The generator uses fragmentation the parametrisation from the CTEQ5L Partition Distribution Function. The generator uses measurements on hard subprocesses, initial- and final-state parton showers, underlying events and beam remnants, fragmentation and decays, and much more.

The Perugia0 tune of PYTHIA6 implements an original parton is pushed off its mass shell by reducing its momentum components [65]. In particular, the transverse-momentum components are reduced, and hence each final-state emission off an initial state radiation parton effectively removes p_{T} from that parton, and by momentum conservation also from the recoiling Drell-Yan pair.

E.4 Phojet

Like EPOS, Phojet is a model based on Gribov-Regge multiple scattering and as the feature of **combining the Dual Parton Model [91] with pQCD**. In this model, hadronic interactions are assumed to be described by the exchange of a single effective Pomeron. The lowest order pQCD process is described by the hard part of the Pomeron, while the remaining soft part is described by a soft Pomeron and an effective Reggeon. Concerning hard-processes, the model uses an energy dependant scale $Q_0(s) \sim Q_0 + C \cdot log(\sqrt{s})$. For the final states, Phojet is using the hadronisation model developed in PYTHIA6.

Among all the MC models presented here, Phojet is the only one which is not tuned on the data from LHC but rather on the one from the CDF experiment.

Appendix F

List of invariant mass spectra fits in pp collisions at $\sqrt{s} = 5.02TeV$

F.1 p_T-single differential analysis

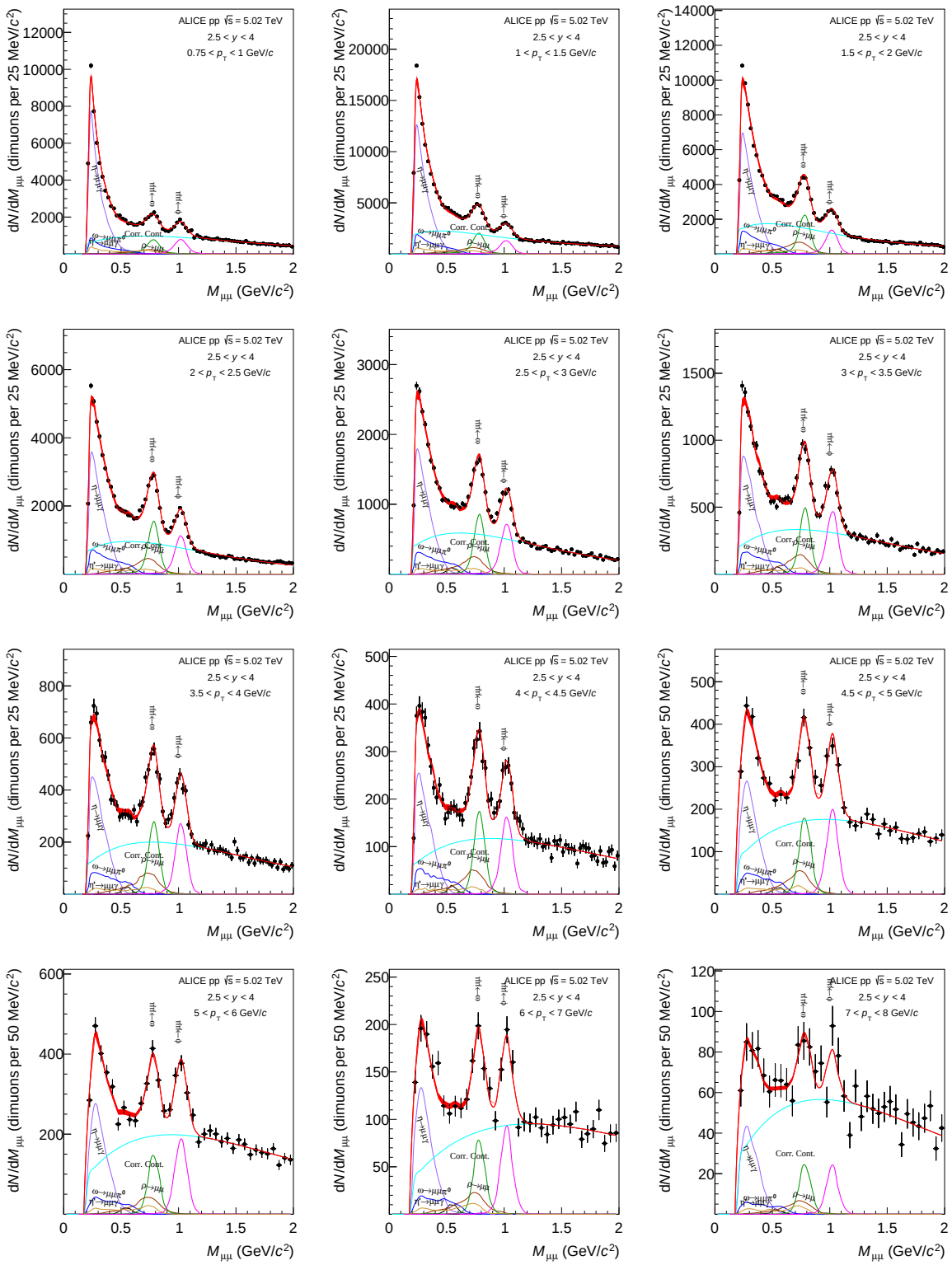

Figure F.1: Fits to the invariant dimuon mass spectra with the hadronic cocktail in pp collisions at $\sqrt{s} = 5.02$ TeV in $2.5 < y < 4$ for twelve p_{T} intervals from 0.75 to 8 GeV/c. In these interpolations the correlated continuum is fitted with a single or double exponential function.

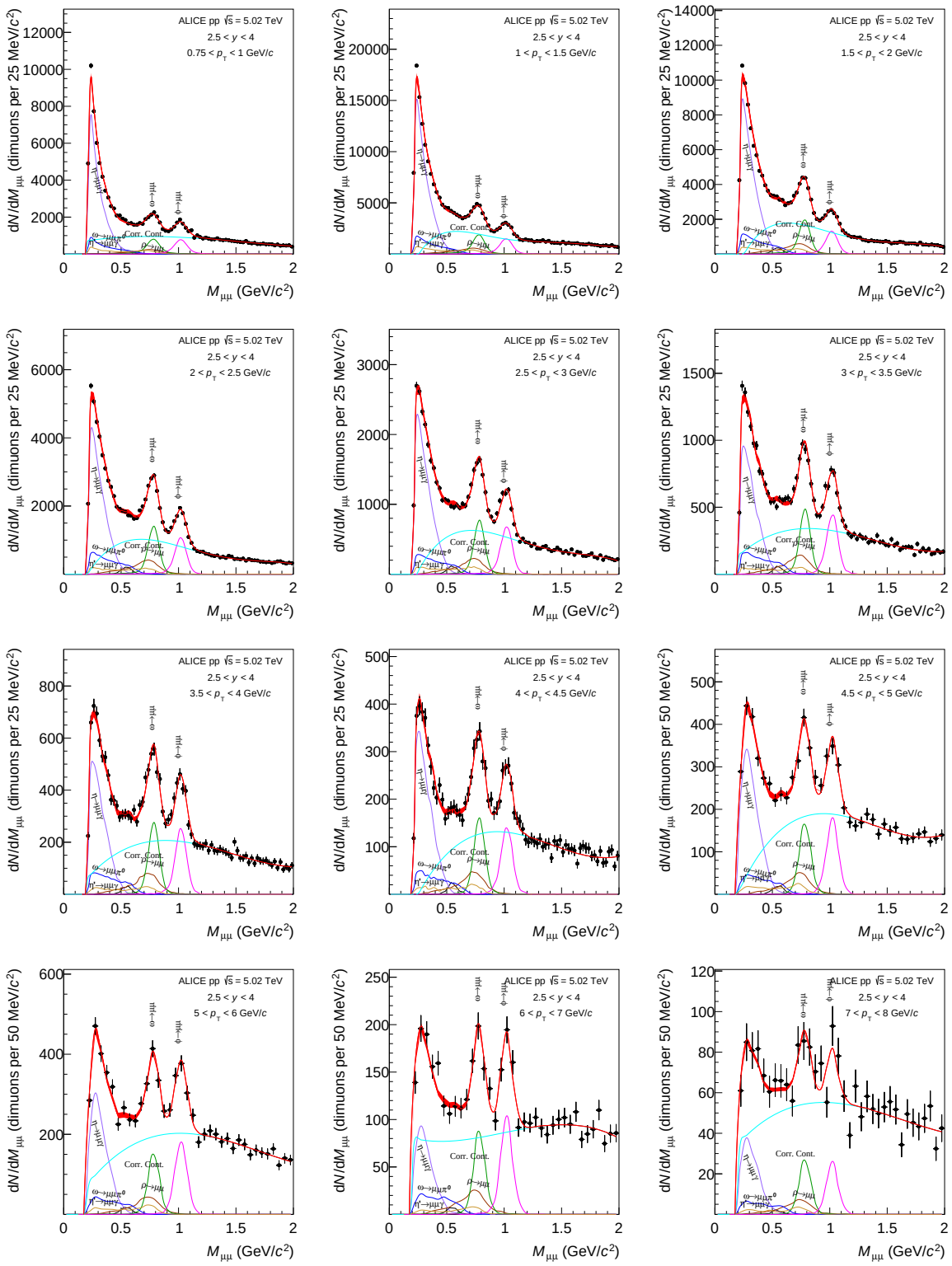

Figure F.2: Fits to the invariant dimuon mass spectra with the hadronic cocktail in pp collisions at $\sqrt{s} = 5.02$ TeV in $2.5 < y < 4$ for twelve p_{T} intervals from 0.75 to 8 GeV/c. In these interpolations the correlated continuum is fitted with an polynomial function.

F.2 p_T-y double differential analysis

F.2.1 Mass spectra in the $3.5 < y < 4$ interval

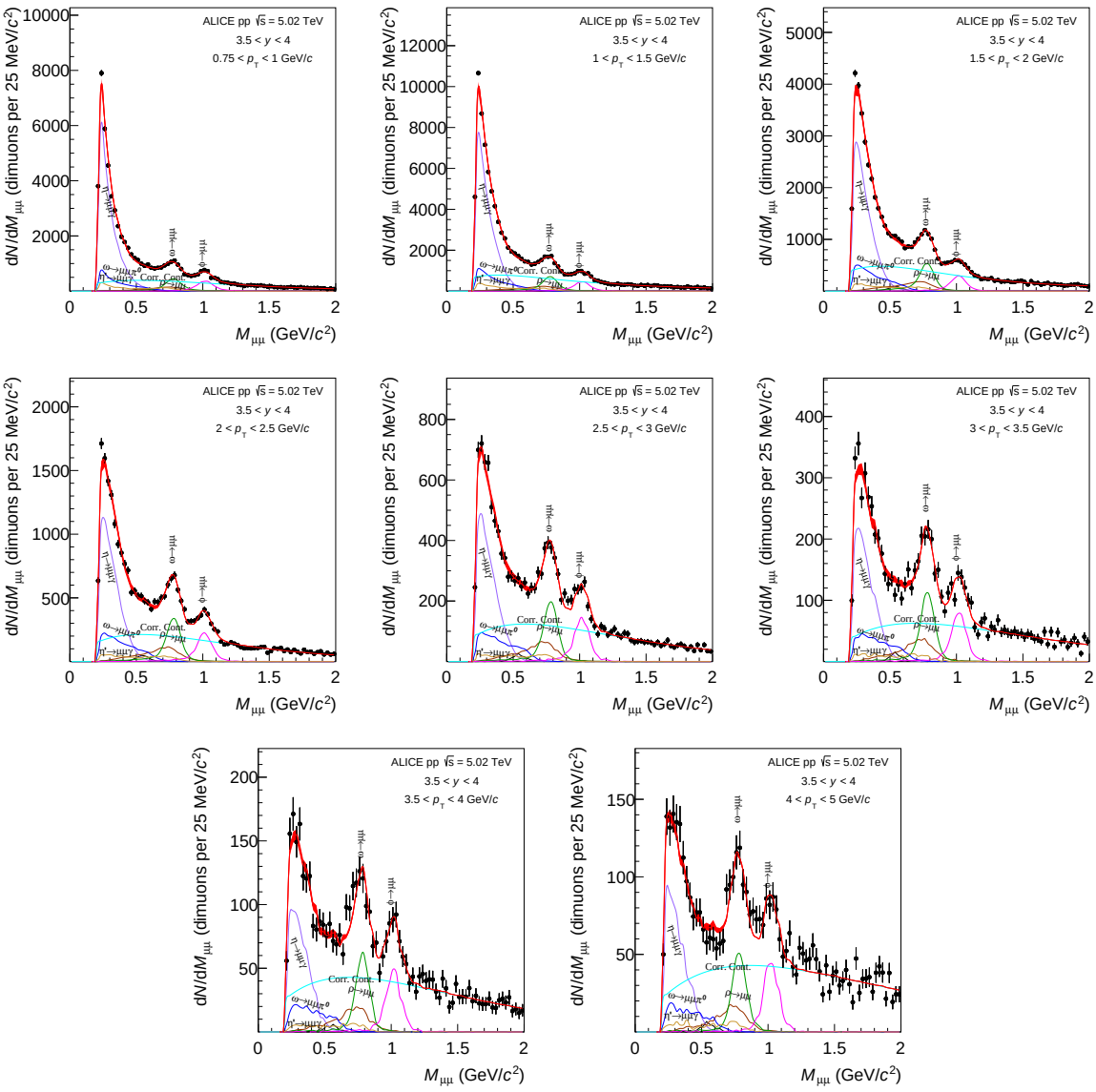

Figure F.3: Fits to the invariant dimuon mass spectra with the hadronic cocktail in pp collisions at $\sqrt{s} = 5.02$ TeV in $3.5 < y < 4$ for nine p_{T} intervals from 0.75 to 6 GeV/c. In these interpolations the correlated continuum is fitted with a single or double exponential function.

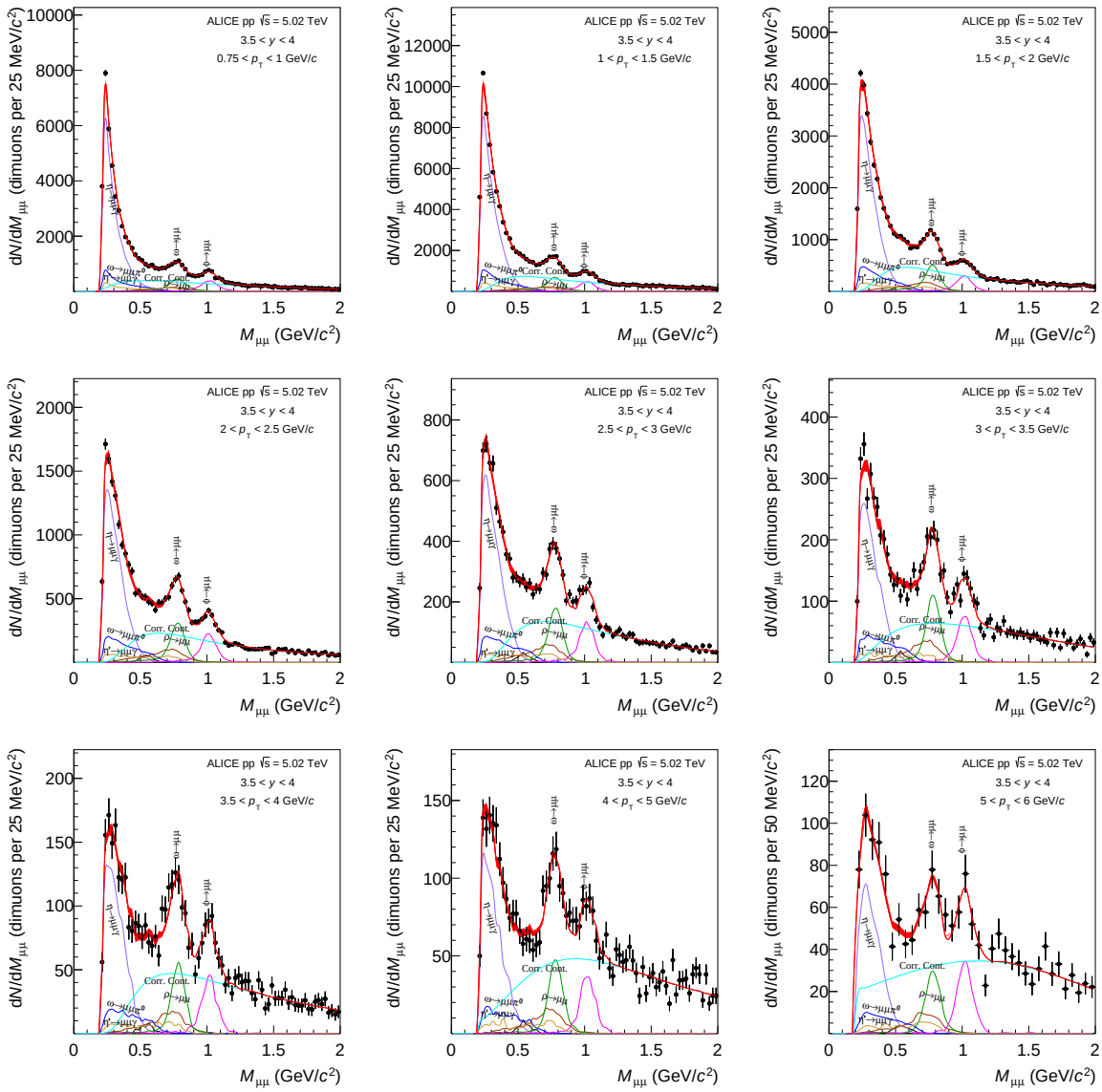

Figure F.4: Fits to the invariant dimuon mass spectra with the hadronic cocktail in pp collisions at $\sqrt{s} = 5.02$ TeV in $3.5 < y < 4$ for nine p_{T} intervals from 0.75 to 6 GeV/c. In these interpolations the correlated continuum is fitted with a variable width gaussian function.

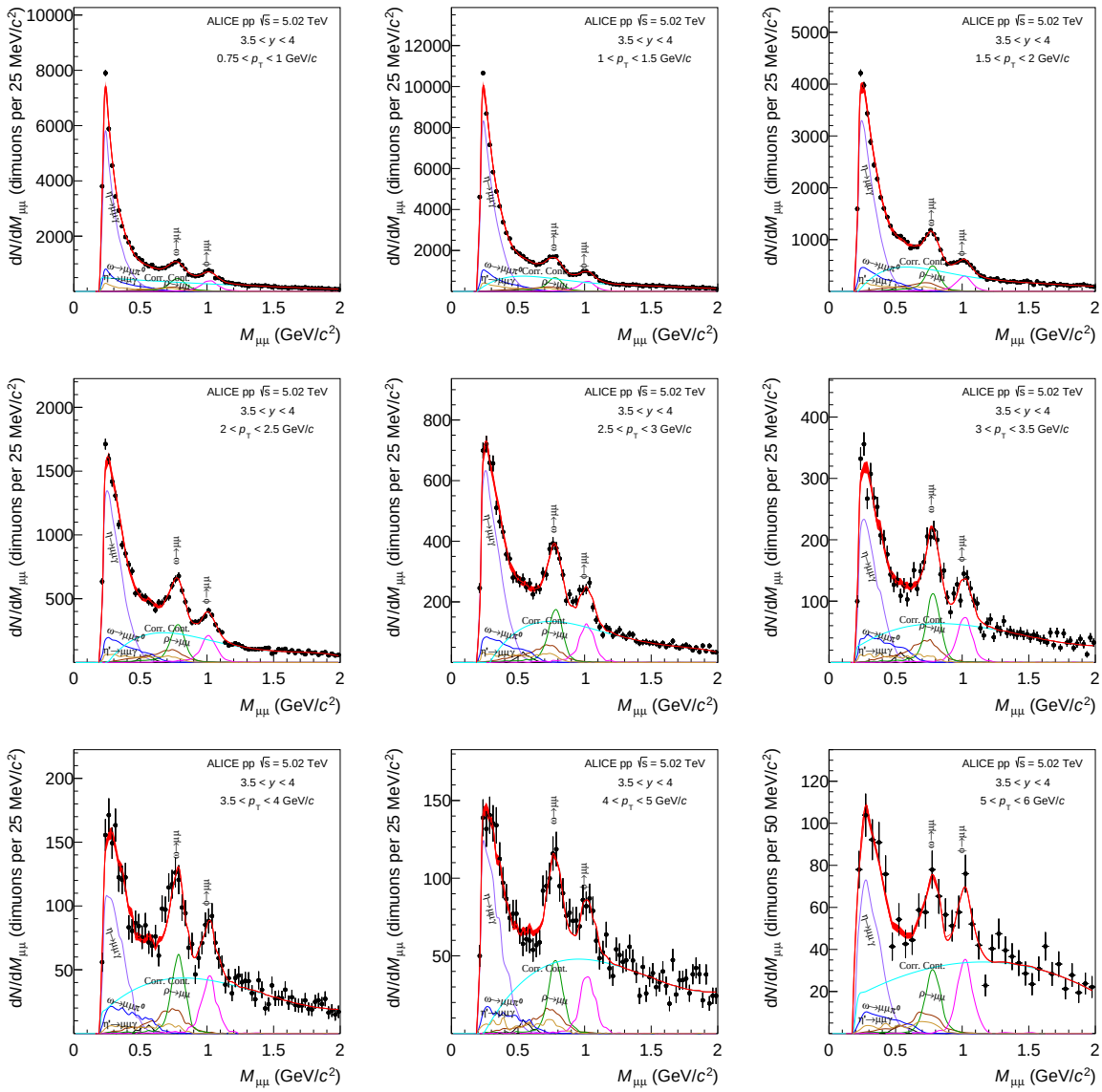

Figure F.5: Fits to the invariant dimuon mass spectra with the hadronic cocktail in pp collisions at $\sqrt{s} = 5.02$ TeV in $3.5 < y < 4$ for nine p_{T} intervals from 0.75 to 6 GeV/c. In these interpolations the correlated continuum is fitted with a polynomial function.

F.2.2 Mass spectra in the $3.25 < y < 3.5$ interval

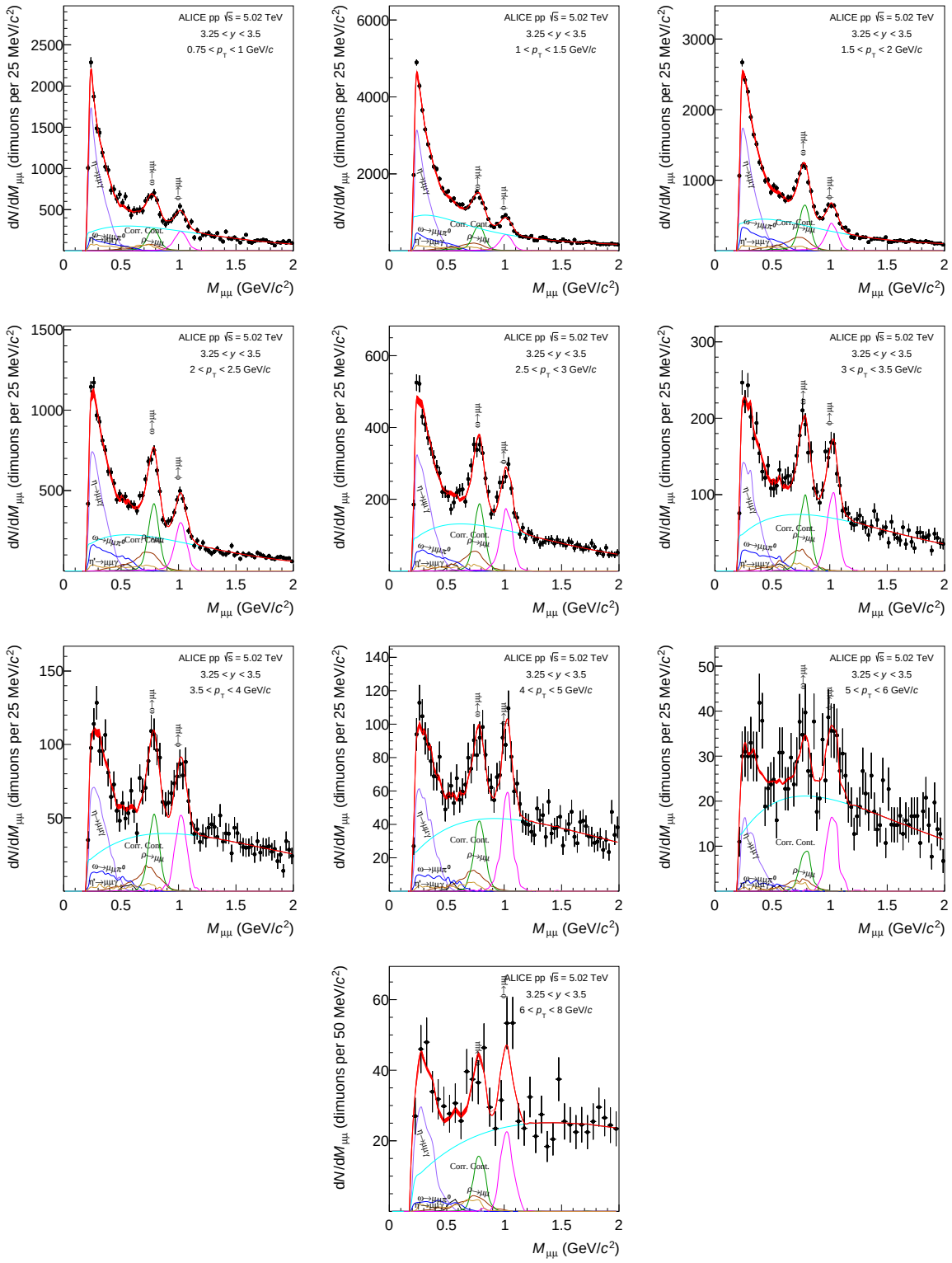

Figure F.6: Fits to the invariant dimuon mass spectra with the hadronic cocktail in pp collisions at $\sqrt{s} = 5.02$ TeV in $3.25 < y < 3.5$ for ten p_{T} intervals from 0.75 to 8 GeV/c. In these interpolations the correlated continuum is fitted with a single or double exponential function.

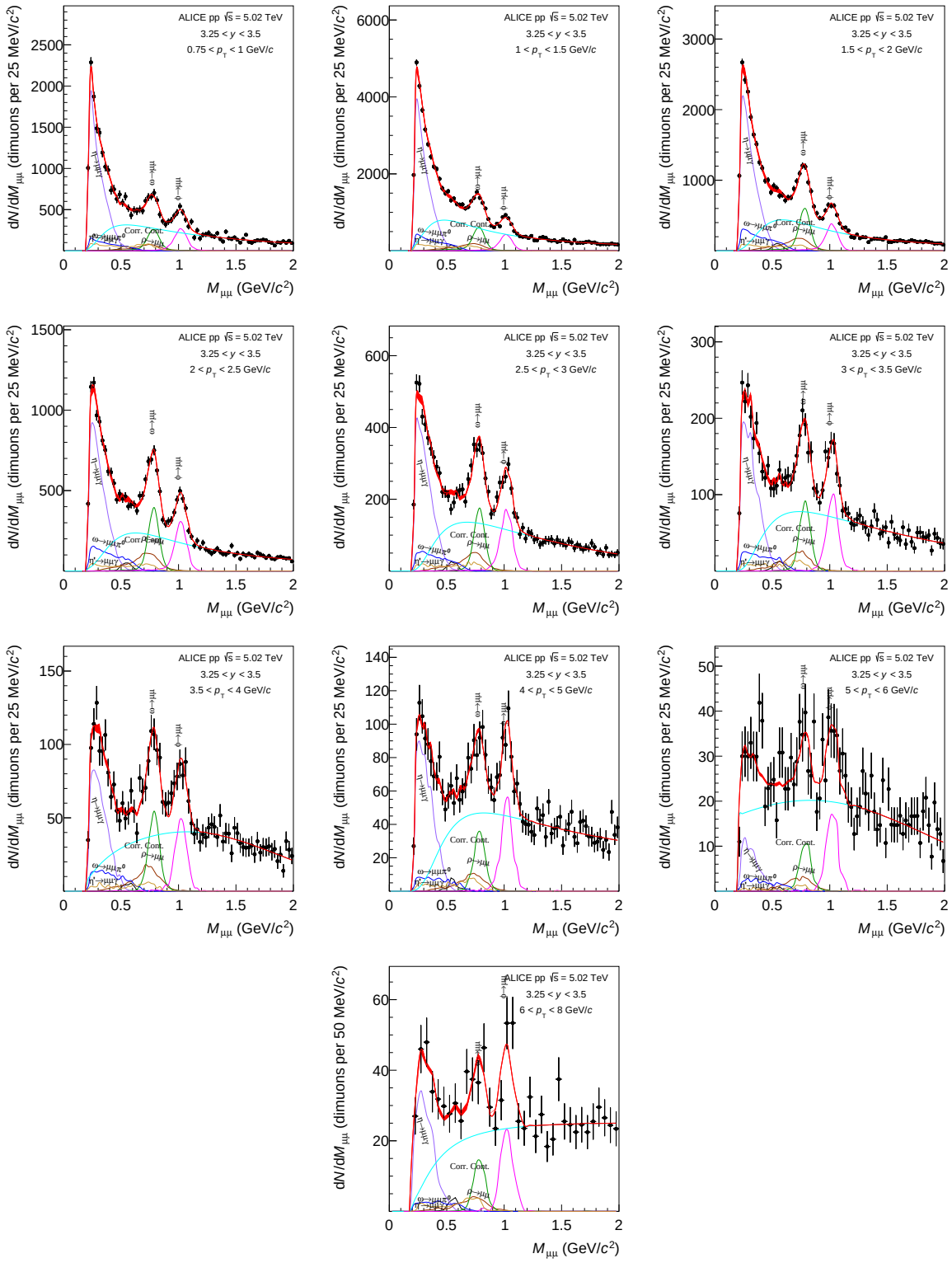

Figure F.7: Fits to the invariant dimuon mass spectra with the hadronic cocktail in pp collisions at $\sqrt{s} = 5.02$ TeV in $3.25 < y < 3.5$ for ten p_{T} intervals from 0.75 to 8 GeV/c. In these interpolations the correlated continuum is fitted with a variable width gaussian function.

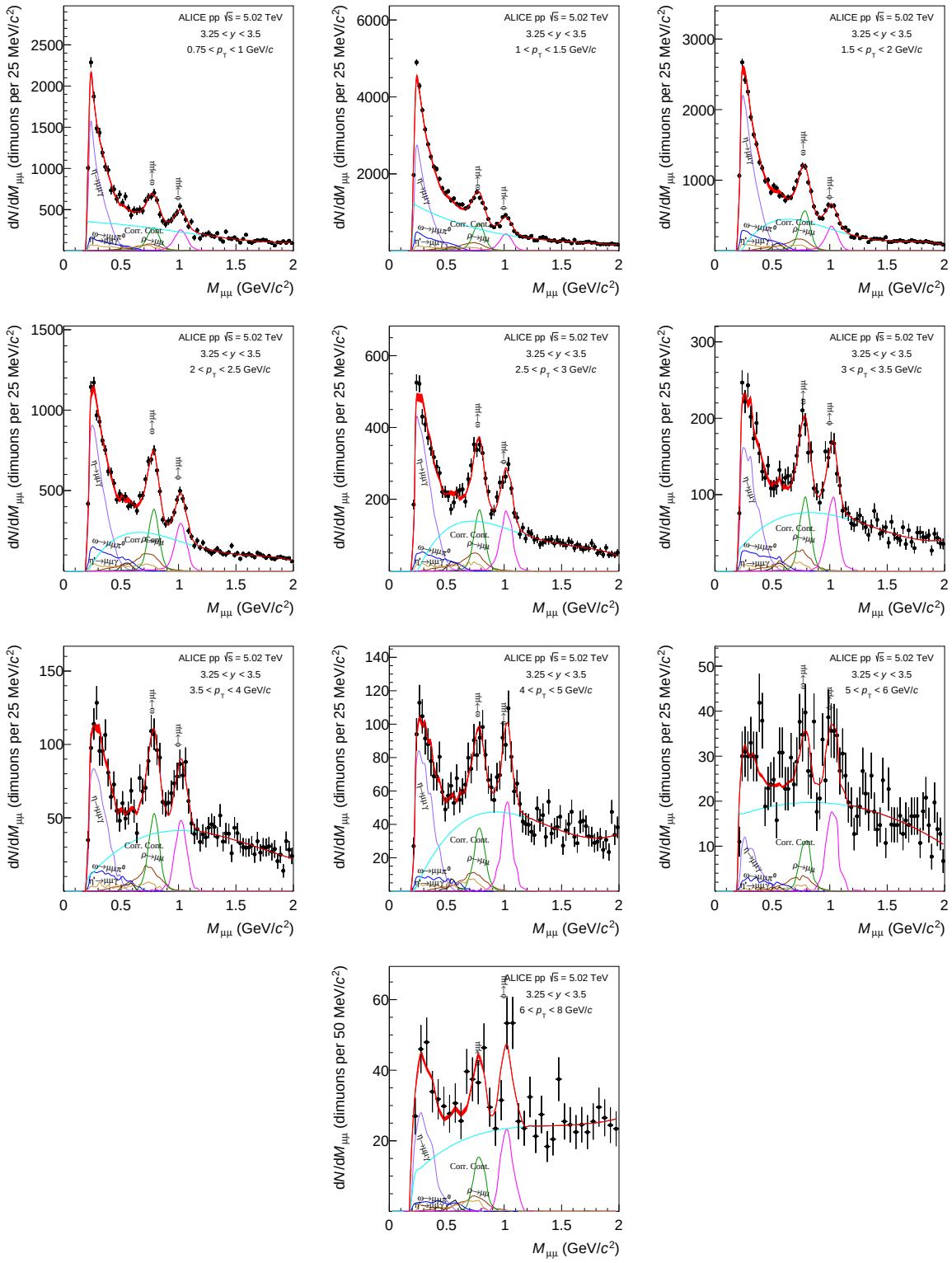

Figure F.8: Fits to the invariant dimuon mass spectra with the hadronic cocktail in pp collisions at $\sqrt{s} = 5.02$ TeV in $3.25 < y < 3.5$ for nine p_{T} intervals from 0.75 to 8 GeV/c. In these interpolations the correlated continuum is fitted with a polynomial function.

F.2.3 Mass spectra in the $3 < y < 3.25$ interval

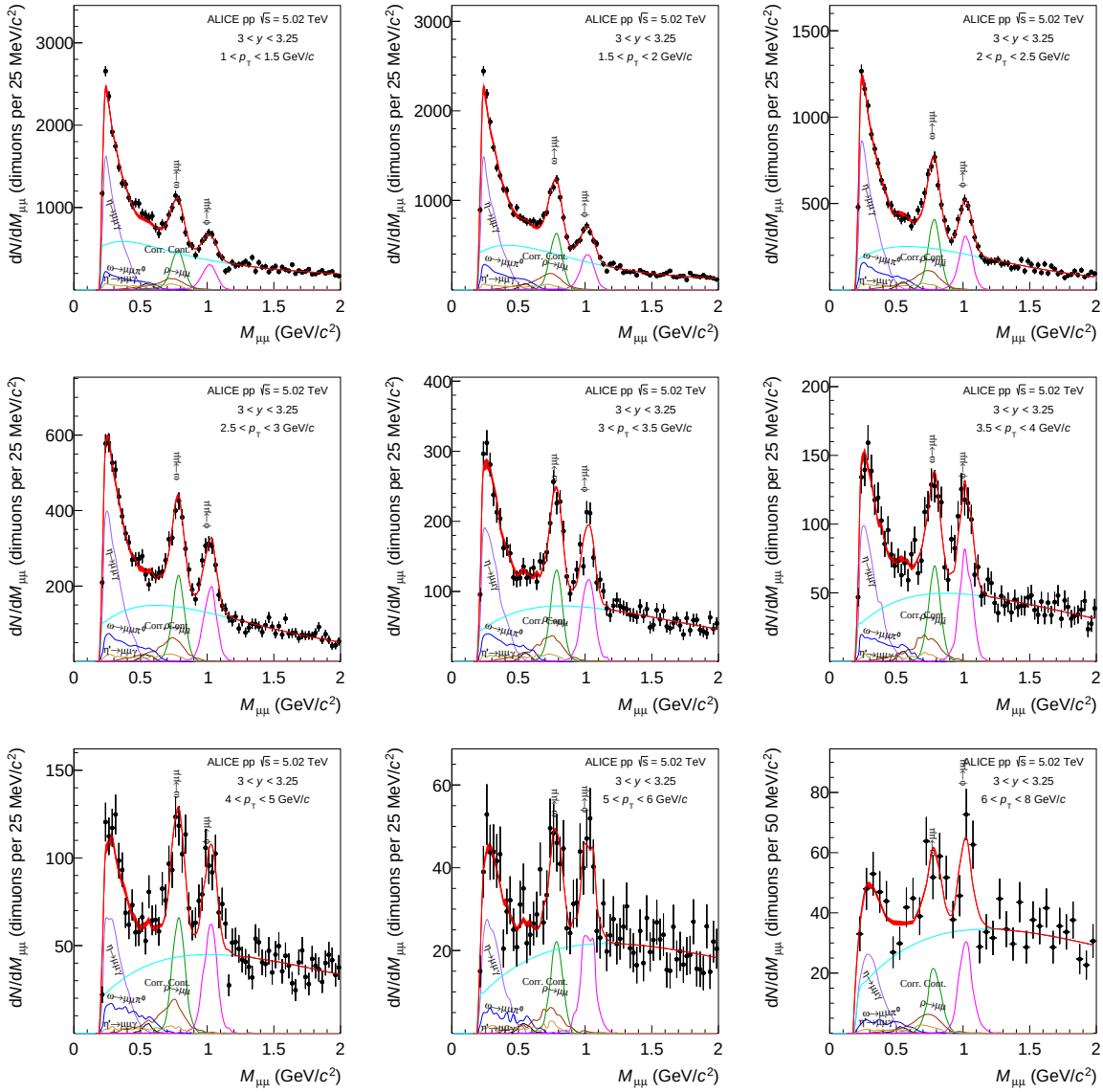

Figure F.9: Fits to the invariant dimuon mass spectra with the hadronic cocktail in pp collisions at $\sqrt{s} = 5.02$ TeV in $3 < y < 3.25$ for nine p_{T} intervals from 1 to 8 GeV/c. In these interpolations the correlated continuum is fitted with a single or double exponential function.

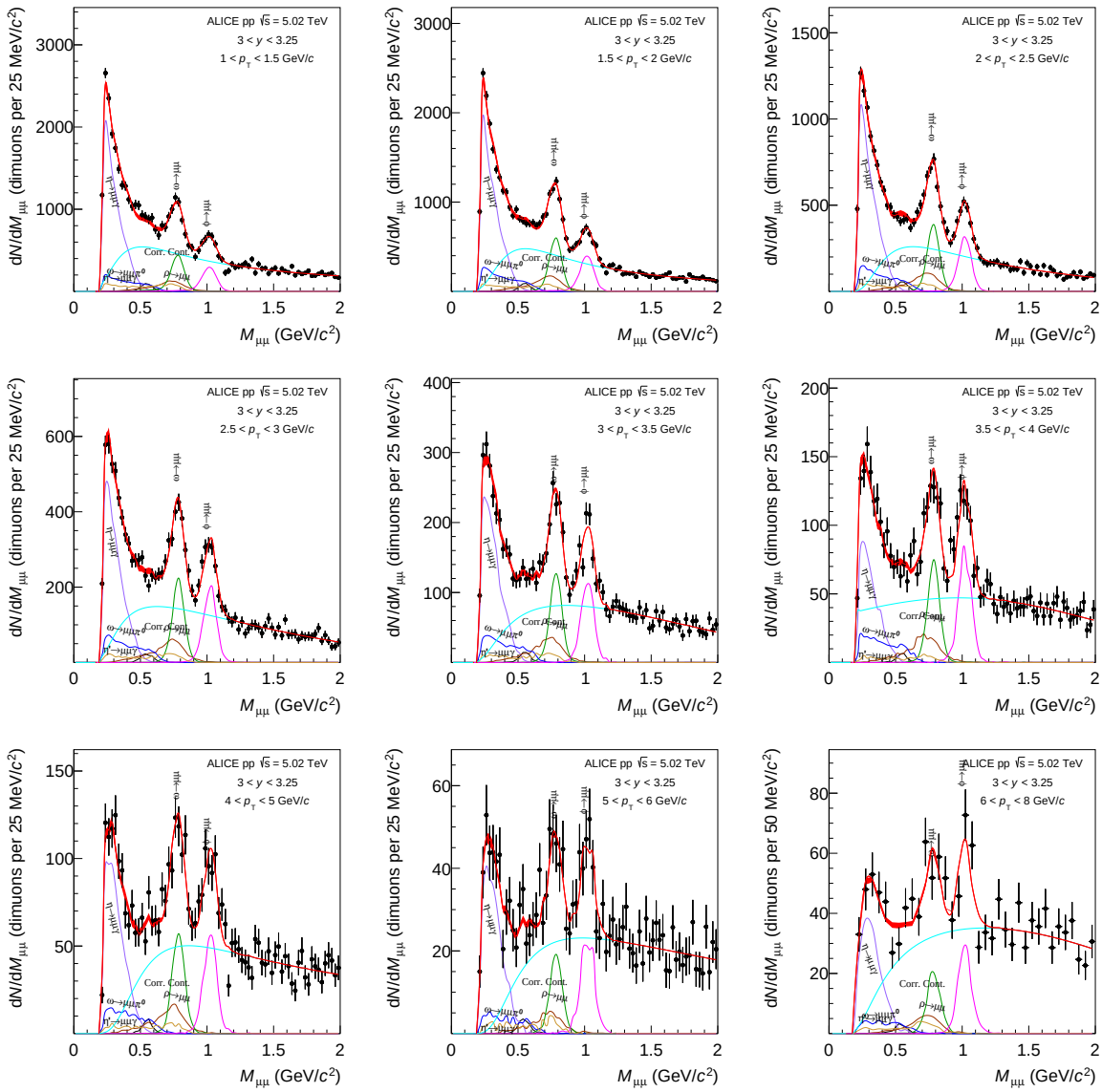

Figure F.10: Fits to the invariant dimuon mass spectra with the hadronic cocktail in pp collisions at $\sqrt{s} = 5.02$ TeV in $3 < y < 3.25$ for nine p_{T} intervals from 1 to 8 GeV/c. In these interpolations the correlated continuum is fitted with a variable width gaussian function.

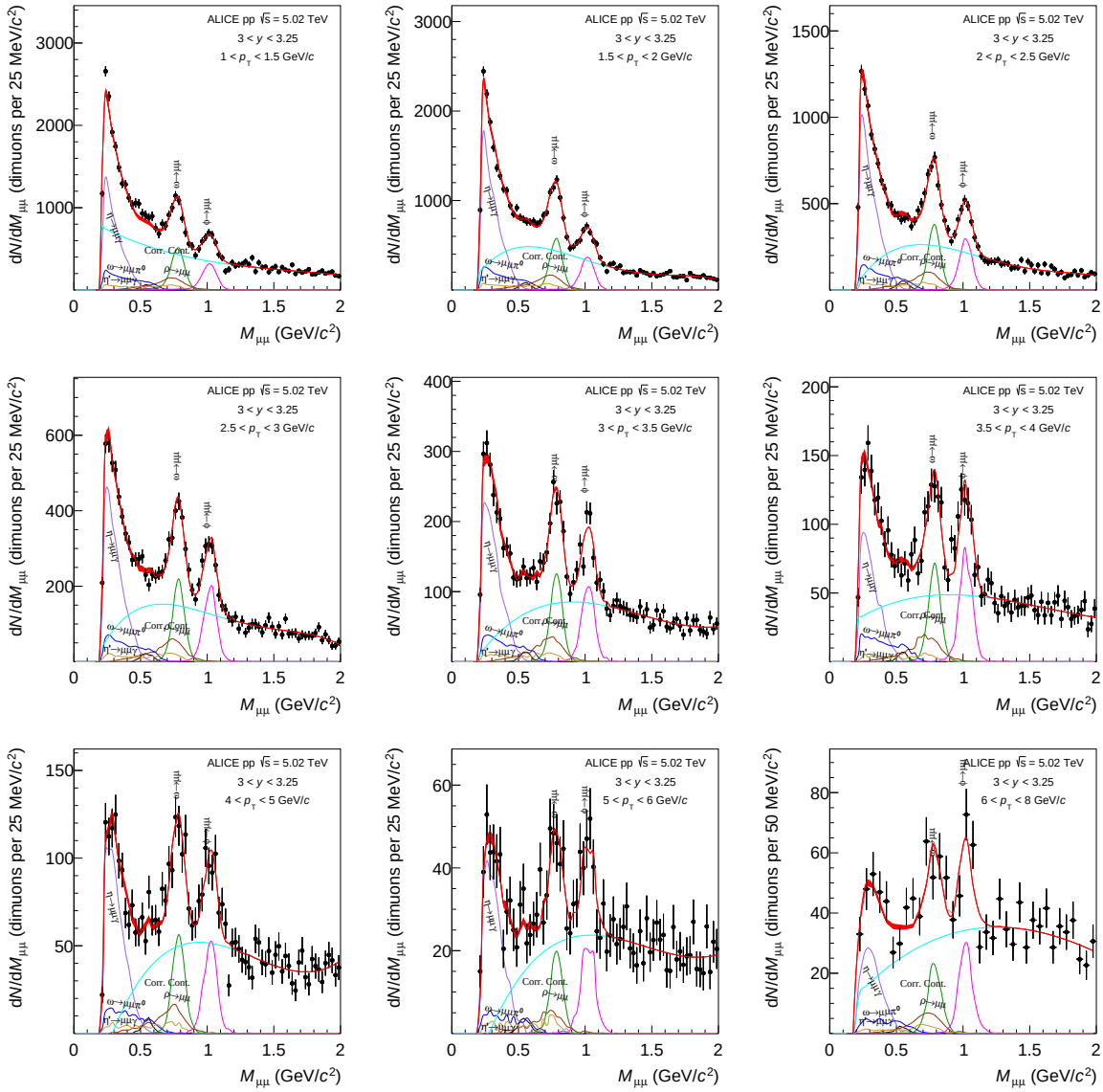

Figure F.11: Fits to the invariant dimuon mass spectra with the hadronic cocktail in pp collisions at $\sqrt{s} = 5.02$ TeV in $3 < y < 3.25$ for nine p_{T} intervals from 1 to 8 GeV/c. In these interpolations the correlated continuum is fitted with a polynomial function.

F.2.4 Mass spectra in the $2.5 < y < 3$ interval

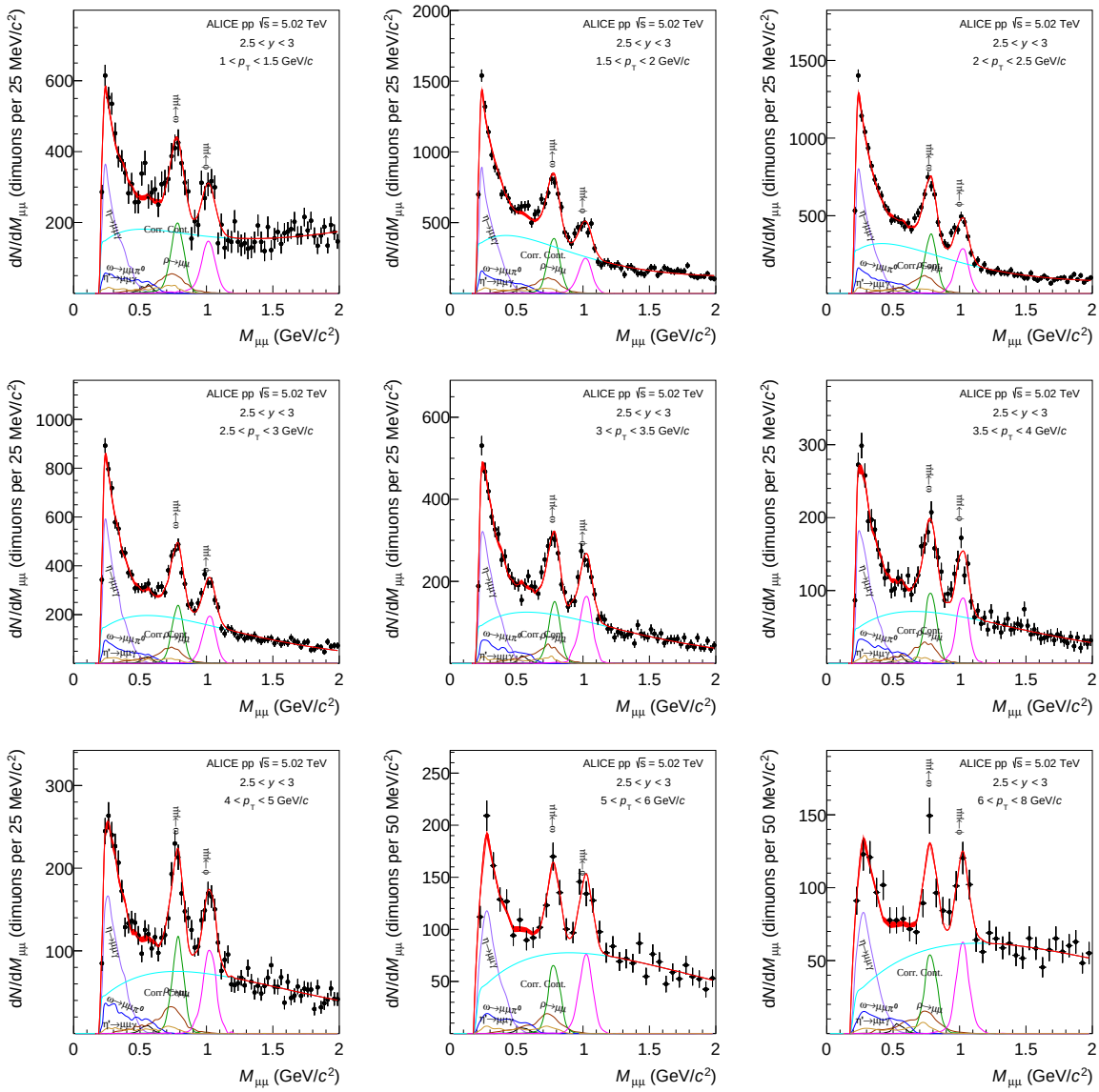

Figure F.12: Fits to the invariant dimuon mass spectra with the hadronic cocktail in pp collisions at $\sqrt{s} = 5.02$ TeV in $3.25 < y < 3$ for nine p_{T} intervals from 1 to 8 GeV/c. In these interpolations the correlated continuum is fitted with a single or double exponential function.

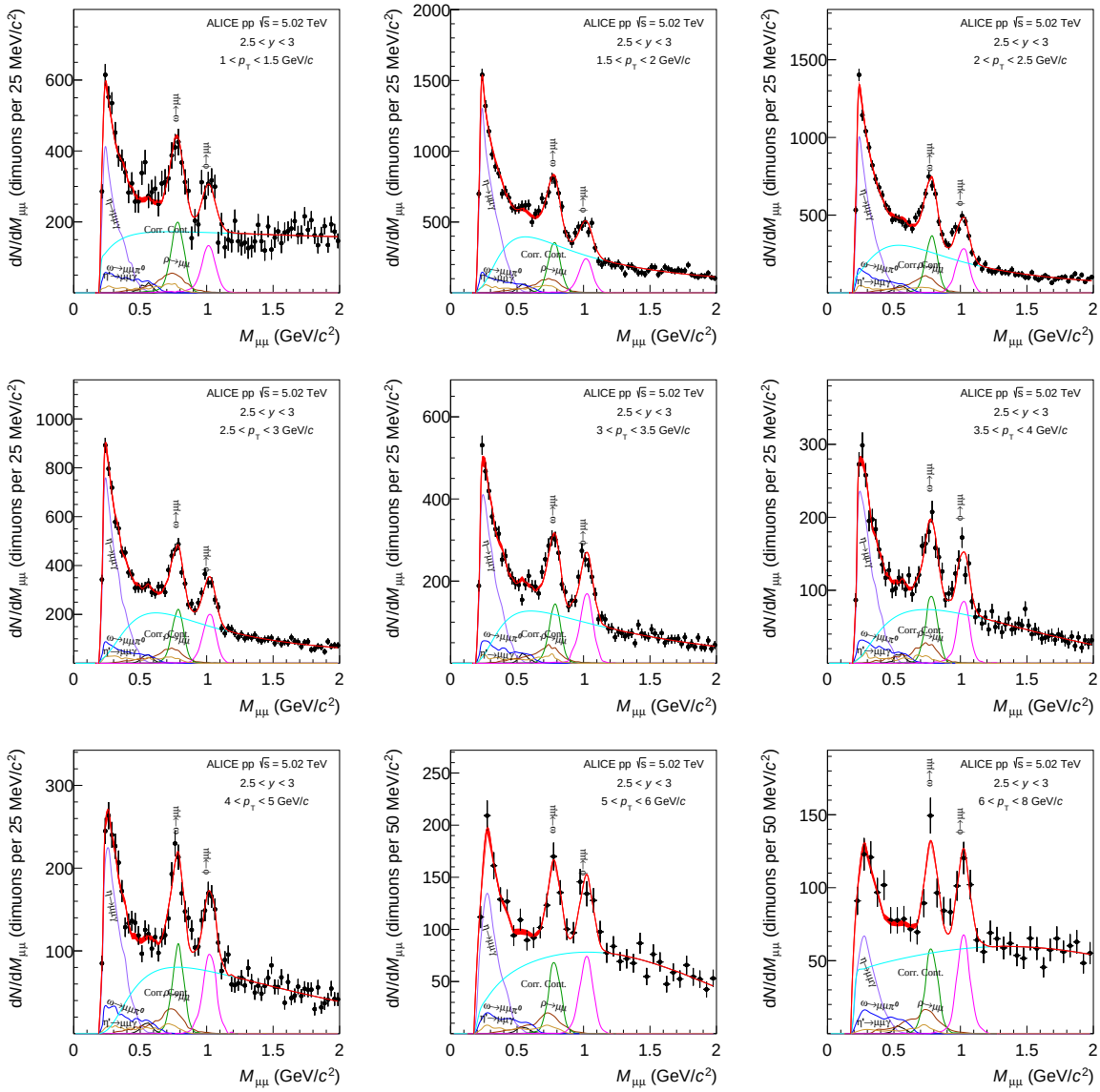

Figure F.13: Fits to the invariant dimuon mass spectra with the hadronic cocktail in pp collisions at $\sqrt{s} = 5.02$ TeV in $2.5 < y < 3$ for nine p_{T} intervals from 1 to 8 GeV/c. In these interpolations the correlated continuum is fitted with a variable width gaussian function.

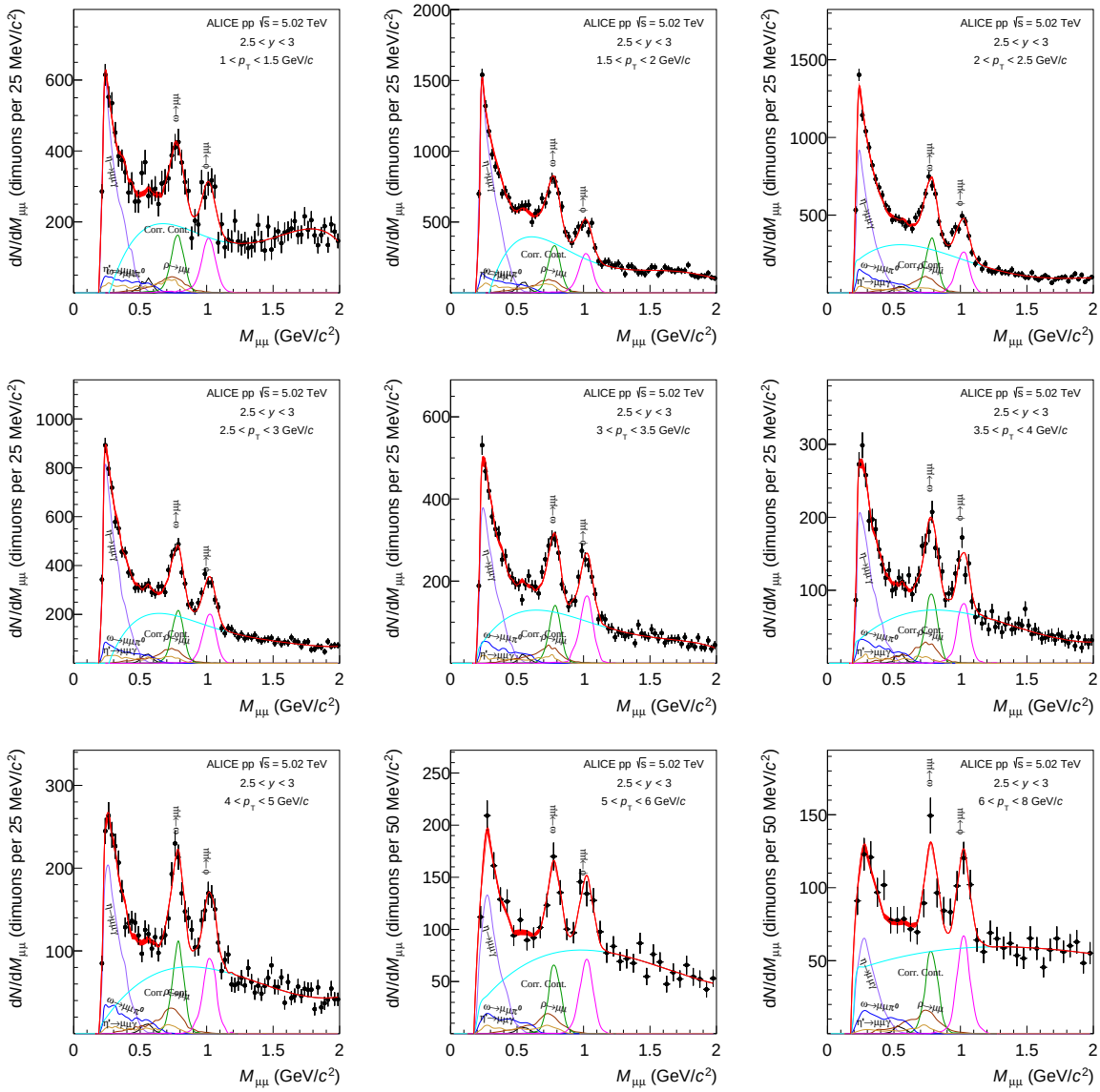

Figure F.14: Fits to the invariant dimuon mass spectra with the hadronic cocktail in pp collisions at $\sqrt{s} = 5.02$ TeV in $2.5 < y < 3$ for nine p_{T} intervals from 1 to 8 GeV/c. In these interpolations the correlated continuum is fitted with a polynomial function.

F.3 p_T-Multiplicity double differential analysis

F.3.1 Mass spectra in the 0-10 % interval

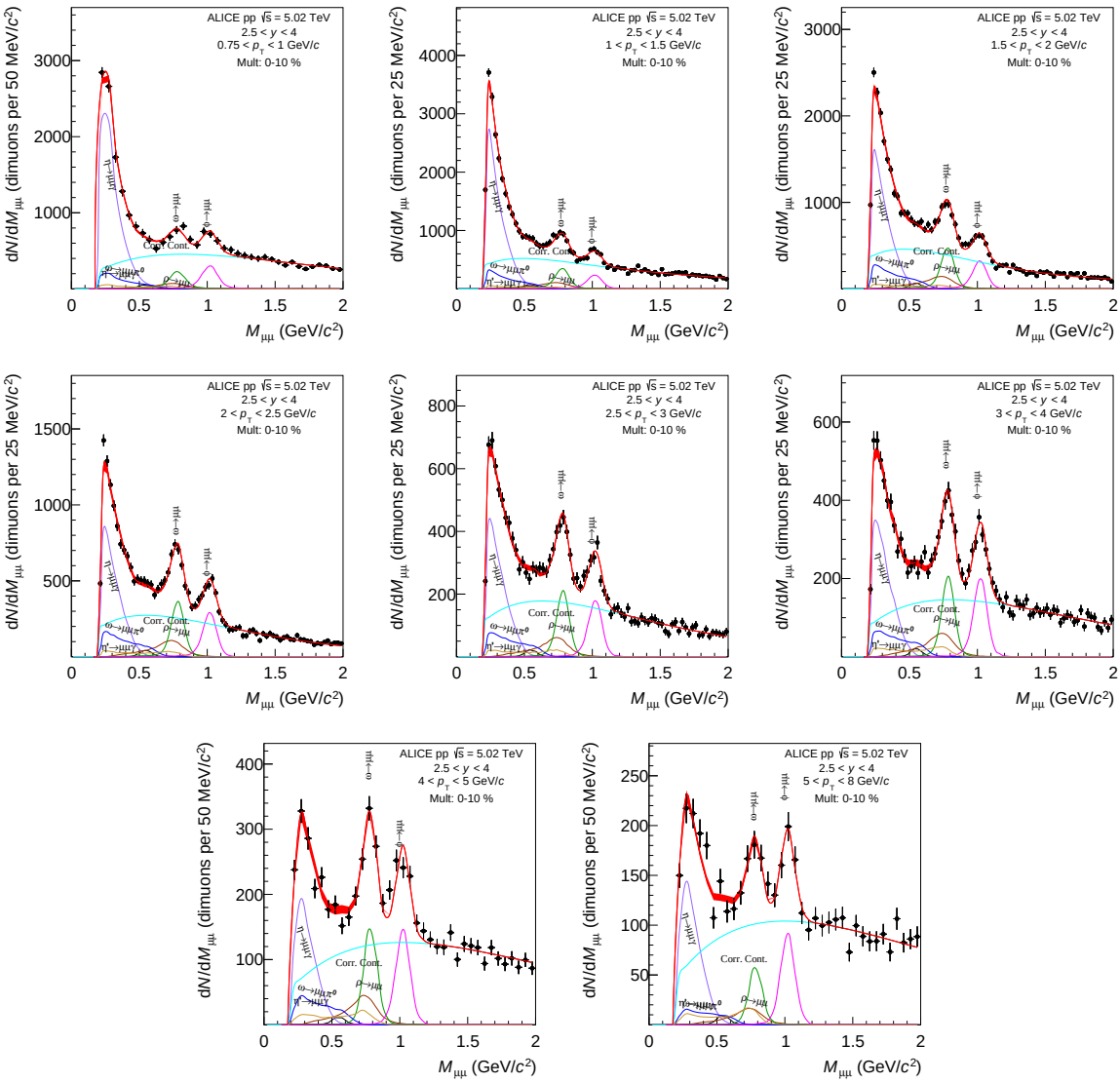

Figure F.15: Dimuon invariant mass spectrum in pp collisions at $\sqrt{s} = 5.02$ TeV for the 0-10 % multiplicity interval, in these spectra a expN was used to describe the continuum

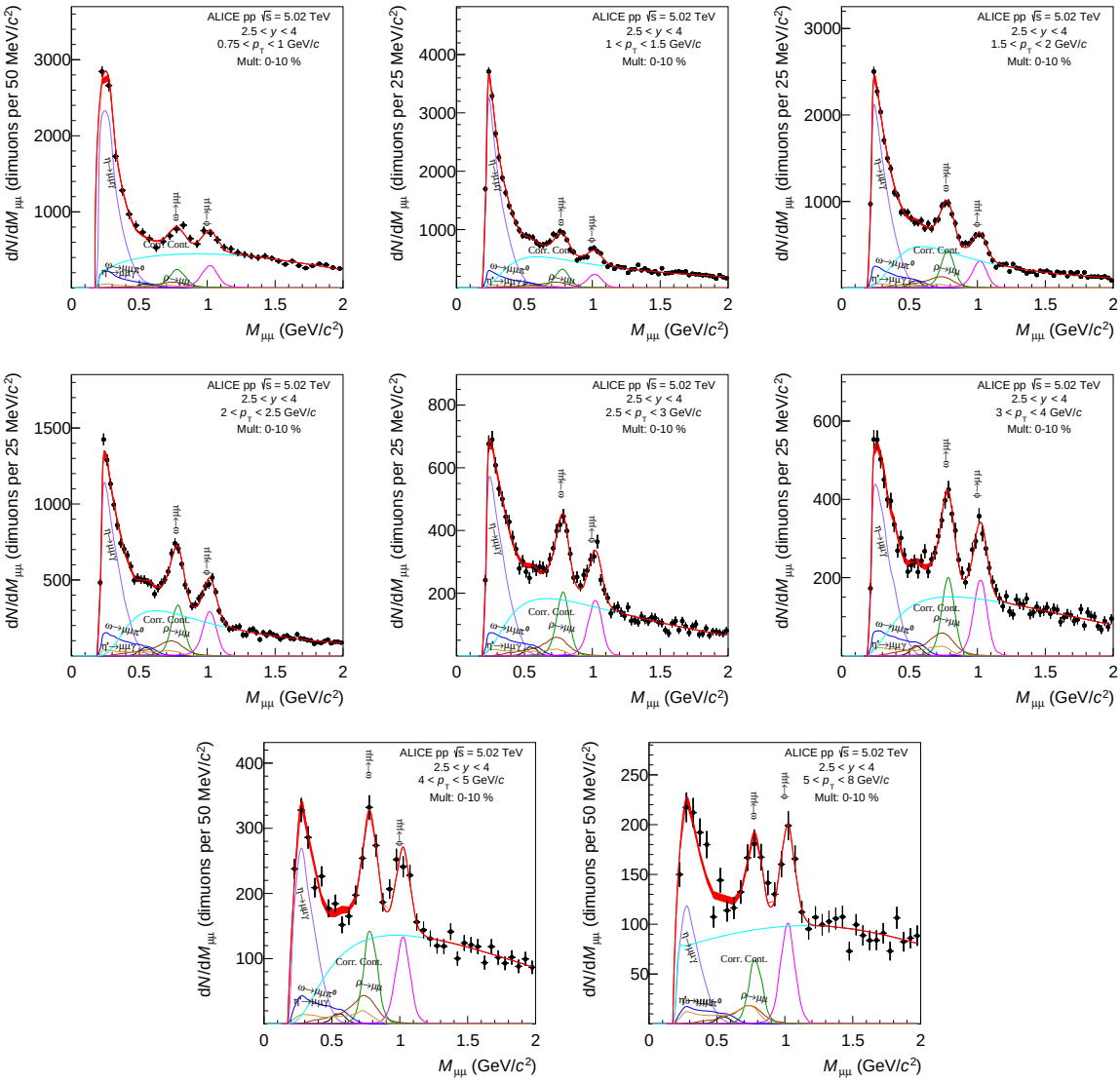

Figure F.16: Dimuon invariant mass spectrum in pp collisions at $\sqrt{s} = 5.02$ TeV for the 0-10 % multiplicity interval, in these spectra a VWG was used to describe the continuum

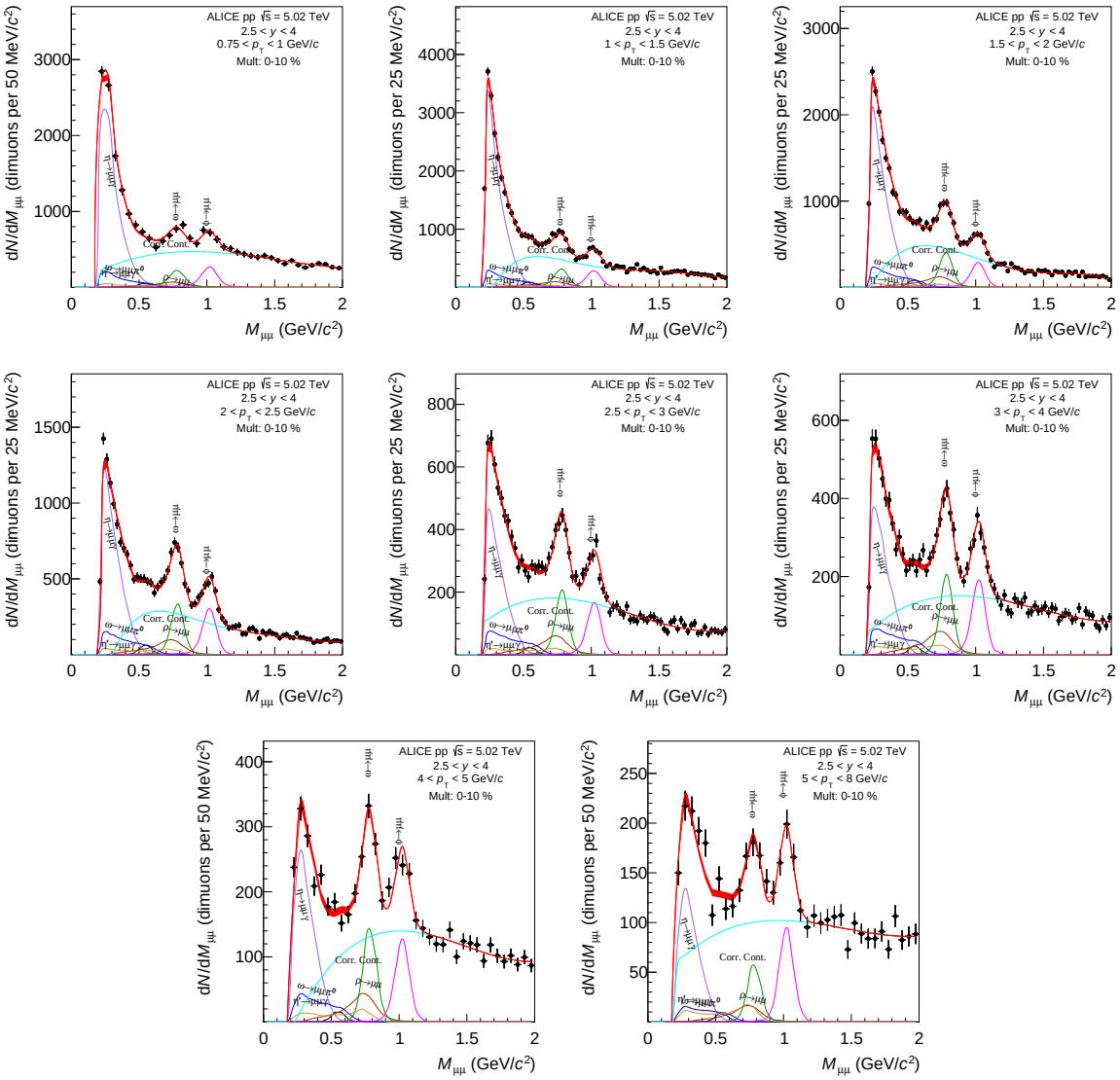

Figure F.17: Dimuon invariant mass spectrum in pp collisions at $\sqrt{s} = 5.02$ TeV for the 0-10 % multiplicity interval, in these spectra a polN was used to describe the continuum

F.3.2 Mass spectra in the 10-20 % interval

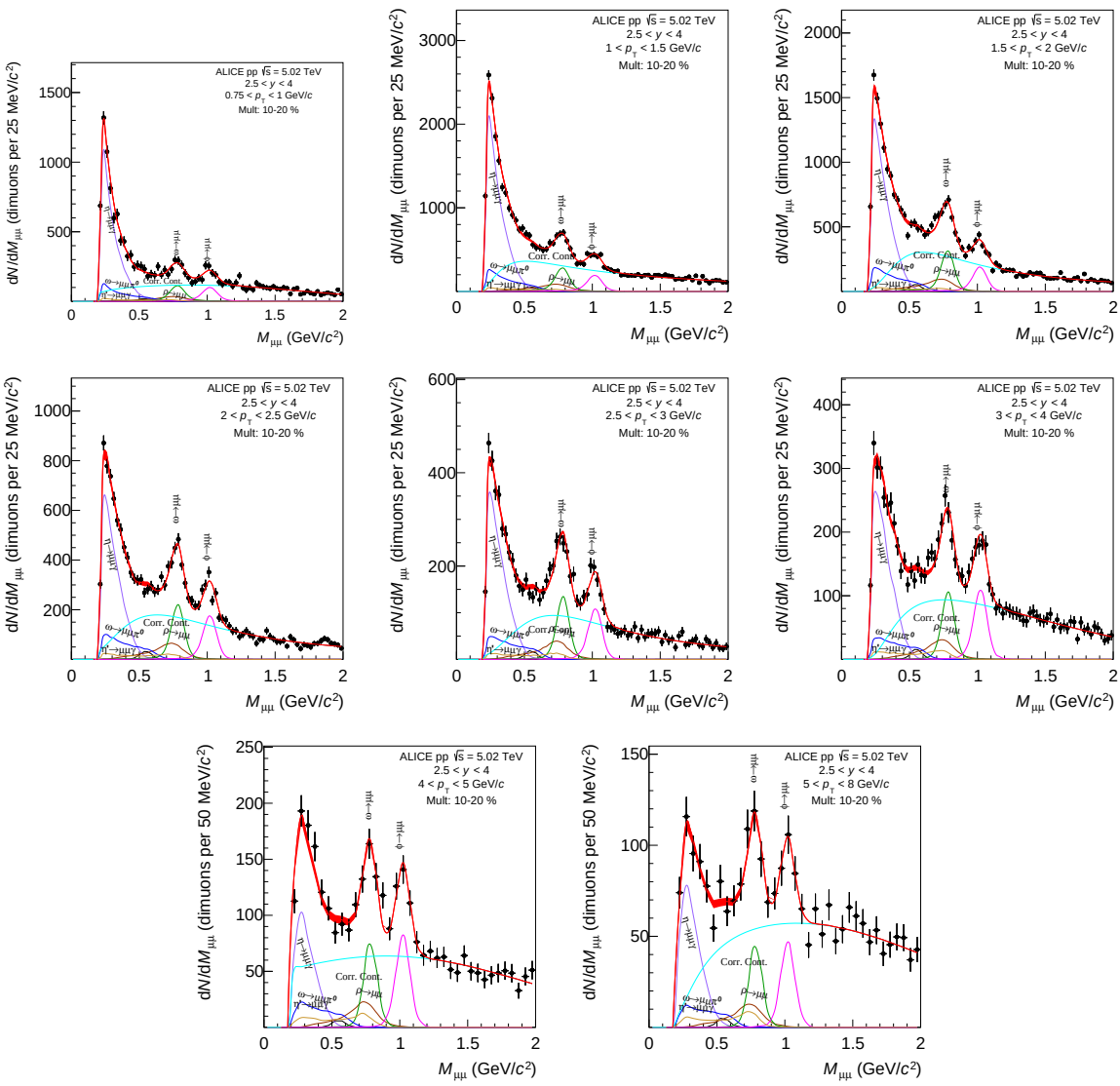

Figure F.18: Dimuon invariant mass spectrum in pp collisions at $\sqrt{s} = 5.02$ TeV for the 10-20 % multiplicity interval, in these spectra a VWG was used to describe the continuum

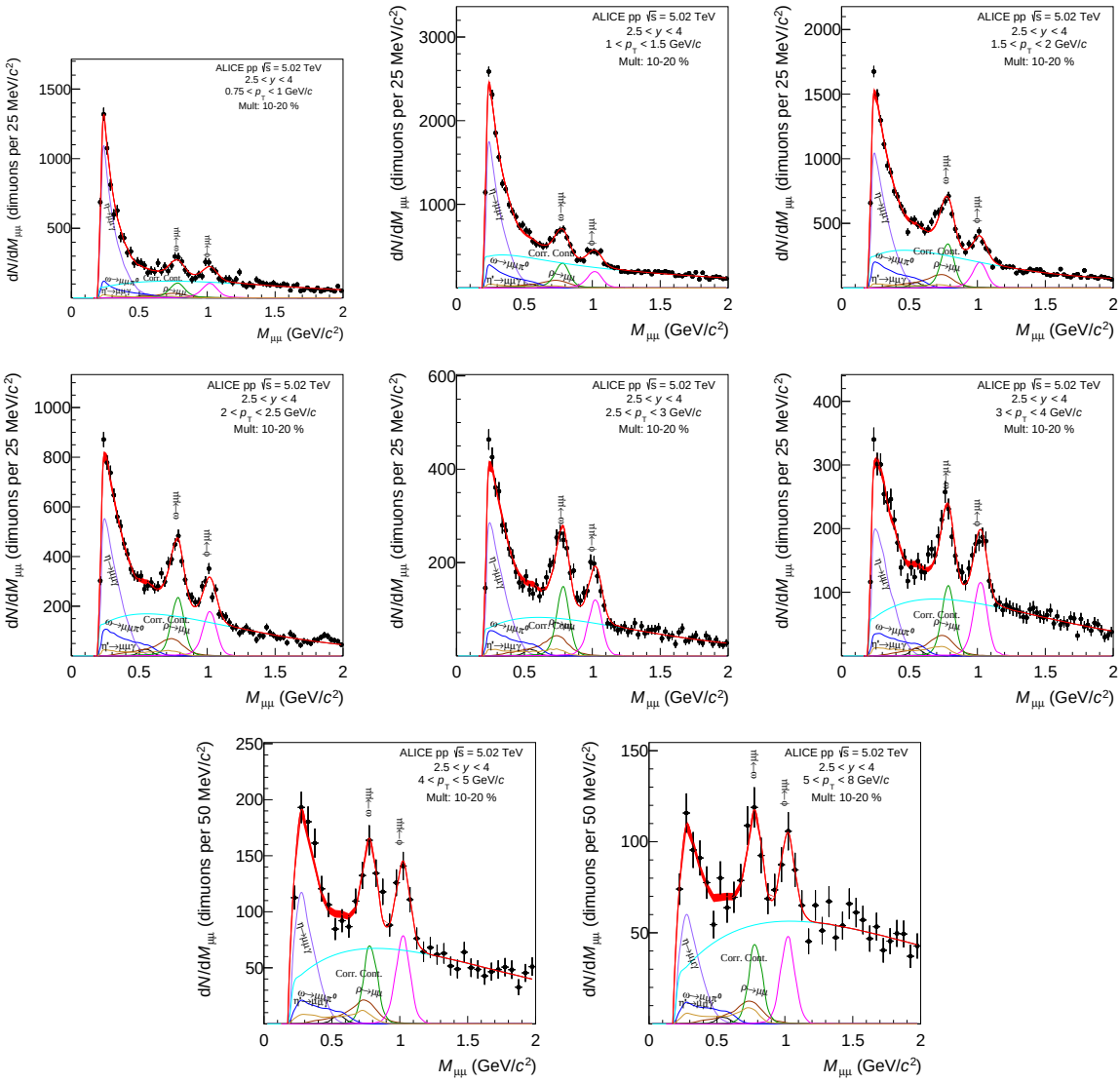

Figure F.19: Dimuon invariant mass spectrum in pp collisions at $\sqrt{s} = 5.02$ TeV for the 10-20 % multiplicity interval, in these spectra a expN was used to describe the continuum

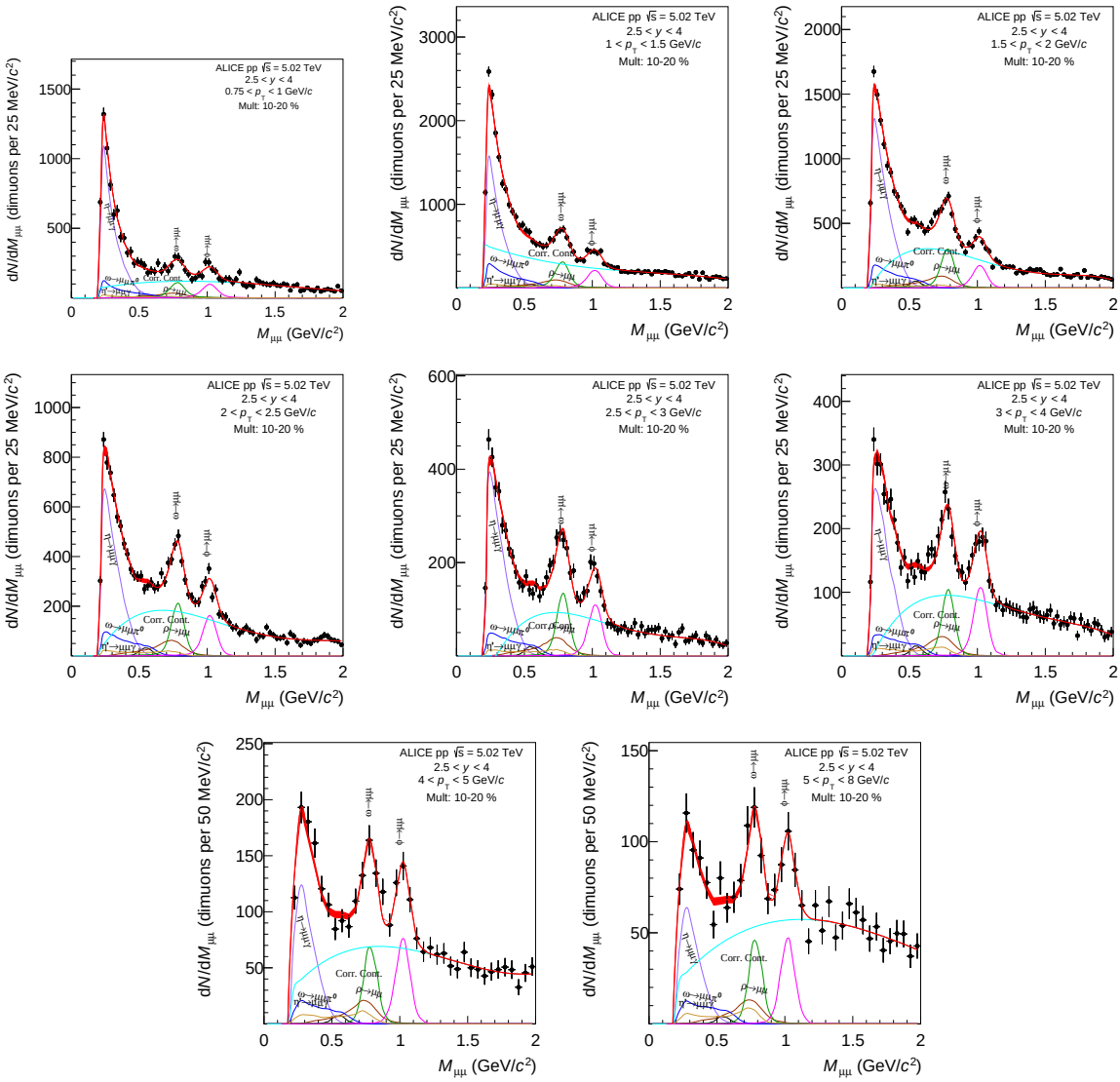

Figure F.20: Dimuon invariant mass spectrum in pp collisions at $\sqrt{s} = 5.02$ TeV for the 10-20 % multiplicity interval, in these spectra a polN was used to describe the continuum

F.3.3 Mass spectra in the 20-50 % interval

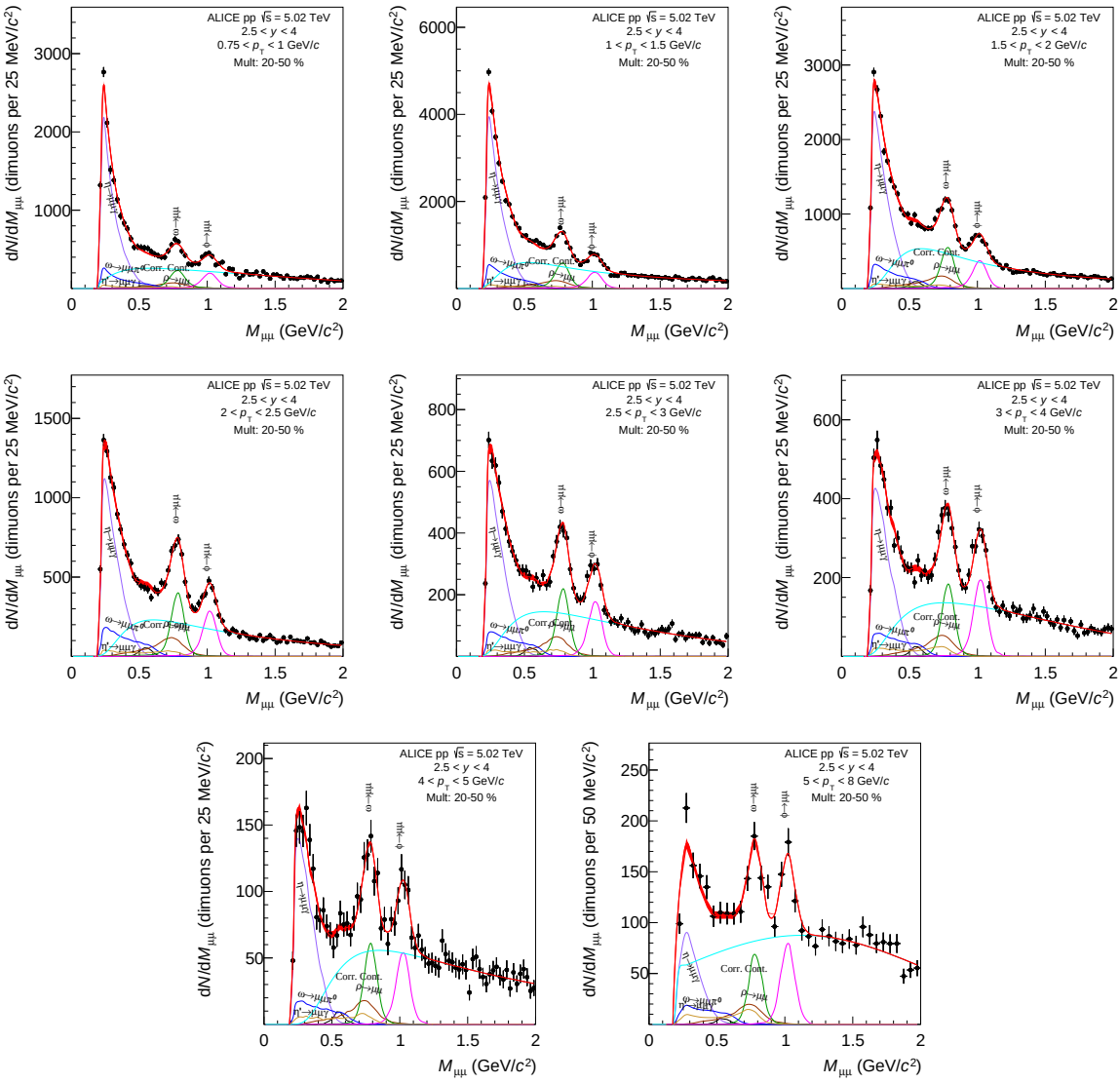

Figure F.21: Dimuon invariant mass spectrum in pp collisions at $\sqrt{s} = 5.02$ TeV for the 20-50 % multiplicity interval, in these spectra a VWG was used to describe the continuum

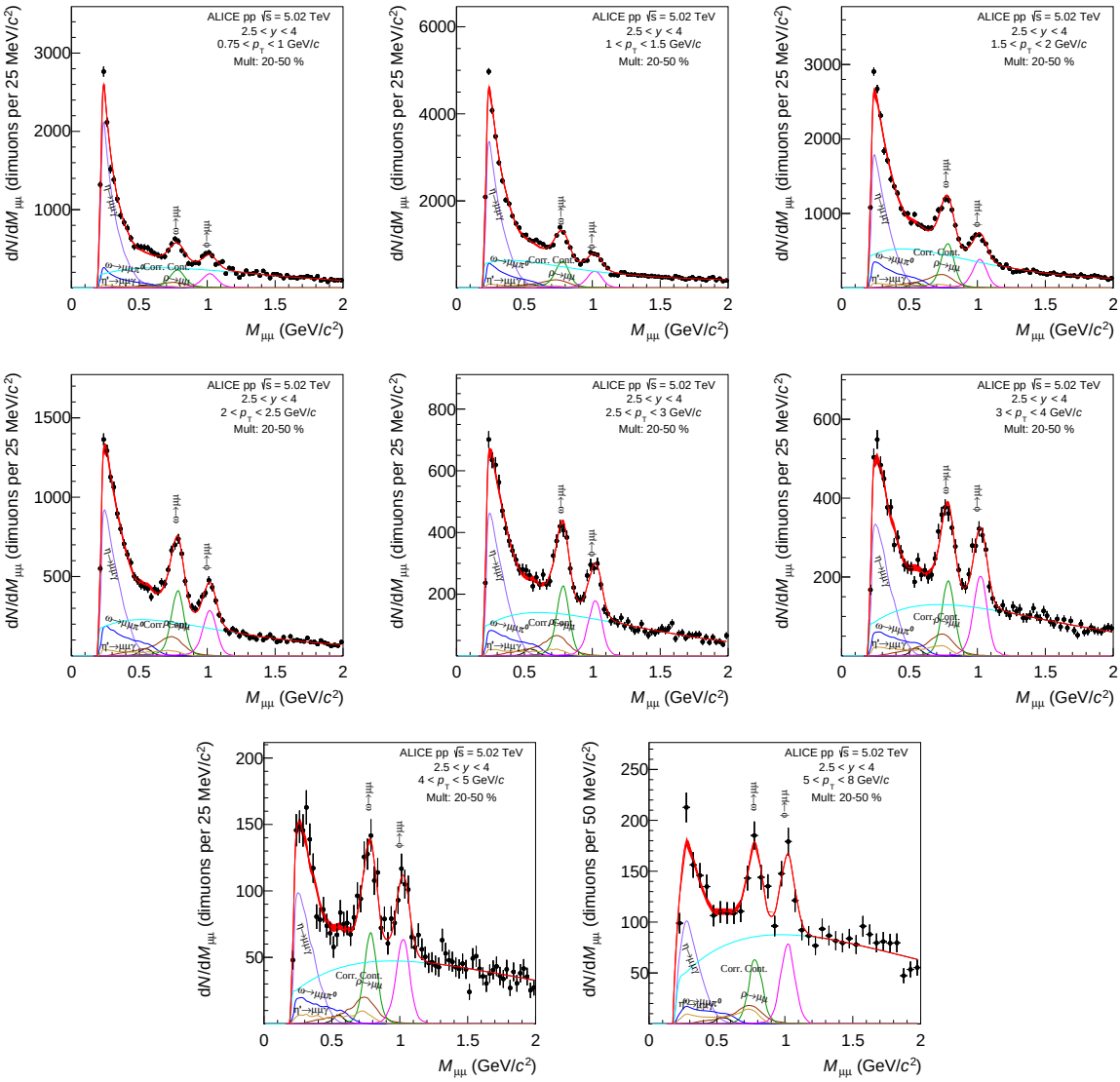

Figure F.22: Dimuon invariant mass spectrum in pp collisions at $\sqrt{s} = 5.02$ TeV for the 20-50 % multiplicity interval, in these spectra a expN was used to describe the continuum

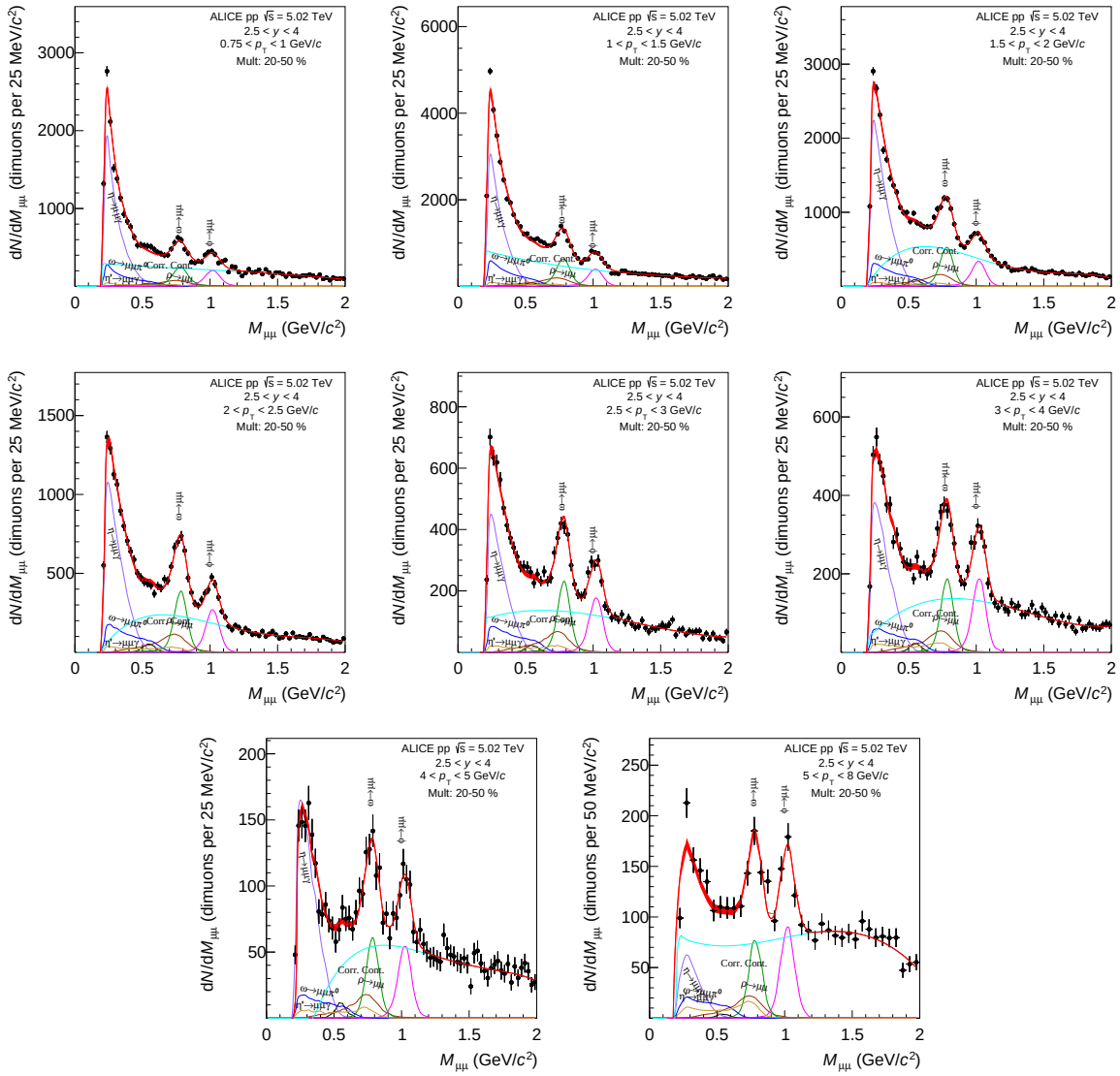

Figure F.23: Dimuon invariant mass spectrum in pp collisions at $\sqrt{s} = 5.02$ TeV for the 20-50 % multiplicity interval, in these spectra a polN was used to describe the continuum

F.3.4 Mass spectra in the 50-100 % interval

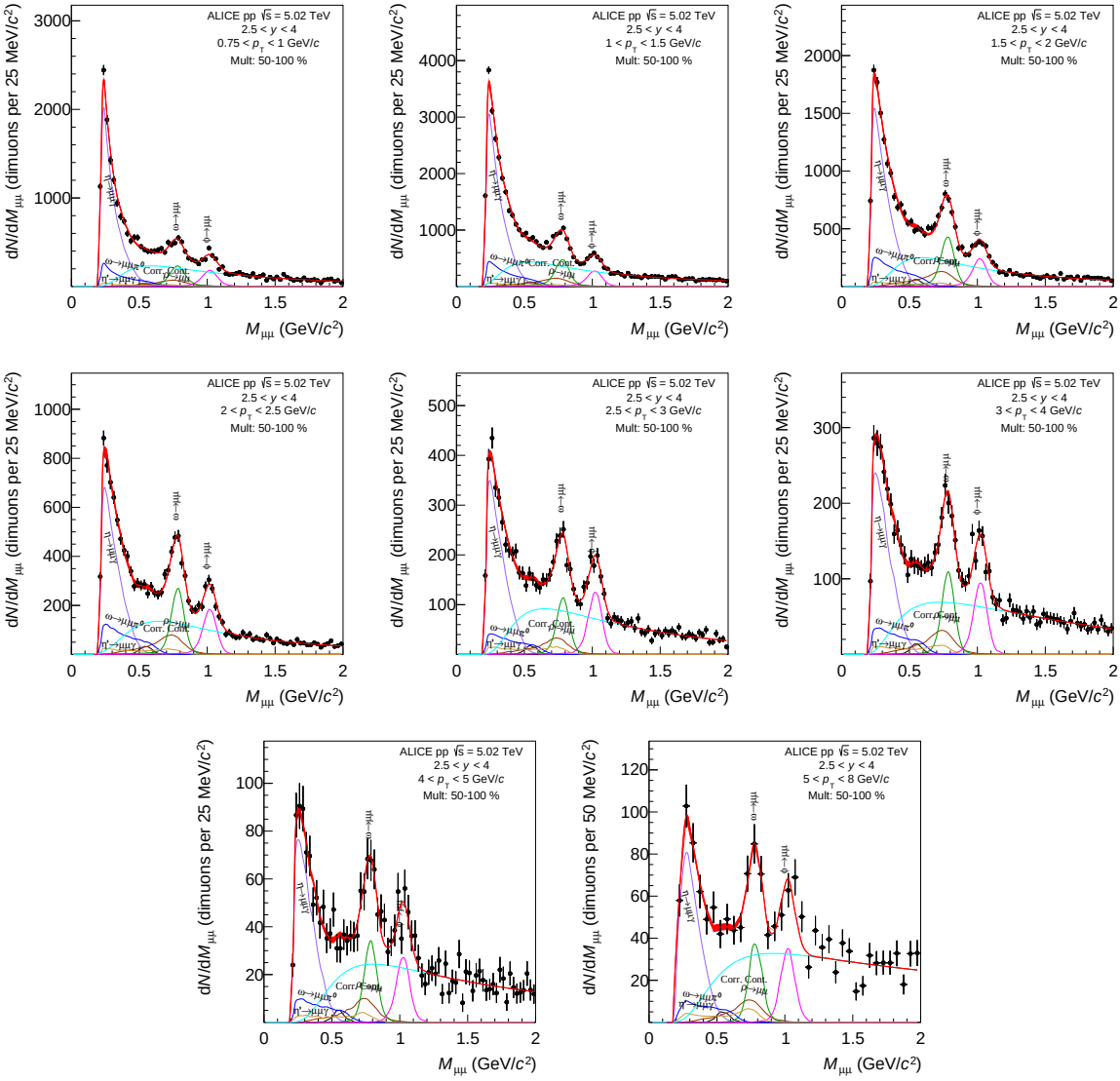

Figure F.24: Dimuon invariant mass spectrum in pp collisions at $\sqrt{s} = 5.02$ TeV for the 50-100 % multiplicity interval, in these spectra a VWG was used to describe the continuum

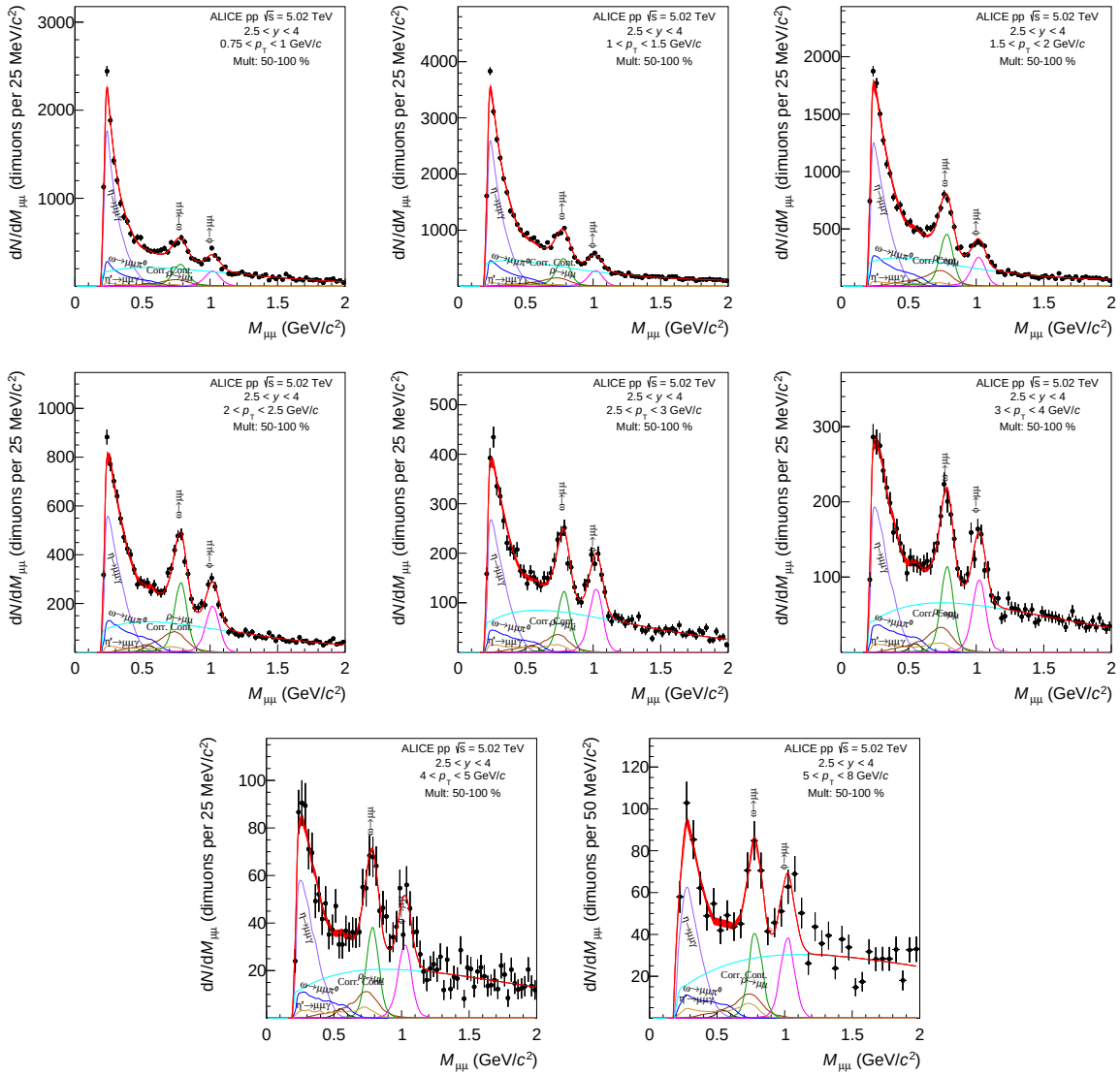

Figure F.25: Dimuon invariant mass spectrum in pp collisions at $\sqrt{s} = 5.02$ TeV for the 50-100 % multiplicity interval, in these spectra a expN was used to describe the continuum

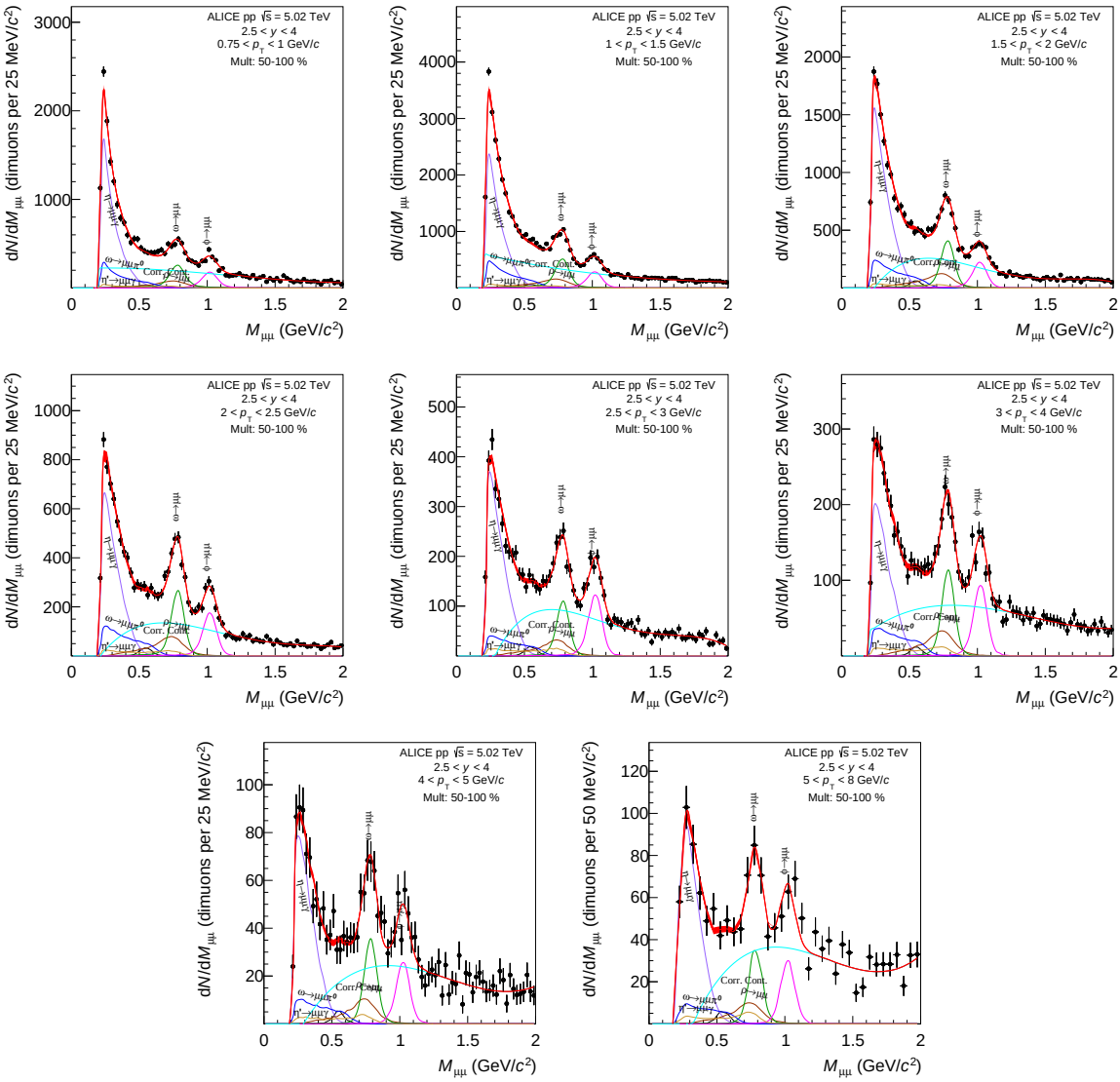

Figure F.26: Dimuon invariant mass spectrum in pp collisions at $\sqrt{s} = 5.02$ TeV for the 50-100 % multiplicity interval, in these spectra a polN was used to describe the continuum

F.3.5 Mass spectra in the 0-100 % interval

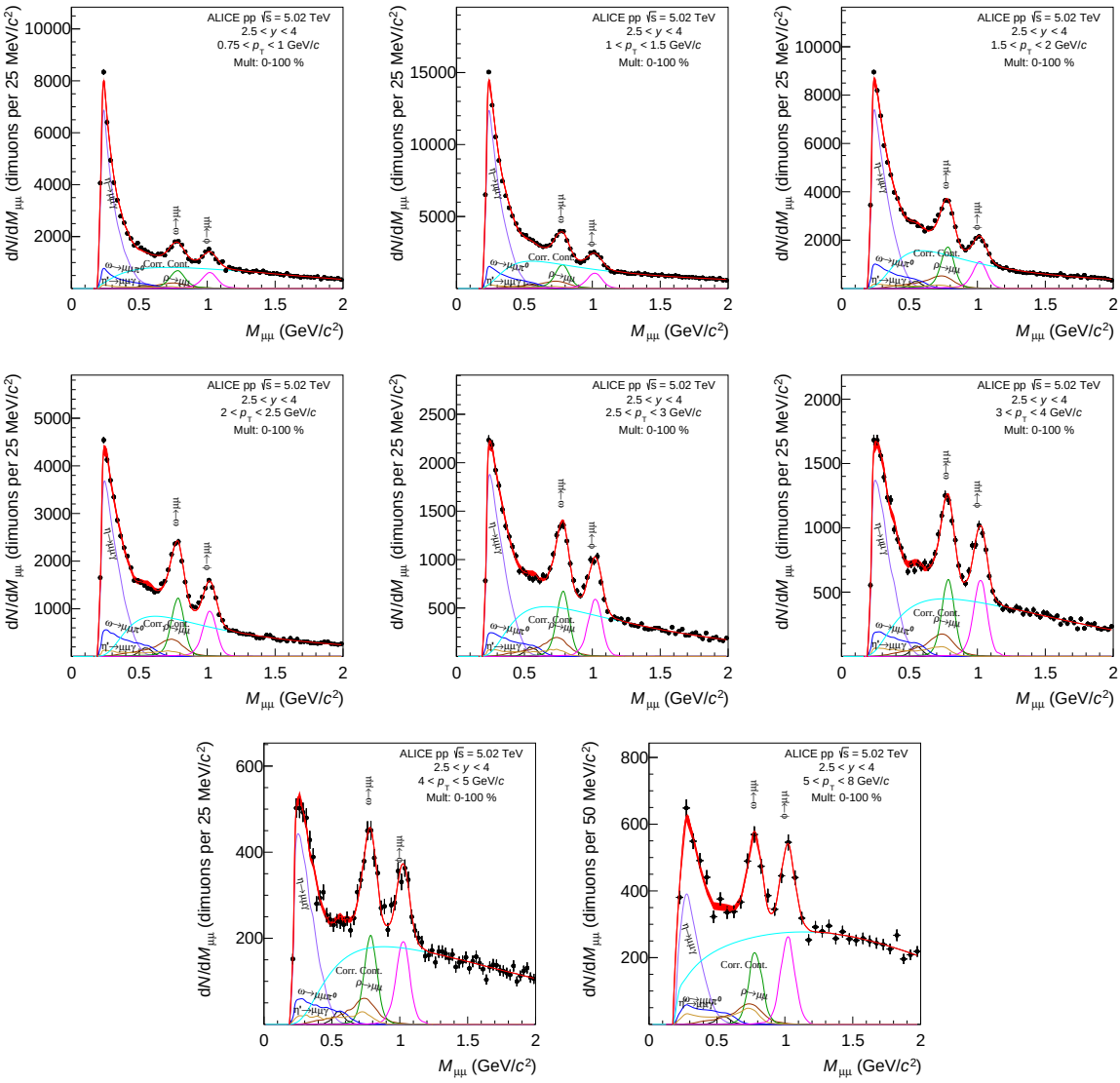

Figure F.27: Dimuon invariant mass spectrum in pp collisions at $\sqrt{s} = 5.02$ TeV for the 0-100 % multiplicity (integrated) interval, in these spectra a VWG was used to describe the continuum

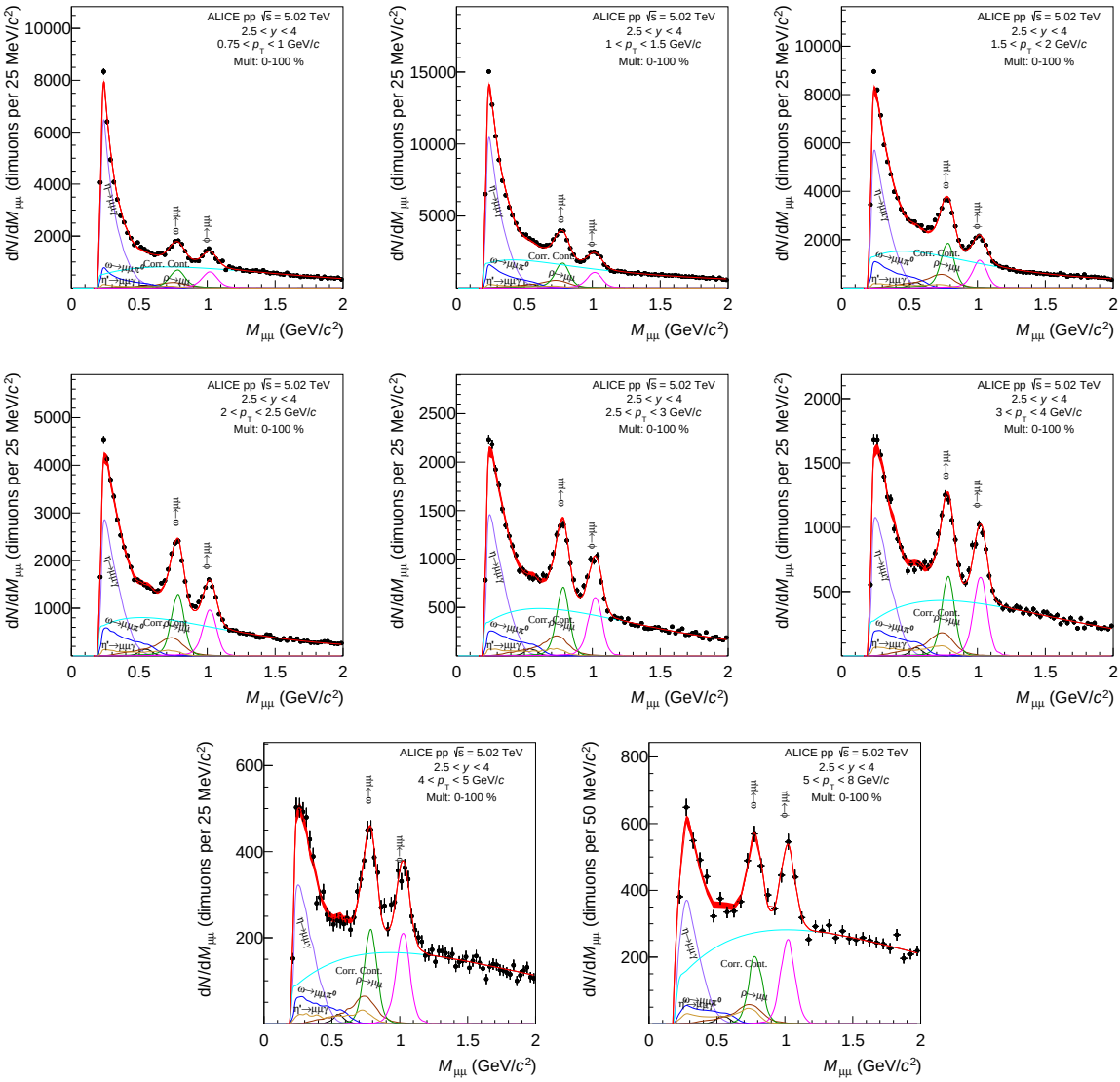

Figure F.28: Dimuon invariant mass spectrum in pp collisions at $\sqrt{s} = 5.02$ TeV for the 0-100 % multiplicity (integrated) interval, in these spectra a expN was used to describe the continuum

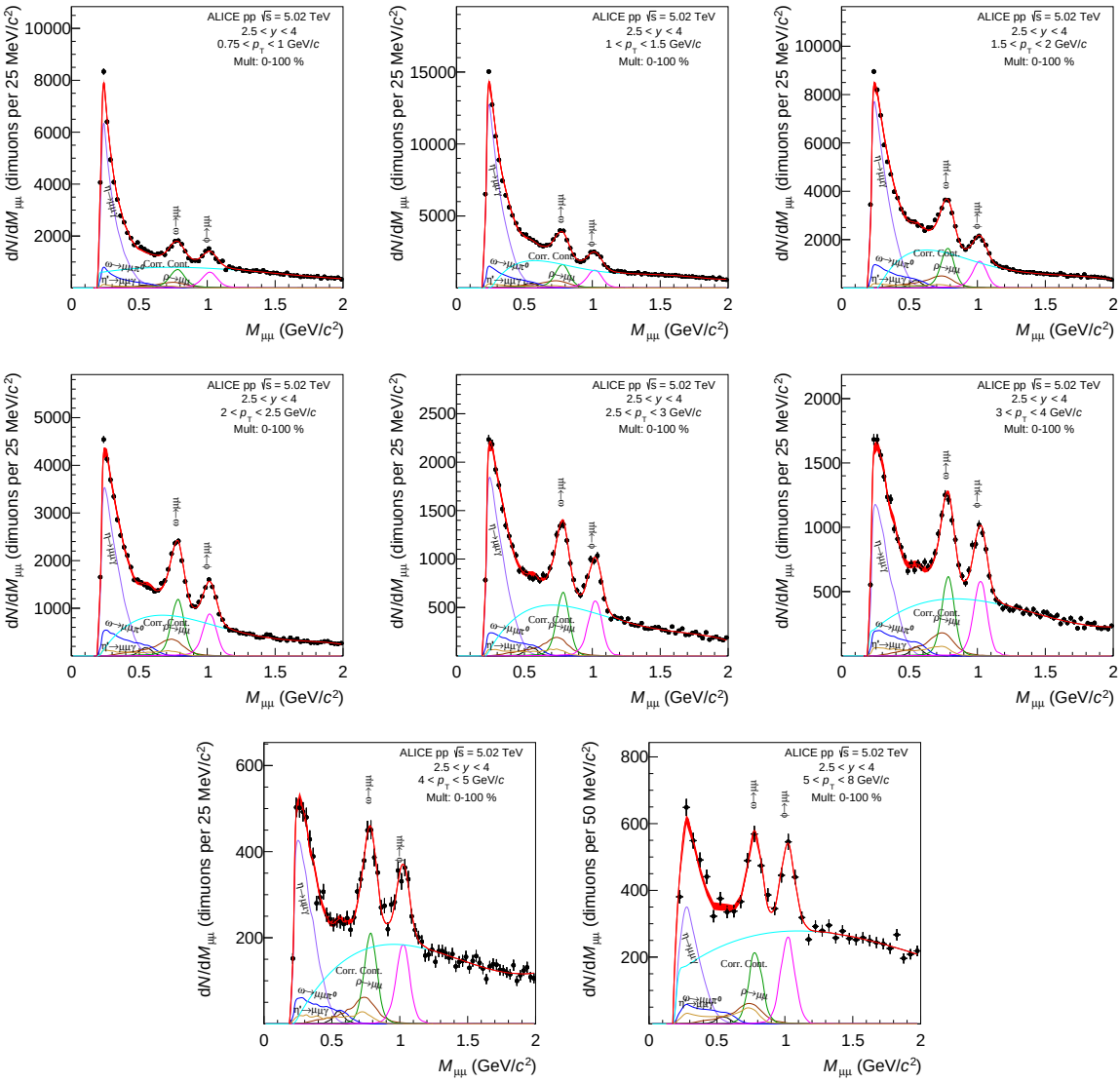

Figure F.29: Dimuon invariant mass spectrum in pp collisions at $\sqrt{s} = 5.02$ TeV for the 0-100 % multiplicity (integrated) interval, in these spectra a polN was used to describe the continuum

Bibliography

[1] Jaroslav Adam, Dagmar Adamova, Madan Mohan Aggarwal, G Aglieri Rinella, Michelangelo Agnello, Neelima Agrawal, Zubayer Ahammed, Shamim Ahmad, Sang Un Ahn, Salvatore Aiola, et al. Enhanced production of multi-strange hadrons in high-multiplicity proton–proton collisions. *Nature Physics*, 13(6):535–539, 2017.

[2] A. Einstein. Zur Elektrodynamik bewegter Körper. *Annalen der Physik*, 322(10):891–921, January 1905.

[3] M. Gell-Mann. A schematic model of baryons and mesons. *Physics Letters*, 8(3):214–215, February 1964.

[4] DONUT Collaboration, K. Kodama, et al. Observation of tau neutrino interactions. *Physics Letters B*, 504(3):218–224, April 2001.

[5] F. Abe and all. Observation of Top Quark Production in $p\overline{p}$ Collisions with the Collider Detector at Fermilab. *Physical Review Letters*, 74(14):2626–2631, April 1995.

[6] S. Abachi and all. Observation of the Top Quark. *Physical Review Letters*, 74(14):2632–2637, April 1995.

[7] Aad G. and all. Atlas Collaboration. Observation of a new particle in the search for the Standard Model Higgs boson with the ATLAS detector at the LHC. *Physics Letters B*, 716(1):1–29, September 2012.

[8] M. Tanabashi and al. Review of particle physics. *Phys. Rev. D*, 98:030001, Aug 2018.

[9] J. C. Collins and M. J. Perry. Superdense matter: Neutrons or asymptotically free quarks? *Phys. Rev. Lett.*, 34:1353–1356, May 1975.

[10] M. Dey, V.L. Eletsky, and B.L. Ioffe. Mixing of vector and axial mesons at finite temperature: an indication towards chiral symmetry restoration. *Physics Letters B*, 252(4):620 – 624, 1990.

[11] R. Hagedorn. Statistical thermodynamics of strong interactions at high-energies. *Nuovo Cim. Suppl.*, 3:147–186, 1965.

[12] Edward V. Shuryak. Quantum chromodynamics and the theory of superdense matter. *Physics Reports*, 61(2):71 – 158, 1980.

[13] Nicola Cabibbo and Giorgio Parisi. Exponential hadronic spectrum and quark liberation. *Physics Letters B*, 59(1):67–69, 1975.

[14] Kenneth G. Wilson. Confinement of quarks. *Phys. Rev. D*, 10:2445–2459, Oct 1974.

[15] Sourav Sarkar, Helmut Satz, and Bikash Sinha, editors. *The physics of the quark-gluon plasma*, volume 785. 2010.

[16] et al. Annala, E. Evidence for quark-matter cores in massive neutron stars. *Nat. Phys.*, 2020.

[17] J. D. Bjorken. Highly relativistic nucleus-nucleus collisions: The central rapidity region. *Phys. Rev. D*, 27:140–151, Jan 1983.

[18] A. Andronic, F. Arleo, R. Arnaldi, A. Beraudo, E. Bruna, D. Caffarri, Z. Conesa del Valle, J. G. Contreras, T. Dahms, A. Dainese, and et al. Heavy-flavour and quarkonium production in the lhc era: from proton–proton to heavy-ion collisions. *The European Physical Journal C*, 76(3), Feb 2016.

[19] S. Acharya and Alice Collaboration. Dielectron and heavy-quark production in inelastic and high-multiplicity proton-proton collisions at $\sqrt{\{\ s\ \}}$ = 13TeV. *Physics Letters B*, 788:505–518, January 2019.

[20] N. H. Christ, C. Dawson, T. Izubuchi, C. Jung, Q. Liu, R. D. Mawhinney, C. T. Sachrajda, A. Soni, and R. Zhou. η and $\eta\prime$ mesons from lattice qcd. *prl*, 105(24):241601, December 2010.

[21] P Petreczky. Lattice qcd at non-zero temperature. *Journal of Physics G: Nuclear and Particle Physics*, 39(9):093002, Aug 2012.

[22] Hendrik van Hees and Ralf Rapp. Dilepton radiation at the CERN super-proton synchrotron. *nphysa*, 806(1):339–387, June 2008.

[23] Szabocls Borsanyi, Zoltan Fodor, Christian Hoelbling, Sandor D. Katz, Stefan Krieg, and Kalman K. Szabo. Full result for the QCD equation of state with 2+1 flavors. *Phys. Lett. B*, 730:99–104, 2014.

[24] Szabolcs Borsányi, Zoltán Fodor, Christian Hoelbling, Sándor D. Katz, Stefan Krieg, and Kálmán K. Szabó. Full result for the qcd equation of state with 2+1 flavors. *Physics Letters B*, 730:99 – 104, 2014.

[25] J Stachel, A Andronic, P Braun-Munzinger, and K Redlich. Confronting LHC data with the statistical hadronization model. *Journal of Physics: Conference Series*, 509:012019, may 2014.

[26] B. Abelev and al. Multi-strange baryon production at mid-rapidity in pb–pb collisions at snn=2.76 tev. *Physics Letters B*, 728:216 – 227, 2014.

[27] B. Abelev and al. $K^*(892)^0$ and $\phi(1020)$ production in pb-pb collisions at $\sqrt{s_{NN}} = 2.76$ tev. *Phys. Rev. C*, 91:024609, Feb 2015.

[28] Jaroslav Adam et al. Production of light nuclei and anti-nuclei in pp and Pb-Pb collisions at energies available at the CERN Large Hadron Collider. *Phys. Rev. C*, 93(2):024917, 2016.

[29] Bo Andersson, G. Gustafson, G. Ingelman, and T. Sjostrand. Parton Fragmentation and String Dynamics. *Phys. Rept.*, 97:31–145, 1983.

[30] Johann Rafelski and Berndt Muller. Strangeness production in the quark-gluon plasma. *Phys. Rev. Lett.*, 48:1066–1069, Apr 1982.

[31] F. Becattini. Universality of thermal hadron production in pp, $p\overline{p}$ and e^+e^- collisions. *arXiv e-prints*, pages hep–ph/9701275, January 1997.

[32] D.S.D. Albuquerque. Hadronic resonances, strange and multi-strange particle production in xe-xe and pb-pb collisions with alice at the lhc. *Nucl. Phys. A*, 982:823–826, 2019.

[33] Tianhao Shao, Jinhui Chen, Che Ming Ko, and Zi-Wei Lin. Enhanced production of strange baryons in high-energy nuclear collisions from a multiphase transport model. *Physical Review C*, 102(1), Jul 2020.

[34] ALICE Collaboration. Multi-strange baryon production in p-pb collisions at $\sqrt{s}$ NN=5.02$tev, 2015$.

[35] J Stachel, A Andronic, P Braun-Munzinger, and K Redlich. Confronting lhc data with the statistical hadronization model. 509(012019):1311–4662, 2014.

[36] A Andronic, P Braun-Munzinger, J Stachel, and M Winn. Interacting hadron resonance gas meets lattice qcd. *Physics Letters B*, 718(1):80–85, 2012.

[37] Peter Braun-Munzinger, Krzysztof Redlich, and Johanna Stachel. Particle production in heavy ion collisions. *Quark–Gluon Plasma 3*, page 491–599, Jan 2004.

[38] F. Becattini, J. Manninen, and M. Gaździcki. Energy and system size dependence of chemical freeze-out in relativistic nuclear collisions. *Physical Review C*, 73(4), Apr 2006.

[39] B. C. Maglic, L. W. Alvarez, A. H. Rosenfeld, and M. L. Stevenson. Evidence for a $t = 0$ three-pion resonance. *Phys. Rev. Lett.*, 7:178–182, Sep 1961.

[40] Nguyen Huu Xuong and Gerald R. Lynch. Evidence confirming the $t = 0$ three-pion resonance. *Phys. Rev. Lett.*, 7:327–329, Oct 1961.

[41] P. L. Connolly, E. L. Hart, K. W. Lai, G. London, G. C. Moneti, R. R. Rau, N. P. Samios, I. O. Skillicorn, S. S. Yamamoto, M. Goldberg, M. Gundzik, J. Leitner, and S. Lichtman. Existence and properties of the ϕ meson. *Phys. Rev. Lett.*, 10:371–376, Apr 1963.

[42] A. Adare et al. Measurement of neutral mesons in p+p collisions at $\sqrt{(s)}$= 200 GeV and scaling properties of hadron production. *Phys. Rev. D*, 83:052004, 2011.

[43] A. Adare and al. Nuclear modification factors of ϕ mesons in $d+\mathbf{Au}$, $\mathbf{Cu}+\mathbf{Cu}$, and $\mathbf{Au}+\mathbf{Au}$ collisions at $\sqrt{s_{NN}} = 200\mathbf{GeV}$. *Phys. Rev. C*, 83:024909, Feb 2011.

[44] A. Adare et al. Production of ω mesons in $p + p$, d+Au, Cu+Cu, and Au+Au collisions at $\sqrt{s_N N} = 200$ GeV. *Phys. Rev. C*, 84:044902, 2011.

[45] Constantino Tsallis. Possible Generalization of Boltzmann-Gibbs Statistics. *J. Statist. Phys.*, 52:479–487, 1988.

[46] B. I. Abelev et al. Strange particle production in p+p collisions at $\sqrt{s}$ = 200 GeV. *Phys. Rev.*, C75:064901, 2007.

[47] Abelev and al. Enhanced strange baryon production in au+au collisions compared to $p + p$ at $\sqrt{s_{NN}} = 200$ gev. *Phys. Rev. C*, 77:044908, Apr 2008.

[48] J. Adam, Dagmar Adamova, M.M. Aggarwal, Gianluca Aglieri Rinella, Michelangelo Agnello, N. Agrawal, Zubayer Ahammed, Shakeel Ahmad, S.U. Ahn, Salvatore Aiola, A. Akindinov, Sartaj Alam, D. Aleksandrov, Borri Alessandro, D. Alexandre, R. Molina, A. Alici, Anton Alkin, Julián Almaraz, and M. Zyzak. Multi-strange baryon production in p–pb collisions at $\sqrt{s_{NN}}$ = 5.02 tev. *Physics Letters B*, 758, 05 2016.

[49] Vardan Khachatryan, AM Sirunyan, Armen Tumasyan, W Adam, T Bergauer, M Dragicevic, J Erö, C Fabjan, M Friedl, R Frühwirth, et al. Observation of long-range, near-side angular correlations in proton-proton collisions at the lhc. *Journal of High Energy Physics*, 2010(9):91, 2010.

[50] ALICE collaboration et al. Production of σ (1385)$\pm$and ξ (1530) 0 in p–pb collisions at snn= 5.02 tev. *European Physical Journal C*, 77(6):389, 2017.

[51] Shreyasi Acharya et al. Multiplicity dependence of K*(892)^0 and ϕ(1020) production in pp collisions at $\sqrt{s}$ =13 TeV. *Phys. Lett. B*, 807:135501, 2020.

[52] The ALICE Collaboration. Performance of the ALICE VZERO system. *Journal of Instrumentation*, 8(10):P10016, October 2013.

[53] Michael L. Miller, Klaus Reygers, Stephen J. Sanders, and Peter Steinberg. Glauber Modeling in High-Energy Nuclear Collisions. *Annual Review of Nuclear and Particle Science*, 57(1):205–243, November 2007.

[54] D. Swoboda, C. De Almeida, A. Meynet, H. Taureg, and A. Tournaire. Results from the alice dipole magnet commissioning. *IEEE Transactions on Applied Superconductivity*, 16(2):1696–1699, 2006.

[55] *ALICE dimuon forward spectrometer: addendum to the Technical Design Report.* Technical Design Report ALICE. CERN, Geneva, 2000.

[56] D. Evans and al. The ALICE central trigger system. *14th IEEE-NPSS Real Time Conference*, 2005.

[57] E Bruna, A Dainese, M Masera, and F Prino. Vertex reconstruction for proton-proton collisions in ALICE. Nov 2009.

[58] S. van der meer, isr-po/68-31, kek 68-64.

[59] ALICE Collaboration. Alice 2017 luminosity determination for pp collisions at $\sqrt{s}$ = 5 tev.

[60] A. Uras. Low mass dimuon production in p–a collisions at $\sqrt{s}$

NN= $27.5 gev with na 60. J. Phys. G : Nucl. Part. Phys., 3, 2011.$

[61] NA60 Collaboration et al. Precision study of the $\eta \rightarrow \mu^+\mu^-\gamma$ and $\omega \rightarrow \mu^+\mu^-\pi^0$ electromagnetic transition form-factors and of the $\rho \rightarrow \mu^+\mu^-$ line shape in na60. *arXiv preprint arXiv:1608.07898*, 2016.

[62] L.G. Landsberg. Electromagnetic decays of light mesons. *Physics Reports*, 128(6):301 – 376, 1985.

[63] A. De Falco E.A.R. Casula. ϕ production at forward rapidity in pb–pb collisions at $\sqrt{s_{\rm NN}} = 2.76$ tev.

[64] A. De Falco E.A.R. Casula. ϕ meson production at forward rapidity in pp collisions at $\sqrt{s}$ = 5.02 tev.

[65] Peter Z Skands. Tuning monte carlo generators: the perugia tunes. *Physical Review D*, 82(7):074018, 2010.

[66] R Brun, F Bruyant, M Maire, A C McPherson, and P Zanarini. *GEANT 3: user's guide Geant 3.10, Geant 3.11; rev. version.* CERN, Geneva, 1987.

[67] S. Agostinelli et al. GEANT4: A Simulation toolkit. *Nucl. Instrum. Meth. A*, 506:250–303, 2003.

[68] R. Aaij et al. LHCb Collaboration. Prompt charm production in pp collisions at $\sqrt{s}$ = 7 tev. *Nuclear Physics B*, 871:1–20, 2013.

[69] R. Aaij et al. LHCb Collaboration. Measurement of σ(pp$\rightarrow$ bbx^{-}) at $\sqrt{s}$ = 7 tev in the forward region. *Phys. Lett. B*, 694:209–216, 2010.

[70] B. Abelev et al. ALICE Collaboration. Light vector meson production in pp collisions at $\sqrt{s}$ = 7 tev. *Phys. Lett. B*, 710:557–568, 2012.

[71] Alessandro De Falco. NA60 results on phi production in the hadronic and leptonic channels in In-In collisions at 158-GeV. *Nucl. Phys. A*, 830:753C–756C, 2009.

[72] Torbjörn Sjöstrand, Stefan Ask, Jesper R. Christiansen, Richard Corke, Nishita Desai, Philip Ilten, Stephen Mrenna, Stefan Prestel, Christine O. Rasmussen, and Peter Z. Skands. An introduction to PYTHIA 8.2. *Computer Physics Communications*, 191:159–177, June 2015.

[73] R. Engel. Photoproduction within the two component dual parton model. 1. Amplitudes and cross-sections. *Z. Phys.*, C66:203–214, 1995.

[74] R. Engel and J. Ranft. Hadronic photon-photon interactions at high-energies. *Phys. Rev.*, D54:4244–4262, 1996.

[75] Rick Field. Physics at the Tevatron. *Acta Phys. Polon.*, B39:2611–2672, 2008.

[76] C. M. Buttar, D. Clements, I. Dawson, and A. Moraes. Simulations of minimum bias events and the underlying event, MC tuning and predictions for the LHC. *Acta Phys. Pol. B*, 35:433, 2004.

[77] J. Adam et al. (ALICE Collaboration). J/ψ suppression at forward rapidity in pb–pb collisions at $\sqrt{s_{NN}}$ = 5.02 tev. *Phys. Lett. B*, 766:212–224, 2017.

[78] A. Uras B. Cheynis, B. Teyssier. Measurement of ω and ϕ-meson production at forward rapidity in pp collisions at $\sqrt{s}$ = 13 tev.

[79] Cheuk-Yin Wong and Grzegorz Wilk. Tsallis fits toptspectra and multiple hard scattering inppcollisions at the lhc. *Physical Review D*, 87(11), Jun 2013.

[80] S. Acharya and al. $K^*(892)^0$ and $\phi(1020)$ production at midrapidity in pp collisions at $\sqrt{s} = 8$ tev. *Phys. Rev. C*, 102:024912, Aug 2020.

[81] J. Adam et al. (ALICE Collaboration). ϕ-meson production at forward rapidity in p-pb collisions at $\sqrt{s}$

NN$= 5.02 tevandinppcollisionsat\sqrt{s}$ = 2.76 tev. *Phys. Lett. B*, 768:203–217, 2017.

[82] B. Abelev et al. (ALICE Collaboration). Light vector meson production in pp collisions at $\sqrt{s}$ = 7 tev. *Phys. Lett. B*, 710:557–568, 2012.

[83] Shreyasi Acharya et al. Evidence of rescattering effect in Pb-Pb collisions at the LHC through production of $\mathrm{K}^*(892)^0$ and $\phi(1020)$ mesons. *Phys. Lett.*, B802:135225, 2020.

[84] Shreyasi Acharya et al. $\mathrm{K}^*(892)^0$ and $\phi(1020)$ production at midrapidity in pp collisions at $\sqrt{s}$ = 8 TeV. 2019.

[85] V. Papikyan A. Grigoryan, H. Gulkanyan. Analysis of forward inclusive production of ϕ(1020) meson via dimuon channel in pp collisions at $\sqrt{s}$ = 8 tev.

[86] Jaroslav Adam et al. ϕ-meson production at forward rapidity in p-Pb collisions at $\sqrt{s_{\mathrm{NN}}}$ = 5.02 TeV and in pp collisions at $\sqrt{s}$ = 2.76 TeV. *Phys. Lett.*, B768:203–217, 2017.

[87] B. Abelev et al. Light vector meson production in pp collisions at $\sqrt{s} = 7$ TeV. *Phys. Lett. B*, 710:557–568, 2012.

[88] K. Werner, Iu. Karpenko, M. Bleicher, T. Pierog, and S. Porteboeuf-Houssais. Jets, bulk matter, and their interaction in heavy ion collisions at several TeV. *Phys. Rev. C*, 85:064907, 2012.

[89] H. J. Drescher, M. Hladik, S. Ostapchenko, T. Pierog, and K. Werner. Parton based Gribov-Regge theory. *Phys. Rept.*, 350:93–289, 2001.

[90] K. Werner, B. Guiot, Iu. Karpenko, and T. Pierog. Analyzing radial flow features in p-Pb and p-p collisions at several TeV by studying identified-particle production with the event generator EPOS3. *Phys. Rev. C*, 89:064903, 2014.

[91] A Capella, U Sukhatme, C-I Tan, and J Tran Thanh Van. Dual parton model. *Physics Reports*, 236(4-5):225–329, 1994.

[92] Peter Skands, Stefano Carrazza, and Juan Rojo. Tuning PYTHIA 8.1: the Monash 2013 Tune. *Eur. Phys. J.*, C74(8):3024, 2014.

[93] Constantin Loizides, Jason Kamin, and David d'Enterria. Improved Monte Carlo Glauber predictions at present and future nuclear colliders. *Phys. Rev.*, C97(5):054910, 2018. [erratum: Phys. Rev.C99,no.1,019901(2019)].

[94] D Elia, J.F Grosse-Oetringhaus, M Nicassio, and T Virgili. The pixel detector based tracklet reconstruction algorithm in ALICE. Technical Report ARDA-Note-2009-005, CERN, Geneva, Nov 2009.

[95] K. Werner, B. Guiot, Iu. Karpenko, and T. Pierog. Analyzing radial flow features in p-pb and p-p collisions at several tev by studying identified-particle production with the event generator epos3. *Phys. Rev. C*, 89:064903, Jun 2014.

[96] J. Adam, D. Adamová, M. M. Aggarwal, G. Aglieri Rinella, M. Agnello, N. Agrawal, Z. Ahammed, I. Ahmed, S. U. Ahn, and et al. Charged-particle multiplicities in proton–proton collisions at $\sqrt{s} = 0.9$ s = 0.9 to 8 tev. *The European Physical Journal C*, 77(1), Jan 2017.

[97] B. Abelev and all. Light vector meson production in pp collisions at s=7 tev. *Physics Letters B*, 710(4):557 – 568, 2012.

[98] Stefan Höche. Introduction to parton-shower event generators. In *Journeys Through the Precision Frontier: Amplitudes for Colliders: TASI 2014 Proceedings of the 2014 Theoretical Advanced Study Institute in Elementary Particle Physics*, pages 235–295. World Scientific, 2016.

[99] A Ortiz Velasquez, Peter Christiansen, E Cuautle Flores, IA Maldonado Cervantes, and Guy Paić. Color reconnection and flowlike patterns in p p collisions. *Physical review letters*, 111(4):042001, 2013.

[100] Christian Bierlich, Gösta Gustafson, Leif Lönnblad, and Andrey Tarasov. Effects of Overlapping Strings in pp Collisions. *JHEP*, 03:148, 2015.

[101] TS Biro, Holger Bech Nielsen, and Joern Knoll. Colour rope model for extreme relativistic heavy ion collisions. *Nuclear Physics B*, 245:449–468, 1984.

[102] Andrzej Bialas and Wieslaw Czyz. Chromoelectric flux tubes and the transverse-momentum distribution in high-energy nucleus-nucleus collisions. *Physical Review D*, 31(1):198, 1985.

[103] Hans Joachim Drescher, M Hladik, S Ostapchenko, T Pierog, and Klaus Werner. Parton-based gribov–regge theory. *Physics Reports*, 350(2-4):93–289, 2001.

[104] Peter Zeiler Skands. Tuning Monte Carlo Generators: The Perugia Tunes. *Phys. Rev.*, D82:074018, 2010.